Development of Nanocarriers for Treatment and Diagnostics of Aspergillosis

Dissertation zur Erlangung des naturwissenschaftlichen Doktorgrades der Julius-Maximilians-Universität Würzburg

vorgelegt von

Sonja Horvat-Csóti, geb. Horvat

aus Vrbas, Serbien

Würzburg 2021

CC BY NC ND

Eingereicht bei der Fakultät für Chemie und Pharmazie am

_____

Gutachter der schriftlichen Arbeit

1. Gutachter: _____

2. Gutachter: _____

Prüfer des öffentlichen Promotionskolloquiums

1. Prüfer: _____

2. Prüfer: _____

3. Prüfer: _____

Datum des öffentlichen Promotionskolloquiums

_____

Doktorurkunde ausgestellt am

_____

Dedicated to patients who during this thesis suffered from invasive aspergillosis.

This work was conducted from October 2015 until July 2019 at the Department for Functional Materials in Medicine and Dentistry, University Hospital of Würzburg, Germany under supervision of Prof. Dr. rer. nat. Jürgen Groll.

Acknowledgments

Firstly, I would like to thank Prof. Dr. Jürgen Groll for selecting me as a research assistant and a Ph.D. candidate in his department, and for giving me an interesting topic to work on. It was a great pleasure to expand my knowledge in the scientific environment he created.

My great acknowledgments go to Dr. Krystyna Albrecht for the trust she had in me and for her patience during my stay at FMZ. She supported me in designing projects while letting me organize and plan the studies freely. Her discussions helped me to broaden my knowledge in study design, nanotechnology, and colloids in general. She adviced me how to organize ideas for the projects in a more structured way and was great support in the review of the thesis and manuscripts.

I want to thank the taxpayers of Germany and King Saud University for financial support, without this thesis would not be possible.

Also, I am greatly thankful for anonymous reviewers for their critics and valuable comments on manuscripts submitted to journals.

Many thanks to Dr. Jörg Teßmar, who helped me significantly in the field of analytics, especially in GPC and HPLC. His ideas and suggestions often inspired me to explore the challenges of polymer and particle synthesis and their characterization in more detail.

This work would not be possible without cooperation partners. Many thanks to Prof. Dr. Andreas Beilhack for his ideas and valuable discussions, and for letting me working in Imib labs; Hannah Manz and Dr. Yidong Yu for wonderful collaboration; Musga Qureischi, Dr. Juliane Medler and Prof. Dr. Harald Wajant for dectin-1 isolation; Dr. Volker C. Behr, Dr. Patrick Vogel and Dr. Thomas Kampf who were responsible for the analysis of magnetic properties of particles; Dr. Ingrid Teßmer and Szalbolcs Böjte for performing AFM analysis of fungal cells

and Prof. Dr. Williams for his suggestions regarding β-glucan isolation and for the synthesis of diamino propane β-glucan phosphate. I would also like to thank Prof. Dr. Taeghwan Hyeon and Dr. Byung Hyo Kim for advices regarding purification of SPIOs; Prof. Dr. Aws Alshamsan, Dr. Andreas Brandl, Dr. Hisham A. Alhadlaq and Dr. Maqusood Ahamed for their collaboration in a project concerning SPIOs.

I am also very grateful to Dr. Andrea Ewald and Simone Werner who supported me in cell studies; Dr. Thorsten Keller for binding affinity studies as well as for the isolation and purification of dectin-1, and his generous support in the review of thesis; Julia Blöhbaum for lab assistance during my first months at FMZ especially in area of poly(2-methyl-2-oxazoline)s; Michaela Rödel for HPLC; Ilona Zilkowski for teaching me basics of poly(glycidol)s; Judith Friedlein and Philipp Stahlhut for EDX measurements; Isabell Biermann for support in XRD; Johanna Lutz for synthesis of carboxyl functionalized poly(glycidol)s; Dr. Tomasz Jüngst for lending me keys for CLSM lab; Christoph Böhm for assistance in Karl Fisher titration; Tanja Dambach and Birgit Langner-Bischof for arranging meetings and handling paperwork, and Anton Hofmann and Harald Hümpfer for assistance in DIY issues.

I would also like to thank Malik Salman Haider from the research group of Prof. Dr. Luxenhofer for interesting discussions we had about drug carriers; Johannes Herbig, Johanna Lutz, Almoatazbellah Youssef, Andrei Hrynevich and the rest of FMZ team for the nice time I had at the department.

I am thankful to my parents, sisters, aunt and grandmother who always encouraged my curiosity.

Finally, this thesis would not exist without my husband Bojan, who gave me love and who tolerated my long working hours and preoccupation with the subject.

List of Publications

1) **Horvat S.**, Yu Y., Böjte S., Teßmer I., Lowman D.W., Ma Z., Williams D.L., Beilhack A., Albrecht K., Groll J., Engineering Nanogels for Drug Delivery to Pathogenic Fungi *Aspergillus fumigatus* by Tuning Polymer Amphiphilicity, Biomacromolecules, **2020,** 21 (8), 3112-3121.
   doi: 10.1021/acs.biomac.0c00489
2) **Horvat S.**, Vogel P., Kampf T., Brandl A.,. Alshamsan A, Alhadlaq H.A., Ahamed M., Albrecht K., Behr V.C., Beilhack A., Groll J., Crosslinked Coating Improves the Signal-to-Noise Ratio of Iron Oxide Nanoparticles in Magnetic Particle Imaging (MPI), ChemNanoMat. **2020**, 6, 755.
   doi: 10.1002/cnma.202000009
3) **Horvat S.**, Yu Y., Manz H., Keller T., Beilhack A., Groll J., Albrecht K., Nanogels as antifungal-drug delivery system against *Aspergillus fumigatus*; Adv. NanoBiomed Res. **2021**, 2000060.
   doi: 10.1002/anbr.202000060

Author contributions for each manuscript are listed under the respective Sections.

Table of Contents

List of Abbreviations

3D	Three dimensional
AEMA	[2-(Acryloyloxy)ethyl]trimethylammonium chloride
AFM	Atomic force microscopy
AmB	Amphotericin B
ANS	8-Anilinonaphthalin-1-sulfonic acid
BA	Thiol modification from dithiobutyric acid
Cac	Critical association / aggregation concentration
CEA	2-Carboxyethyl acrylate
CaH_2	Calcium hydride
CLSM	Confocal laser scanning microscopy
Conc.	Concentration
COOH	Carboxyl group
CROP	Cationic ring-opening polymerization
CW	Cell wall
$Đ$	Polydispersity index (GPC)
DA	Diacrylate
DCC	N,N'-Dicyclohexylcarbodiimide
DCR	Derived count rate
d_h	Hydrodynamic radius as determined by intensity weighted size distribution by DLS
DL	Drug loading
DMAP	4-Dimethylaminopyridine
DMF	Dimethylformamide
DMSO	Dimethyl sulfoxide
DTPA	Dithiopropionic acid
DTT	Dithiothreitol

EDC	1-Ethyl-3-(3-dimethylaminopropyl)-carbodiimide
EDX	Energy dispersive X-ray spectroscopy
EE	Encapsulation efficiency
EEGE	Ethoxy ethyl glycidyl ether
em.	Emission
evp.	Evaporation
exc.	Excitation
Fc	Fragment crystallizable region
$Fe(acac)_3$	Iron (III)-acetonate
Fe-oleate	Iron-oleate
FFL	Field-free line
FFP	Field-free-point
FOV	Field of view
FT IR	Fourier-transform infrared spectroscopy
GFP	Green fluorescent protein
GNP	Gold nanoparticles
GPC	Gel permeation chromatography
GSH	Glutathione
HCl	Hydrochloric acid
HEA	2-Hydroxyethyl acrylate
HLB	Hydrophilic-lipophilic balance
^1H NMR	Proton nuclear magnetic resonance
HPLC	High-performance liquid chromatography
IA	Invasive aspergillosis
incl.	Including
Int.	Intensity
ITZ	Itraconazole
k_i	Constant of initiation
k_p	Constant of propagation

k_t	Constant of termination
K_D	Constant of dissociation
KOtBu	Potassium *tert*-butoxide
LCROP	Cationic ring-opening polymerization with a living character
mAb	Monoclonal antibody
$MgSO_4$	Magnesium sulfate
MIC	Minimal inhibitory concentration
Mn	Number average molecular weight
MPI	Magnetic particle imaging
MPS	Magnetic particle spectroscopy
MRI	Magnetic resonance imaging
Mw	Weight average molecular weight
NaCl	Sodium chloride
NGs	Nanogels
NHS	N-hydroxysuccinimide
OA	Oleic acid
OH	Hydroxyl group
ORO	Oil red O
PA	Thiol modification from dithiopropionic acid
PBS	Phosphate-buffered saline
PDI	Polydispersity index (DLS)
pEEGE	Poly(ethoxy ethyl glycidyl ether)
pEG	Poly(ethylene glycol)
pEI	Poly(ethyleneimine)
PF127	Pluronic f127
PF127DA	Pluronic f127 diacrylate
pG	Poly(glycidol)s
pMOx	Poly(2-methyl-2-oxazoline)
pMOx-EI	Poly(2-methyl-2-oxazoline)-co-(ethyleneimine)

pPO	Poly(propylene oxide)
pTsOH	p-Toluenesulfonic acid
r_2	Transverse relaxivity
R_2	Transverse relaxation rate
ran	Random
RBC	Red blood cells
Rh6g	Rhodamine 6g
RI	Refractive index
RNA/DNA	Ribonucleic / deoxyribonucleic acid
ROS	Reactive oxygen species
RT	Room temperature
R&D	Research and development
S(T)EM	Scanning (transmission) electron microscopy
SH	Thiol group
SNR	Signal-to-Noise-Ratio
SPIOs	Superparamagnetic iron oxides
SPR	Surface plasmon resonance
T_2	Relaxation time
TCEP	Tris(2-carboxyethyl)phosphine
TEA	Triethylamine
THF	Tetrahydrofuran
TMAO	Trimethylamine N-oxide
TWMPI	Traveling wave magnetic particle imaging
UV	Ultraviolet
UV-Vis	Ultraviolet-visible light spectroscopy
v/v	Volume percent
w/v	Weight/volume percent
w/w	Weight/weight percent

1 Introduction

In the lecture "There´s Plenty of Room at the Bottom: An Invitation to Enter a New Field of Physics" held in 1959 to American Physical Society at the California Institute of Technology, Nobel Laureate Richard Feynman introduced possibilities of molecular-scale engineering and challenged the scientific community to think small.[1] This is often acknowledged as the "birth of nanotechnology", where the matter is manipulated at near-atomic scales.[2]

By definition, nanomaterials are all objects with dimensions of 1-1000 nm and as such, they are intermediates between macroscopic objects and molecules. Thanks to their unique properties that arise at the nanoscale, such as high surface-to-volume ratio and change in physicochemical properties due to quantum effects, nanoparticles are used in various industries, such as chemical, automotive and healthcare and are incorporated into more than 2000 consumer products.[3-4]

Nanomedicine is the field of nanotechnology which is focused on the use of nanomaterials in medicine for treatment or diagnosis of diseases. Most commonly, nanomedical research and development is focused on cancer treatment, while research activities for the application of nanomaterials for other therapeutic conditions remained poorly explored. However, this field have recently gained in importance as well.[5] One of the promising applications of nanomaterials lays in the treatment of infectious diseases caused by pathogenic bacteria, fungi and yeasts.[6]

Invasive fungal infections occur relatively rarely, but the mortality rate of the patients affected is devasting and despite progress in antifungal therapy can reach up to 80 % in case of invasive aspergillosis (IA) caused by *Aspergillus fumigatus*.[7-9] IA most often starts from lungs, and in a short time spreads to other organs such as brain, liver or kidneys, causing their malfunctioning and life-threatening complications.[7-9] These infections occur to immunocompromised patients such as those who suffer from IA are those who receive(d) chemotherapy or

immunosuppressive drugs, or recipients of organs such as heart or lungs. Moreover, invasive fungal infections are considered as the main cause of death of patients after cell stem transplantation.[10] IA occurs not only to immunocompromised patients but also to critically ill ones, which makes it a severe threat to intensive care unit patients.[11-12] Fungi form biofilms, which further complicates treatment due to the increased resistance of biofilms against antifungals.[13]

Currently, there is a rise in the discovery of antifungals, but despite advances, there is an urgent need for innovative strategies.[10, 14] One of the new approaches in IA treatment is nano-mediated drug delivery.[15]

Among nanomaterials, nanogels occupy considerable scientific attention in drug delivery and diagnostics.[16] They have both properties of nanomaterials, that is nanoscale dimensions and high surface area to volume ratio, and those of hydrogels, high water content, tunable chemical and mechanical properties, controllable crosslinking density and possibility for encapsulation of small drug molecules and biomacromolecules.[16]

Of special interest are nanogels composed of poly(glycidol)s which are considered as alternative polymers to polyethylene glycol, the gold standard in biomedical applications. Poly(glycidol)s contain hydroxyl group in each monomer unit available for further functionalization in comparison to poly(ethylene glycol) which contains two hydroxyl groups per polymer the most, one at each end. This makes poly(glycidol)s attractive for nanogel synthesis.[17-19] Part of the thesis of Dr. Singh dealt with functionalization of these polymers with thiols and their potential use in nanomedicine.[20] Her work served as a basis for this thesis. On the other hand, although there are papers that reported on the application of nanomaterials against fungal species,[21-23] there are no records about the use of poly(glycidol)-based nanoparticles against *A. fumigatus* prior this work.

1.1 Aim of the thesis

This thesis deals with the optimization of nanoparticles based on thiol

functionalized polymers for antifungal therapy and diagnostics. Nanogels were investigated as candidate vehicles for antifungal drugs, while superparamagnetic nanoparticles were optimized for magnetic particle imaging.

Chapter 2 gives a short overview of the application of nanogels and current status of the nanoparticle-assisted treatment of fungal diseases. **Chapter 3** discusses the results obtained within this thesis and is divided into several sections. **Section 3.1** describes the synthesis nanogels based on poly(glycidol)s and poly(2-methyl-2-oxazoline)s. Herewith, the influence of polymer type and the surface charge on the absorption and internationalization of nanogels by fungal cells was investigated. Also, the interaction of nanogels with mammalian cells was evaluated to understand the potential faith of the nanogels when administrated *in-vivo*. **Section 3.2** deals with the nanogels formed spontaneously by self-assembly. The main goal was to evaluate the influence of amphiphilicity of the polymers in nanogels on the interaction with fungi. Antifungal drug amphotericin B was encapsulated in nanogels and toxicity profile of nanoparticles was analyzed. **Section 3.3** is focused on narrowing the size distribution of nanogels while important properties discovered in previous chapters remained. Nanogels with low polydispersity index were loaded with itraconazole utilizing "breathing-in" method. **Section 3.4** describes the synthesis of magnetic nanoparticles optimized for imaging purposes by magnetic resonance and traveling wave magnetic particle imaging. In the **Section 3.5**, the possibility of targeting the fungal cell wall polysaccharides by conjugation of dectin-1 protein to poly(glycidol)-decorated gold nanoparticles was evaluated by binding affinity studies.

Chapter 4 summarizes the results of the thesis and gives the outlook for future research and perspectives in this field.

Chapter 5 provides experimental data for all studies presented in this thesis.

2 Background

2.1 Invasive aspergillosis – brief description

Invasive fungal infections are frequent complications of the patients with the compromised immune system. It is estimated that these infections cause more than 1.5 million deaths per year worldwide.[24] In the European Union (EU 25) including Norway, Iceland and Liechtenstein aspergillosis is cathegorizied as a rare disease, and it is estimated that approximately 2.2 in 10,000 people in the union are at the risk of developing the pulmonary fungal infections (EU/3/06/391, 2006). In Germany the most common invasive fungal infection is invasive aspergillosis (IA) caused predominantly by filamentous fungi *Aspergillus fumigatus*.[25-26] These fungi are ubiquitous and their conidia are found in concentrations of 1–100 conidia/m^3 of air, both indoors and outdoors.[25] Conidia are inhaled by mammals where in case of an insufficient number of immune cells germinate into hyphal structures in the lower respiratory tract.

Healthy individuals have enough mechanisms to cope with inhaled conidia, which absorb on lung epithelium and are either recognized by immune cells such as macrophages, neutrophils, and T-cells immediately or after germination (Figure 2.1- 1).

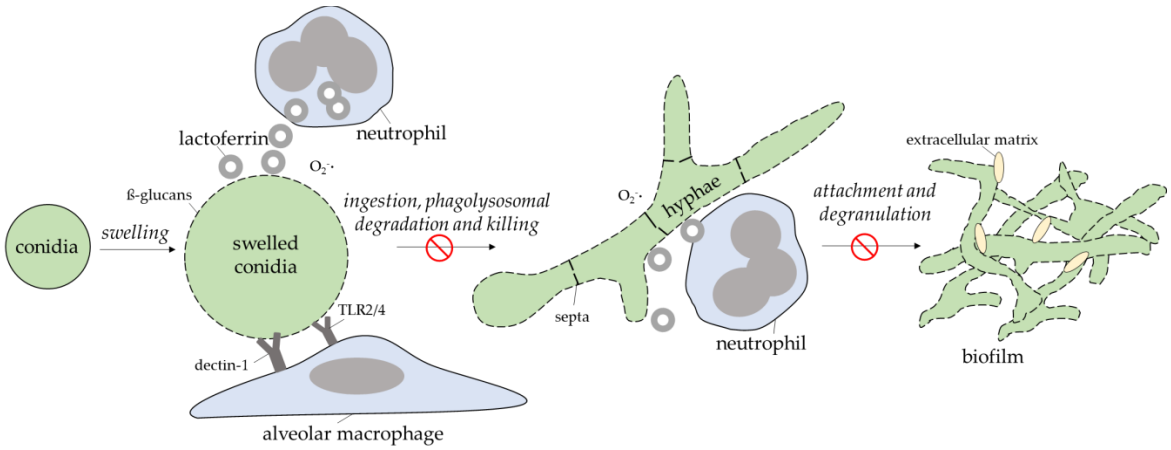

Figure 2.1- 1: Schematic presentation of the start of the fungal infection upon inhalation. Reproduced with permission from reference [27]. Copyright © 2019, American Society for Microbiology, Copyright Clearance Center, Inc.

However, in immunocompromised patients who do not have essential immune cells, germinating conidia transform to hyphae and form a hyphal network called mycelium. Hyphae produce extracellular matrix, and, in this stage, fungal biofilm is particularly resistant to antifungals. If infection is not treated correctly, the hyphal network further degrades lung tissue and reaches the bloodstream. Subsequently, the infection is spread to other organs such as kidneys, brain and heart, causing life-treatening complications and often death.[25] Scans of the lungs and brain of one of the fataly infected patient by *A. fumigatus* are shown in the Figure 2.1- 2.[28]

2.2 Antifungals in IA

Several classes of antifungals are used for the treatment of systemic fungal infections. Three classes of antifungals are most commonly chosen for the treatment of IA, all of them causing severe toxicity, as summarized in Table 2.1-1, which also provides information about drug mechanism of action.

Amphotericin B (AmB) is a drug from the class of polyenes and because of its high effectiveness is usually a drug of the first choice. Additionally, AmB is one of the rare antifungals which does not cause the resistance by *A. fumigatus*. Unfortunately, the use of AmB in IA treatment is limited because of high renal toxicity. Development of nanoparticulate liposomal drug Ambisome® in the 1990s significantly reduced the toxicity and increased the efficacy of AmB in IA treatment.[29]

Triazoles are also commonly used in the first-line therapy of IA, especially voriconazole and itraconazole, but other drugs from this class might also be selected. This class of antifungals has lower toxicity in comparison to AmB, but fungal resistance towards these drugs is considered as the main limitation.[30]

Finally, caspofungin from the class of echinocandins is used alone or in combination with other antifungals, having better safety profile. However, it is a relatively new drug on the market, and its high price and signs of fungal resistance still limit its broad use.[31-32]

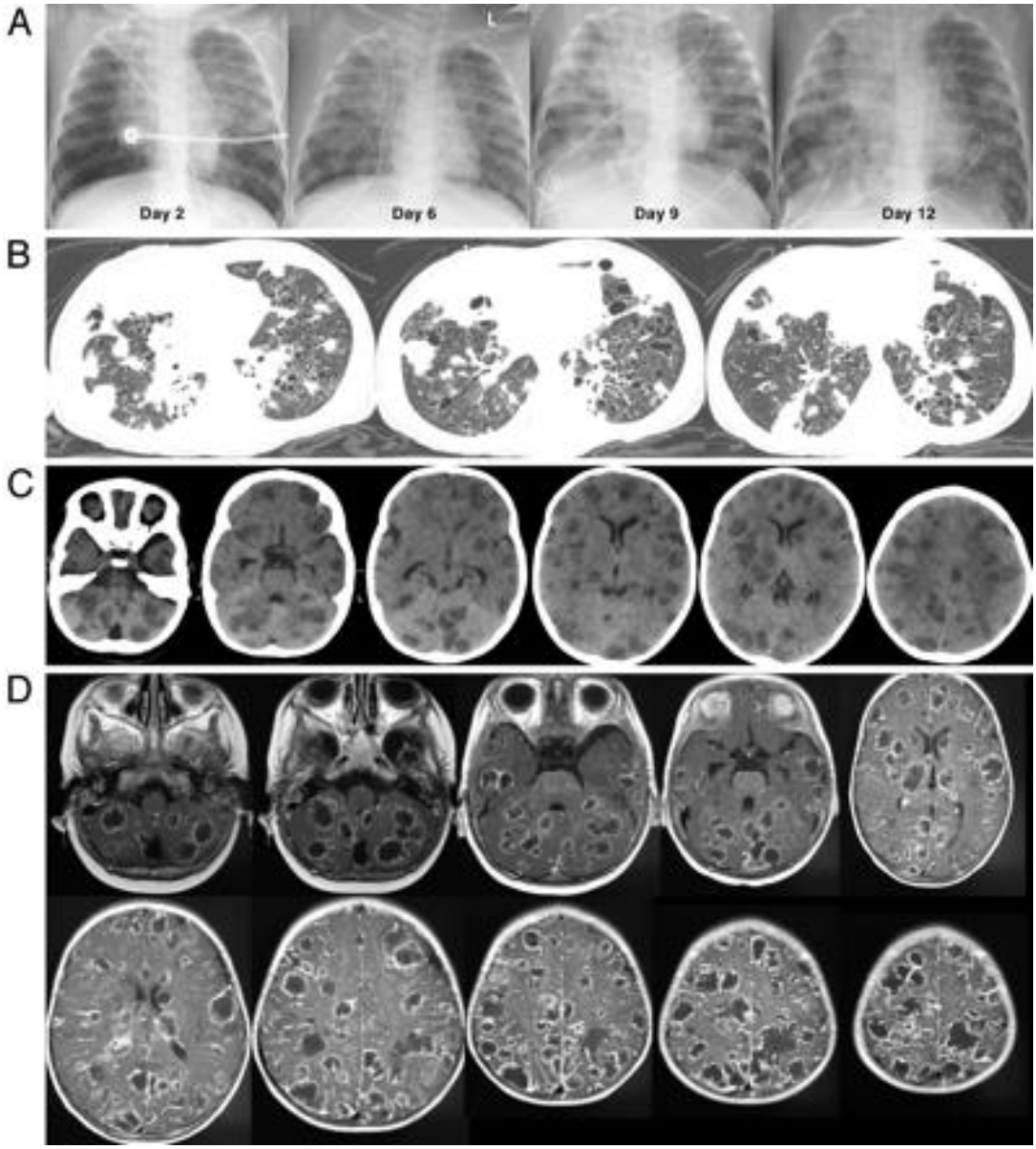

Figure 2.1- 2: Chest and brain scans of the 10-month old female patient. (A) Chest radiograph on days 2, 6, 9, and 12 upon arrival in the hospital. (B) High-resolution computed tomography of the chest on day 14 showing destructive lesions caused by *A. fumigatus*. (C) Computed tomography of the brain on day 14. (D) Magnetic resonance imaging of the brain on day 14 (T1-weighed + gadolinium) showing multiple hypodense lesions in the brain. Patient deceased on day 16 due to a course of IA. Reproduced with permission from Journal the American Academy of Pediatrics, Vol. 118, Pages e509-e513 , Copyright © 2020 by the APP.[28]

Unfortunately, almost 50 % of the infected patients do not respond to currently available treatments and 30 % of patients die within the first 12 weeks.[33] Therefore, it is urgently needed to find new therapies and strategies to cope with invasive fungal infections.

Table 2.1- 1: List of most important antifungals in the treatment of IA.[34]

Class	Agent	Mechanism of action	Common side effects
Polyenes	AmB	Binding to ergosterols in cell membrane leading to the formation of pores and electrolyte leakage	Nephrotoxicity Anemia Hypotension
Triazoles	Itraconazole Posaconazole Voriconazole	Inhibition of the ergosterol synthesis	Hepatotoxicity Hypokalemia
Echinocandins	Caspofungin	Inhibition of the β-glucan synthesis	Hepatotoxicity Hypotension

2.3 Nanocarriers for antifungals

Although it is estimated that every fourth hospitalized patient suffers from bloodstream fungal infection, there is still a tremendous need for a proper antifungal treatment which would slow down a spread of disease to other organs and ideally complete cure the patient.[23] Almost all antifungals used today are hydrophobic and therefore have a low oral bioavailability. Most of them also have high toxicity, resulting in severe side effects. Another issue of antifungals is fungal resistance after multiple dosing.[35] Because of these limitations, innovative antifungal therapies are urgently needed.

One of the strategies for overcoming high drug toxicity and low bioavailability is nanoparticle-mediated antifungal therapy.[23, 35] As stressed before, nanoparticles are used for encapsulation of drugs to increase drug bioavailability and efficacy while reducing drug side effect.[15, 22, 35] Interest in nanoparticles as antifungal carriers increased considerably in the last decade (Figure 2.1- 3), and there are several trial studies of nanoparticle-based formulations currently ongoing.[35]

Various types of nanoparticles have been investigated for antifungal therapy, such as nanovehicles, polymeric micelles, dendrimers, lipid, and metallic nanoparticles.[22]

It was shown that silver nanoparticles act as antifungal/antimicrobial agents

against *Candida* spp. as Ag^+ ions bind to the proteins of the cell membrane or intracellular proteins and phosphorus containing molecules, thus damaging the cell.[22, 36-37] Similar antifungal action has been shown for gold nanoparticles.[38]

Liposomes are nanoparticulate vesicules that consist of one or multiple membranes composed of phospholipid bilayers. This class of nanoparticles is extensively studied as antifungal carriers.[39-40] Liposomal preparation AmBisome® is one example of the nanoparticle-based products containing AmB as drug substance approved by the Federal Drug Administration (FDA) and some European countries, e.g. United Kingdom. However, as liposomes are not targeted and therefore not specific to only fungal cells, some toxicity still remains.[15, 29, 35] Despite promising results of this advanced therapy, one-year survival among patients with invasive aspergillosis is still poor. Attempts to introduce generics of this drug on the marked failed due to the much higher toxicity, although the same composition and apparently same manufacturing process were used as for the reference product AmBisome®.[41]

Nanoparticles composed from polymers offer flexibility such as: control over surface charge, hydrophobicity, functionalization with ligands, and drug release. Nanogels are relatively new class of polymeric nanoparticles explored to be used as antifungal nanocarriers. It was shown in the study of Roudbarmohammadi et al., 2018[42] that chitosan-based nanogels were able to efficiently encapsulate farnesol and to inhibit the fungal growth of *Candida albicans* while remaining non-toxic to the mammalian cells. However, a potential of the use of nanogels as drug carriers in the antifungal therapy still remains to be evaluated.

Antifungal drugs were also encapsulated in dendrimers. For example, it was shown that poly(amidoamine) dendrimers increased antifungal activity of water insoluble drug clotrimazole agains *Candida* spp.[43] Unfortunately, despite that this class of nanoparticles received a lot of attention in nanomedical research due to the high surface functionality, branching points and control over size, they are poorly translated to the clinic mainly because of the solubility problems, non-defined drug-dendrimer compound mixtures and high production costs.[44]

2.4 Nanogels

In the last two decades, much of the attention has been driven to the chemically or physically crosslinked polymeric hydrogel-like networks called nanogels. From 2016 to mid of 2019, in which this dissertation was carried out, around 35000 papers with an emphasis on nanogels were published (Figure 2.1- 3). Cause of the interest for nanogels lays in the broad application of such nanocarriers and their characteristics. Nanogels swell by adsorption of solvent without dissolution as they are composed from the crosslinked polymer network.[45] They are considered as the promising drug delivery carriers since they have high loading capacity and high stability. Moreover, nanogels can be formed either from hydrophilic and amphiphilic polymer chains. This property ensures the loading of hydrophilic, amphiphilic and hydrophobic drugs.[46-47]

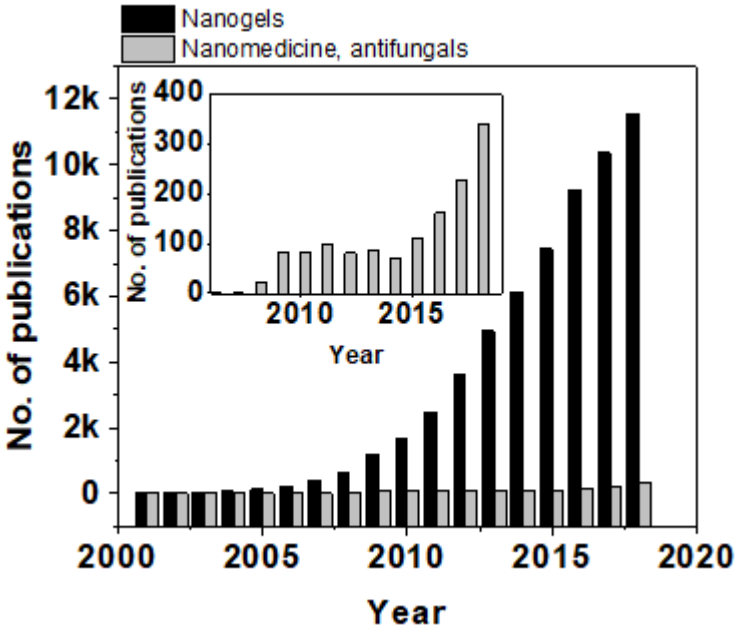

Figure 2.1- 3: Number of publications with the emphasis on "nanogels" and "nanomedicine and antifungals". (Web of Science®, April 2019).

Swelling behavior is an important property of nanogels. It is controlled by the crosslinking density, charge density of polymers, pH, temperature, and other environmental parameters. Higher amounts of crosslinker or higher crosslinking

density lead to the lower swelling degree. In the case of polyanionic nanogels, the swelling degree increases with the pH and decreases in the case of polycationic nanogels. Shrinkage can also occur when the ionic strength of the solution is higher. Similarly, swelling-shrinkage induced by temperature is observed in the case of thermo-responsive nanogels.[16]

There are three methods used for drug loading in nanogels: physical entrapment, covalent attachment, and controlled self-assembly of oppositely charged solutes.[16] Physical entrapment is the method in which cargo is loaded during the synthesis of the nanogels. In this case, cargo is trapped inside nanogels as soon as the crosslinking reaction takes place. It is important, however, to take care of the mesh size of the crosslinked polymeric network, since cargo does not have an affinity to the polymer chains and may escape from the nanogels by diffusion before reaching the target site.

Cargo can also be covalently bound to the polymers before the crosslinking reaction. In this case, two steps must occur to release the drug: (1) cleavage or contraction of the nanogels and (2) cleavage of the bond between polymers and the drug.

Last approach of drug loading is using polyelectrolyte-based nanogels. Cargo is usually oppositely charged from the polymer chains and the resulting nanomaterials are characterized by high binding cooperativity. Very often, physical entrapment is combined with self-assemby of polyelectrolytes, and in this case combination of polyionic and hydrophobic interactions considerably stabilizes drug-nanogel formulations.[16]

Depending on the type of crosslinking and of polymer type, nanogels are considered cleavable or non-cleavable. Drug release from non-cleavable nanogels is usually achieved by ion displacement, energy input or by deswelling caused by a certain change in the temperature or pH value. In the case of cleavable nanogels, presence of certain molecules in the surrounding environment leads to cleavage of crosslinking bonds or polymer chains and finally to the cargo release.[16, 48]

2.4.1 Redox-responsive nanogels

Since 1970s when the term stimuli-responsive nanoparticles first appeared, the concept of drug release from the nanoparticles triggered by the stimuli has drawn great scientific attention. Among other stimuli-responsive nanoparticles, pH-, enzyme- and redox-responsive nanoparticles can release the cargo in the intracellular environment. Intracellular delivery is important when therapeutics need to reach specific organelles,[49] especially in delivering pharmaceutical peptides, proteins, and nucleic acids. For example, siRNA, mRNA, and miRNA should be delivered to the cytosol where they are translated. Another example is encapsulation of DNA for transfection, which for efficient action needs to cross not only the cell membrane but also the nuclear one.[50]

Next to pH- and enzymatic-responsive nanoparticles, redox-responsive systems are of particular interest in nanomedicine research. Presence of disulfide bonds is the main characteristic of redox-responsive nanogels. This bond is sensitive to reducing agents, which convert it into two free thiols. Glutathione (GSH) is the main molecule which keeps the cytosol in reductive conditions. This happens dynamically, by constant exchanging between glutathione-oxidized GSSH to glutathione-reductive GSH state. Keeping the intracellular matrix under these conditions, the cell ensures that the reactive oxygen species (ROS) and other toxic products of the cell metabolism are digested and inactivated. Since the concentration of the glutathione is much higher inside mammalian and fungal cells (2-10 mM) than in extracellular matrix (2-20 μM), redox-responsive nanogels stay intact and are stable until they are up-taken.[49,51-52] Inside cells disulfide bonds cleave by GSH, which leads to the drug release.[17, 51, 53-56]

It was reported elsewhere that e.g. gold nanoparticles bind to the cell wall of microbes due to the thiol-thiol interactions.[22] This might also happen in the case of redox-responsive nanogels, where the thiol-thiol exchange is possible.[57]

There are two approaches to the payload encapsulation in the redox-responsive nanogels, similarly as in another type of nanoparticles. The first approach includes conjugation of the cargo to the polymer by disulfide bonds and subsequent

formation of the nanogels by crosslinking or self-assembly. In this case, a covalent bond between the drug and the polymer keeps the drug intact inside nanogels until reaching the cytosol. In the work of Navath et al.[58] the N-acetyl cysteine, small molecular weight drug was conjugated to the 6- and 8-armed thiol functionalized poly(ethylene glycol) (pEG) from which nanogels were formed. After intracellular release, the drug remained in its free form and remained active because its chemistry was not changed during the conjugation. Drug-loaded nanogels showed pronounced inhibition of the nitrite production and ROS in cells and had higher anti-inflammatory activity in the BV-2 cells than free drug, even in much lower concentrations due to the higher uptake. Similar promising results were observed by Ghersi et al.[59] They reported successful conjugation of the Bcl-2 siRNA and anticancer drug doxorubicin and subsequent formation of the nanogels by a disulfide spacer. Drug and nucleic acid release happened only in cancerogenic cells, which were achieved by designing the systems that cleaved only in the highly reductive environments (20 mM GSH). Their work further showed that modification of the siRNA necessary for conjugation did not affect the activity of this molecule, and proved that these nanogels could be used in the cancer treatment. Other examples include conjugations of siRNAs to the pEG-based nanogels formed by lithography method as reported by Dunn et al.[60] To prevent siRNA escape from the nanogels during systematic administration, which leads to the loss of the efficiency of gene silencing, the group decided to conjugate the siRNA to the pro-drug by amide bond and, further, to bind it to the pEG chains by disulfide bonds. They altered the toxicity of these nanocarriers by changing the amounts of amines in the nanogels and showed that desirable gene-knock-down silencing occurred already in the nanogel concentrations well below the limits of toxicity.[60]

The second approach in drug loading in redox-responsive nanogels is by physical entrapment of the drug inside the polymer network of nanogels. In this way, the drug functionalization with the thiol groups to be encapsulated inside the nanogels is not required. Therefore, there are no issues such as loss of therapeutic

activity.[61] However, the hydrodynamic size of the payload has to be larger than the mesh size of the polymer network, because, otherwise, the payload releases before reaching its target point. One of the first reports about physically entrapped payload in redox-sensitive nanogels were done by Park et al.[62] They showed that plasmid DNA could be stabilized in the DMSO by the thiol-functionalized 6-arm pEG without denaturation. Spontaneously, the polymer was assembled around the DNA chains, and particles were formed in the presence of crosslinkers. They observed that these particles swell in the presence of water and release DNA in the reductive medium. In another approach, Hennik et al.[63] also used neutrally charged nanogels for gene transfection. They produced nanogels with the core containing poly(hydroxypropyl methacrylamide) crosslinked with the disulfide moieties together with the plasmid DNA. These nanogels were further decorated with pEG, which led to the lower cytotoxicity in comparison to the positively charged particles. Maryjaszewski et al.[64-65] synthesized redox-responsive nanogels formed by electron transfer atom transfer radical polymerization in inverse miniemulsion from methacrylates crosslinked with the disulfide containing moieties. After that, plasmid DNA and siRNA were complexed with these nanogels and released intracellularly in *Drosophila* S2 cell-line and osteoblasts.[64-65] Similarly, Groll et al. [56] used poly(glycidol) based nanogels covalently bound to positively charged cell penetrated peptide (TAT) for physical entrapment of mRNAs. They showed that these nanogels were able to deliver genetic material to the transfection-resistant OPM-2 cells.[56]

Not only nucleic acids were successfully encapsulated within the redox-responsive nanogels, but drugs as well. Paik et al.[66] used atom transfer radical polymerization approach to synthesize 250 nm nanogels with the pEG-based monomer and pEG disulfide crosslinker for photodynamic therapy. After freeze-drying, nanogels were hydrated in tetrahydrofuran in which chlorine e6 was dissolved. Finally, nanogels were dialyzed in water to obtain water dispersive nanogels. On the other hand, Yang et al.[67] produced pH and redox-responsive poly(N-isopropyl acrylamide)-ss-acrylic acid nanogels by precipitation

polymerization and *in-situ* encapsulation of the anticancer drug doxorubicin. They proved that doxorubicin was released from the nanogels in the lysosomes followed by the endosomal escape and complete release by the GSH-triggered nanogel digestion. Their results also indicated that drug-loaded nanogels had higher efficiency and fewer side effects in *in-vivo* studies in comparison to the drug delivered in its free form.

Similarly, Nguyen et al.[52] used thiol-functionalized Pluronic-heparin copolymer to self-assembly the proteins. Using prolonged stirring, sonication, and addition of hydroxide-peroxide, the free thiols oxidized and entrapped the proteins. They further showed that the release profile could be controlled by varying the number of disulfide bonds, while the hydrodynamic diameter of the nanogels remained less than 100 nm. In another work, Ma et al.[68] reported the promising results in the nanogel-based vaccine delivery. Cationic alginate-polyethylene polymers were self-assembled into nanoparticles and crosslinked either by the (3,3′-dithiobis(sulfosuccinimidyl propionate)) or by bis(N-hydroxysuccinimide ester) to obtain cleavable and non-cleavable nanogels, respectively. Protein ovalbumin as a model drug was subsequently added to the nanogel dispersion and was loaded into the nanogels by the electrostatic interactions. By changing the crosslinking density, it was possible to alter the stability of nanogels in the aqueous solution over time. The group also analyzed the ovalbumin-specific immune response in mice in *in-vivo* experiments and observed that production of all isotypes of immunoglobins G was increased when redox-responsive cleavable nanogels were used. Few reports also dealt with the dual-responsive nanogels. In this way, nanogels not only cleaved under reducing conditions, but they responded simultaneously to e.g. UV light or external magnetic field as well.[69-70] Another example is work of Lee et al.[71] which reports that methoxy(poly(ethylene glycol))-block-poly(dopamine-diethylenetriamine-L-glutamate) crosslinked with the disulfide bonds could be assembled with magnetic nanoparticles and fluorescent probes, which served as the potential magnetic and infrared imaging vector for cancer diagnostics.

2.5 Drug delivery and design consideration for polymeric nanocarriers

Understanding the mechanism of the clinical condition leads to the discovery of new drugs "that in a specific way, block or activate proteins or pathways in the cells responsible for the occurrence of the disease".[72] However, despite tremendous progress in drug discovery nowadays, there are certain limitations concerning therapeutic drug efficiency.

After drug administration to the patient, therapeutic efficacy is usually lower than expected and is often followed by side effects. Therapeutics commonly have a molecular weight not higher than several hundred g/mol and diffuse non-selectively into tissues. This leads to the broad drug distribution in the patient´s body and low concentration of the drug in the site of interest.[73] Therefore, to achieve the desired effect, drug doses are elevated, which results in toxicity. Besides that, there are problems regarding fast clearance and difficulties related to the inability of the drug to cross specific biological barriers. The organs that usually suffer from drug-induced toxicity are kidneys, liver, brain, gastrointestinal and cardiovascular organs. This is especially the case in the highly toxic drugs with the narrow therapeutic index that are used to treat life-threatening diseases including invasive fungal infections.[74-77]

Encapsulation of a drug in polymer assemblies is a promising way to overcome mentioned challenges. In polymeric nanocarriers, such as polymeric nanoparticles, polymeric micelles, nanogels and polymersomes, the drug is loaded in the polymeric matrix which is not larger than 1000 nm in diameter.[78-80] As soon as the nanocarrier reaches the site of interest, it should respond to the environment and release the drug as described previously. This approach considerably improves therapeutic efficiency and lowers drug-induced toxicity. Responsiveness can be pH triggered,[47] temperature,[81] ionic strength[82] or redox-depended,[83] to mention a few.

The function of polymers in nanocarriers is thus both protecting the cargo from non-targeting cells and proteins that would degrade it, and the organism from the toxic cargo. In designing polymeric nanoparticles, there are several parameters

that dictate their physical, chemical and biological properties: size, shape and surface chemistry.[84-87]

Circulation time of drug nanocarriers depends on the presence of polymers that have a stealth effect.[88] A higher density of stealth polymer on the surface of the particles ensures better results, but this is, however, also depended on the molecular weight of polymers. A layer of stealth polymers on the surface of the nanocarrier should be thick enough to overcome the van der Waals attractive forces between cargo and proteins in the blood.[89] On the other hand, smart moieties which enhance uptake by cells, such as cell-penetrating peptides, specific antibodies, certain small molecules etc. might trigger the specific cell uptake and ensure targeted drug delivery.[85, 90]

2.6 Endocytosis in fungal cells

As highlighted earlier, interaction of nanoparticles with fungi is an essential aspect to be considered when designing nanoparticulate systems that need to release a payload intracellularly. Therefore, it is crucial to understand the internalization mechanisms of fungi.

In comparison to mammalian cells, the cell wall (CW) of fungal species and microbials is the first barrier that nanoparticles need to cross to reach the cell membrane and cytosol. Approximately 20 - 30 % of a dry fungal mass accounts for the CW. His primary function is protective, but it also keeps fungal cell integrity and is actively involved in mating and adherence to substrates.[91]

CW of filamentous fungal species is mainly composed of polysaccharides chitin and glucans. β (1,3)-glucans are connected by hydrogen bridges forming a 3D network attached to the inner side of CW, while chitin and β (1,6)-glucans are placed on the outer side. Other polysaccharides such as mannans, galactomannans, and alkali-soluble glucans are present in fewer amounts. Proteins are also important constituents of CW. It is believed that glycoproteins control CW permeability and are responsible for fungal adherence to hosts. Other CW proteins are hydrophobins, which dictate fungal hydrophobicity.[91-92]

Besides the CW, fungal cells also have a membrane, which is similar to a membrane of mammalian cells. It is situated beneath the CW and is mainly composed of the lipid bilayer (approx. 5 nm) in which membrane proteins are unevenly distributed. Lipids in the bilayer of the cell membrane are always in the motion, which makes the cell membrane dynamic hydrophobic barrier.[93]

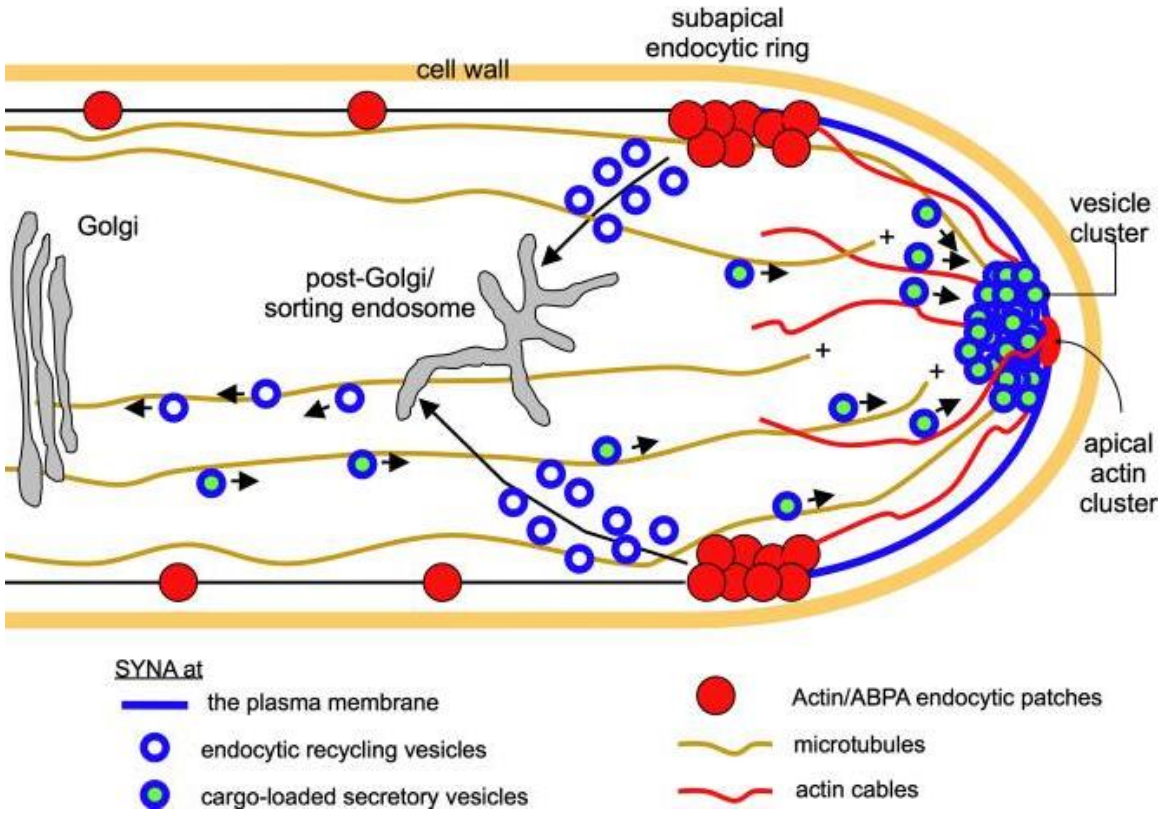

Figure 2.1- 4: Model for endocytosis pathway in filamentous fungi according to Taheri-Talesh et al.[94] Reproduced with permission from reference[94]. Copyright © 2019, American Society for Cell Biology.

Although fungal morphology is well-known to the scientific community, discussion about endocytosis in filamentous fungi is still ongoing. It is proved that endocytosis exists in filamentous fungi as a counterpart to exocytosis and that both pathways are essential for apical growth of filamentous fungi.[95] Endocytosis is important for the uptake of signal molecules, removal and recycling of membrane proteins, and lipid degradation. It is proved that not only filamentous fungi endocytose,[96] but also that endocytosis happens even in the stage of conidial germlings.[93] Although there are speculations about the mechanism of endocytosis

pathways, it is believed that fungal hyphae uptake nutrients in the Spitzenkörper where the subapical endocytic ring is situated. According to Taheri-Talesh et al. (Figure 2.1- 4)[94] vesicles containing components necessary for tip growth are extracted toward Spitzenkörper, while actin endocytic ring near the hyphal tip is moving forward and recycles the exosomes into endosomes which are constantly moved by microtubule towards Golgi apparatus. Unfortunately, the exact mechanism is still not completely known, and further investigations are in progress.[94, 97]

2.7 Conclusions

In summary, *A. fumigatus* causes serious fungal infections linked to high morbidity and mortality of immunocompromised and critically-ill patients. Due to the toxicity and limited effectiveness and toxicity of commercially available antifungals, nanoparticle-mediated treatment of invasive fungal infections attracts more attention. Among other types of nanoparticles, nanogels are a versatile tool for drug delivery and might be used in IA therapy. However, there are challenges that need to be considered, such as endocytosis pathways and the presence of CW in addition to the cell membrane.

3 Results and Discussion

3.1 Influence of charge on nanogel-fungi interaction

3.1.1 Introduction

Nanoparticle charge very often dictates the the fate of nanoparticles conforting the cells.[98-99] It is shown that positively charged nanoparticles are internalized to a greater extent in mammalian cells in comparison to neutral or negatively charged nanoparticles of the same size.[98] Several previous studies have been made to understand how particle size and charge influences the interaction with fungal cells as well.[100-102] Nomura et al.[100-101] showed that positively charged polys(styrene) latex nanoparticles bound to the cell wall of the hyphae, leading to the toxicity of fungal species. In their study, uptake of amine-functionalized particles depended on the ionic strength and the fungal strains. Lyden et al.[102] additionally showed that particle charge and size also influences the binding of nanoparticles to the cell wall. They observed that amine-functionalized particles did not bind to the cell wall as strong as carboxylate functionalized particles and that binding force of particles to fungi is higher in case of smaller particles. Further, there is an evidence that negatively charged nanoparticles bind to a greater extent to *Aspergillus fumigatus* dormant conidia, although it is believed that nanoparticle size has the highest impact on the nanoparticle accumulation on the cell wall of this fungi.[103] However, to the extent of our knowledge at the time during this thesis was written, there was no report available about how the soft nanogels interact with fungal pathogen *A. fumigatus* in its hyphal form.

This section evauates how nanogel charge influences the interaction of nanogels with fungi *Aspergillus fumigatus*.

3.1.2 Synthesis of polymers

Polymers used for the preparation of nanoparticles dictate their functionality in drug delivery. Choosing one polymer over another usually depends on the nature of the cargo and routes of carrier administration.

Poly(ethylene glycol) (pEG) has long been used as the main constituent of nanoparticles or for their coating.[104] PEGylated nanoparticles have long circulation time due to the ´stealth´ effect of pEG which prevents spontaneous adsorption of the blood proteins and subsequent recognition and uptake by immune cells. Because of that, pEG is considered as the gold standard in the nanobiotechnology. However, a recent study showed that pEGylated nanoparticles might induce immunogenic response after repeated administration.[105-106] These findings addressed a need for discovery and development of alternative polymers.

On the other hand, poly(ethyleneimine)s (pEI) are cationic polymers widely used in the research in the field of nanomedicie due to their positive charge. As other polycations, pEI can be condensed with negatively charged biomolecules such as DNA and siRNA. Because of that, it is extensively studied for gene delivery. Moreover, secondary amines in the backbone of the linear pEI offer versatile possibilities for functionalization. However, the application of pEI is limited by the pronounced cytotoxicity which is result of the high density of positive charges.[107] Therefore, positively charged polymers as alternative to pEI with lower toxicity are being developed.[107-108]

Poly(2-oxazoline)s are the class of the polymers that have been recently considered as promising macromolecules for surface functionalization and drug delivery.[109] Their polymer backbone consists of the ethylene unit between heteroatom analogous to pEG. Although poly(2-oxazoline)s are almost non-biodegradable due to their tertiary amines,[110] studies of Essler et al. showed that the polymers with molecular weight of around 4500 g/mol are eliminated from the body much faster than the pEG analogues.[111] They showed that polymers are being secreted from the body through kidneys fast enough not to induce toxicity and without accumulation in other organs.[111-112] Poly(2-oxazoline)-based nanoparticles, such as poly(2-methyl-2-oxazoline) (pMOx) modified liposomes, had long

circulation time and were not opsonized.[113-114] The similarity was observed when this kind of polymer served as a protein-repellant coating of Nb_2O_5-surfaces.[115] pMOx-coated surfaces showed high biocompatibility as well.[111, 116-117]

Under acidic or basic conditions or under influence of enzimes, linear poly(2-alkyl-2-oxazoline)s hydrolyze to linear pEI.[108] Usually, water soluble poly(2-alkyl-oxazoline)s, such as pMOx or poly(2-ethyl-2-oxazoline)s are used for this purpose, although poly(2-phenyl-2-oxazoline) and poly(2-isopropyl-2-oxalines) can be used as well.[108]

When only partial hydrolysis of poly(2-alkyl-2-oxazoline)s takes place, copolymers consisting of poly(2-alkyl-2-oxazoline)s and pEI are synthesized. With the ethyleneimine part, the secondary amine is introduced to the polymer backbone. This group then can act as a reactive spot of the polymer for the introduction of new functional groups by covalent binding.[118-119] Another potential application of such polymers is in complexation with negatively charged molecules such as nucleic acids by electrostatic interactions, which is often used for genetic modification of cells.[120] These copolymers not only carry positive charge necessary for functionalization or complexation, but are in the same time less toxic than pEI homopolymer.[108]

Thus, pMOx has a great potential to be used as the alternative to pEG and pEI.

Poly(glycidol)s (pG) belong to the class of polymers that are proved to have similar properties as pEG, such as bioavailability and ´stealth´ behavior. Study of Haag et al.[121] showed that pG decorated gold substrates not only prevented adsorption of proteins, such as fibrinogen, pepsin, albumin and lysozyme, but were also two times more prone to proteins in undiluted human plasma. Indeed, the backbone of this polymer is similar to pEG, but pGs have hydroxyl groups in the side chain, which can be further functionalized and conjugated to the antibodies or other ligands. This makes them attractive for the applications in the nanomedicine.[122-123] In addition, pGs do not cause immunogenic response after long use and are biocompatible when tested *in-vivo*. For instance, liposomes decorated with pG had long circulation time without inducing cytotoxicity. These liposomes did not show accelerated blood clearance after repeated injection in mice, in comparison to pEG-ylated lyposomes[124] and were biodegradable due to the presence of

ester bonds in backbone.[122]

Because of the above mentioned properties, linear pMOx and pG with comparable molecular weight of around 4500 g/mol were used for the preparation of nanogels. While pG served for the synthesis of nanogels with slightly negative charge, pMOx hydrolyzed to pEI was a pre-polymer for synthesis of positively charged nanogels.[125] Polymers were functionalized with thiol goups to enable the crosslinking to nanogels via simple thiol oxidation.

3.1.2.1 Synthesis of the pMOx

3.1.2.1.1 Synthesis of pMOx by cationic ring-opening polymerization with a living character

PMOx was synthesized by a cationic ring-opening polymerization with a living character (LCROP)[118] under the action of cationic initiators. It was aimed to synthesise polymers with molecular weight of around 4300 g/mol.

LCROP proceeds in three steps: initiation, propagation and termination. Living character of the LCROP ensures that a number of activated chain-ends remains constant, which hindrances the termination and ensures predictable polymeric molar masses.[119, 126-127]

To synthesize polymers with low polydispersity index (*Đ*), it is necessary that the reaction of initiation proceeds faster than propagation. In other words, the constant of initiation (k_i) has to be higher than constant of propagation (k_p).

The scheme of the reaction is presented in Figure 3.1- 1.

Briefly, electrophile creates an oxazolinium cation which serves as propagation species. The cationic oxazolinium attacks the next monomer resulting in the ring opening. Finally, the reaction terminates by the addition of terminating agent, which needs to have a higher nucleophile capacity than a monomer and initiator.[119, 126-127]

During propagation step of LCROP, coupling and chain transfer also known as a ß-elimination may occur as side reactions, which are especially evident in the synthesis of polymers with molecular weight greater than 10000 g/mol.[119, 126-128]

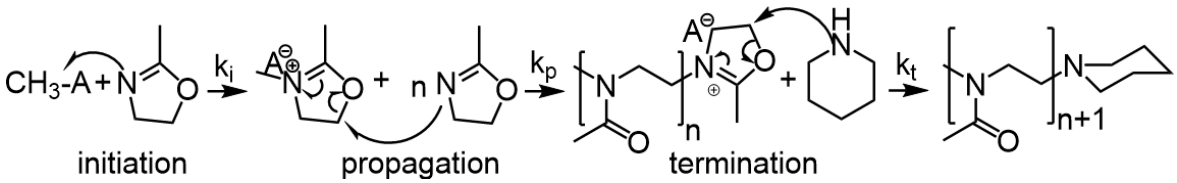

Figure 3.1- 1: Synthesis of pMOx with 55 repeat units. k_t – constant of termination; A- CF_3SO_3.

During chain transfer, monomer acts as a base, and receives the proton from the living polymer in the propagation step terminating the reaction. Coupling, on the other hand happens when polymer with enamine group synthesized by chain transfer reacts with living polymer. Both reactions end in the polymer with high polydispersity.[119, 126-128]

Initiator and termination agent dictate the functionality of the end groups of the polymer chain. In this work, methyl trifluoromethanesulfonate was used as initiator as it initiates the reaction even at ambient temperature. Pyridine was used as termination agent, as it has higher nucleoficity than initiator.

The pMOx was synthesized in the microwave reactor, as it was shown that these conditions considerably accelerate the polymerization of 2-alkyl-2-oxazolines.[129] Different temperatures (100 °C and 140 °C), as well as reaction times, were examined to optimize the synthesis (Table 3.1-1).

^1H NMR analysis was used to determine the number of repeat units per polymer by taking the methyl group (a) in the spectra as an internal reference. This is done by setting the value of integral of the signal at around 2.99 ppm (duplet) as 2 protons and at 2.84 ppm (singlet) as 1 proton (Figure 3.1- 2). The number of repeat units can be calculated by dividing the integral of (c) or (b) by 3 or 4, respectively.

GPC elugrams showed that polymer molecular weight had the bimodal distribution (Figure 3.1- 3). Increase of reaction time was followed by an increase of $Đ$ (Table 3.1-1), but the correlation of reaction time with molecular weight was not observed. Also, the increasing temperature did not influence significantly the obtained elugrams.

Table 3.1- 1: Characterization of pMOx polymers.

	T (°C)	t (min)	$M_{n,theory}$[a] (g/mol)	$M_{n,NMR}$[b] (g/mol)	$M_{n,SEC}$[c] (g/mol)	$M_{w,SEC}$[c] (g/mol)	$Đ$[c]	Yield (%)
P1	100	30	4300	4600	6000	7500	1.25	88
P2	100	60		4700	6400	8600	1.34	95
P3	100	90		4500	5000	6500	1.30	90
P4	100	120		4700	6300	8600	1.37	91
P5	140	10		4600	6500	8100	1.25	95
P6	140	30		4600	7000	8800	1.26	90

[a] as calculated from $[M]_0/[I]_0$.

[b] as calculated from end-group and side-chain analysis based on ^1H-NMR.

[c] as calculated from the GPC analysis in DMF, polymethylmethacrylate (PMMA) standards.

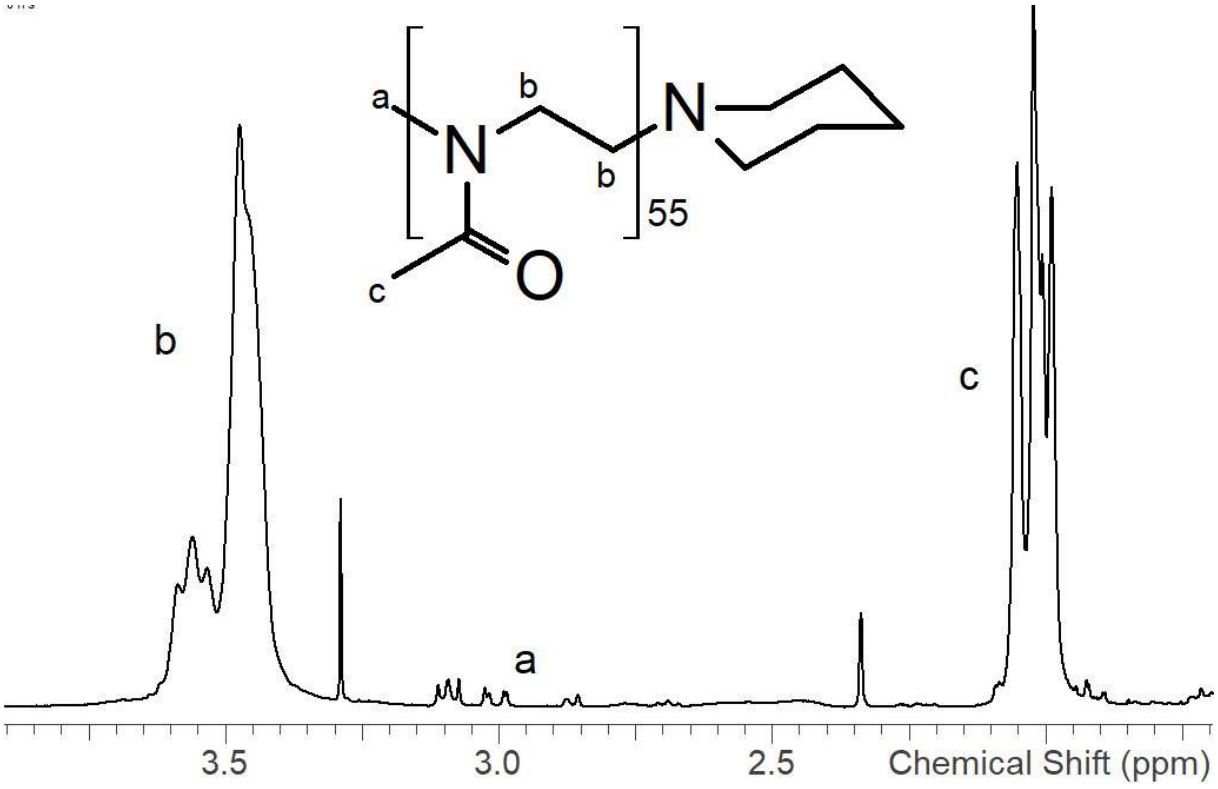

Figure 3.1- 2: ^1H NMR spectra of pMOx with 55 repeat units.

To understand the the bimodal distribution, GPC analysis was done before addition of quencher and when water was used as a quencher. Surprisingly, component at 13.3 min was not visible in chromatograms in both cases. This outcome led to the conclusion that pyridine end of the polymer induced interaction with the column, leading to the false

GPC results, and that the polymer is eluiting at around 14.5 min. This was further confirmed in the master thesis of Ilona Paulus.[130]

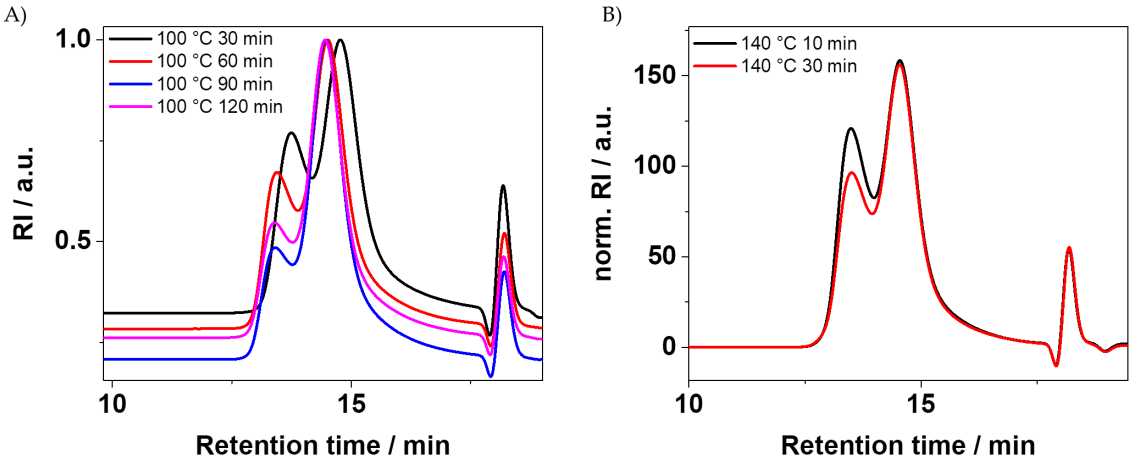

Figure 3.1- 3: GPC elugrams of pMOx polymers synthesized at (A) 100 °C and (B) 140 °C.

3.1.2.1.2 Hydrolysis of pMOx

Copolymers of poly(2-alkyl-2-oxazoline)s and poly(ethylene imine)s (pEI) can be synthesized by hydrolysis under acidic or alkaline conditions, or by the influence of enzymes.[108] It is reported that alkaline hydrolysis degrades the polymer backbone, although the exact mechanism is not described in detail. In contrary, it was shown that the hydrolysis under acidic conditions does not degrade the polymer backbone.[108, 131] Because of that, latter approach was selected.

PMOx with 55 repeat units was hydrolyzed to obtain pMOx-EI copolymer under the mild acidic condition to achieve 30 % conversion (Figure 3.1- 4). Temperature of 120 °C was chosen, since accordingly to Rosa et al.[118] this temperature was high enough to ensure fast conversion while not affecting the polymer backbone integrity.

With longer hydrolysis, amount of secondary amines in the polymer increased followed by the decrease of the GPC signal. This was explained by the interaction of amine with the GPC column. Therefore, the correct analysis of polymers was not possible, and further analysis of the copolymers was done by ^{1}H NMR.[108, 119]

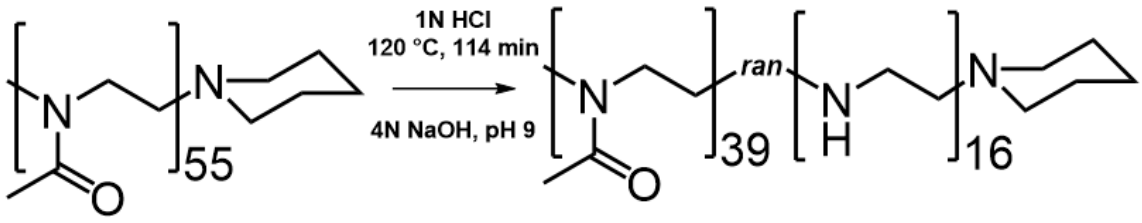

Figure 3.1- 4: Reaction scheme of pMOx hydrolysis to pMOx-EI.

Degree of hydrolysis was calculated by ^{1}H NMR spectroscopy. Proton signals at 2.5 – 2.8 ppm were attributed to the ethylene imine backbone units (c) of the polymer (Figure 3.1- 5).

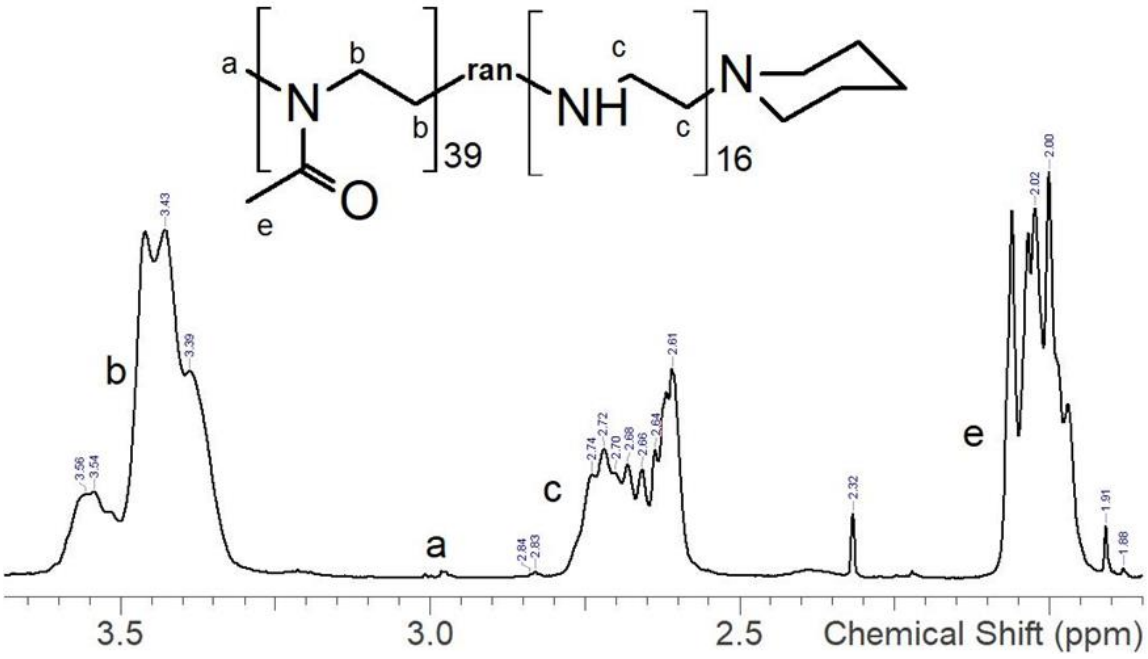

Figure 3.1- 5: ^{1}H NMR spectra of the PMOx-EI copolymer.

Results were plotted against reaction time to evaluate the reaction rate as a slope of a function (Figure 3.1- 6A). The results revealed linearity from which time necessary to obtain desirable conversion of 30 % was easily calculated.

Fourier-transform infrared spectroscopy (FT IR) spectra of the synthesized co-polymer revealed the presence of band at 3270 cm^{-1} at (Figure 3.1- 6B) which confirmed the presence of secondary amines.

3.1.2.1.3 Thiol modification of pMOx-EI

Thiol modification of pMOx-EI with 30 % of hydrolysis degree was performed following carbodiimide coupling mechanism between dithiocarboxylic acid, herewith dithiodipropionic acid (DTPA), and secondary amines of the EI part of the polymer backbone activated by N,N'-dicyclohexylcarbodiimide (DCC) and 4-dimethylaminopyridine (DMAP).

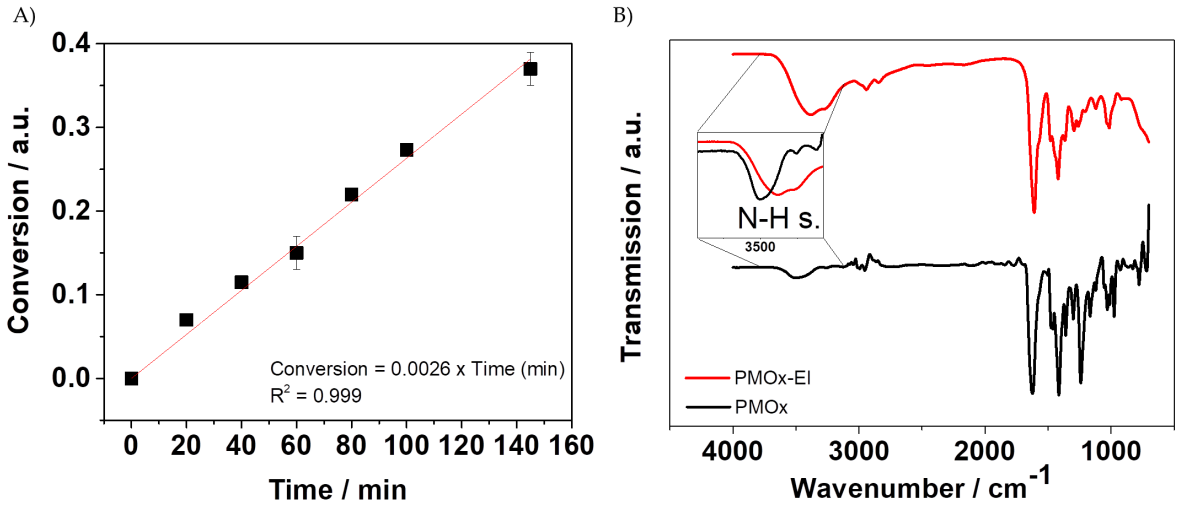

Figure 3.1- 6: (A) Kinetics of polymer hydrolysis, (B) FT IR spectra of pMOx and pMOx-EI.

After amidation, disulfide bond was cleaved to thiol functionalized random copolymer (pMOx-EI-SH) under reduction condition achieved by addition of tris(2-carboxyethyl)phosphine (TCEP) (Figure 3.1- 7).

^1H NMR spectra of the polymers before and after functionalization are shown in Figure 3.1- 8A. Proton signals at 2.5 – 2.8 ppm attributed to the ethylene imine backbone units present after polymer hydrolysis decrease after thiol functionalization as part of them are occupied with the thiol carrying side chain, while proton signals for thiol carrying side chain appears at 2.4 - 2.6 ppm.

Degree of functionalization was calculated by analysis of ^1H NMR spectra to be 15 % of the whole polymer, which equals to 8 theoretical number of thiol groups per polymer.

Further, Raman analysis proved thiol modification of polymers, where the band at

2570 cm^{-1} was assigned to free thiols (Figure 3.1- 8B).

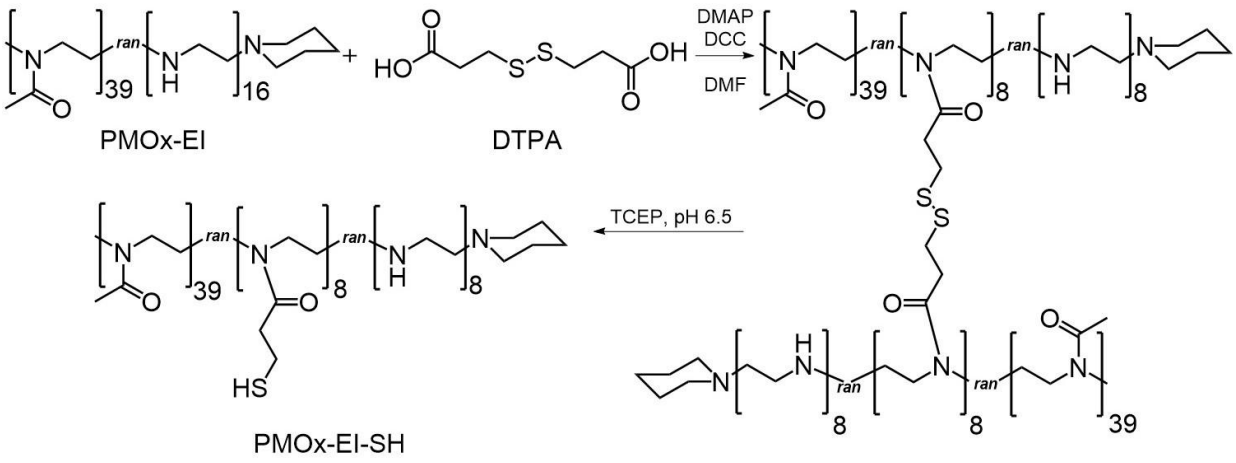

Figure 3.1- 7: Synthesis of pMOx-EI-SH with 15 % of thiol functionalization.

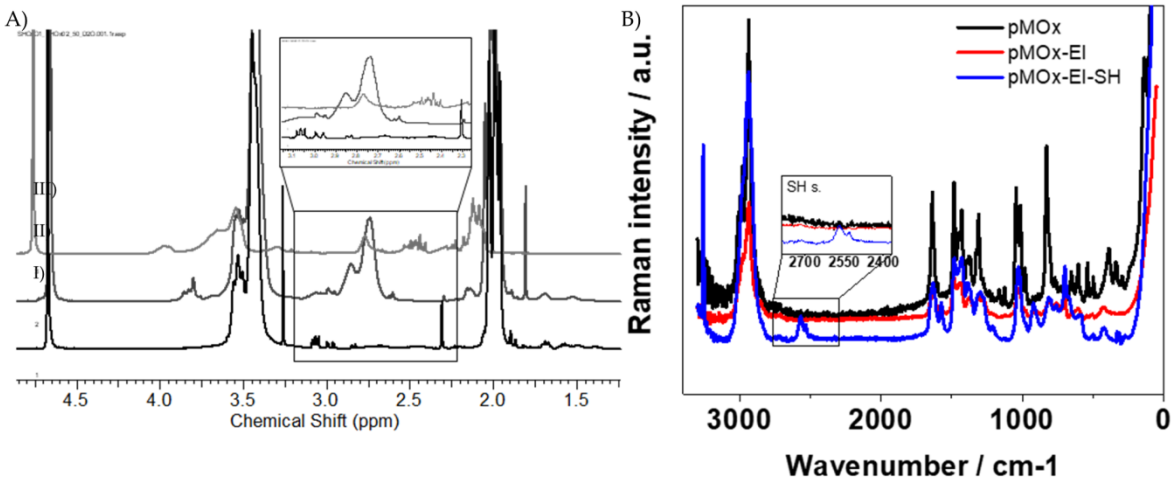

Figure 3.1- 8: (A) ^{1}H NMR spectra of (I) pMOx, (II) pMOx-EI and (III) pMOx-EI-SH and (B) Raman spectra of polymers.

3.1.2.2 Synthesis of the linear poly(glycidol) pGs

3.1.2.2.1 Synthesis of the ethoxy ethyl glycidyl ether (EEGE)

Because glycidol contains hydroxyl group, polyethers synthesized from this monomer contain hydroxyl group and in each structural unit as well. However, direct polymerization of glycidol leads to branched polymers.[132-133] In order to synthesize linear pGs, monomers with protected hydroxyl groups need to be used, such as EEGE.

EEGE as a monomer for the synthesis of linear pGs was used in this thesis because its hydroxyl groups are protected. The acetal protecting group of the polymer can be easily removed after polymerization to yield linear polymer by deprotection using hydrochloric acid (HCl) solution.[132-133]

However, EEGE was not commercially available and was, therefore, synthesized by the reaction of glycidol and ethyl vinyl ether which served both as a reactant and a solvent, as shown in Figure 3.1- 9.[134] In this reaction, p-toluenesulfonic acid (p-TosOH) was used as a catalyst for the reaction.

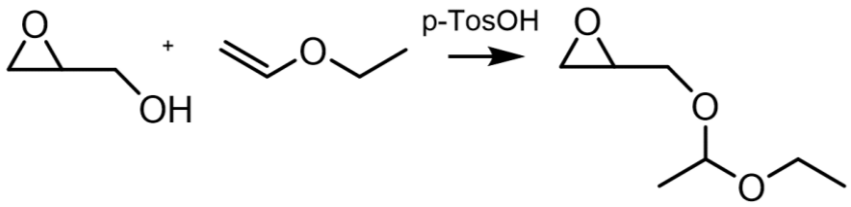

Figure 3.1- 9: Synthesis of monomer EEGE.

3.1.2.2.2 Polymerization of EEGE to poly(ethoxy ethyl glycidyl ether) (pEEGE) and deprotection to pG

Polymerization of EEGE proceeded by mechanism of living ring-opening anionic polymerization in bulk. The reaction of was initiated by alkali metal-based initiator potassium tert-butoxide (KOtBu) according to literature.[135]

In this type of reaction, the activated polymer end chain reacts with the monomer until termination, which happens after proton donation from e.g. methanol (Figure 3.1- 10).

The molar ratio of initiator to monomer EEGE was set to 1 : 60, resulting in a theoretical 60 repeat units. According to GPC analysis in DMF, Mw of the polymer was around 8900 g/mol which was close to the predicted value.

In further steps, pEEGE was deprotected to linear pG by addition of HCl as shown in Figure 3.1- 11. However, polymers with a moderate polydispersity (*Đ* of 1.3) and higher Mw (4850 g/mol) were obtained as shown by GPC analysis. This outcome also observed previously by Stichler et al.[136] They explained such results by polymer coiling behavior,

side reaction products, or interactions with the column. Also, the calibration of the GPC was done by poly(methyl methacrylate) standards, which have different hydrodynamic radius and coiling behavior than pG. Therefore, these results could not be directly compared.[136]

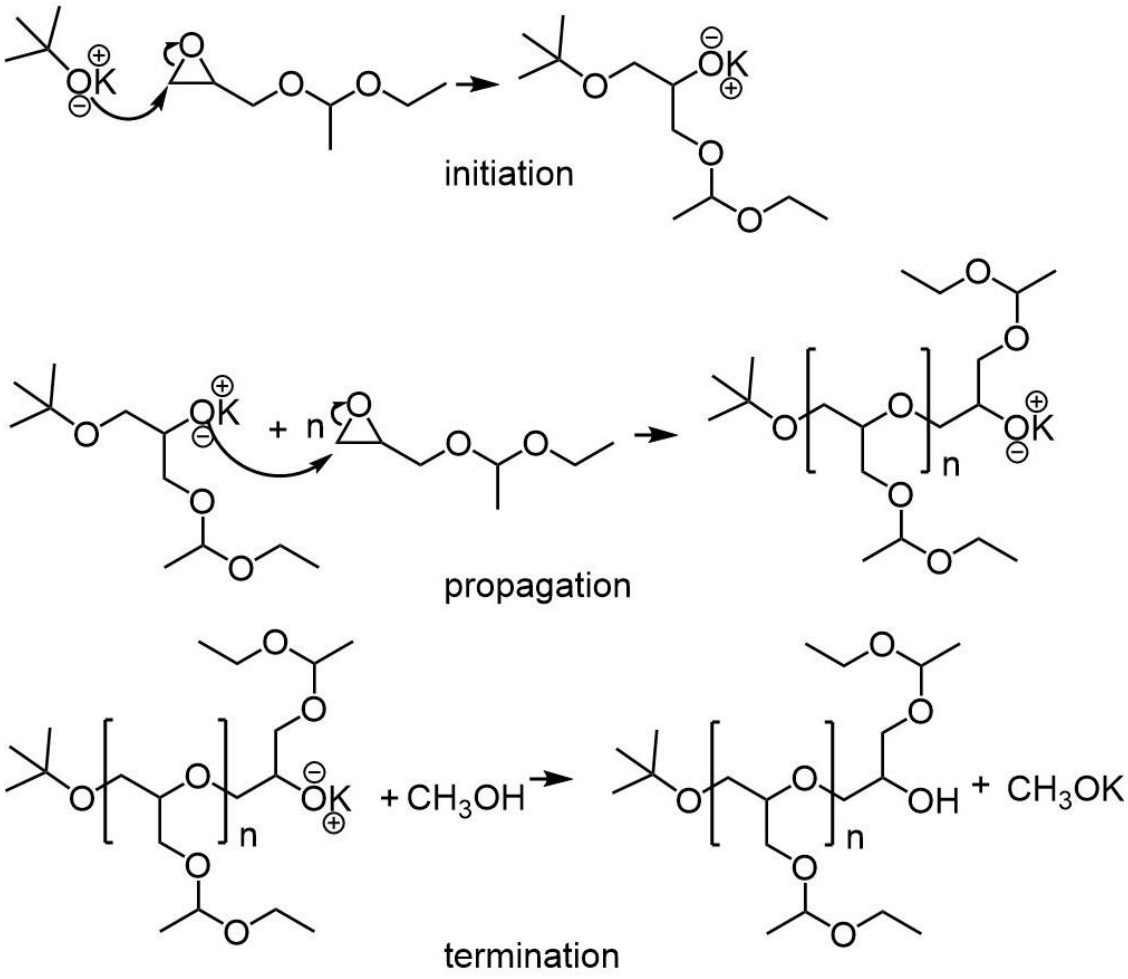

Figure 3.1- 10: Synthesis of pEEGE by anionic polymerization in bulk.

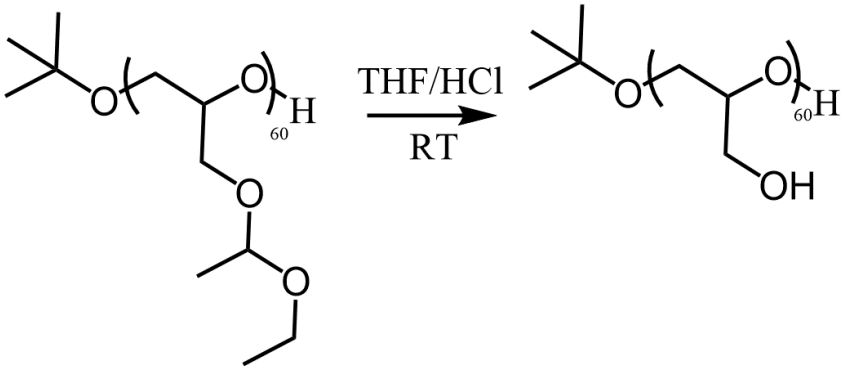

Figure 3.1- 11: Deprotection of pEEG to linear pG.

3.1.2.2.3 Thiol modification of linear pG

The obtain ester-containing thiol-functionalized linear polymers, pG was functionalized by thiol groups by Steglich esterification similarly as previously described in **Section 3.1.2.3**.

Briefly, upon activation of hydroxyl groups of pG by DMAP and DCC, DTPA was added, and the reaction proceeded under inert conditions and in dry solvents. After 4 hours the gel was formed, and disulfide bridges were cleaved to thiols under the influence of reducing agent TCEP. The polymer was purified by dialysis to yield thiol functionalized hydrolytically cleavable pG-SH (Figure 3.1- 12).

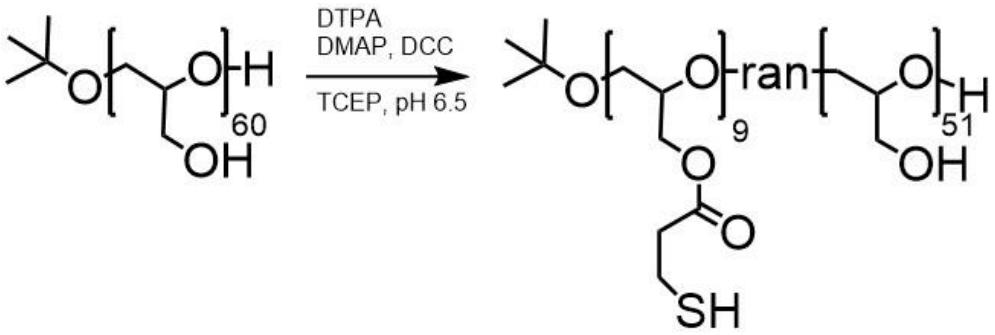

Figure 3.1- 12: Thiol modification of pG.

In ^{1}H NMR spectra, the signals at 2.6-2.8 ppm were assigned to the ethyl protons next to the ester group and according to data, degree of functionalization of around 15 % was obtained (Figure 3.1- 13).

Successful functionalization was proved by Raman and FT IR spectroscopy (Figure 3.1-14), where bands at 2550-2570 cm^{-1} and 1730 cm^{-1} were assigned to thiol and ester group respectively, present only in thiol functionalized polymer.

3.1.3 Bulk gelation of the polymers

To estimate the gelation´s kinetics of polymers in bulk prior synthesis of nanogels, polymers were crosslinked to hydrogels.

Thiol functionalized polymers can be crosslinked by simple oxidation. In basic conditions

and under the influence of oxidation agents, thiols are deprotonated and form disulfide bridges (Figure 3.1- 15A).[138]

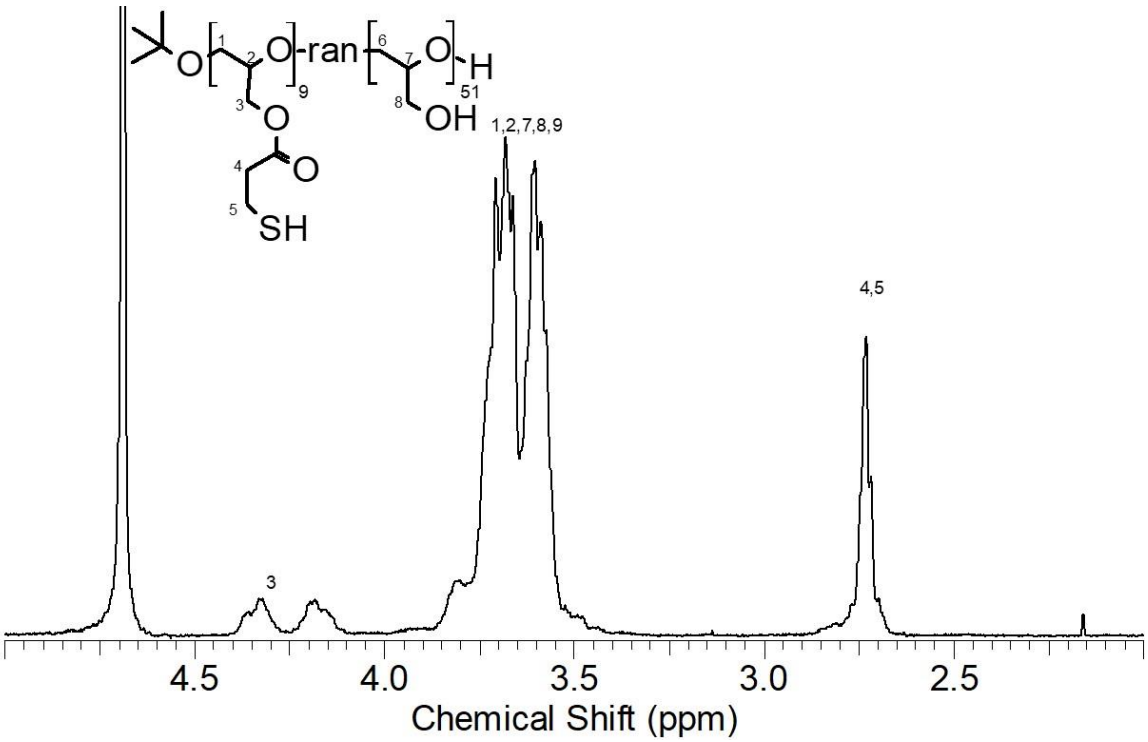

Figure 3.1- 13: ^{1}H NMR spectra of ester-containing thiol-functionalized pG.

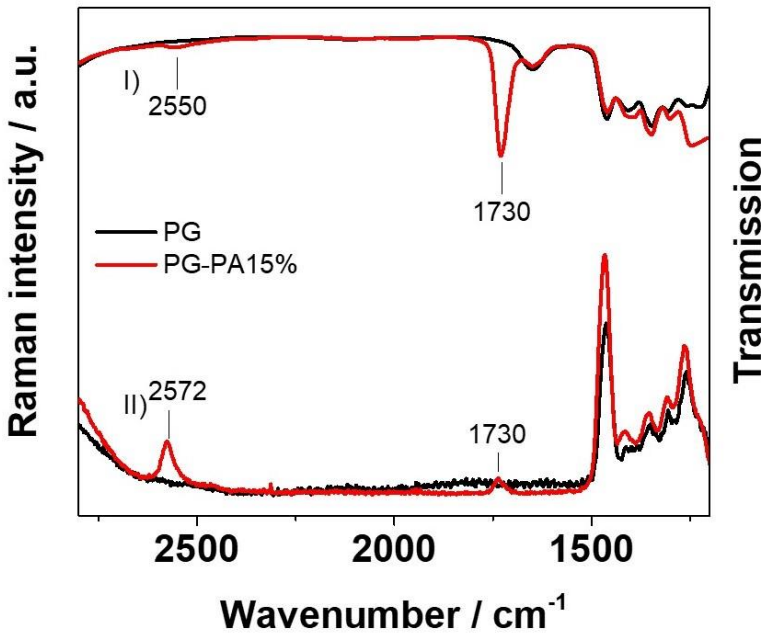

Figure 3.1- 14: FT IR (I) and Raman (II) spectra of the polymers. pG-PA15% stands for thiol functionalized pG with 15 % thiol functionalization.

In comparison to hydrogen peroxide, a strong oxidation agent which might cause unwanted side reactions during oxidation, it has been shown that alloxan is milder oxidant which does not show adverse effects.[55] Because of that, in this thesis alloxan was used as the oxidation agent.

Thiols are reactive towards acrylates as well, and the reaction follows the thiol-to-acrylate Michael addition under basic pH values (Figure 3.1- 15B-C).

Acrylates also react with amines following the same mechanism. It is found that acrylate reactivity towards secondary amines is higher than reactivity towards primary amines, which opens the possibility to the crosslink pMOx based copolymers using polyacrylate crosslinkers.[139]

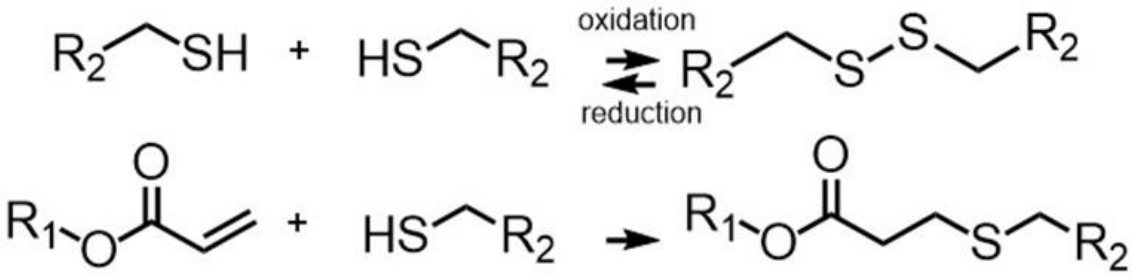

Figure 3.1- 15: Principle of (A) thiol-thiol oxidation to disulfide bridges and (B) thiol-acrylate Michael addition.

Therefore, in this section it was investigated whether pG-SH and pMOx-EI-SH gelate upon oxidation and upon addition of acrylate containing crosslinkers.

Gelation of thiol modified copolymers was initiated by addition of different amounts of oxidation agent alloxan or crosslinker pEG-diacrylate (pEG-DA). Reactions proceeded in the polymer solution at pH of 8.4. The influence of the pH on the gelation time of polymers crosslinked with pEG-DA via Michael addition was investigated (Figure 3.1- 17). With the increase of pH value, gelation time decreased. This was expected, since in Michael-type reaction OH^- anions attack Michael acceptor, so reaction rate depends on the concentration of OH^- anions or pH value.[140]

With the highest amounts of crosslinkers, gelation occurred immediately as presented in Figure 3.1- 16. When the highest concentrations of crosslinkers were used, there was no

difference between the gelation time between samples. However, when lower crosslinker concentrations were used, gelation slowed down and was slower in the case of crosslinking by Michael addition.

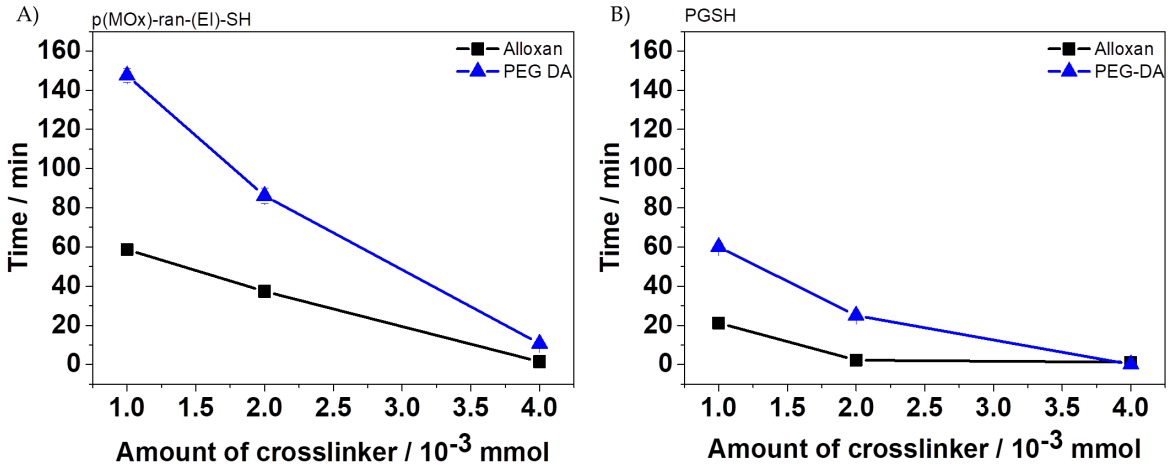

Figure 3.1- 16: Oxidation of (A) pMOx-EI-SH and (B) pG-SH by oxidation induced by addition of oxidation agent alloxan or by Michael addition using pEG-DA as a crosslinker at pH 8.4.

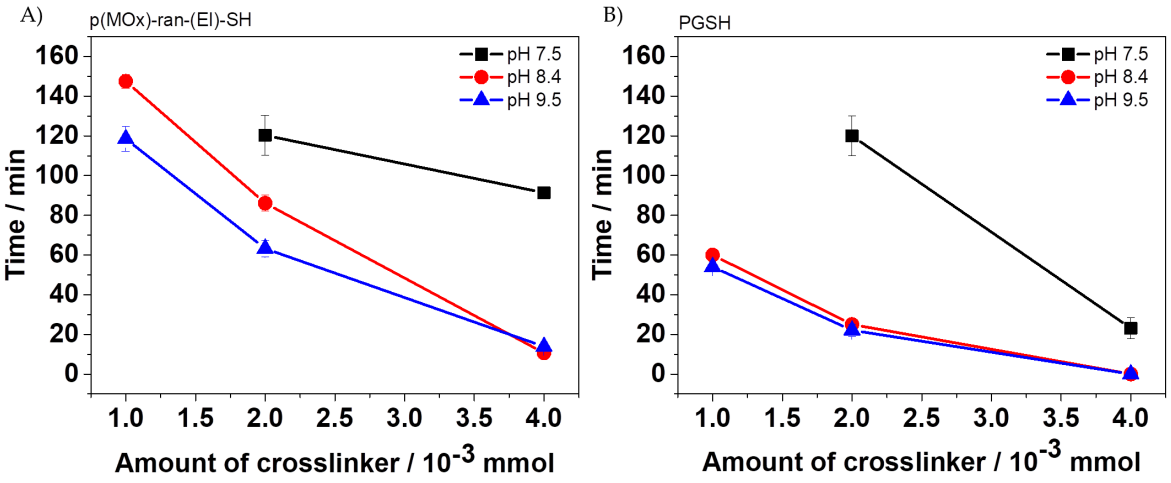

Figure 3.1- 17: Influence of pH value on crosslinking of (A) pMOx-EI-SH, and (B) pG-SH by pEG-DA.

Finally, Raman analysis was performed to confirm the crosslinking (Figure 3.1- 18). The band at 2570 cm^{-1} assigned to the free thiols disappeared after gelation while other bands at 500-600 cm^{-1} appeared. These were, specifically, bands at 505 cm^{-1} and 512 cm^{-1} assigned to disulfide bridges and band at 665 cm^{-1} that corresponded to the C-S bond. Presence of the band at 2570 cm^{-1} confirmed the hypothesis that in case of a pMOx-EI-SH copolymer,

acrylates preferred binding to amines, although some reactivity towards thiols was still observable due to the lower intensity of band in comparison to the polymer before gelation.

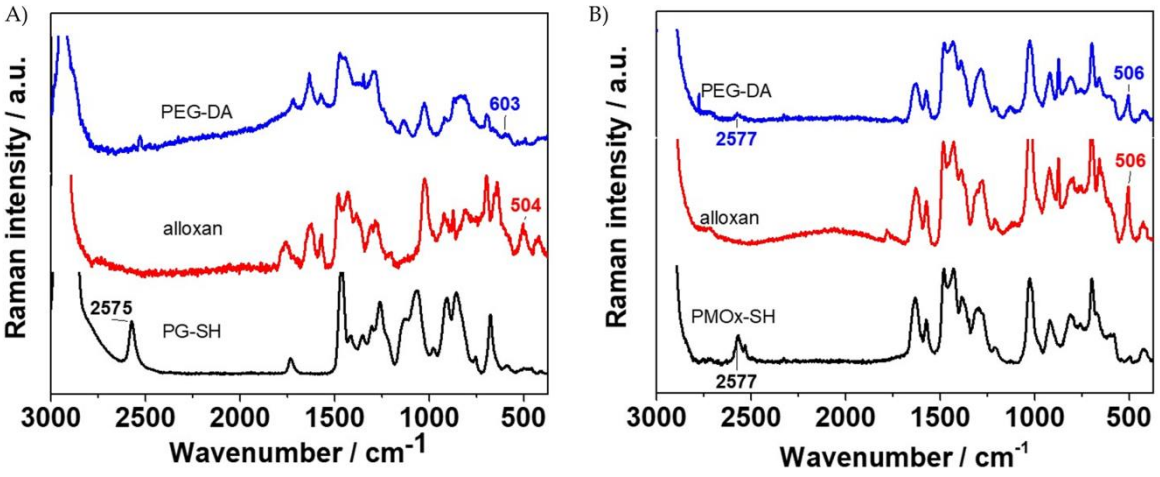

Figure 3.1- 18: Raman spectra of (A) pG-SH and (B) pMOx-EI-SH crosslinked by oxidation and by following Michael addition.

3.1.4 Preparation of nanogels

After analysis of bulk gelation, rough parameters for nanogel preparation using two types of thiol-functionalized polymers pG-SH (for simplicity in further text named as pG) and pMOx-EI-SH (for simplicity in further text named as pMOx) were determined. Michael addition was used to introduce quenchers carring different charges.

In this study, nanogels were prepared by inverse miniemulsion method (Figure 3.1- 19) using pG and pMOx polymers with 60 and 55 repeat units with 9 and 8 thiol groups, respectively.[55] Similarly to pEG, pG carries weakly basic ether linkages and hydroxyl groups, both responsible for a slightly negative charge.[125] Because of that, pG-based nanogels served as model for nanogels with slightly negative charge. On the other hand, pMOx nanogels served as model for nanogels carrying positive charges.[125] Both polymers were conjugated to Atto 647N dye by thiol-maleimide coupling prior the synthesis of nanogels.

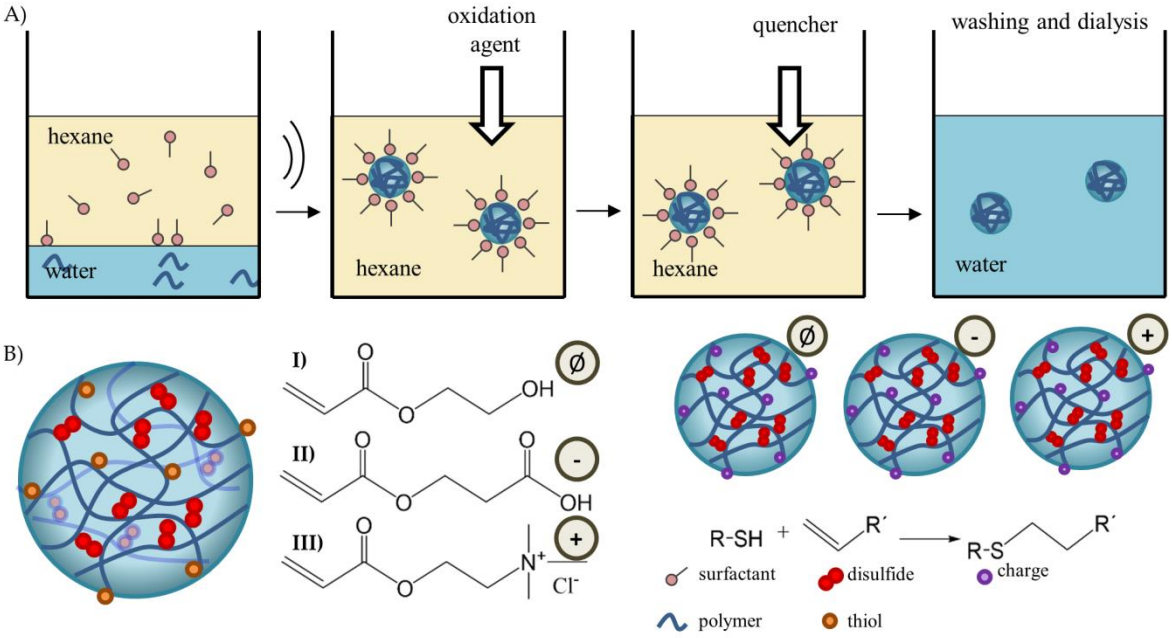

Figure 3.1- 19: (A) Schematic illustration of nanogel synthesis by inverse miniemulsion method. (B) Introduction of the functionalization groups by quenching by Michael addition: (I) HEA, (II) CEA and (III) AEMA.

Briefly, to obtain redox responsibe nanogels, thiol-functionalized polymers were dissolved in the aqueous phase and mixed with the organic phase in which surfactants and co-surfactants were previously dissolved.[46] Presence of surfactants during the synthesis of particles was necessary for decreasing the particle size distribution of nanogels. Surfactants stabilize thermodynamically unstable nanodroplets and prevent coalescence and Ostwald ripening.[141] Ultrasonication was used to induce droplet formation in inverse water-in-oil miniemulsion, and homogenization.

Finally, the thiols were quenched wih acrylates to add charges to pG-based nanogels, as shown in Figure 3.1- 19. Crosslinking of the polymeric network was achieved by the addition of oxidative agent alloxan.[55]

In order to prohibit further oxidation between different nanogels, and thus aggregation of pG-based nanogels, the remaining thiol groups were quenched via Michael addition with the acrylate reactants including 2-hydroxyethyl acrylate (HEA), [2-(acryloyloxy)ethyl]trimethylammonium chloride (AEMA) and 2-carboxyethyl acrylate

(CEA), allowing the introduction of -OH, -$N(CH_3)_3^+$ and -COOH groups, respectively. This reaction followed Michael addition mechanism and was faster at basic conditions as shown in **Section 3.1.4**.[139] Since pMOx nanogels carried a positive charge due to the presence of secondary amines, only HEA was used as a quencher.

Since the results of gelation studies of pG corresponded well to the results of gelation study of the same polymer reported in the thesis of Smriti Singh[20], it was assumed that the pG will behave similarly during the nanogel preparation and, therefore, the protocol for the preparation of pG based nanogels was not developed further and was taken as described in her thesis. In contrast to pG based nanogels, which synthesis was previously established,[17, 20, 55] parameters for the synthesis of pMOx based nanogels needed to be optimized.

The influence of the amount of polymer and oxidation, hydrophile-lipophile balance (HLB) altered by varying the ratio of surfactants, sonication time before and after the addition of alloxan and type and concentration of buffers (Table 3.1- 2) was analyzed. However, after analysis of DLS data, the highest impact on the nanogel size had sonication time before the addition of an oxidation agent. With shorter sonication of 30 s, nanogels got smaller, but, interestingly, sonication which took 20 s or 15 s did not result in the formation of nanogels. Ionic strength and type of the buffer also influenced the size of nanogels. Smallest nanogels were prepared when borate buffer (BB) with ionic strength of 0.01 M was used.

Table 3.1- 2: Influence of different synthesis parameters on the hydrodynamic radius of pMOx based nanogels.

No.	Buffer**	HLB	m_{pol} (mg)	1st sonication (s)	V_{allox}* (µL)	2nd sonication (s)	d_h (nm)
1	0.05 M BB	7	12.5	60	18	60	600 ± 210
2	0.05 M BB	7	12.5	60	18	45	580 ± 205
3	0.05 M BB	7	12.5	60	18	30	470 ± 230
4	0.05 M BB	7	12.5	30	18	60	340 ± 120
5	0.05 M BB	7	12.5	30	18	45	320 ± 110
6	0.05 M BB	7	12.5	30	18	30	290 ± 100
7	0.05 M BB	7	12.5	30	9	30	240 ± 120
8	0.05 M BB	7	12.5	30	12	30	230 ± 90
9	0.05 M BB	7	12.5	30	15	30	270 ± 120
10	0.05 M BB	7	12.5	30	18	30	240 ± 70
11	0.05 M BB	6	12.5	30	18	30	250 ± 80
12	0.05 M BB	5	12.5	30	18	30	250 ± 100
13	0.05 M BB	4.3	12.5	30	18	30	250 ± 100
14	0.05 M BB	4.3	10	30	18	30	270 ± 110
15	0.05 M BB	4.3	15	30	18	30	bimodal distribution
16	0.05 M BB	4.3	17.5	30	18	30	240 ± 80
17	0.1 M BB	4.3	15	30	18	30	540 ±180
18	0.01 M BB	4.3	15	30	18	30	180 ± 60
19	0.05 M PBS	4.3	15	30	18	30	340 ± 120
20***	0.1 M PBS	4.3	15	30	18	30	210 ± 70
21	0.01 M PBS	4.3	15	30	18	30	280 ± 180

*32 mg/mL solution in water.

**BB-borate buffer, pH 8.4; PBS-phosphate buffered saline, pH: 7.4.

***Conditions used to prepare pMOx-based nanogels in the further studies.

Size of nanogels in almost all cases varied between 200 nm and 350 nm, which was within the range of pG based nanogels reported in previous studies.[17-18, 55-56] This was important, as in order to evaluate the influence of charge on the fungi-nanogel interaction, size of nanogels should be comparable.

The hydrodynamic diameter of final nanogels that were used to study nanogel-fungi interaction was around 200 nm ± 60 nm and 280 nm ± 120 nm for pG and pMOx based nanogels, respectively (Table 3.1- 3). Quenchers altered the surface charge of pG nanogels as determined by ζ-potential measurements, while pMOx nanogels remained positive as expected.

Table 3.1- 3: Particle sizing by DLS and NTA of unlabeled and fluorescent-labeled nanogels.

		non-fluorescent NG			
			pG-SH		**pMOx-EI-SH**
		HEA	**AEMA**	**CEA**	**HEA**
DLS	ζ* (mW)	-9 ± 5	3 ± 4	-21 ± 3	16 ± 3
	d_h** (nm)	170 ± 60	180 ± 60	170 ± 60	290 ± 120
NTA	mean d_h (nm)	160 ± 60	180 ± 110	220 ± 100	310 ± 130
		Cy5 labeled NG			
			pG-SH		**pMOx-stat-EI-SH**
		HEA	**AEMA**	**CEA**	**HEA**
DLS	ζ* (mW)	-13 ± 4	3 ± 4	-17 ± 3	21 ± 4
	d_h** (nm)	280 ± 180	210 ± 90	150 ± 50	250 ± 80
NTA	mean d_h (nm)	180 ± 130	170 ± 80	220 ± 150	320 ± 160

*zeta potential, **hydrodynamic radius.

Analysis of nanogels in dry state was done using atomic force microscopy (AFM). As shown in Figure 3.1- 20, both pG and pMOx based nanogels had a diameter of around 120 nm and 210 nm, respectively, with height of only a few nm. Flattened surface might be explained by high affinity of mica surface towards nanoges. In addition, elastic

deformations of the dried nanogels may result in the lower height of these systems.[142]

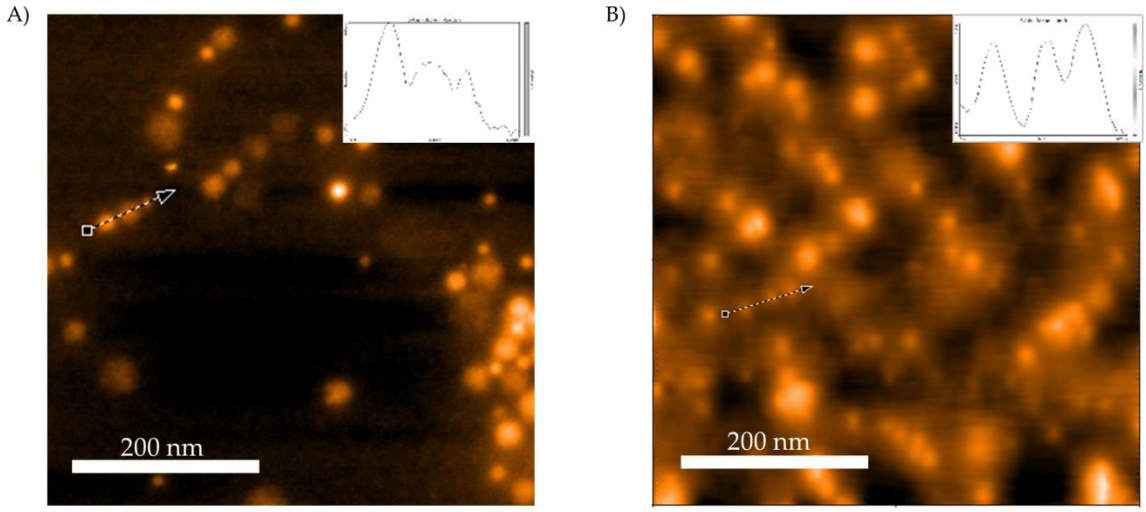

Figure 3.1- 20: (A) pMOx and (B) pG based nanogels in dry state analyzed by AFM.

3.1.5 Interaction of nanogels with fungi

Nanogels were incubated with *Aspergillus fumigatus* and samples were analyzed by fluorescence and confocal microscopy (Figure 3.1- 21).

Nanogel-fungi interaction was depended on nanogel concentration. Fungal fluorescence increased with nanogel concentration as shown in Figure 3.1- 21A.

Fluorescence intensity was also higher when fungal hyphae were incubated with the pG nanogels after conidia germination which occurred 2 h after start of incubation (Figure 3.1- 21). This result suggested that there was a decreased interaction with conidia.

It was observed that when fungi was pre-incubated for 5 h without and 2 h with pG nanogels, nanogel-fungi interaction was dependent on nanogel surface charge (Figure 3.1- 22). Fungal hyphae started to fluorescence after 2 h of incubation firstly with pG-CEA nanogels with negative surface groups. In this point, germinating conidia were fully fluorescent. In contrast, other nanogels showed only slight interaction after 2 h of incubation, although after 24 h all types of nanogels interacted with fungal hyphae. However, by using this method it was not possible to conclude whether the nanogels were internalized or were only adsorbed on the fungal cell wall.

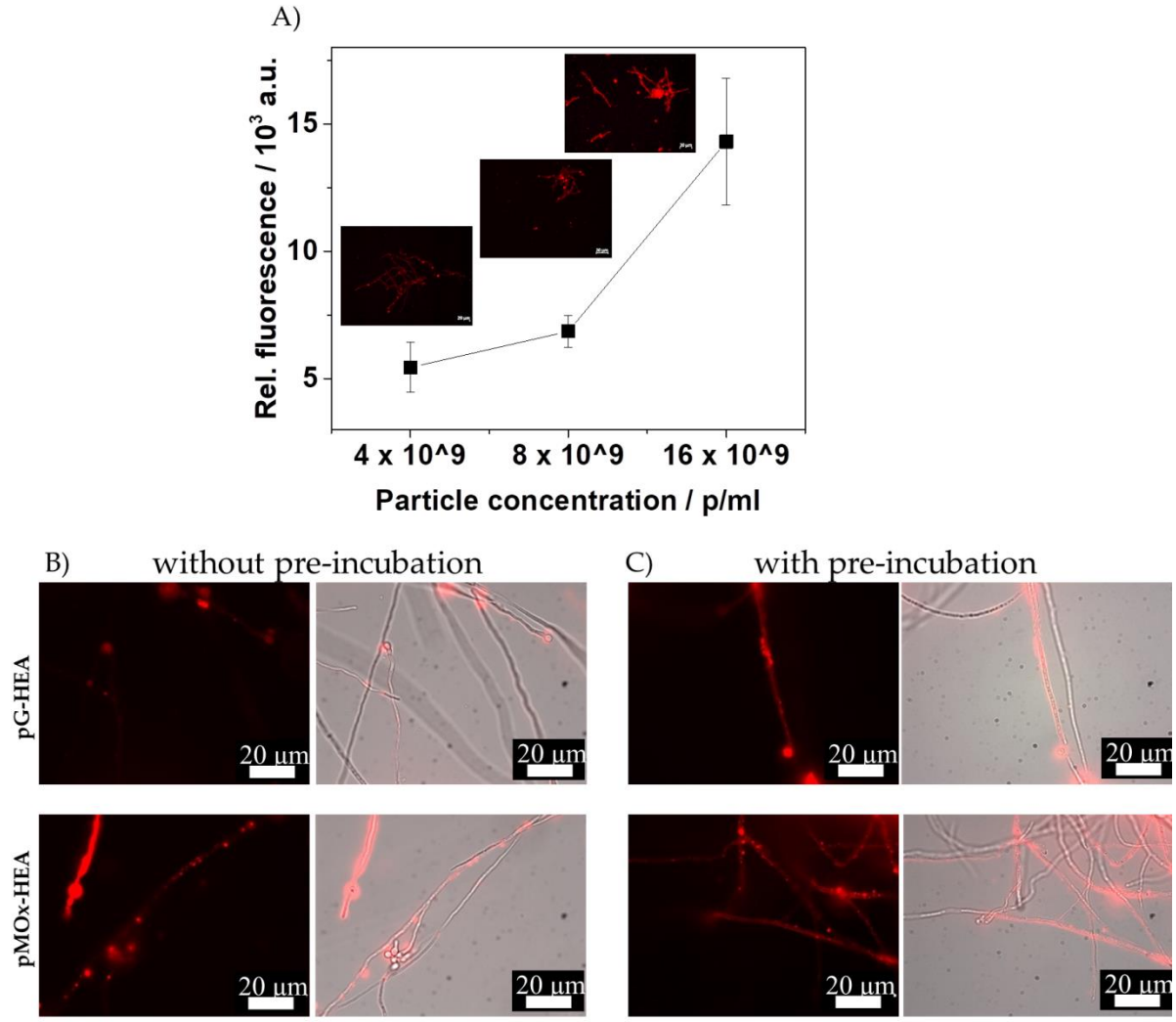

Figure 3.1- 21: (A) Influence of nanogel concentration on fluorescence intensity. Incubation of the fungal cells with nanogels was 7 h, with 2 h of cells pre-incubation in incubation medium only. (B) Incubation of fungi with Cy5 labeled pG and pMOx nanogels with the concentration of 8 x 10^9 p/mL after 24 h incubation, without pre-incubation of the fungal cells and (C) 24 h incubation with the fungal cells pre-incubated for 5 h in the growing medium.

To explore whether particles were present on the surface or were internalized, fungal cells in both conidia and hyphal form were analyzed in more detail by confocal laser scanning microscopy (CLSM).

CLSM analysis of the fungal hyphae revealed that internalization of particles depended on the nanogel surface groups (Figure 3.1- 23). Nanogels were not internalized by conidia but were found adsorbed on the cell wall (CW) regardless of the nanogel type. Slightly higher

binding was observed for pG nanogels. pG-CEA nanogels with negative surface groups were internalized, while particles with other surface groups and higher ζ-potential were found mainly attached on the CW.

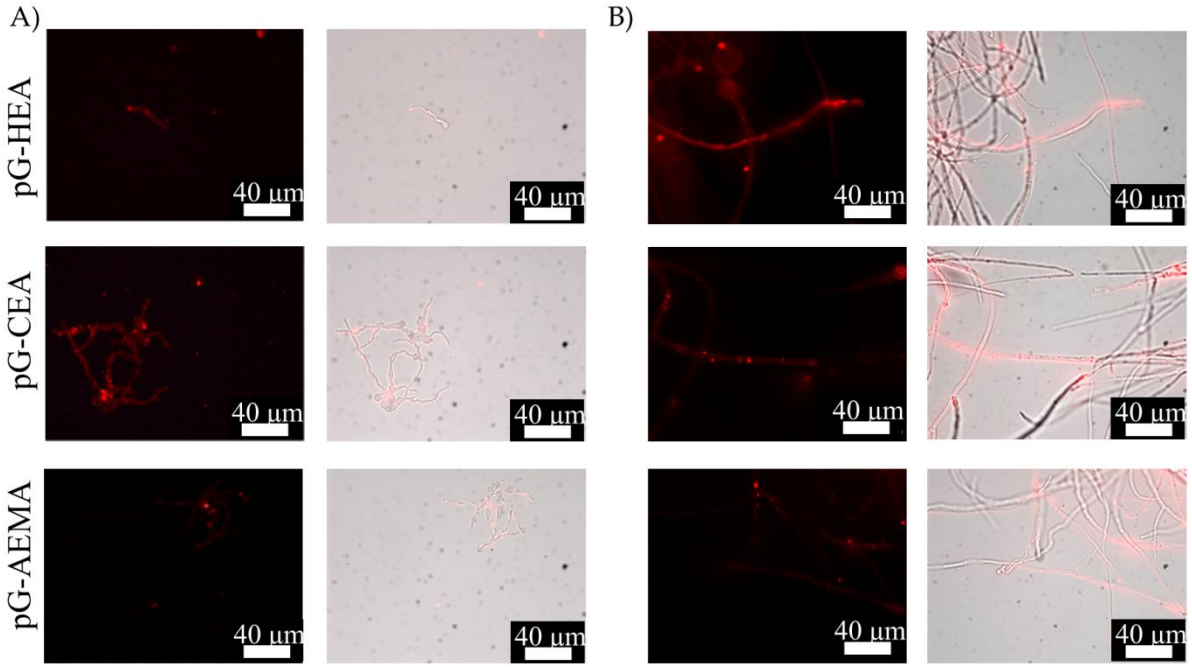

Figure 3.1- 22: Incubation of fungi pre-incubated for 5 h without nanogels and (A) 2 h - germlings and (B) 24 h – mature hyphae with Cy5 labeled pG nanogels with the concentration of 8 x 10^9 p/mL.

Fungi incubated with pG-HEA with hydroxyl surface groups were found both internalized and on the CW. On the other hand, pMOx-HEA nanogels were found mostly on the surface of the cells. This might be explained by the presence of the positive secondary amines in the polymers, which triggers the nanogel absorption to the cell wall. It is, however, important to note that pMOx-HEA and pG-AEMA nanogels also internalized in cells, but in less extent and in vesicle-like structures than in case of pG-CEA nanogels, where the dye was evenly distributed inside cells suggesting nanogel cleavage.

Westmeier et al.[143] already addressed that although fungal spores are negatively charged, there was a higher absorption of negatively charged nanoparticles on their surface in comparison to positively charged nanoparticles. They explained these unexpected results

with the conformation of proteins and exposure of positive protein domains on fungal CW for binding of negatively charged particles.

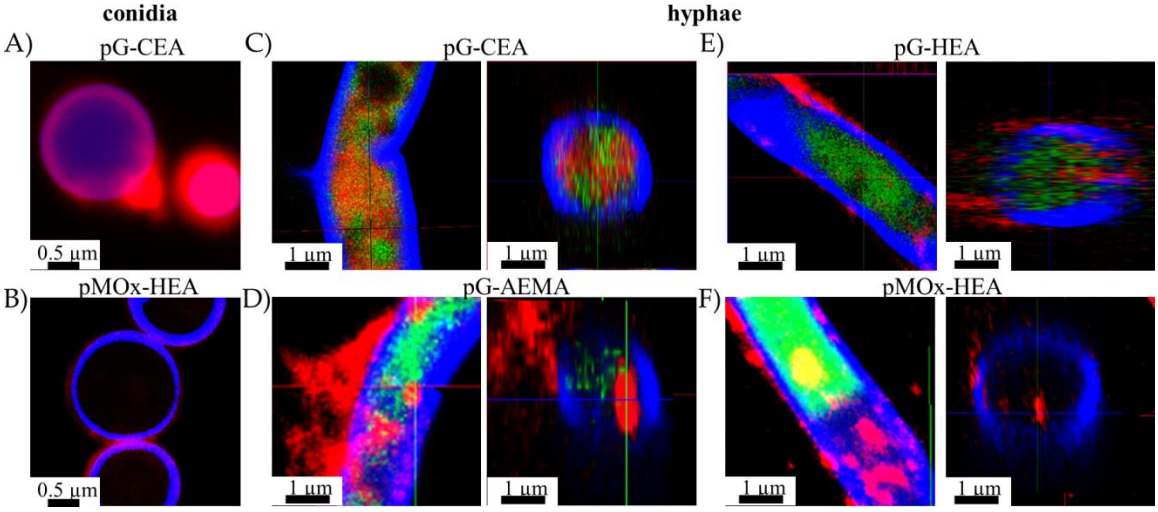

Figure 3.1- 23: CLSM of fungal cells in hyphal form incubated with particles for 24 h without pre-incubation in the transverse and longitudinal plane: (A) pG-CEA, (B) pG-HEA, (C) pG-AEMA (D) pMOx-HEA. Spores incubated for 2 h with (E) pG-CEA and (F) pMOx-HEA nanogels. Legend: blue: cell wall; red: nanogels; green: cytoplasm.

Differences in the interaction of nanogels with a conidial and hyphal form of fungi might be explained by differences in a composition of the CW. The CW of conidia differs from the CW of mature hyphae. It is covered by hydrophobic rodlets which disappear or rearrange during germination and hyphal growth, while glucan layer dominates on the surface of the CW of mature hyphae.[144-146] Therefore, the presence of different polysaccharides and proteins on the hyphal CW might increase the interaction of negatively charged nanogels leading to their faster internalization. Further, it was shown that positively charged latex particles absorb on the surface of filamentous fungi.[100] According to authors, electrostatic interactions between positive amine groups on the surface of latex nanoparticles and negatively charged CW of the fungi led to the formation of the nanoparticles dense layer on the fungal CW, which had an antifungal effect.[100, 147] Other studies addressed the significance of negatively charged plasmid DNA as a carrier for the genetic material of interest in the genetic transformation of fungi.[148-149] It is believed

that the DNA carrier increased the efficiency of transformation by stronger binding to the CW, which affected the uptake of the genetic material of interest.[148-149]

3.1.6 Interaction of nanogels with mammalian cells

In the study of the interaction of neutrophils and nanogels done by Hannah Manz at the group of Prof. Dr. MD. Beilhack was shown that nanogels were recognized by immune cells already within 3 h of incubation (results not shown). This was expected since the primary function of immune system cells such as neutrophils is to recognize microbes and other particles present in the body or tissues.[151]

Furthermore, the interaction of nanogels with human adherent cells and neutrophils was analyzed to investigate the potential faith of nanogels in *in-vivo*. When nanogels were co-incubated with *A. fumigatus* GFP positive AfS148 strain[150] and with neutrophils, negatively charged pG-CEA nanogels were not only recognized and phagocytized by neutrophils already after 3 h of incubation, but were also found internalized in fungi (Figure 3.1- 24). Neutrophils did not lose the ability to recognize fungal hyphae with the addition of nanogels and were found attached to the fungal CW. On the other hand, nanogels still strongly interacted with fungi, which suggested that nanogels have high potential to be used as drug carriers in the treatment of fungal diseases induced by *A. fumigatus*.

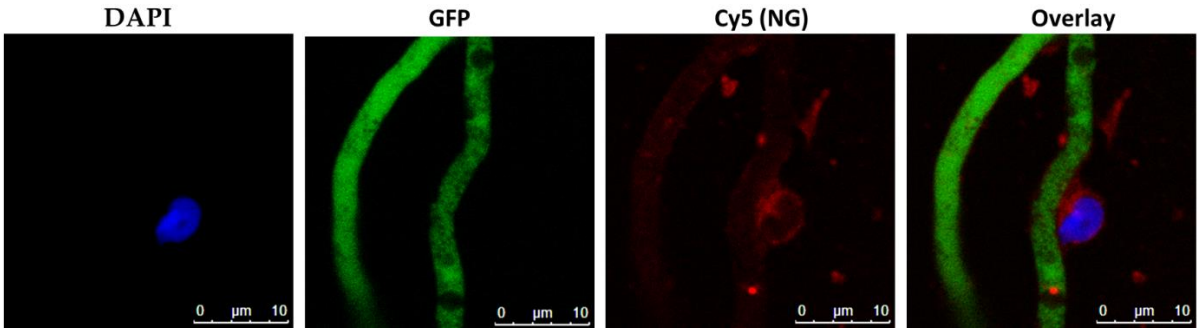

Figure 3.1- 24: Co-incubation of pG-CEA nanogels with *A. fumigatus* and neutrophils after incubation of 3 h. Legend: blue: neutrophil nucleus; green: cytoplasm of fungi; red: nanogels.

To evaluate the interaction of nanogels with other types of mammalian cells, nanogels

were incubated with Caco2 and endothelial cells for 24 h. Results (Figure 3.1- 25) showed that there was no high uptake of nanogels as previously observed with neutrophils. In this case, the uptake was depended on the surface functionalization of nanogels. pG nanogels with positive groups on surface internalized in both cell types in greater extent in comparison to other nanogels. This result was expected since it is known that negatively charged cell membrane reacts with positive charges on particles, which triggers particle internalization.[152]

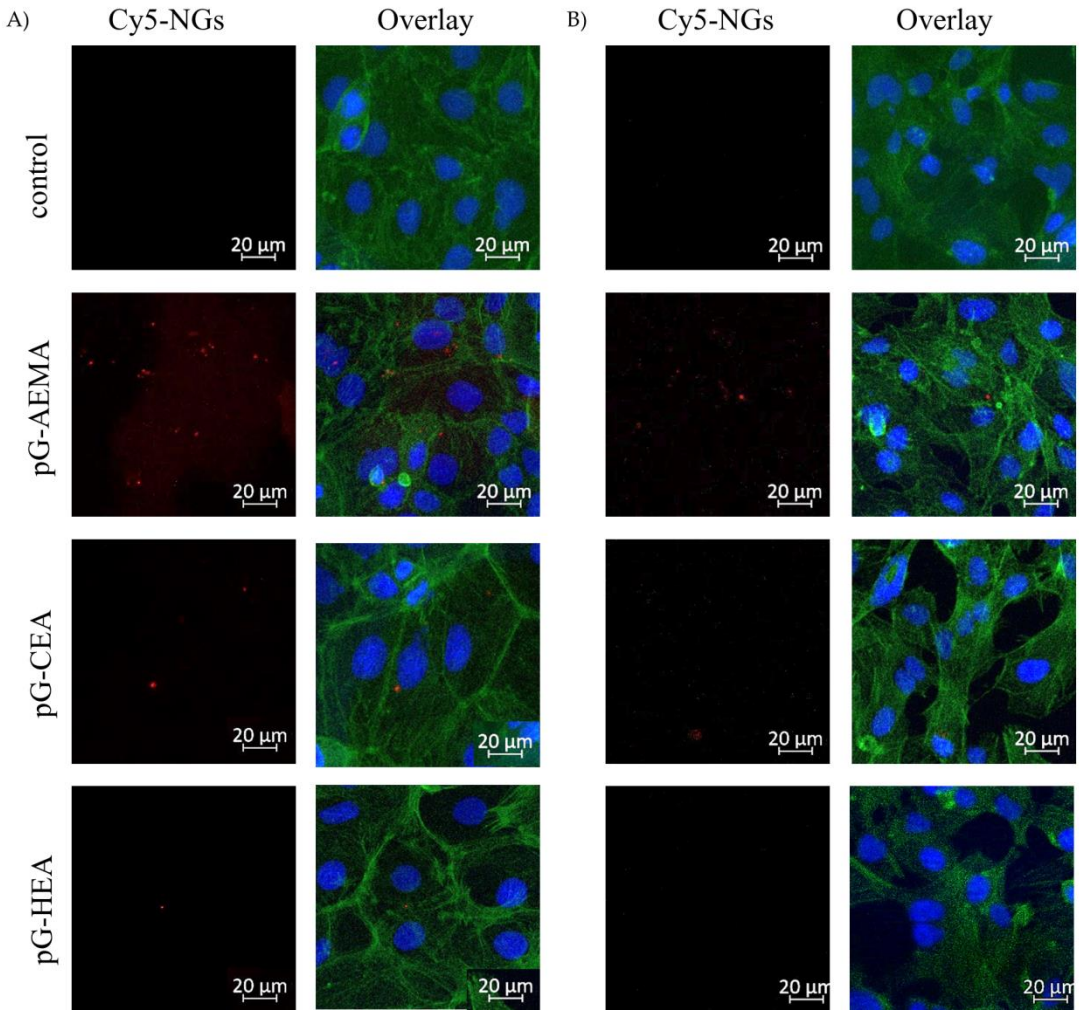

Figure 3.1- 25: Uptake of nanogels with different charges by (A) Caco-2 and (B) endothelial cells.

3.1.7 Conclusions

In this study it was evaluated how surface charge of nanogels influence nanogel

interaction with *A. fumigatus*. Positively charged nanogels were found mainly adsorbed on the fungal cell wall, while negatively charged nanogels were internalized to a higher extent than negatively charged nanogels.

In-vitro studies showed that nanogels were recognized by neutrophils, but this did not suppress the interaction of nanogels with *A. fumigatus* during co-incubation with neutrophils. Finally, nanogels with positive surface groups were internalized in greater extent in Caco2 and epithelial cells.

In summary, this study showed that nanogels with negative surface charge were better candidates for the drug delivery to *A. fumigatus*.

3.2 Influence of polymer amphiphilicity on the interaction of nanogels with *Aspergillus fumigatus*

This section was published as original research article and is adapted with permission from: Engineering Nanogels for Drug Delivery to Pathogenic Fungi Aspergillus fumigatus by Tuning Polymer Amphiphilicity; Sonja Horvat, Yidong Yu, Szalbolcs Böjte, Ingrid Teßmer, Douglas W. Lowman, Zuchao Ma, David L. Williams, Andreas Beilhack, Krystyna Albrecht, and Jürgen Groll; Biomacromolecules 2020 21 (8), 3112-3121.
DOI: 10.1021/acs.biomac.0c00489. Copyright (2020) American Chemical Society.

The chapter is based on the work of the author of this thesis Sonja Horvat-Csóti, who performed major part of experiments as listed in Author Contributions, analyzed data and wrote the manuscript.

Author Contributions

Contributor	Contributions
Sonja Horvat	Designed research; performed major part of the experiments and analyzed data; wrote the manuscript
Yidong Yu	Supported culturing the fungal cells; provided feedback on the manuscript
Szalbolcs Böjte	Performed AFM analysis of fungal cells
Ingrid Teßmer	Performed AFM analysis of fungal cells; provided feedback on the manuscript
Douglas W. Lowman	Synthesis of a reference sample of ß (1-6) glucan
Zuchao Ma	Synthesis of a reference sample of ß (1-6) glucan; provided feedback on the manuscript
David L. Williams	Synthesis of a reference sample of ß (1-6) glucan; provided feedback on the manuscript
Andreas Beilhack	Designed research; provided feedback on the manuscript
Krystyna Albrecht	Designed research; provided feedback on the manuscript
Jürgen Groll	Designed research; provided feedback on the manuscript

3.2.1 Introduction

In this section, nanogels were designed for encapsulation of the antifungal drug amphotericin B. The interaction between the nanocarriers ang fungi *Aspergillus fumigatus* was studied. Nanogels based on pG were prepared by simple self-assembly approach without the need of surfactants. Polymer architecture was controlled by the functionalization degree and length of the alkyl side chains, while crosslinking of thiol-containing copolymers was done under mild oxidative conditions. The goal of the study was to analyze how amphiphilicity of copolymers used for the synthesis of nanogels influenced dye uptake by mature fungal hyphae.

3.2.2 Characterization of polymers

Linear poly(glycidol)s (pG) with 60 repeat units (Mw of 4850 g/mol) were functionalized with thiol groups either by dithiopropionic acid (DTPA) or with dithiobutyric acid (DTBA) resulting in pG-PA and pG-BA polymers, respectively. The reaction between hydroxyl and carboxyl groups proceeded following the mechanism of Steglich esterification. Subsequent disulfide reduction by TCEP yielded thiol functionalized pG, as described in **Section 3.1**. Degree of functionalization (DF) was controlled by varying the amounts of DTPA or DTBA added to the polymer solution. Side chains introduced in this way carried not only thiol groups but also alkyl chains which render the polymers more hydrophobic.[17] Thus, it was possible to control the hydrophobicity of the polymers by both DF and length of the side chains.

DFs were estimated by ^{1}H NMR and were close to the predicted values (Table 3.2-1), confirming quantitative reaction of the hydroxyl groups of the pG with carboxyl groups of the dithiocarboxylic acids.[135]

Fourier-transform infrared (FT IR) and Raman spectra confirmed the successful reduction of the disulfide bridges and thiol functionalization of polymers (Figure 3.2- 1).

Table 3.2- 1: Characterization of polymers used in this study.

	Mn* (g/mol)	Mw* (g/mol)	*Đ**	FD** (%)	-SH/chain**
pG-PA5%	4000	5500	1.4	5.3	3
pG-PA10%	3800	4500	1.2	11.3	7
pG-PA20%	3500	4100	1.2	18.7	11
pG-BA5%	4000	5100	1.3	4.9	3
pG-BA10%	3800	4500	1.2	10.3	6
pG-BA20%	3500	4100	1.2	22.2	13

*determined by GPC, DMF with 1g/l LiBr.

**calculated by ^{1}H NMR.

Bands at 2572 cm^{-1} or 1256 cm^{-1} corresponded to the thiols in Raman and FT IR, respectively, while band at 1730 cm^{-1} corresponded to the esters which formed after functionalization. The latter band absent in FT IR and Raman spectra of non-functionalized pG. The absence of band at 511 cm^{-1} was the indication that oxidation of thiols did not happen during the synthesis and purification of polymers.[153]

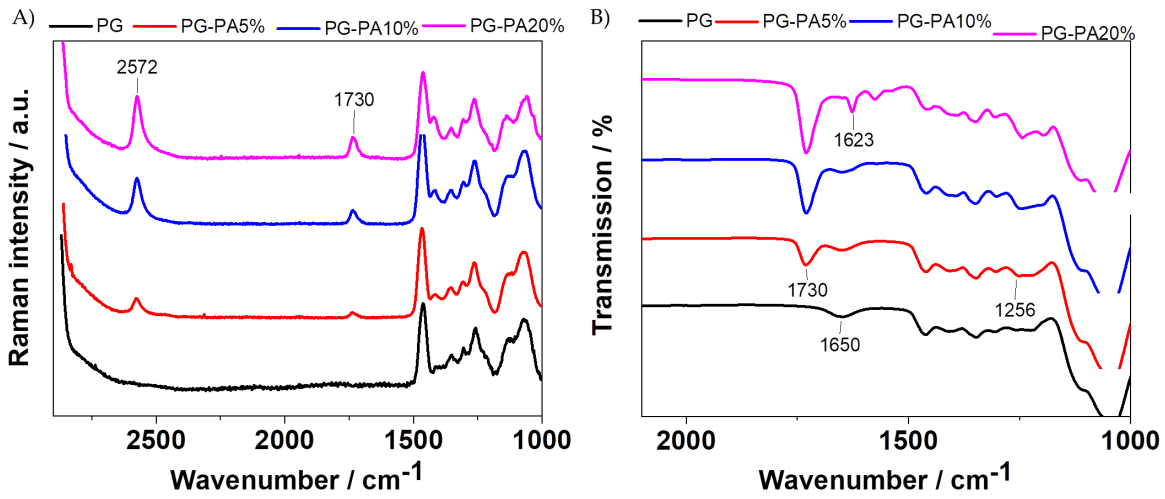

Figure 3.2- 1: (A) Raman and (B) FT IR spectra of pG-PA polymers.

3.2.3 Preparation of nanogels

3.2.3.1 Formation of polymeric aggregates

Functionalization of polymers with thiol groups introduced hydrophobic alkyl chains which altered polymer solubility in water. It is known that amphiphilic polymers associate and form polymeric aggregates above a certain concentration

called critical association concentration (*cac*).

Cac was determined by two methods: dynamic light scattering (DLS) and fluorescence spectroscopy. In the first method, *cac* was estimated by analyzing the count rate of the linearly diluted polymer solutions in water (Figure 3.2- 2A). In the latter method, *cac* was evaluated by monitoring the change in fluorescence spectra of 8-anilino-1-naphthalenesulfonic acid (ANS) (Figure 3.2- 2B).[154-155]

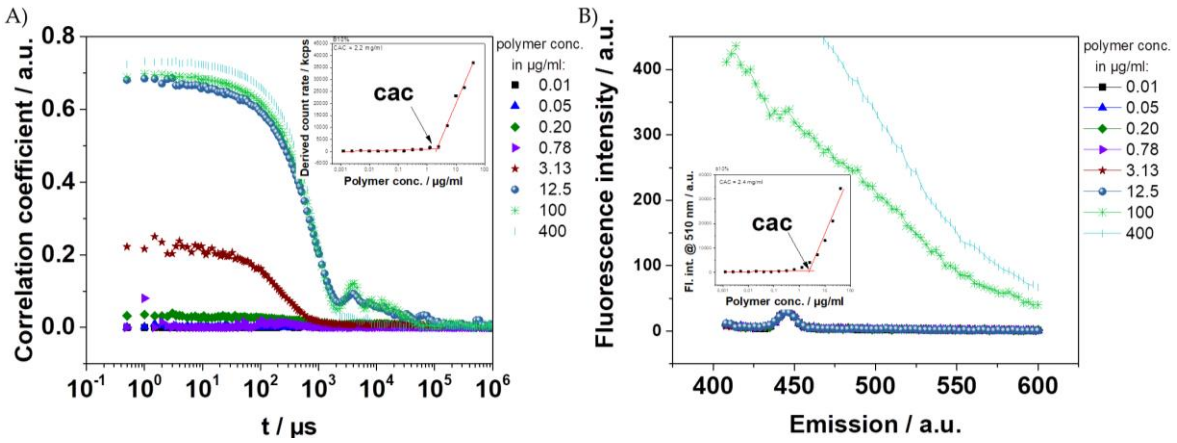

Figure 3.2- 2: (A) Correlation curve (DLS) and (B) fluorescence spectra of the pG-BA10%. Examples of *cac* determination of pG-BA10% by (C) DLS and (D) ANS.

Results of both methods gave similar similar trend of *cac* values (Table 3.2- 2). The highest *cac* had polymers with DF of 5 % and the lowest had polymers with DF of 20 %. Further, generally lower *cac* were obtained for pG-BA polymers, except the polymers with DF of 20 %, where *cac* of both pG-BA and pG-PA had the same value. Hence, polymers with more hydrophobic chains formed aggregates at lower concentrations.

Table 3.2- 2: Cac of polymers determined by ANS and DLS.

DF (%)	*cac* (mg/mL)			
	pG-PA	pG-BA	pG-PA	pG-BA
	Fluorescence spectroscopy		DLS	
5	6.7	3.9	8.1	2.5
10	4.3	2.5	2.5	2.2
20	0.1	0.1	0.5	0.6

3.2.3.2 Synthesis of nanogels

Nanogels were prepared by a simple approach without the need for surfactants followed by simple crosslinking of polymeric aggregates (Figure 3.2- 3). Polymers were dissolved in aqueous solution above their *cac* and crosslinked by oxidation of free thiols to disulfides.[16, 55]

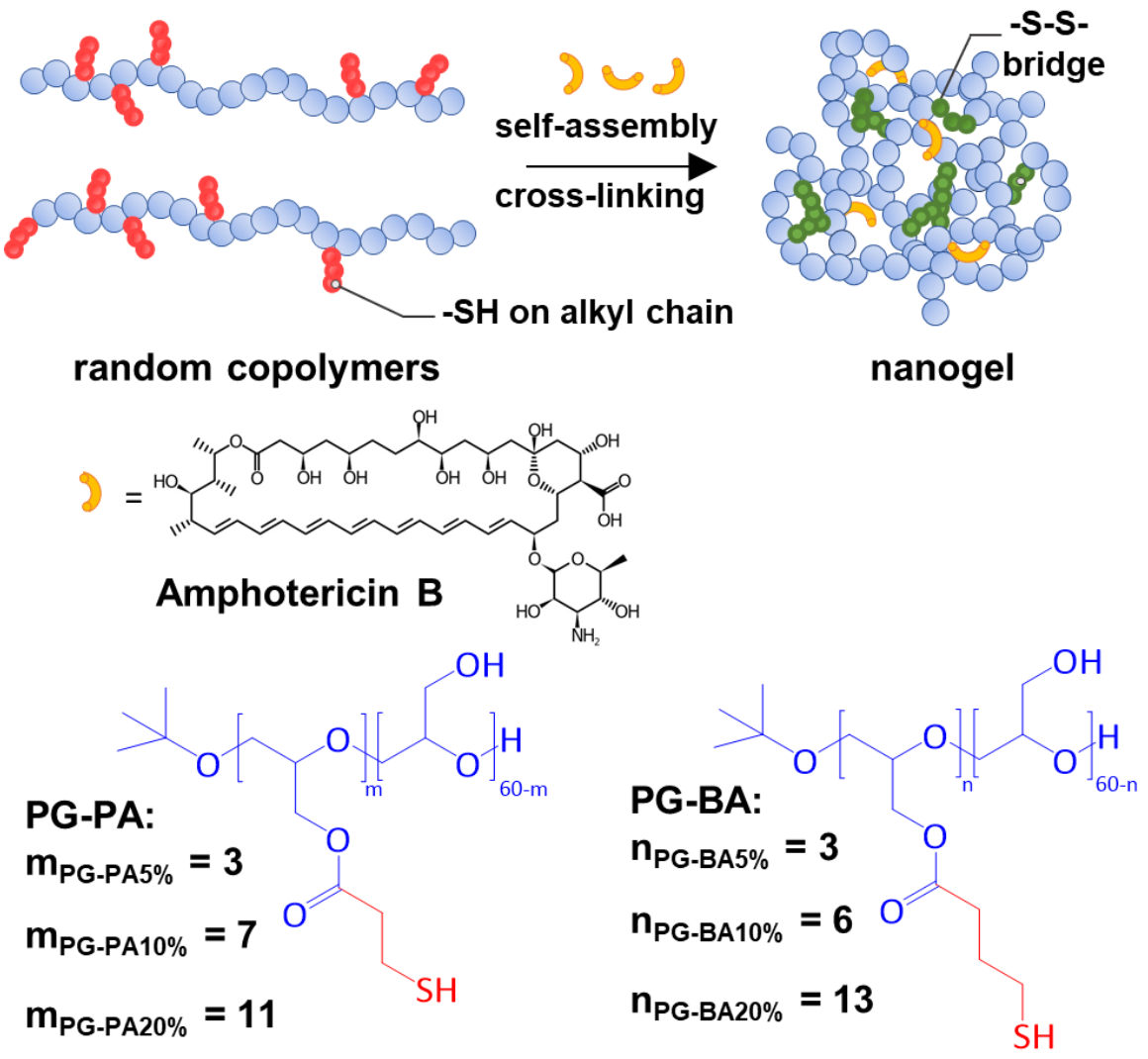

Figure 3.2- 3: Synthesis of polymers and illustration of nanogel preparation.

To prove that formed nanogels were composed of the covalently crosslinked polymer network, nanogels and aggregates were treated with various concentration of urea. Urea is a small molecule widely used in protein chemistry as denaturation agent as it breaks hydrogen bonds in proteins leading to their unfolding.[156] Therefore, it was expected that polymeric aggregates would also unfold in the presence of urea.[157-159] Derived count rate (DCR) decreased over time

with the addition of urea, and this change was tremendous for the non-crosslinked polymeric aggregates in comparison to crosslinked nanogels which only slightly increased the DCR over time (Figure 3.2- 4). Since DCR is proportional to number particles able to scatter light, it could be concluded that aggregates disassociated with the addition of urea, which led to the lower DCR. These results indicated that crosslinking improved stability of the aggregates.[160] However, it was noticed that more time and higher concentrations of urea were necessary to observe this effect than shown previously.[157] This could be explained by the high number of hydroxyl groups within the polymeric chains which might slow down the solvation of the polymers.[158]

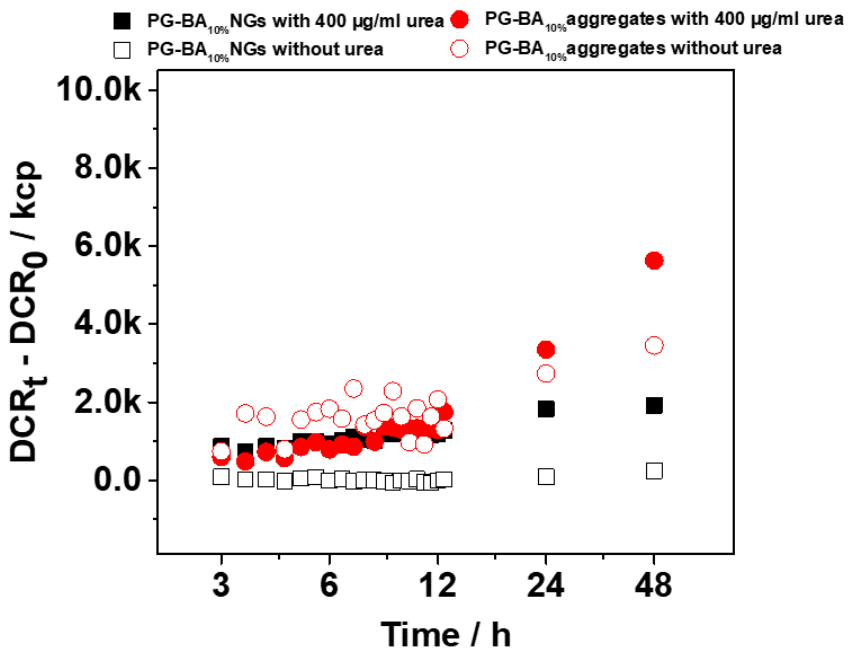

Figure 3.2- 4: Change of DCR with and without urea.

After crosslinking, nanogels had a smaller hydrodynamic radius in comparison to polymeric aggregates as determined by DLS, as well as higher stability (Table 3.2-3).

Hydrodynamic iameter varied from approx. 200 nm to 450 nm depending on the DF and alkyl chain. The hydrodynamic radius of pG-PA nanogels increased with DF, but interestingly, the opposite was observed for pG-BA nanogels. However, the polydispersity index (PDI) of nanogels decreased with DF, meaning that more

defined nanogels were formed when polymers with higher DF were used.

Table 3.2- 3: DLS analysis of nanogels.

	PDI			d_h (nm)			ζ-potential (mV)					
							water			PBS		
	empty	ORO	AmB	empty	ORO	AmB	empty	ORO	AmB	empty	ORO	AmB
pG-PA5%	0.59	0.30	0.25	270 ± 100	170 ± 30	210 ± 70	-2 ± 8	-11 ± 5	-23 ± 8	-1±7	-13 ±5	-18±9
pG-PA10%	0.48	0.30	0.34	320 ± 45	180 ± 40	245 ± 50	-11 ± 12	-13 ± 4	-18 ± 9	-14±12	-15 ±5	-16±24
pG-PA20%	0.34	0.40	0.29	420 ±140	420 ± 115	330 ± 120	-25 ± 7	-17 ± 5	-25 ±10	-11±20	-15±5	-22±12
pG-BA5%	0.46	0.35	0.43	390 ±70	120 ± 30	260 ± 40	-8 ± 15	-16 ± 5	-24 ±10	-7±6	-18±5	-26±11
pG-BA10%	0.30	0.25	0.31	450 ± 90	110 ± 35	190 ± 35	-17 ± 4	-21 ± 6	-28 ± 7	-8±9	-22±8	-20±8
pG-BA20%	0.20	0.27	0.45	210 ± 80	160 ± 35	210 ± 35	-14 ± 5	-19 ± 5	-14 ± 7	-23±9	-20 ±4	-24±15

3.2.4 Interaction of nanogels with *A. fumigatus*

β-glucans are polysaccharides in the cell wall (CW) of fungal and yeast species. Together with chitin, they provide mechanical stability of the CW.[161] As shown by Chavan et al.[162] these polysaccharides were responsible for absorption of pEGylated liposomes on the hyphae of *A. fumigatus*. Due to the similarities of pEG and pG, a similar outcome was hypothesized and therefore the interaction of nanogels with β-glucans and fungal hyphae was studied.

β-(1-3, 1-6) glucans were extracted from *Saccharomyces cerevisiae* by basic digestion and were phosphorylated to increase their water solubility.[163] Nanogels were incubated with polysaccharides and their interaction was analyzed by DLS (Figure

3.2- 5). Nanogels from copolymers with DF of 20 % did not change in size in the presence of β-(1-3, 1-6) glucans within 360 min of incubation. On the other hand, there was an increase in the hydrodynamic radius of nanogels composed of polymers with lower DF. After 150 min pG-PA5%, pG-PA10%, pG-BA5% and pG-BA10% nanogels increased their hydrodynamic diameter by 240 nm, 400 nm, 350 nm and 410 nm, respectively. Thus, DLS results suggested that the highest affinity toward fungal CW had nanogels synthesized from polymers with DF of 10 %.

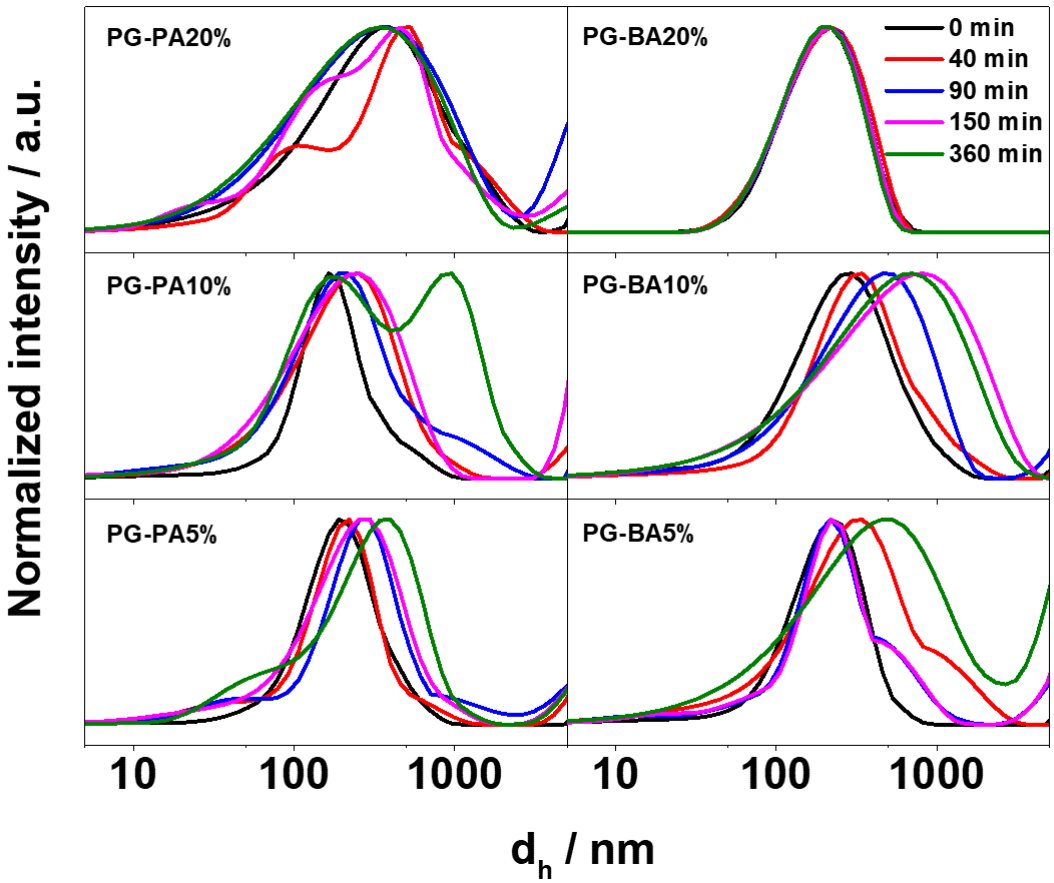

Figure 3.2- 5: Size distribution of nanogels incubated with β-(1-6)-glucan phosphate.

To investigate the interaction and uptake of the nanogels with mature fungal hyphae, nanogels were loaded with the hydrophobic dye Oil red O (ORO),[164-165] which served as a model for hydrophobic antifungal drugs. Dye was entrapped in the hydrophobic regions of the nanogels via hydrophobic-hydrophobic interactions during polymer aggregation. Size of the ORO loaded nanogels was smaller than of the empty nanogels, probably due to the contraction of polymer

chains around hydrophobic dye molecules (Table 3.2- 3). The compaction decreased for increasing hydrophobic side chain content of the polymer.

The mature fungi were incubated with the ORO loaded nanogels and internalization of the dye was monitored by confocal laser scanning microscopy (CLSM) (Figure 3.2- 6). Internalization of the dye was the highest in the case of nanogels with DF of 10 %. After already 1 h, fluorescence signal mainly originated from round-like organelles and was still not diffusive but rather punctuative. On the other hand, after 3 h of incubation signal broadened into the cytoplasm. These results showed that both nanogels and dye internalized in fungi during the first 1 h of incubation. After 1 h under the influence of intracellular reducing agents, disulfide bridges in nanogels started to cleave, which explains the diffusive signal. This, however, should be investigated in more detail. In contrast, only slight fluorescence signal originated from the cytoplasm in case of pG-PA5% nanogels. In the case of pG-PA20% and pG-BA20% dye was found on the cell wall or the extracellular matrix, and there was no internalization of the dye even after 3 h of incubation.

Furthermore, when fungi were incubated with ORO nanogels at 4 °C, no fluorescence signal was observed for all types of nanogels at all-time points tested (Figure 3.2- 7). It is known that fungal metabolism at low temperatures is slow, which suggested that nanogels were internalized by active mechanism and not passively by diffusion.

Although there is an open and controversial discussion about endocytosis in fungal species, there is evidence that endocytosis occurs in hyphae of filamentous fungi such as *A. fumigatus*.[95] Study of Rispail et al.[166] proved internalization of negatively charged quantum dots in filamentous fungi *Fusarium oxysporum*, while positively charged magnetic nanoparticles remained on the fungal cell wall.

In the current study, it was questionable whereas internalization of nanogels together with dye occurred, or only kiss-and-run scenario happened. In the latter case, nanogels could serve as dye delivery vehicles, where a dye was internalized without nanogel uptake.[167] On the other hand, since β-glucans are synthesized in

higher amounts and are exposed to the surface during the fungal growth phase,[162] higher accumulation of a dye was expected in the regions of primary and secondary septa, which was not the case.

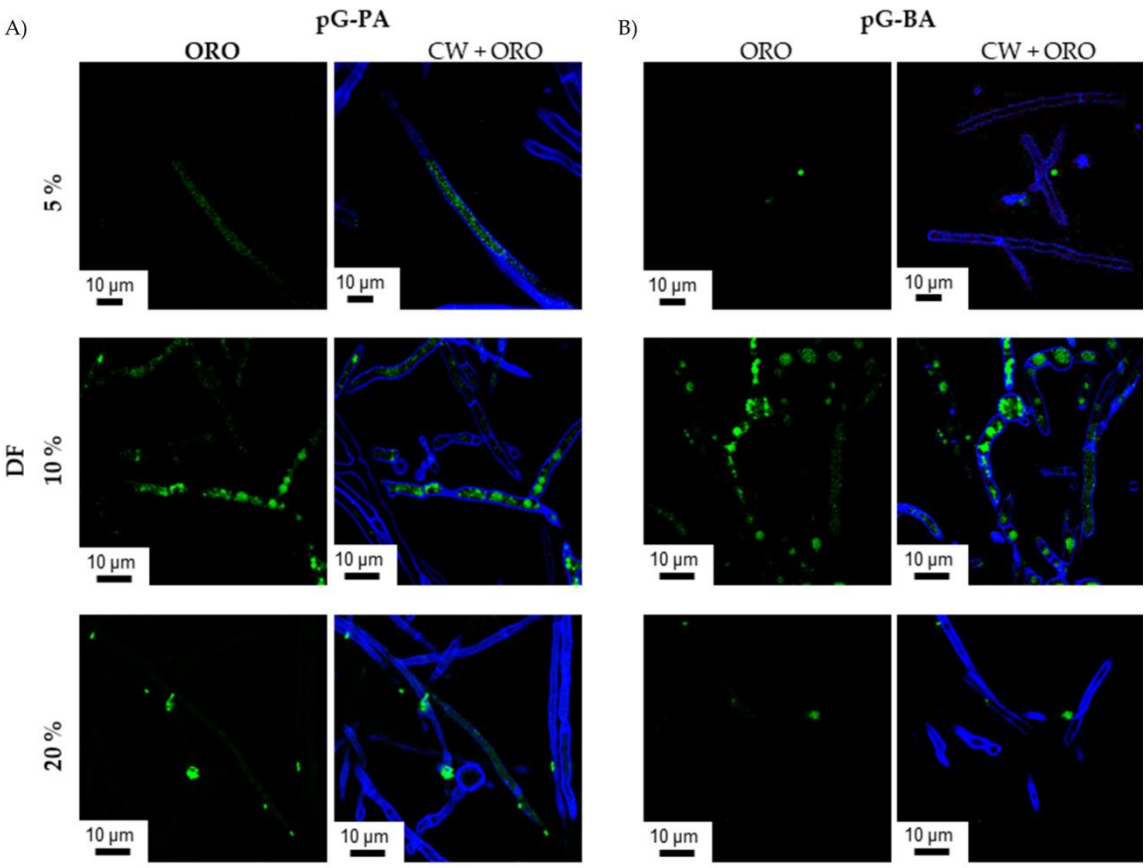

Figure 3.2- 6: CLSM images of *A. fumigatus* pre-incubated for 24 h without and 1 h with ORO (green colour) loaded (A) pG-PA and (B) pG-BA nanogels. Chitin in the CW was stained with calcofluor white (blue color).

The results rather suggested that β-glucans are not the only constituents of a cell wall that dictate the interaction of nanogels and uptake by fungi. The presence of CW proteins and/or other polysaccharides, such e.g. mannoproteins, galactomannan, chitin and other β-glucans might be also important for the interaction, which remains to be investigated in the future.

3.2.5 Drug-loaded nanogels

Amphotericin B (AmB) is considered as the most efficient antifungal drug against

invasive aspergillosis (IA) due to high efficacy and rare fungal resistance.[92]

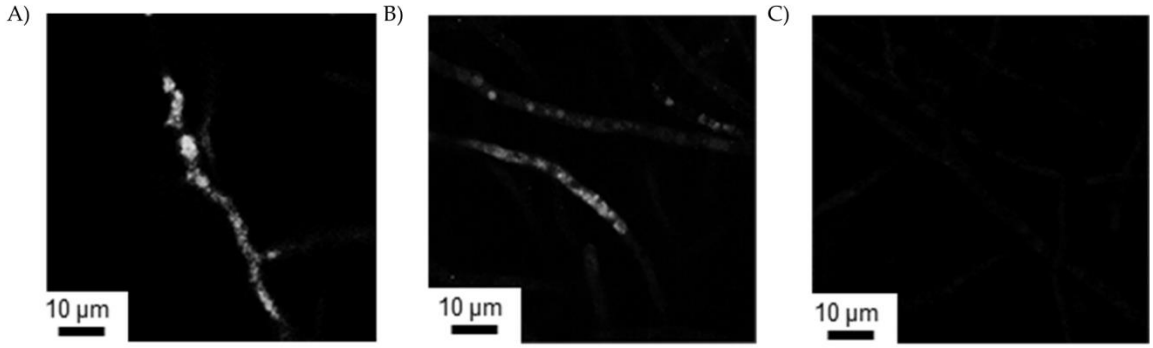

Figure 3.2- 7: CLSM images of fungi incubated with pG-BA10% for (A) 1 h and (B) 3 h with ORO loaded pG-BA10% nanogels. (C) Cells incubated with only ORO dye for 3 h. In this figure is shown only channel for ORO dye (white).

Its mechanism of action relies on binding to ergosterol at the fungal cell membrane, leading to the leakage of ions due to the increased membrane permeability.Unfortunately, direct delivery of this antifungal shows strong adverse side effects such as high renal toxicity, which limits its application. Therefore, various nanoparticle-based AmB formulations were developed, mainly based on the liposomes and colloidal dispersions, which showed improved biocompatibility and efficacy.[162, 168] However, the mechanism and interaction of nanoparticles is still not completely understood.[169]

In this study, AmB was encapsulated through physical interaction during self-assembly of the amphiphilic precursor polymers to nanogels. After drug encapsulation particles became slightly more negatively charged, except pG-BA20% (Table 3.2- 3). DL increased with an increase of hydrophobicity of copolymers in nanogels, either by changing DF or alkyl chain length (Table 3.2- 4). It was lowest for pG-PA5% and highest in case of pG-BA20%. This was expected, since higher hydrophobicity of nanogels enabled encapsulation of higher amounts of hydrophobic drug loading. The size of AmB loaded pG-PA20% and pG-BA20% decreased with the drug loading, while this was not the case in other nanogels. This might be explained by contraction of the polymeric chains with higher hydrophobicity around drug molecules leading to the decreased nanogel size as in the case of ORO loaded nanogels.

Table 3.2- 4: Drug loading (DL) of AMB in nanogels.

	DL (%)	
DF (%)	pG-PA	pG-BA
5	2.8 ± 0.0	3.7 ± 0.0
10	6.5 ± 0.1	15.3 ± 0.1
20	8.9 ± 0.1	16.1 ± 0.0

Nanogels remained spherical after drug loading as revealed by AFM and scanning transmission electron microscopy (STEM) (Figure 3.2- 8).

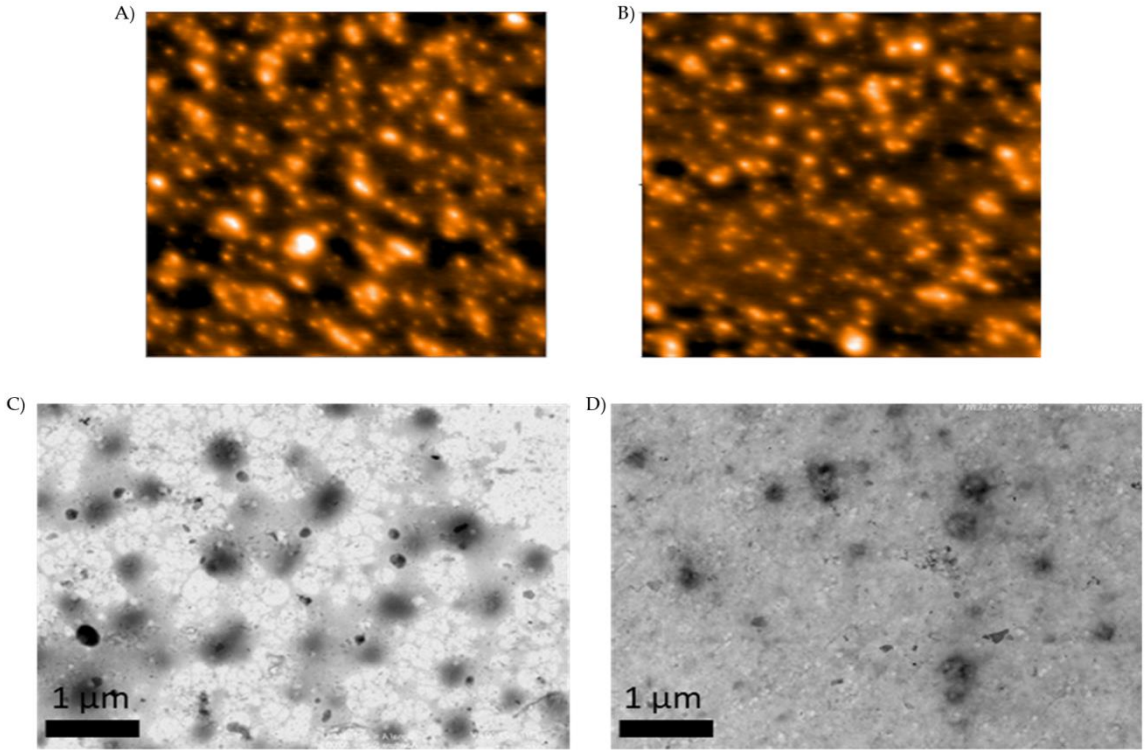

Figure 3.2- 8: AFM images of pG-PA10% nanogels without (A) and with AmB loading (B). STEM images of (C) empty and (D) AmB loaded nanogels. Size of the AFM picture is 5 µm x 5 µm.

X-ray powder diffraction (XRD), Raman and Fourier-transform infrared (FT IR) spectra confirmed encapsulation and amorphous state of the drug in nanogels (Figure 3.2- 9). Bands at 1557 cm^{-1} and 1157 cm^{-1} in Raman spectra belonged to the C=C and C-C stretching of bonds, respectively, and band at 1010 cm^{-1} belonged to asymmetric vibration of ß-glycoside linkage, characteristic for AmB molecules. To further ensure that the drug is dissolved in nanogels and not found freely in the

solution, XRD studies were performed. Results showed that in comparison to the typical crystalline form of the pure drug where peaks were sharp and well defined, AmB loaded samples had a spectrum with a peak broadening. This confirmed that drug was present in an amorphous state, meaning that drug solubility was increased by incorporation in nanogels.

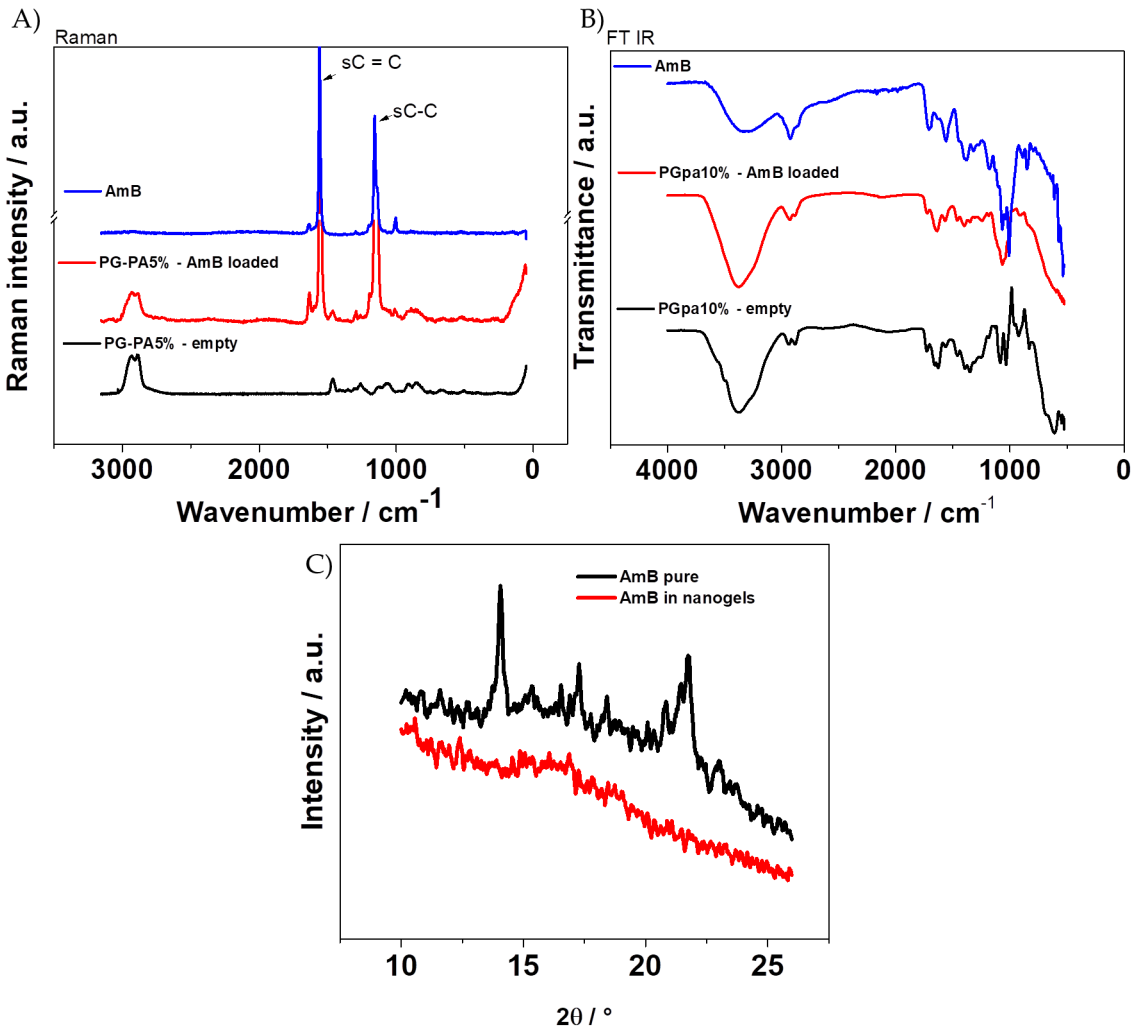

Figure 3.2- 9: (A) Raman, (B) FT IR and (C) XRD spectra of samples.

Finally, the aggregation state of AmB was analyzed (Table 3.2- 5). It is known that this drug self-aggregates in aqueous solution, due to its slightly amphiphilic nature. Drug aggregation is found to be responsible for high cytotoxicity of AmB toward mammalian cells in comparison to its monomeric form. Aggregation number of AmB was evaluated by ultraviolet-visible (UV-Vis) spectrometric studies, by calculation of ratios of the first (I) and fourth (IV) peak of the spectrum.

When dissolved in organic solvents, such as DMSO, UV-Vis spectrum showed four characteristic peaks at 342 nm, 372 nm, 391 nm and 417 nm.[170] During encapsulation in nanogels, the ratio of I/IV peaks had values near 7 for pG-PA5% and pG-PA10% nanogels, which suggested high aggregation state of AmB. However, with increased polymer DF and hydrophobicity by altering the alkyl side chain, the aggregation number of AmB decreased and was minimal for pG-BA20% nanogels. These results indicated that pG-BA samples could more efficiently reduce aggregation of AmB and, therefore, cytotoxicity.

Table 3.2- 5: Aggregation state of AmB in samples.

	I/IV ratio
pG-PA5%	6.67
pG-PA10%	6.67
pG-PA20%	5.57
pG-BA5%	5.57
pG-BA10%	5.88
pG-BA20%	2.32
AmB in DMSO	0.99

Fungal cells, as well as mammalian cells, contain high intracellular concentrations of glutathione (up to 10 mM).[51] This small molecule plays an important role in the metabolism of stress response of the cells and is vital for the fungal cell growth.[51] Because of disulfide bridges in nanogels, it was expected that nanogels show redox-responsive behavior. Results showed that AmB was released from nanogels in the redox-responsive way (Figure 3.2- 10). This was expected due to the presence of disulfide bonds, which were cleaved in the presence of a reducing agent. To exclude the influence of dithiothreitol (DTT) on the drug absorption on resins, both pure AmB drug and AmB-deoxycholate (Fungizone) as the commercial drug for treatment of life-threatening fungal diseases were incubated with the same concentrations of reducing agent (Figure 3.2- 10B-C).

Therefore, nanogels might release their cargo inside fungal cells under the

influence of reducing agents which could explain diffusive fluorescence signal in the fungal cells after 3 h of incubation with ORO loaded nanogels (Figure 3.2- 6, Figure 3.2- 7).

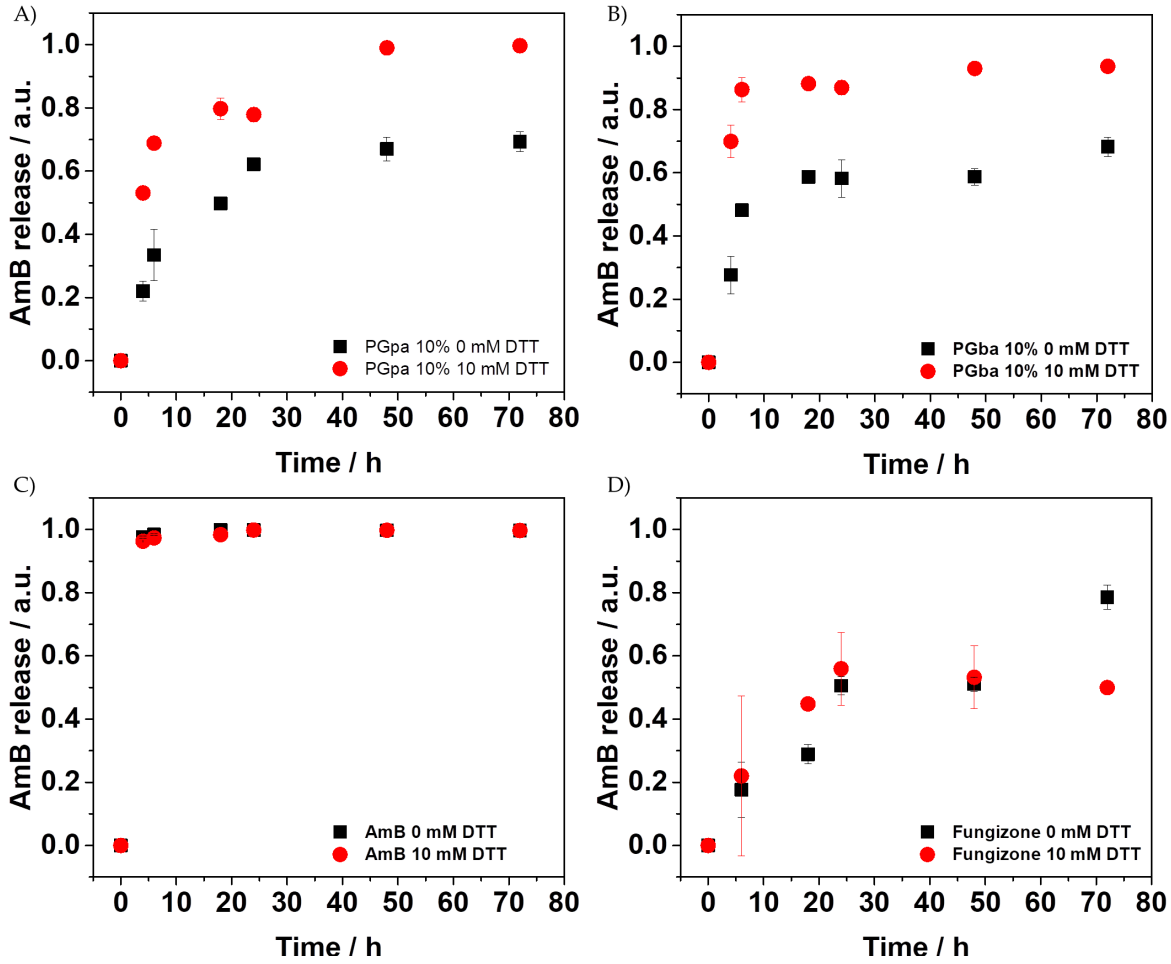

Figure 3.2- 10: Drug release profiles of (A) pG-PA10% and (B) pG-BA10% nanogels (C) pure AmB drug and (D) Fungizone in presence or absence of a reducing agent in a concentration of 10 mM.

3.2.6 Toxicity of AmB loaded nanogels towards *A. fumigatus*

The fungi were treated with empty and AmB loaded nanogels, while PBS and Fungizone was used as a negative and positive control, respectively. Neither empty nanogels nor supernatants taken after final washing step by centrifugation of nanogels did not show the toxic effects on the fungal growth (results not shown). This result again confirmed that nanogel suspensions did not contain the free drug.

Incubation medium influenced the toxicity of drug towards fungus (Table 3.2- 6).

In a minimal medium (MM), which is a growth medium for the fungi, MIC of AmB and AmB loaded nanogels was 2.5 μg/mL for pure drug and pG-PA20% and pG-BA20%. Nanogels with DF of 5 % and 10 % showed lower minimal inhibitory concentration (MIC), with higher efficiency for pG-PA nanogels. These results correspond to the results with studies of nanogel interaction with β-glucans, where higher interaction was observed with nanogels with DF of 5 % and 10 %. On the other hand, in RPMI-1640 medium, which is culture medium for mammalian cells, MIC of pure drug AmB reached 0.63 μg/mL and 0.16 μg/mL for AmB loaded nanogels, regardless on DF or alkyl chain. Also, MIC of Fungizone was 2 times higher than nanogels, indicating that AmB encapsulation in nanogels enhanced its antifungal efficacy. Better antifungal properties of AmB encapsulated in nanogels could be attributed to the increased interaction of nanogels with fungal cells. Since it is known that chemistry of the hyphal CW differs when fungi are incubated in RPMI-1640 medium in comparison to MM,[146] increased antifungal efficacy of tested samples in RPMI-1640 medium might be explained due to the higher interaction of nanogels with CW, which in this case contains more β-glucans.

Table 3.2- 6: MIC of AMB loaded nanogels and pure drug in different incubation mediums.

	MIC (μg/mL)	
	MM	**RPMI-1640**
pG-PA5%	1.25	0.16
pG-PA10%	1.25/2.50	0.16
pG-PA20%	2.50	0.16
pG-BA5%	1.25/2.50	0.16
pG-BA10%	2.50	0.16
pG-BA20%	2.50	0.16
AmB	2.50	0.63
Fungizone	2.50	0.32

Biofilm formation is a preferred form of fungal growth and was firstly observed by Mowat et al.[9] showing that biofilm is the main cause of the resistance of the

fungal pathogens against antifungals and failed treatments. The change in biofilm formation in the presence of nanoparticles after 48 h and 24 h after one-day preincubation without any supplement in the medium (24 + 24 h) was examined. Lower drug concentrations inhibited biofilm formation, also well below the MIC as seen in scanning electron microscopy (SEM) images (Figure 3.2- 11).

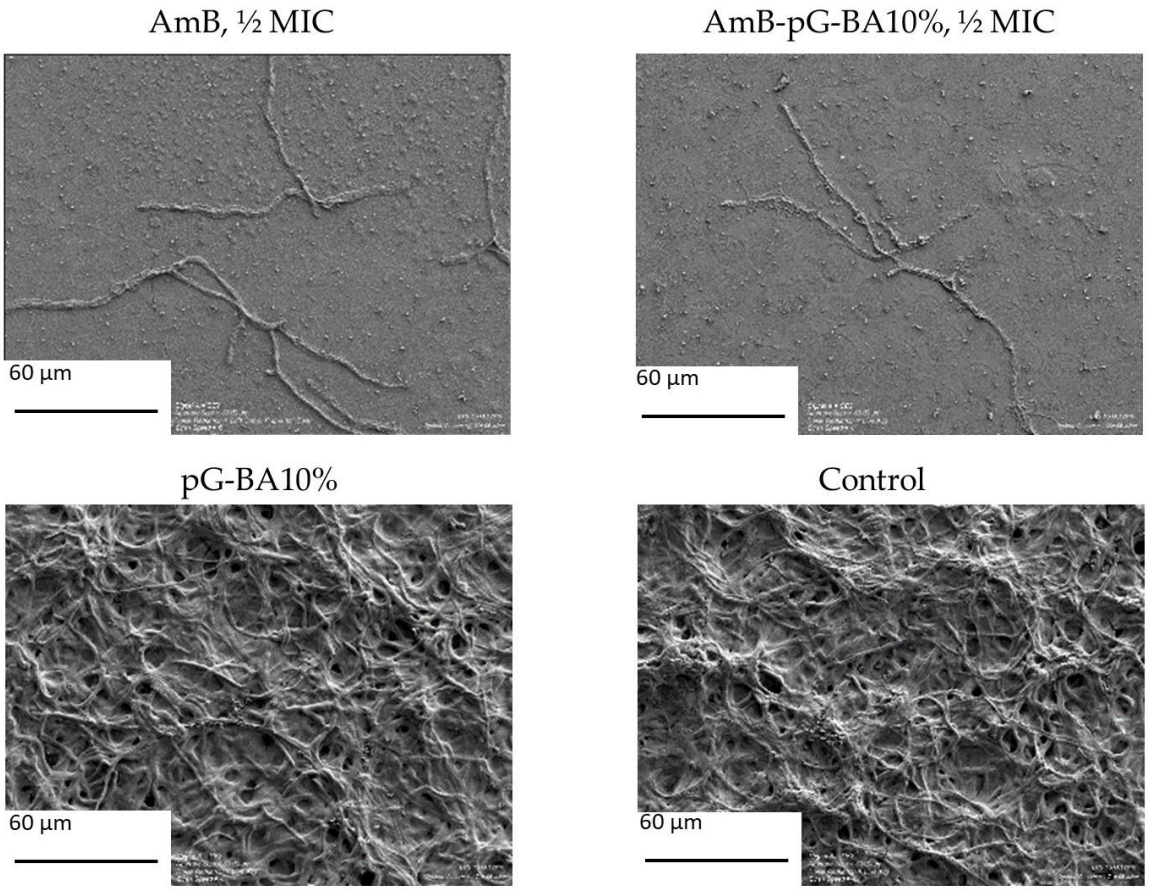

Figure 3.2- 11: SEM analysis of *A. fumigatus* biofilms after treatment with drug and nanogels. Control sample was incubated with PBS. The drug inhibited the fungal growth and hindered biofilm formation.

However, pG-BA5% and pG-BA20% lost their antifungal properties faster than the rest of the nanogels below the MIC when incubated for 48 h (Figure 3.2- 12). The latter sample even completely lost its antifungal properties at a concentration of 0.5 x MIC. Also, there was a slight decrease in the antifungal activity of pG-PA20% in comparison to pG-PA5% and pG-PA10% at 0.3 x MIC, but still higher than pG-BA20%.

These results were related to observations of nanogel interactions with β-glucans and fungal hyphae, which indicated that, indeed, better antifungal properties could be explained by increased interaction of nanogel with polymers with DF of 10 % with fungal cells. Also, slightly higher uptake and absorption of ORO loaded pG-PA5% and pG-PA20% nanogels in comparison to BA counterparts (Figure 3.2-6) might explain increased antifungal effects of pG-PA nanogels. Correlation between increased interaction of nanoparticles with fungal cells and increased antifungal effects was observed in other studies as well.[171] Adler-Moore et al.[172] showed that improved antifungal properties of liposome-encapsulated AmB were related to nanoparticle interaction with CW of *Candida* spp., while Shimizu et al.[173] showed that internalization of nanoparticles improved antifungal property toward yeast *S. cerevisiae*. Finally, improved antifungal properties of AmB formulation might not be induced by binding to the cell membrane but also in binding to other organelles such as vacuoles if internalization of the drug occurs.[174]

To get information about CW morphology before and after treatment with nanogels or drug, the hyphal surface was analyzed by SEM and AFM. AFM surface analysis revealed smoother CW characterized by order of magnitude lower surface roughness of samples treated with nanogels in comparison to untreated control (result not shown). Results showed that cell surface structure changed upon the incubation with empty nanogels suggesting that pG had a similar impact on the CW and possibly membrane of the fungal hyphae.[175] It might be possible that it induced defects on the hyphal surface, increasing permeability for drug molecules. It was shown by Boni et al.[176] that pEG could induce membrane dehydration and that it was able to solvate the polar head group of membrane phospholipids acting as cell-fusogen, which could be transferred to fungi as well.

Higher smoothness of fungal cells treated with nanogels might be associated with the loss of hydrophobicity, which was observed while handling with biofilms. Differences in the textures and material properties between the different samples were particularly prominent in AFM phase images (Figure 3.2- 13).

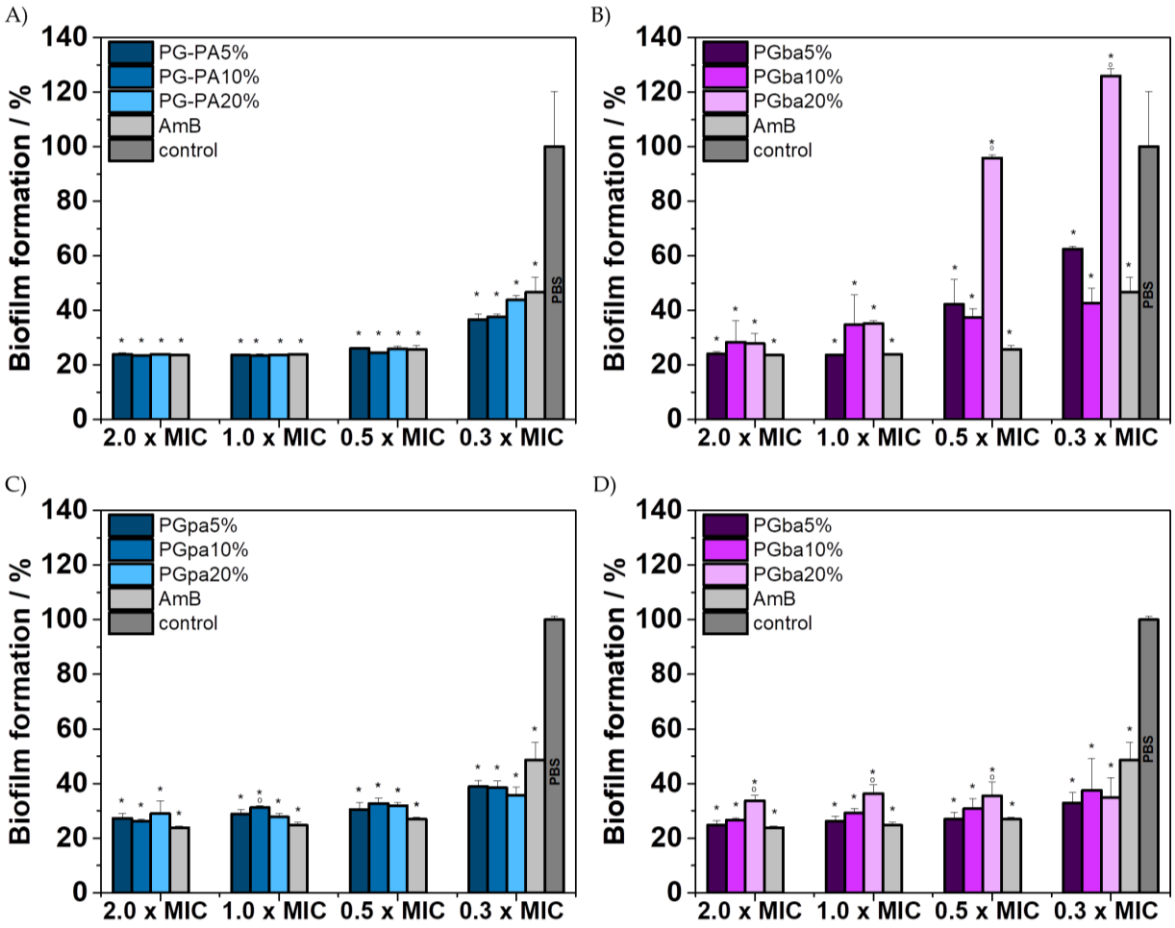

Figure 3.2- 12: Reduction of biofilm as determined by crystal violet: (A) cells were incubated 48 h with the pG-PA and (B) pG-BA nanogels from the very beginning, and (C) cells were pre-incubated without supplements in medium for 24 h, after which medium with pG-PA and (D) pG-BA nanogels was added and samples were incubated for further 24 h. The fungi were left to grow in the medium for 24 h before adding nanoparticles or drug. During this period, fungi already formed biofilm, which accounts of 20 % of the film mass formed after 48 h. One-way ANOVA followed by Tukey's post-hoc test was used for statistical analysis, $P < 0.001$: * - compared to untreated control; o - compared to AmB pure.

Contrary to samples treated with PBS, biofilms incubated with empty nanogels floated in the medium without spontaneous attachment to the polystyrene surface (data not shown). To test this hypothesis and according to the results of AFM roughness analysis, hydrophobicity of hyphal biofilm was estimated using hydrophobic fluorescent silica microparticles.[177-178]

Indeed, incubation of nanogels altered the hydrophobicity of formed biofilm (Figure 3.2- 14).

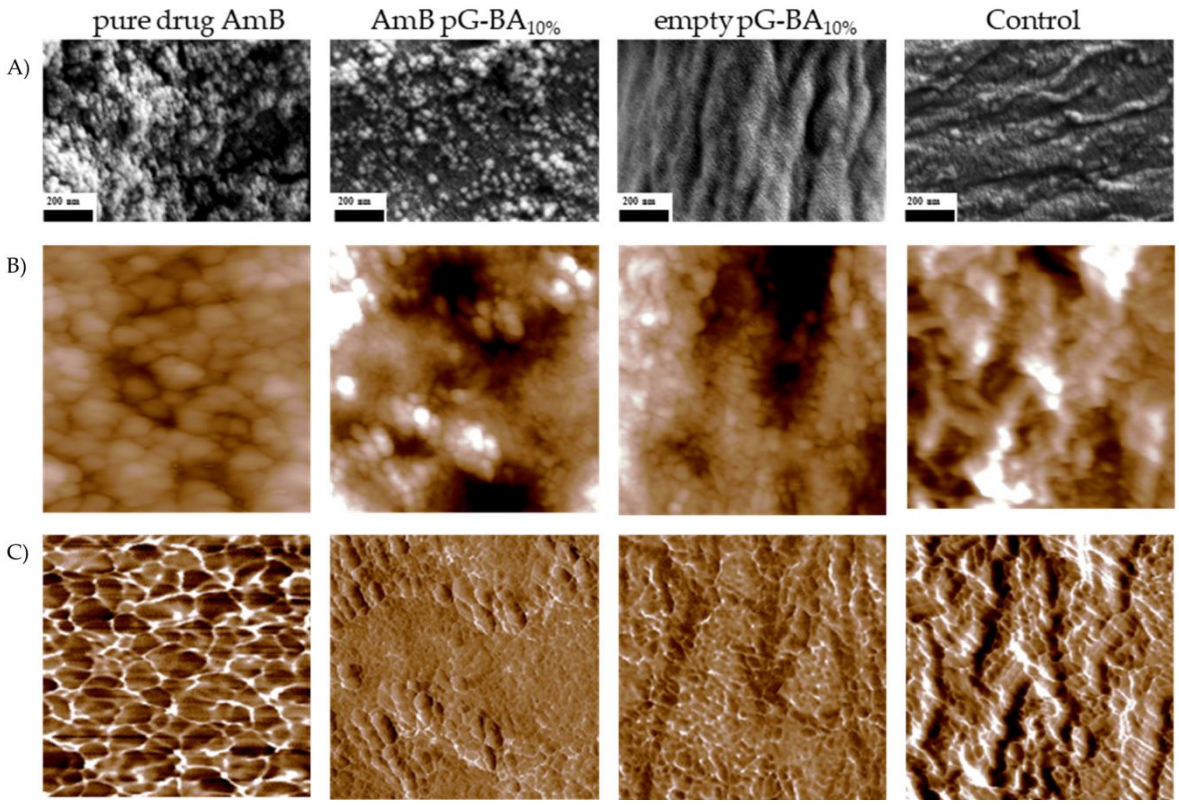

Figure 3.2- 13: (A) SEM (top) and (B), (C) AFM images of fungal cell wall after treatment with pure drug AmB, AmB loaded pG-BA10% nanogels, pG-BA10% nanogels and control sample, respectively. AFM height images (B) have a height scale of 50 nm except for the control sample, which has a scale of 150 nm (three-fold higher) due to its enhanced surface roughness. The data scale in all phase images (C) is 10°. All AFM images are 800 nm x 800 nm.

Higher silica bead absorption was observed for the control sample, in comparison to lower absorption of particles on the fungal cells treated with empty nanogels. After drug loading, nanogels with polymers of DF of 20 %, regardless on alkyl chain length, did not alter cell hydrophobicity, while other nanogels decreased biofilm hydrophobicity, so that almost none of the particles was bound to the CW.It was reported by Ellepola et al.[179] that AmB reduced cell surface hydrophobicity of *Candida* spp. They speculated that AmB bound not only to ergosterols on the cell membrane but also on various membrane-bound enzymes which led to the reduction of surface hydrophobicity.

Results of the current study, together with results of suppression of biofilm formation and MIC values in MM medium, suggested that loading altered the interaction of nanogels with the fungi. This explained differences between DLS

results for the analysis of the interaction of nanogels with β-glucans and observations made by CLSM.

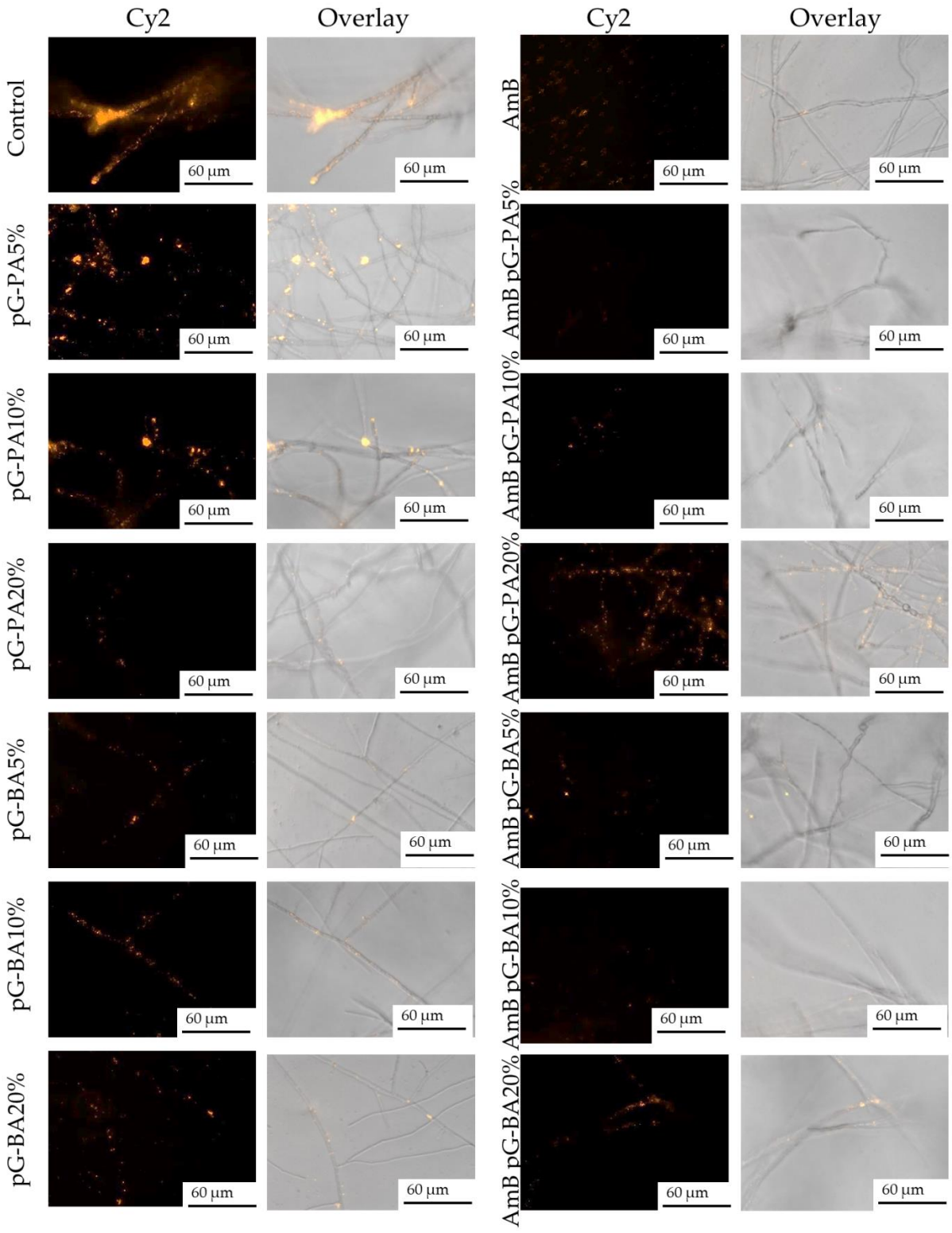

Figure 3.2- 14: Fluorescent images of fungal biofilms after microsphere hydrophobicity assay. The more silica particles (Cy2 channel, yellow) attached the fungal cells, the more hydrophobic the fungal cell was.

3.2.7 Toxicity of nanogels towards mammalian cells

It is known that the main drawback of the application of AmB drug in antifungal therapy is its high toxicity, which leads to the anemia and kidney malfunction.[180] AmB is a polyene drug which binds to ergosterols present not only on the membrane of fungal cells but also on the membrane of other cells. Therefore, the cytotoxicity of all formulations in this study was evaluated on red blood cells (RBC) and Vero kidney cells. In comparison to free AmB and solubilized drug form (Fungizone), all nanogels were able to significantly lower drug toxicity (Figure 3.2- 15). Empty nanogels also did not show signs of toxicity (results not shown). The most moderate toxicity towards RBS showed pG-BA20% nanogels, as predicted by aggregation state of these nanogels (Table 3.2- 5) although all drug-loaded nanogels were considered non-toxic. These results showed that drug is encapsulated inside of nanogels and not on its surface, which hindered its binding to the cell membrane.

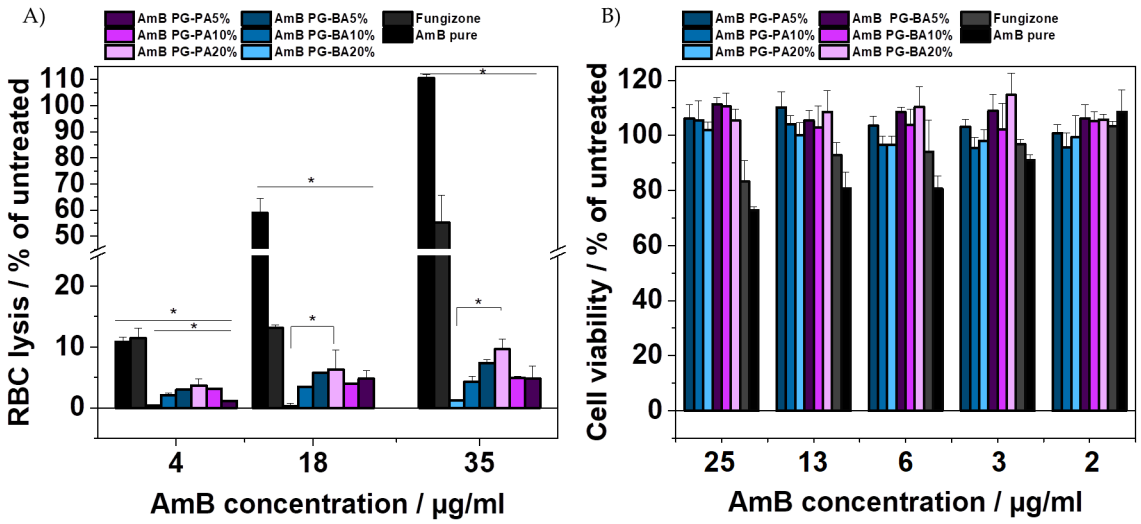

Figure 3.2- 15: (A) RBC lysis after incubation of 24 h with AmB containing samples and (B) cell viability of Vero kidney cells after incubation of 48 h with samples as determined by CellTiter Glo assay. One-way ANOVA followed by Tukey's post-hoc test was used for statistical analysis, $P < 0.001$: * - compared to AmB drug.

3.2.8 Conclusions

This study demonstrates that fine tuning of the amphiphilicity of polymers played

the important role in the interaction of nanogels with *A. fumigatus*. Antifungal drug was encapsulated within nanogels and drug antifungal properties were enhanced by the encapsulation. Finally, it was shown that nanogels were also efficient against fungal biofilm formation and were not toxic to mammalian cells, which is important for antifungal therapy.

3.3 Itraconazole loaded nanogels prepared by inverse nanoprecipitation

This section was published as original research article and is adapted with permission from: Nanogels as antifungal-drug delivery system against Aspergillus fumigatus; Sonja Horvat, Yidong Yu, Hannah Manz, Thorsten Keller, Andreas Beilhack, Jürgen Groll, Krystyna Albrecht; Advanced NanoBiomed Research 2021, 2000060.

DOI: 10.1002/anbr.202000060. Copyright © 2021 The Authors. Advanced NanoBiomed Research published by Wiley-VCH GmbH.

The chapter is based on the work of the author of this thesis Sonja Horvat-Csóti, who performed major part of experiments, analyzed data and wrote the manuscript. The original text was slightly modified to improve readability.

Author Contributions

Contributor	Contributions
Sonja Horvat	Designed research; performed major part of experiments and analyzed all data; wrote the manuscript
Krystyna Albrecht	Designed research; provided feedback on the manuscript
Yidong Yu	Supported fungal studies; provided feedback on the manuscript
Hannah Manz	Supported fungal studies; provided feedback on the manuscript
Thorsten Keller	Supported cell studies; provided feedback on the manuscript
Andreas Beilhack	Designed research; provided feedback on the manuscript
Jürgen Groll	Designed research; provided feedback on the manuscript

3.3.1 Introduction

The previous **Section 3.2** described the formation of nanogels without need of surfactants. However, although the results of antifungal properties were promising, the nanogels had moderate to broad size polydispersity. Therefore, the nanogel synthesis had to be improved.

The following section reports on the simple method of preparation of poly(glycidol) (pG) based nanogels by inverse nanoprecipitation. To maximize the chances for drug delivery and internalization, nanogels were designed to be both redox-sensitive and hydrolytically degradable. As a proof-of-concept, the possibility of the nano-encapsulation of the antifungal drug itraconazole (ITZ) by the "breathing-in" method is investigated and it is explored how these nanogels interact with *Aspergillus fumigatus*.

3.3.2 Synthesis of nanogels by nanoprecipitation

Thiol-functionalized poly(glycidol)s (pG-SH) with 60 repeat units and an ester linkage at the side-chain were used for the synthesis of nanogels. Thiol functionalization proceeded by Steglich esterification of pG with dithiopropionic acid as described before.[55-56, 135] Polymers with three different functionalization degrees of 5%, 10% and 15% were synthesized. Such functionalization results not only in the incorporation of thiol groups but also renders hydrophilic pG polymer chains to be more amphiphilic due to the presence of hydrophobic propionic groups.

Figure 3.3- 1 illustrates the synthesis procedure of nanogels by inverse nanoprecipitation without surfactants. The aqueous polymer solution was precipitated in acetone, which induced the formation of polymeric nanoclusters. Polymeric nanoclusters were further cross-linked by oxidation of the thiol to disulfide groups to yield stable nanogels.

Several parameters were considered for the optimization of nanoparticles: the influence of the polymer concentration, volume of acetone during precipitation and polymer hydrophobicity. Generally, nanogels had a smaller size in acetone

than in water (Figure 3.3- 2).

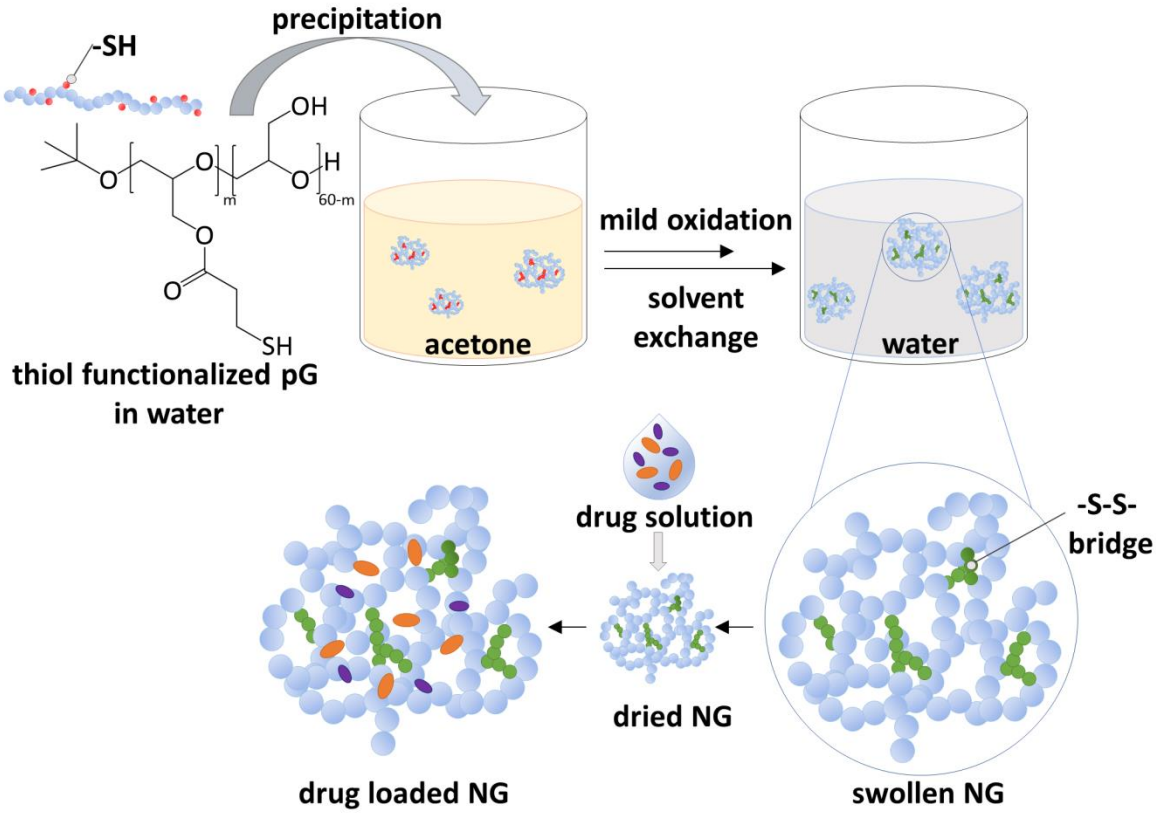

Figure 3.3- 1: Illustration of nanogel synthesis and loading.

This could be explained by the nanogel swelling due to the presence of a hydrophilic polymer matrix, leading to an increase in size.

When the volume of acetone used during precipitation of 6 mg of the polymer was above 4 mL, nanogels exhibited a low polydispersity index (PDI) (Figure 3.3- 3). PDI of nanogels was lower in acetone, implicating that nanogels in this solvent were more defined than in water.

Final nanogels had the size of around 300 nm ± 15 nm and PDI of around 0.1 when measured in water. The narrow size distribution of nanoparticles synthesized by nanoprecipitation and inverse nanoprecipitation were reported earlier.[181-183] The process of nanoparticle formation upon mixing of polymer aqueous solution with non-solvent could be explained by interfacial phenomena between two liquid phases. At first, polymer chains were relaxed in water solution before mixing with an organic solvent. Upon mixing of the polymer solution with acetone, water

diffused from associated polymer chains leading to their dehydration.[184-185] When polymer concentration in acetone reached the critical supersaturation concentration, thermodynamically unstable polymer molecules associated and formed nuclei which grew into nanoparticular polymeric clusters.[184-186]

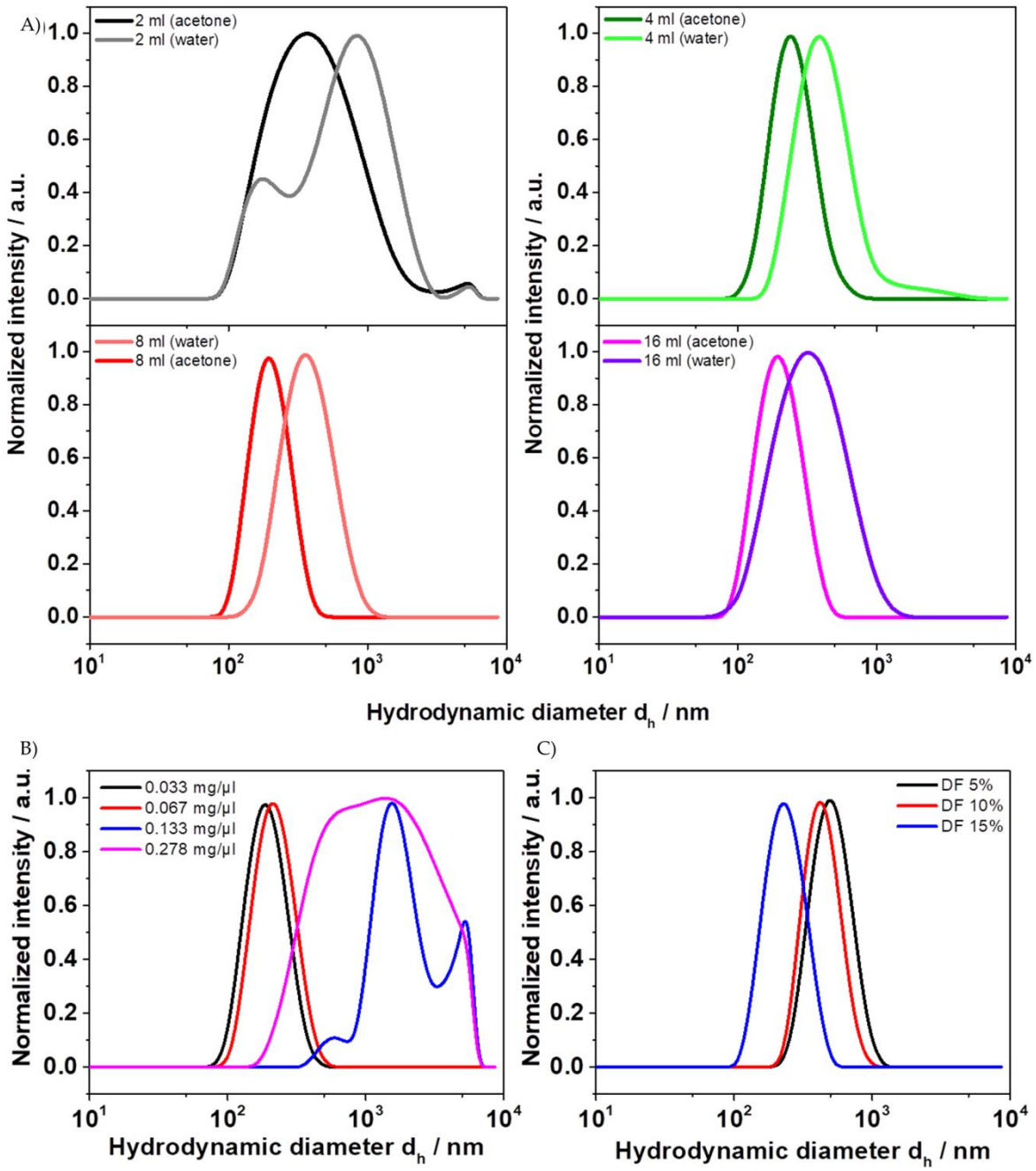

Figure 3.3- 2: Dynamic light scattering (DLS) analysis of: (A) nanogels in acetone and water prepared by precipitation of aqueous polymer solution (0.067 mg/µL) in different volumes of acetone; (B) nanogels prepared by precipitation of loading polymer solution with different polymer concentrations in 4 mL of acetone and (C) nanogels prepared out of polymers (0.067 mg/µL) with different degree of polymerization (DF) precipitated in 4 mL of acetone. (B) and (C) show results of final nanogels in water.

When 2 mL or 4 mL of acetone was used to precipitate 6 mg of polymer, synthesized nanogels had a larger diameter and higher PDI (Figure 3.3- 2). This was expected, since in suspensions with low amounts of acetone nanoclusters were in close proximity to each other, resulting most likely in interparticlulate crosslinking after addition of oxidative agent. Further, the hydrodynamic diameter increased with a higher polymer concentration in the loading solution. Well-defined nanogels with low PDI were obtained while using the polymer loading solution with concentration of 0.033 mg/μL and 0.067 mg/μL, respectively. According to Doelker et al.[184] increase of the size with polymer concentration could be explained either by a number of polymer chains per unit solvent and the influence of viscosity. A larger number of polymer chains in concentrated loading solutions resulted in more frequent polymer interactions, which led to the formation of particles with larger diameters. In other words, during the diffusion of water from a polymeric solution to acetone, more polymeric chains clustered together forming larger nanogels.[184]

On the contrary, when lower polymer concentration was used, fewer polymers were involved in the formation of nanoparticles leading to smaller hydrodynamic diameters.[184]

Another factor to consider during nanogel synthesis was the influence of polymer amphiphilicity. Upon the increase of the degree of thiol functionalization and thus polymer hydrophobicity due to the presence of the propionic spacer, the size of nanogels decreased This outcome was similar to the results of the previous **Section 3.2**, where it was already noticed that nanogels composed from polymers with a higher degree of functionalization were generally smaller.

3.3.3 Loading of itraconazole (ITZ) to nanogels

The "breathing-in" method introduced firstly by Lyon et al.[187-188] was used for loading nanogels with the antifungal drug. In this method, freeze-dried nanogels are loaded y soaking with a volume of drug solution that is absorbed by the nanogels. providing the opportunity to generate drug encapsulating nanogels

with the valuable property for redispersion after lyophilization.

Because almost all antifungal drugs are hydrophobic and could be dissolved in DMSO, recovery of freeze-dried nanogels in this solvent was improved by the addition of cryoprotectants. Cryoprotectants are usually used for the prevention of irreversible aggregation of nanosuspensions after freeze-drying.[189] Therefore, it was crucial to determine their effective concentration since both high and low amounts of cryoprotectants could negatively influence the stability of nano-suspensions.[189] Glucose was shown to be a good cryoprotectant for pG-SH nanogels in the tested concentration range between 5 % and 20 % and ensured redispersion of nanogels in DMSO (Table 3.3- 1). As shown by DLS analysis, samples containing glucose concentration of 10 % had the same PDI (0.1) after lyophilization although the particle size was increased.

Table 3.3- 1: Influence of glucose as a cryoprotectant for redispersion of nanogels in DMSO.

Solvent DMSO	Z-Ave (nm)		PDI		d_h (nm)	
	BL	*AL*	*BL*	*AL*	*BL*	*AL*
20 % glucose	260	330	0.1	0.2	300 ± 15	390 ± 30
10 % glucose		320		0.1		370 ± 35
5 % glucose		340		0.2		440 ± 30
0 % glucose		n.m.*		0.5		520 ± 95

*n.m. not measurable.

BL – before lyophilization, AL – after lyophilization.

Scanning electron transmission microscopy (STEM) confirmed that there was no change in nanogel shape was observed after lyophilization and redispersion in DMSO (Figure 3.3- 3).

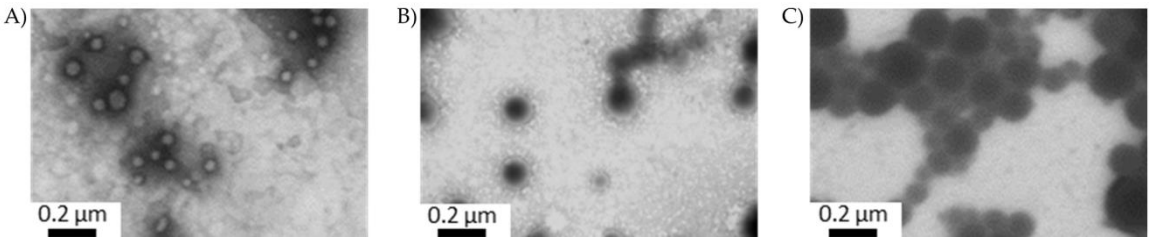

Figure 3.3- 3: STEM pictures of nanogels in (A) acetone, (B) water and (C) in water after lyophilization, respectively.

As a proof of principle, to test the hypothesis that drug could be loaded by "breathing-in" approach, freeze-dried nanogels were firstly loaded with iron salts (Fe^{2+} and Fe^{3+}) and precipitated so-prepared nanogels in sodium hydroxide solution. The basic conditions led to the formation of iron oxide nanocrystals[190] *in-situ* within nanogels as observed by scanning transmission electron microscopy confirming the initial hypothesis (Figure 3.3- 4).

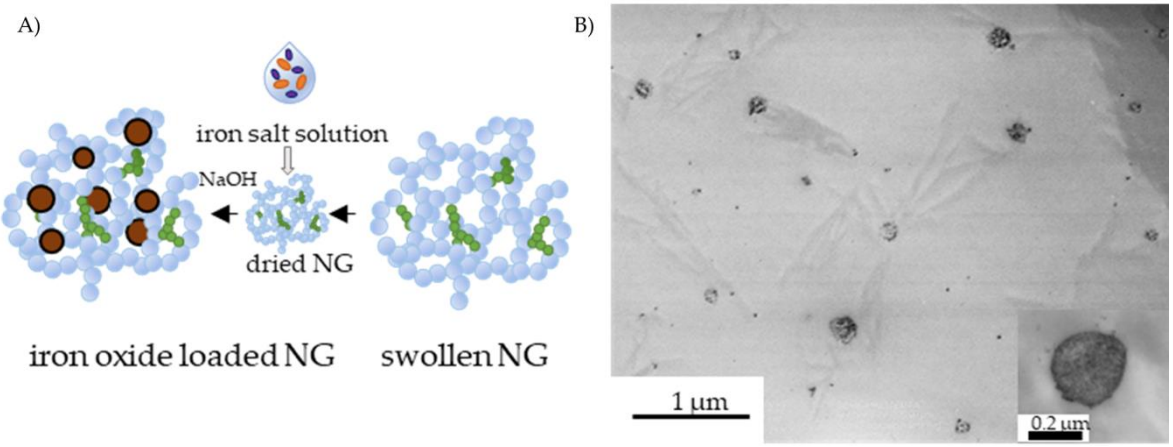

Figure 3.3- 4: (A) Illustration of iron oxide nanocrystals encapsulation in nanogels *in-situ*. (B) STEM analysis of iron oxide loaded nanogels.

After optimal parameters for the synthesis of nanogels were determined, it was investigated how ITZ concentration during loading influences encapsulation efficiency (EE) and drug loading (DL) (Table 3.3- 2). It was observed that at the highest drug loading concentration of 10 mg/mL the EE was the smallest, while 1 mg/mL of drug loading showed the highest EE (30 ± 4 %). On the other hand, DL was the highest when 10 mg/mL was used for loading. However, after drug loading with the highest ITZ concentration of 10 mg/mL, large crystallites were immediately formed upon the addition of water, which was explained by poor water solubility of this drug. Therefore, the further studies were performed with the ITZ concentration of 1 mg/mL.

Scanning electron microscopy (SEM) and STEM analysis showed that nanogels remained spherical after drug encapsulation (Figure 3.3- 5).

Drug encapsulation within nanogels was confirmed by Raman and Fourier transform infrared spectroscopy (FT IR) (Figure 3.3- 6).

Table 3.3- 2: Influence of ITZ lading concentration on particle charge, EE and DL.

ITZ (μg/mL)	ζ-potential (mV)	EE (%)	DL (%)
10000	-32 ± 8	11 ± 1	0.96 ± 0.12
1000	-22 ± 7	30 ± 4	0.27 ± 0.05
100	-28 ± 7	22 ± 7	0.02 ± 0.01
0	-24 ± 6	-	-

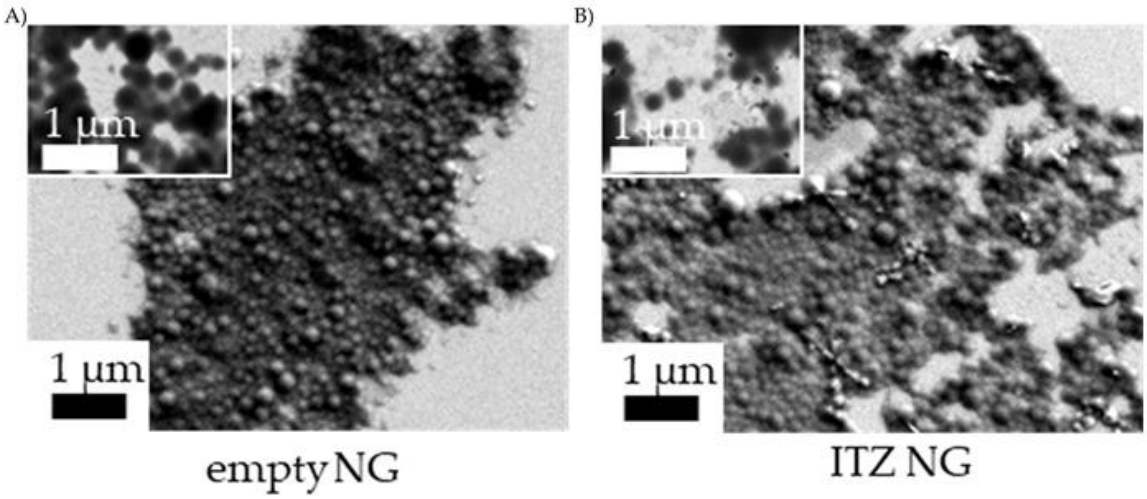

Figure 3.3- 5: SEM images of (A) empty and (B) ITZ loaded nanogels (NGs) with STEM insets.

Majority of bands was assigned to the pGs, but bands characteristic for ITZ, such as at 1613 cm^{-1} and 1582 cm^{-1} assigned to C=N bonds of the triazole group and NH_2 deformation, respectively, were also present.[191]

Additionally, analysis of the encapsulation of drug in nanogels was done by X-ray powder diffractometry (XRD) (Figure 3.3- 6C). Compared to the pure drug which spectra had well-defined peaks, ITZ loaded nanogels did not show any sharp peak. This result led to the conclusion that the drug was present in the amorphous state inside nanogels.[192]

3.3.4 Redox-responsive behavior of nanogels

Drug release from nanogels was investigated in the presence or absence of reducing agent dithiothreitol (DTT). Reducing agents are present in fungi similarly to mammalian cells and are involved in the control of reactive oxygen species.[51] As polymers in nanogels were crosslinked by disulfide bridges, it was expected that nanogels respond redox-responsive.

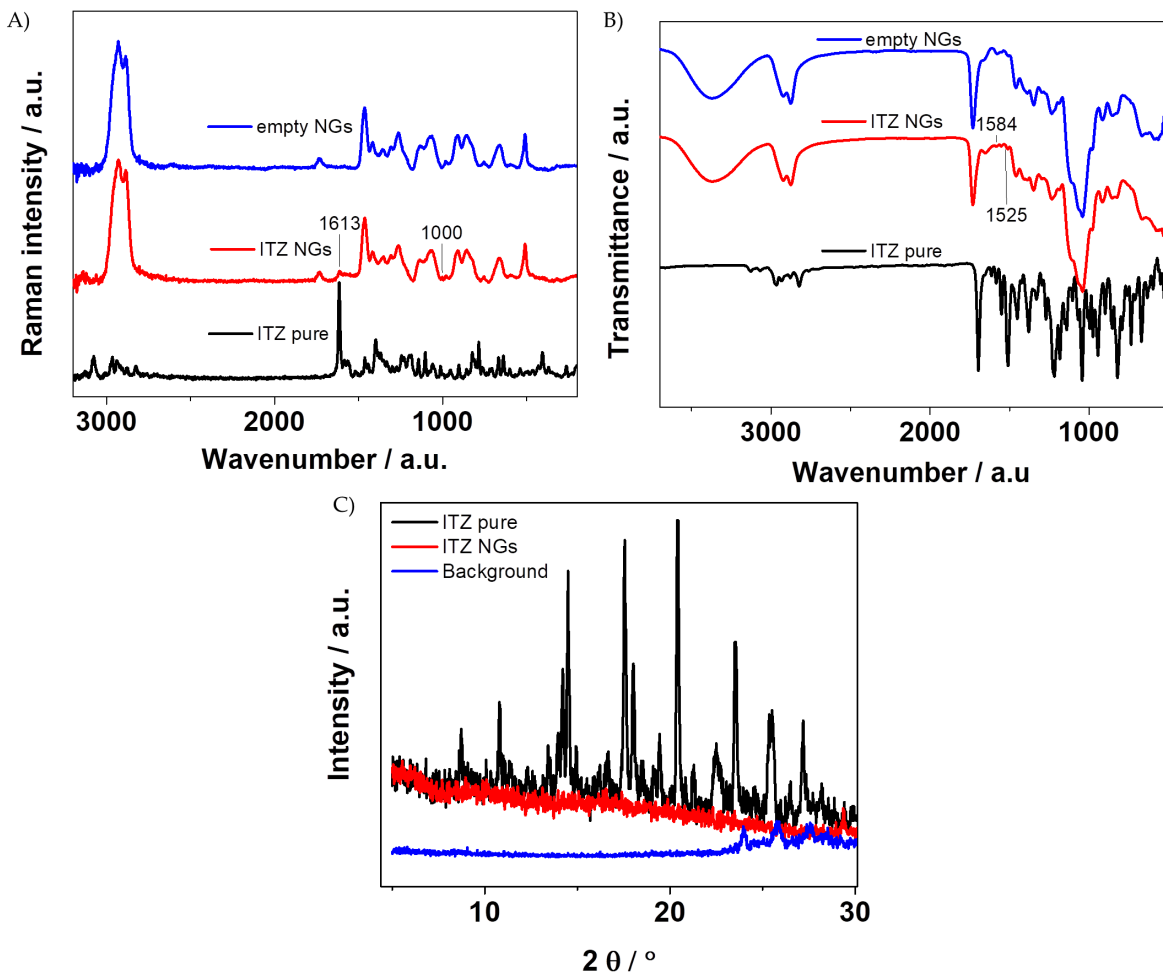

Figure 3.3- 6: (A) Raman, (B) FT IR and (C) XRD spectra of samples.

Firstly, the cleavage of nanogels under the influence of reducing agents (Figure 3.3- 7) in PBS at 37 °C was investigated by measuring the absorbance of nanogel suspension over time. Nanogel cleavage was dependent on the concentration of the reducing agent. They were cleaved entirely already after 10 min when DTT in concentrations of 10 mM and 100 mM DTT, which was the range of glutathione concentration in fungus[51] while cleavage was completed after 30 min when DTT concentration was 1 mM. On the other hand, nanogels were stable for 2 days and then started to degrade. After 1 week of incubation at 37 °C nanogels were almost completely degraded. The degradation was explained by the presence of ester groups which were susceptible to hydrolytic cleavage, making nanogels biodegradable.[135, 193]

The release of ITZ from nanogels was investigated within the first 48 h (Figure 3.3-

7B). ITZ release was redox-responsive, but there was no complete release of drug within investigated time.

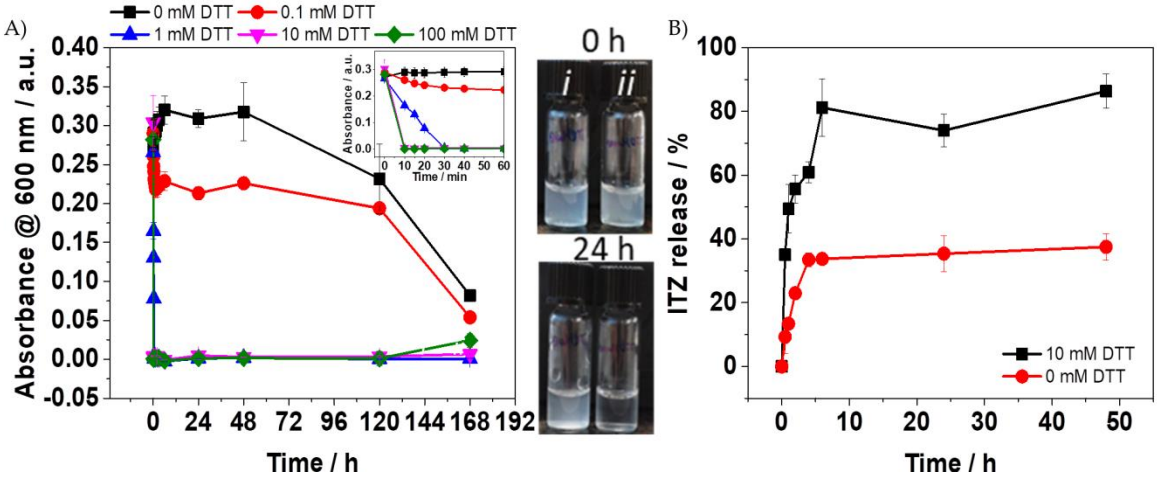

Figure 3.3- 7: Degradation study of (A) empty nanogels. (B) Release study of ITZ loaded nanogels. i) Nanogels incubated with PBS or ii) PBS with the addition of 10 mM DTT at 37 °C.

In the **Section 3.2**, the formation of nano-aggregates from thiol functionalized pGs was described due to the presence of hydrophobic regions in the side-chains carrying thiol group.[56] Since there was no complete release of the drug after 2 days, the incomplete release was assigned to the self-assembly of the cleaved polymeric networks around drug molecules.

3.3.5 Interaction of *A. fumigatus* with nanogels

To study the interaction of nanogels with *A. fumigatus*, nanogels containing fluorescently labelled polymers (conjugated to Atto 647N) were prepared to evaluate the uptake with confocal microscopy (CLSM, Figure 3.3- 8A-C). When nanogels were added to fungal spores, it was noticed that within the first 10 h of incubation, no interaction was observed (results not shown). After 10 h nanogels began adhering on the cells and after 15 h, nanogels started strongly interacting with the fungal cell wall with possible internalization as observed by live-imaging mode in CLSM. However, it was challenging to evaluate the internalization of nanogels due to the high noise coming from the background, although the

internalization of particles was observed (Figure 3.3- 8, insets). After 24 h of incubation, samples were washed, fixed and analyzed. The strong signal in the red fluorescent color channel inside of *A. fumigatus* hyphae suggested internalization of nanogels (Figure 3.3- 8D-F).

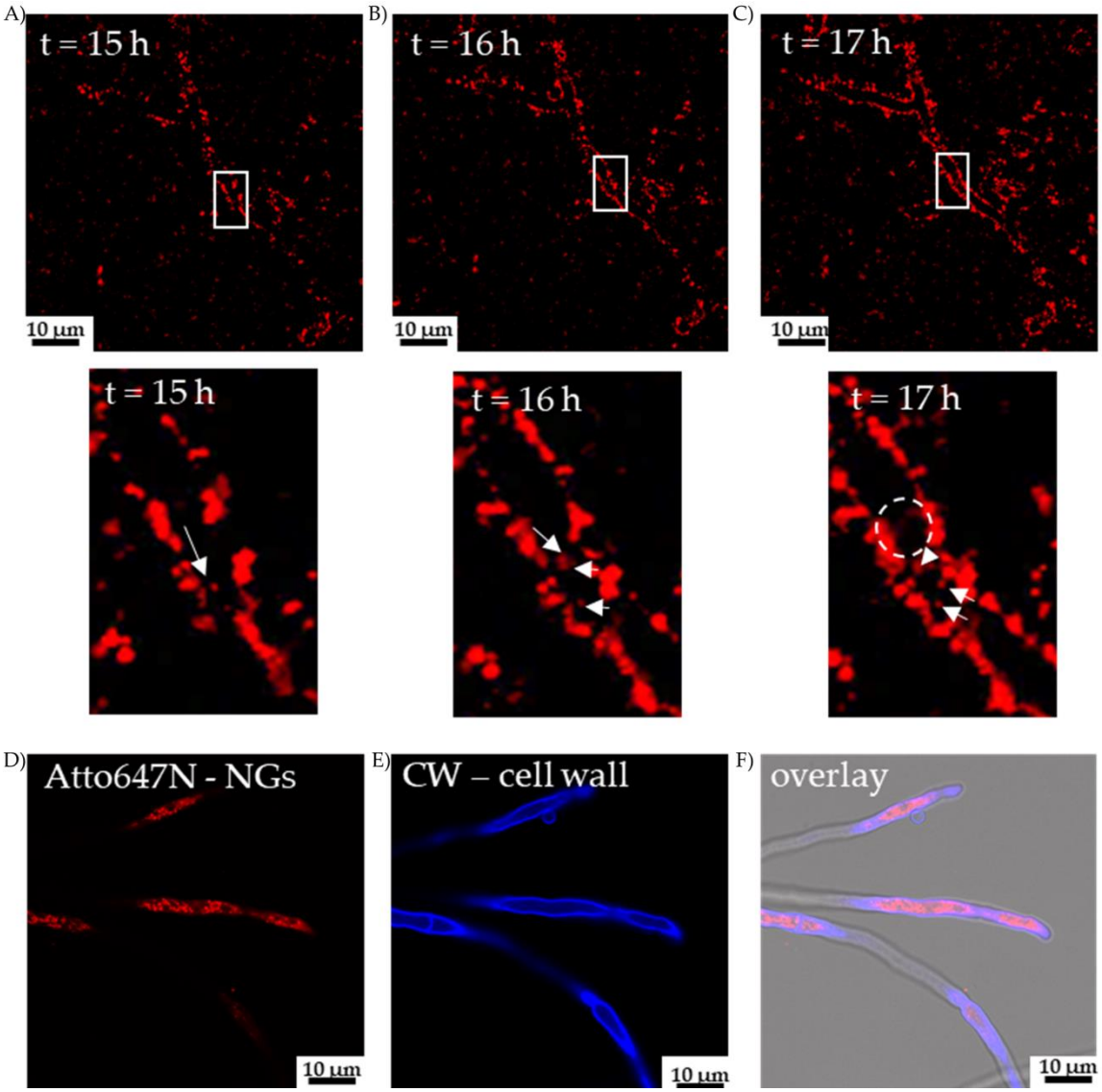

Figure 3.3- 8: Interaction of nanogels (NG) with fungus as analysed by live-imaging by CLSM after (A) 15 h, (B) 16 h and (C) 17 h. Insets show an increase of internalization of nanoparticles in fungus over time. After 17 h, the blurry signal is visible in fungus, depicting nanogel cleavage. (D)-(F) Internalization of nanogels after 24 h of incubation. Red signal – nanogels, blue signal – CW.

Nanogels conjugated with fluorescent dye were also loaded with amphiphilic rhodamine 6 (Rh6g) or hydrophobic Oil red O (ORO) dyes by the "breathing-in" method. CLSM analysis revealed that before loading to fungal cells red signal of

nanogels and green signal of a dye overlapped (Figure 3.3- 9). Again, this result confirmed that "breathing-in" method could be used for the encapsulation of both hydrophobic and amphiphilic moieties.

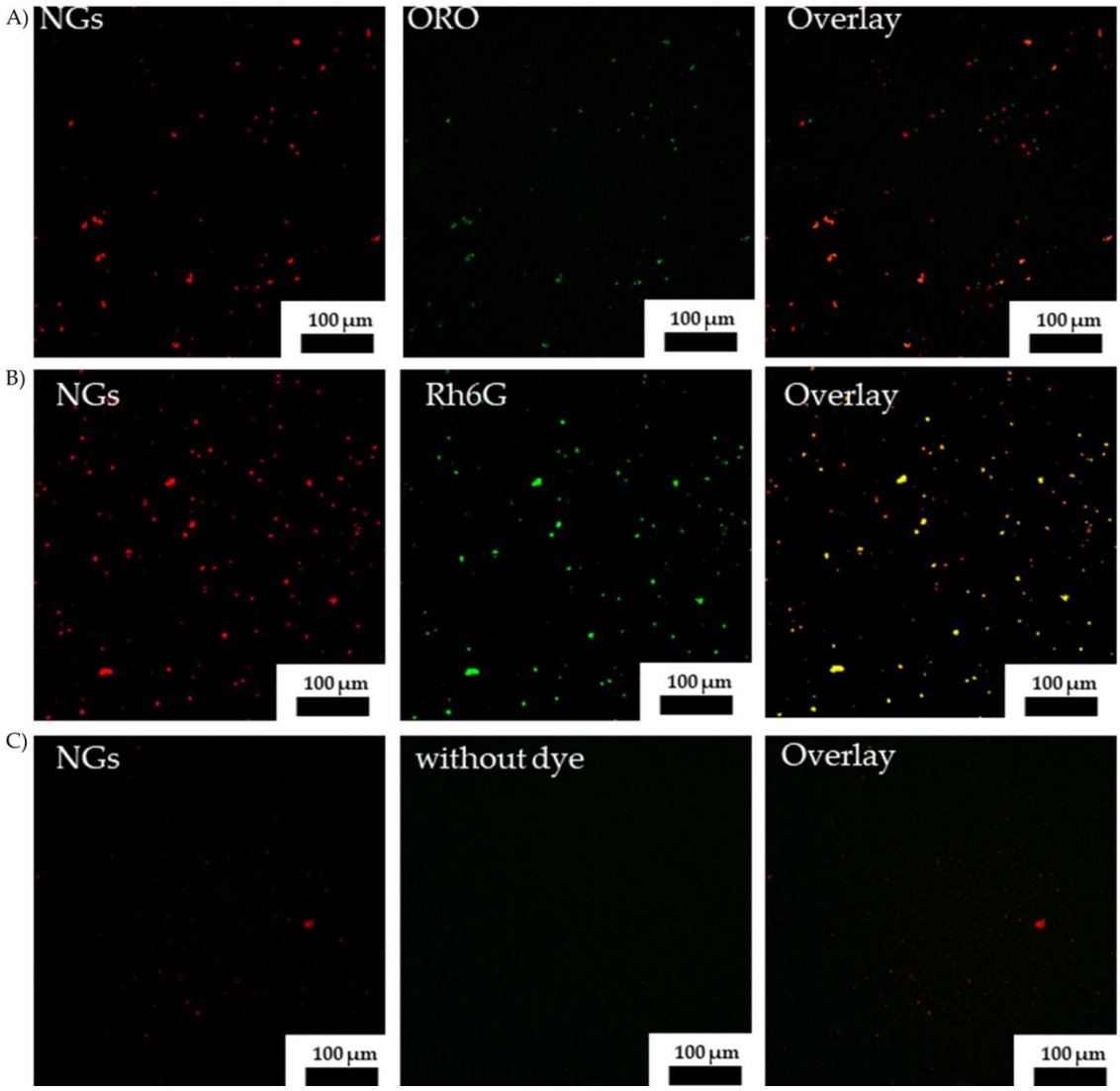

Figure 3.3- 9: (A) ORO, (B) Rh6 and (C) empty fluorescently labeled NGs in suspension under CLSM. Red: Atto647 NGs, green: encapsulated dye and yellow/orange: overlap between dye and nanogels.

Filamentous fungi *A. fumigatus* form biofilms containing high amounts of extracellular polymeric matrix, which increases pathogenicity. To investigate the interaction of nanogels with fungal biofilm dye-labeled nanogels were incubated with biofilm of A. fumigatus for 1 h and samples were analyzed with CSLM (Figure 3.3- 10). Nanogels delivered the fluorescent dye to the fungus and

remained adhered to the fungal cell wall. Moreover, the dye was detected inside fungal cells, suggesting internalization. These results suggested that the adherence of nanogels might trigger the dye release and internalization.

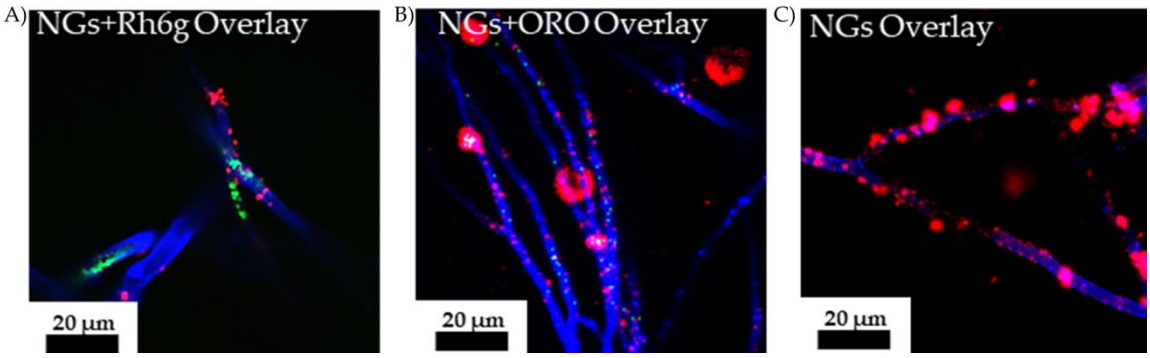

Figure 3.3- 10: Mature fungi incubated with (A) Rh6g, (A) ORO and (C) empty fluorescently labeled nanogels. Red: Atto647 NGs, blue: fungal cell wall, green: encapsulated dye and yellow/orange: overlap between dye and nanogels.

3.3.6 Antifungal properties of ITZ loaded nanogels

ITZ loaded nanogels were found to be more effective than the reference drugThe minimal inhibitory concentration (MIC) of ITZ loaded nanogels (0.09 µg/mL) was two times lower in comparison to the drug alone (0.19 µg/mL). In addition, ITZ loaded NGs inhibited the biofilm formation at sub-MIC values with slightly higher efficiency (Figure 3.3- 11). In comparison to 24 h incubation, after 48 h of incubation, ITZ loaded nanogels at concentrations as low as 0.001 µg/mL inhibited 60 - 80 % of biofilm formation, which was significantly higher than biofilm inhibition caused by the free drug. Empty particles (3 mg/mL) on the other hand, did not show adverse effects on biofilm formation.

The improvement of drug efficiency toward fungal cells by encapsulation in nanocarriers has been reported before.[169, 171, 194] It has been postulated that enhancement of antifungal drugs is a result of increased interaction of nanoparticles with the fungal cell wall in comparison to the free drug which passively enters the fungal cell.[169, 171, 194] As shown previously nanogels were found adherent to the cell wall and were able to deliver the dye already after an hour of

incubation, which might happen with the drug as well. Since nanogels had a higher affinity to the fungal cell wall than free drug, higher drug concentrations were internalized, which ultimately resulted in the higher antifungal efficiency.

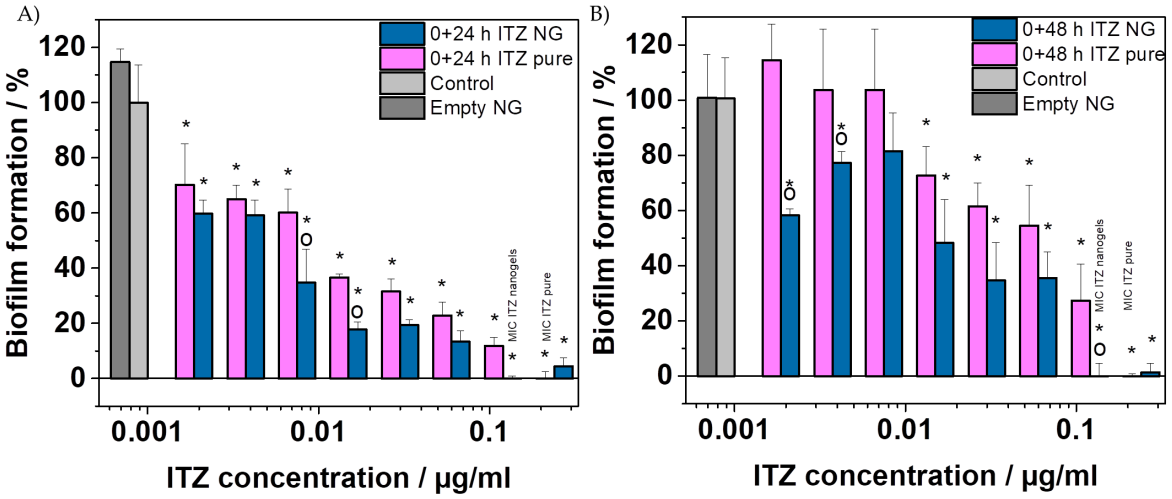

Figure 3.3- 11: Inhibition of biofilm formation after (A) 24 h and (B) 48 h incubation with sub-MIC of drug encapsulated in nanogels and free drug. Test was done in triplicates and one-way ANOVA followed by Tukey's post-hoc test was used for statistical analysis. P values ($P < 0.001$): * - compared to untreated control; o - compared to pure drug.

3.3.7 *In-vitro* biocompatibility studies

For systemic administration of nanogels, it is crucial that formulation does not cause hemolysis of red blood cells (RBC). Antifungal drugs often have a high hemolytic potential[195] causing the release of hemoglobin from RBC, which can lead to undesirable clinical conditions such as renal dysfunction and kernicterus, just to mention a few.[196]

Although it is known that ITZ hemolytic activity is lower than those of other antifungal drugs such as amphotericin B,[195] the present study shows that free ITZ started to induce RBC lysis already at concentrations of 7 µg/200 µL and exceeded 10 % at ITZ 15 µg/200 µL, while ITZ nanogels did not induce any hemolytic effects (Figure 3.3- 12A). Previous reports showed that cytotoxic and hemolytic activities could be decreased by drug encapsulation in nanoparticles. As the likely explanation, this happens because polymer coating or polymer network around

drug hinders drug interaction with RBC, thus decreasing hemoglobin release and cytotoxicity.[195, 197-198] However, the toxicity of the free drug and drug-loaded nanogels did not differ significantly towards liver and kidney cells (Figure 3.3-12B-C). This indicates uptake of drug loaded nanogels by these cells (Figure 3.3-12B-C).

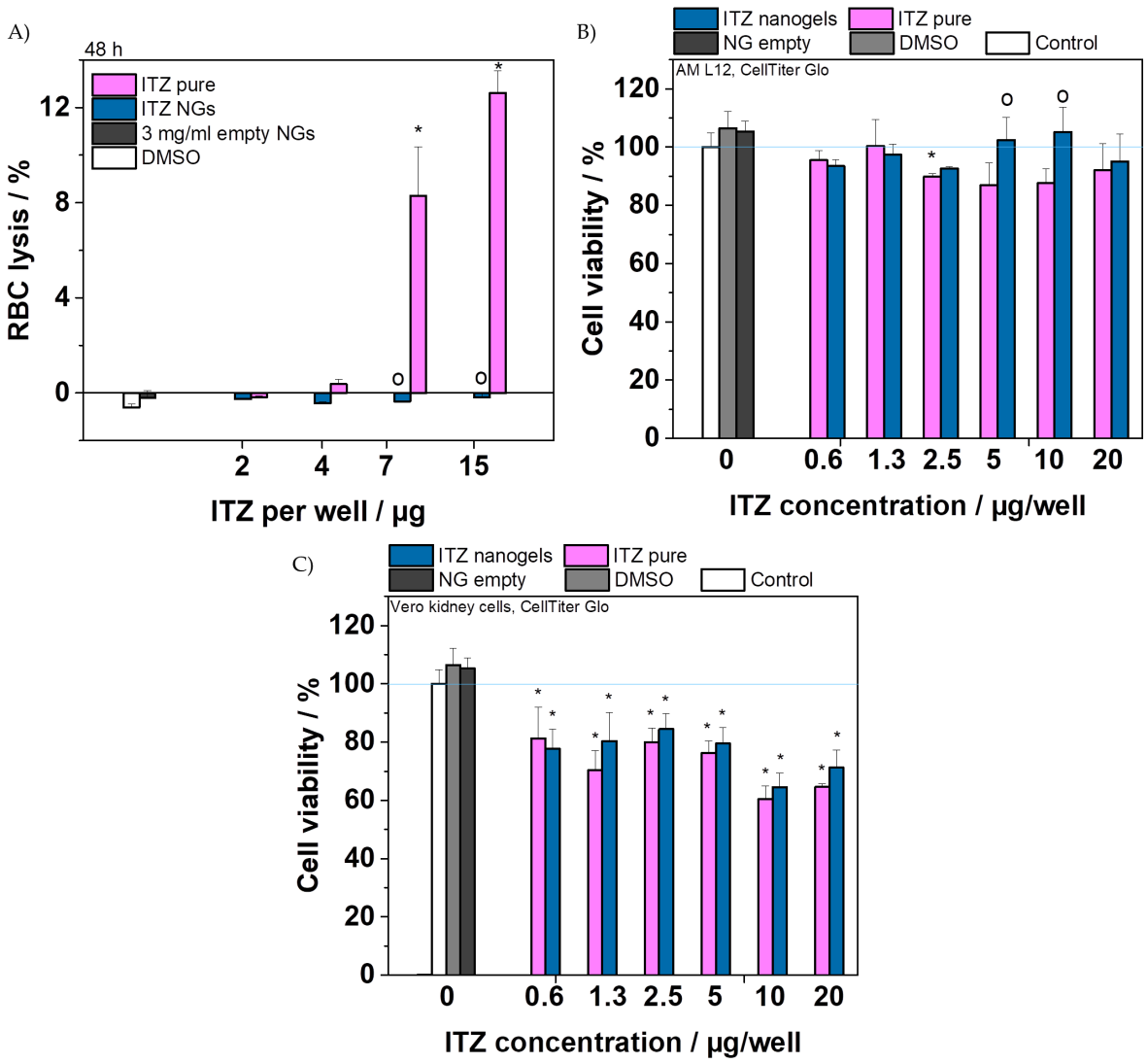

Figure 3.3- 12: (A) RBC lysis induced by ITZ loaded nanogels and free drug over 48 h of incubation. Cell viability of (B) AM L12 liver cells and (C) Vero kidney cells after 48 h of incubation. One-way ANOVA followed by Tukey's post-hoc test was used for statistical analysis. P values ($P < 0.001$): * - compared to untreated control; o - compared to pure drug.

3.3.8 Conclusions

This section evaluated the applicability of nanogels for the uptake by and the drug delivery into the lethal fungus *A. fumigatus*. For this, pG-based nanogels were

synthesized by inverse nanoprecipitation. The "breathing-in" method of drug loading by soaking lyophilized nanogels with a solution of the cargo proved advantageous for encapsulation of both amphiphilic and hydrophobic dyes as well as the antifungal drug itraconazole. Itraconazole-loaded nanogels exhibited improved antifungal properties, such as two-fold lower minimal inhibitory concentration and longer inhibition of biofilm formation than the reference drug alone. Drug-loaded nanogels exhibited lower toxicity towards red blood cells but similar cytotoxicity profile towards liver and kidney cells, suggesting internalization of nanogels in mammalian cells. The nanogels in this study were designed to facilitate drug delivery through redox sensitive disulphide groups and ester groups as part of the polymer network and no specific targeting strategy was yet applied in this proof-of-principle investigation. Accordingly, these results encourage to further advance strategies for targeted nanogel delivery to pathogenic fungi, which bear significantly different patterns of surface markers than mammalian cells which makes targeting strategies a reasonable approach. However, although nanogels showed promising results in the antifungal applications, further studies in targeted delivery to fungal cells would be needed.

3.4 Development of superparamagnetic tracers for imaging

This section was published as original research article and is adapted with permission from: S. Horvat, P. Vogel, T. Kampf, A. Brandl, A. Alshamsan, H. A. Alhadlaq, M. Ahamed, K. Albrecht, V. C. Behr, A. Beilhack and J. Groll, ChemNanoMat.
DOI: 10.1002/cnma.202000009. Copyright© 2020 The Authors. Published by Wiley-VCH Verlag GmbH & Co. KGaA.

The chapter is based on the work of the author of this thesis Sonja Horvat-Csóti, who performed major part of experiments, analyzed data and wrote the manuscript. The original text was slightly modified to improve readability. Some sections regarding imaging and analysis of fungal cells are not included in the original article and are added to this thesis.

Author Contributions

Contributor	Contributions
Sonja Horvat	Designed research; performed major part of experiments, analyzed data; wrote the manuscript
Patrick Vogel	Designed, performed and analyzed the MRI, MPS and MPI measurements; provided feedback on the manuscript
Thomas Kampf	Designed, performed and analyzed the MRI, MPS and MPI measurements; provided feedback on the manuscript
Andreas Brandl	Analyzed the data fom biological experiments; provided feedback on the manuscript
Aws Alshamsan	Designed research; provided feedback on the manuscript
Hisham A. Alhadlaq	Designed research; provided feedback on the manuscript
Maqusood Ahamed	Designed research; provided feedback on the manuscript
Krystyna Albrecht	Designed research; provided feedback on the manuscript
Volker C. Behr	Designed, performed and analyzed the MRI, MPS and MPI measurements; provided feedback on the manuscript
Andreas Beilhack	Analyzed the data fom biological experiments; provided feedback on the manuscript
Jürgen Groll	Designed research; provided feedback on the manuscript

3.4.1 Introduction

Magnetic nanoparticles imbedded in polymeric micelles or coated with hydrogel networks are of great interest due to their potential as magnetic resonance imaging (MRI) contrast agents, drug carriers or tracers for magnetic particle imaging (MPI).[199] Superparamagnetic iron-oxide nanoparticles (SPIOs) are considered as promising contrast agents in MRI due to their low toxicity in comparison to gadolinium-based agents.[200] Magnetic particle imaging (MPI) is a novel tomographic method used for determination of the spatial distribution of SPIOs. It is shown that MPI is capable of making high-resolution images of distribution of SPIOs accumulated in lungs, blood vessels and cancer tissues, and recently it has been even used to image brain on a human scale with high precision and sensitivity.[201]

MPI is based on the non-linear response of SPIOs magnetization to time-varying magnetic fields and provides direct access to information about the local concentration of SPIOs which is not possible by magnetic resonance imaging (MRI). For imaging, a strong gradient in the form of a field-free point (FFP) or field-free line (FFL) is rapidly moved through the field of view (FOV) collecting successively MPI signal from SPIOs utilizing the fact that only in the vicinity of FFP or FFL MPI signal is generated. Traveling wave MPI used in this study provides a FOV enabling scanning probes with the size of small rodents with high temporal and spatial resolutions and high sensitivities.[202-205]

Besides hardware design, the spatial resolution in MPI depends strongly on the SPIOs.[199, 203-204, 206-207] To evaluate the suitability of nanoparticle system for imaging, magnetic particle spectroscopy (MPS) is usually employed. In comparison to MPI, MPS gives more specific information about the particle system, because of the absence of a gradient required for spatial encoding.[208-209] Larger crystallites have larger magnetic moments resulting in a steeper magnetization curve, which led to a spectrum of higher harmonics with higher amplitudes.[210-211]

Aside from optimization of the core size for imaging, SPIOs require a coating to ensure stability and biocompatibility for pre-clinical and clinical applications,[212-213]

which might impact their physical properties and, therefore, image resolution. It has been shown that crosslinking of a coating to a hydrogel-like network significantly improved relaxivity of SPIOs in MRI,[214] but the impact of the crosslinking of polymer coating of SPIOs in MPI has not been studied to our knowledge so far.

This section reports the preparation of iron oxide nanoparticles as biocompatible tracers for MPI and MRI and evaluate the influence of particle coating, especially crosslinked versus non-crosslinked, on signal intensity in MPS and image resolution in MPI and evaluates how these traces interact with *Aspergillus fumigatus*.

3.4.2 Synthesis of tracers and coating of particles

SPIOs were synthesized by decomposition of an iron-oleate complex under elevated temperatures, as described by Park et al.[215] In this study, an iron oleate complex was thermally decomposed in 1-octadecene in the presence of excess oleic acid as a surfactant.[213]

Previous studies addressed the significance of the quality of iron-oleate for the resulting nanoparticles.[213, 216] It was crucial that iron oleate complex was pure and free of the excess of oleic acid (OA) since this could influence the shape and crystallinity of the final particles. To remove OA from iron oleate complex, the product was formed on elevated temperatures in the reaction of Fe^{3+} and OA and washed extensively with ethanol.[216] Fourier-transform infrared (FT IR) spectra (Figure 3.4- 1) of the synthesized precursor showed characteristic bands reported by others.[215,216] C=O stretching peak at 1714 cm^{-1} and bands at 673 cm^{-1} and 586 cm^{-1} assigned for metal-oleate complex proved the identity of the product. The band at 1576 cm^{-1} belonged either to C=C vibration or carboxylate groups, as reported by Bronstein et al.[216] and broad band at 3478 cm^{-1} was assigned to -OH groups, which the same authors correlated with ethanol residues that replaced OA.

The ratio of OA to iron-oleate of 7.4 was optimal for preparation of particles of a size of 18 nm ± 4 nm as determined by scanning transmission electron microscopy

(STEM) (Figure 3.4- 2).

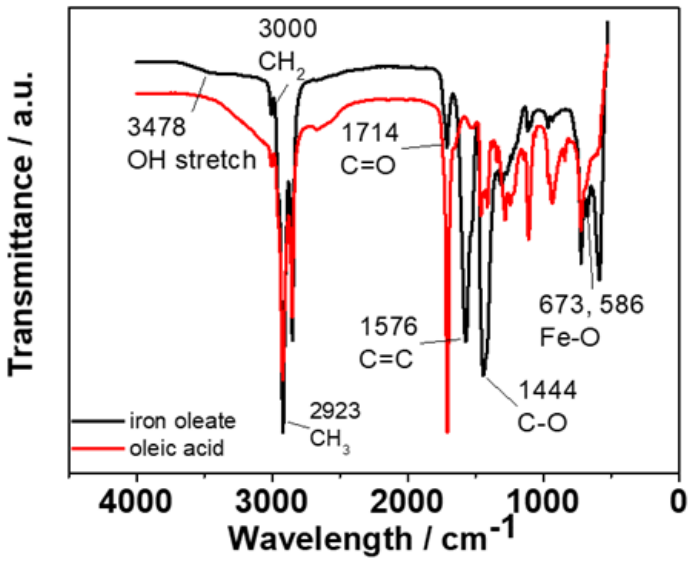

Figure 3.4- 1: FT IR spectrum from Fe-oleate and OA.

X-ray powder diffraction (XRD) pattern of SPIOs showed characteristic (220), (311), (400), (511) and (440) reflections which matched with the pattern of the magnetite (RRUFF Database, ID: R061111.9).[217] Following Scherrer equation[218] using the line broadening, the analysis of the (311) peak at 2θ of 35.4 °, the diameter of SPIO was calculated to be 12.1 nm, which was smaller than estimated by STEM. These differences could be explained by the loss of XRD signal due to the less ordered material surrounding a magnetic core.[219]

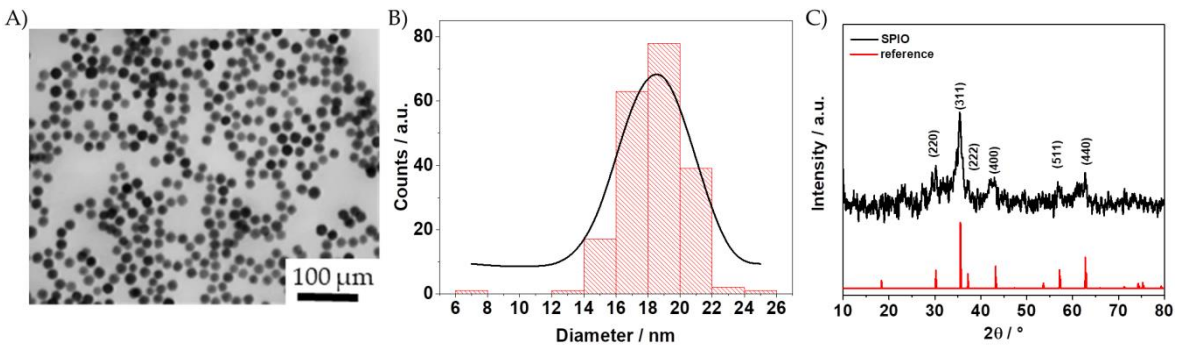

Figure 3.4- 2: (A) STEM image of iron oxide nanoparticles synthesized by thermal decomposition of Fe-oleate and size distribution of particles. (B) Particle sizes were determined by counting method. (C) XRD of SPIOs synthesized by thermal decomposition of Fe-oleate and standard pattern of magnetite.

Subsequently, particles were coated by poloxamer Pluronics F127 (PF127) to render them water-dispersible. These copolymers contain a hydrophobic part composed of poly(propylene oxide) (pPO) and a hydrophilic part of poly(ethylene oxide). The phase transfer was done by the wet method, in which evaporation of organic solvent led to the assembly of amphiphilic copolymers around SPIOs and their transfer to the aqueous phase. The hydrophobic part pPO formed a layer around iron oxide cores stabilized with OA, while the hydrophilic part pEO was oriented outwards (Figure 3.4- 3).[220-222] In addition, PF127 was modified with acrylate groups (PF127DA) to enable the conjugation of polymers containing thiol groups, such as biocompatible thiol functionalized poly(glycidol)s (pG-SH).[223]

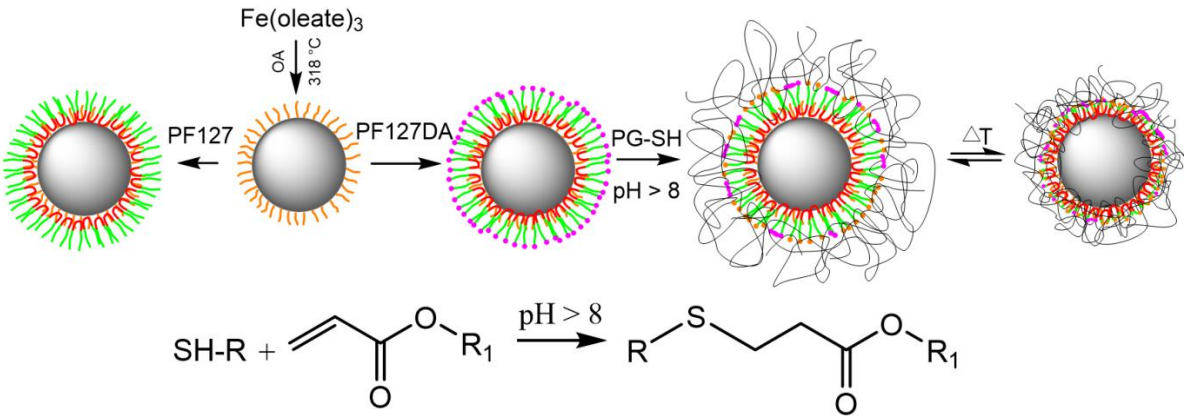

Figure 3.4- 3: Schematic diagram of the preparation of thermo-responsive SPIOs.

Hydroxyl groups positioned on each end of the Pluronics F127 copolymer reacted with acryloyl chloride, producing acrylated polymer, while triethanolamine captured chloride ion by producing triethanolamonium hydrochloride salt, which was easily removed by filtration.[223] ^{1}H NMR spectra showed characteristic peaks for the acrylate groups in the range of 5.8-6.5 ppm (Figure 3.4- 4A) and FT IR spectra proved the chemistry of the PF127DA, which was in agreement with previous reports (Figure 3.4- 4B).[224-225] Here, the important band was C=O stretching at 1720 $cm^{-1,}$ which was present only in the acrylate-functionalized polymer.

After phase transfer using PF127DA, conjugation of biocompatible thiol

functionalized poly(glycidol)s (pG-SH) to the PF127DA coating on the SPIO surface was achieved by thiol-acrylate Michael addition.[223, 226-227]

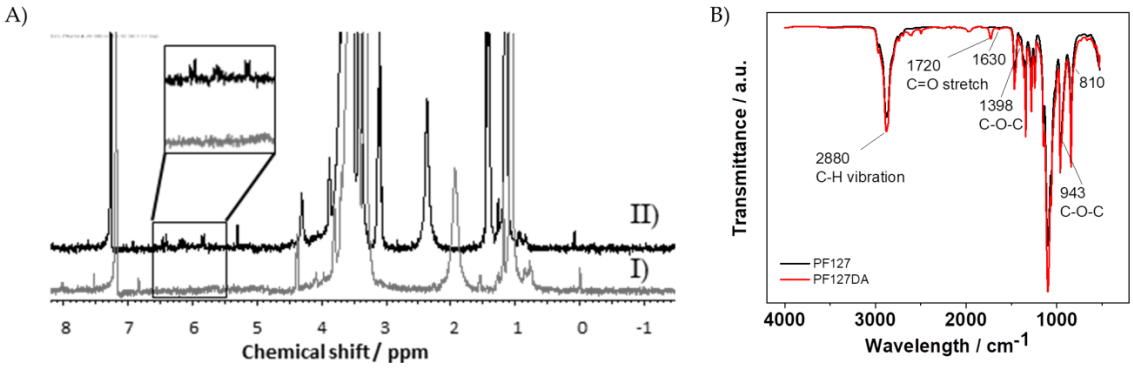

Figure 3.4- 4: (A) ^{1}H NMR ($CDCl_3$) of PF127 (I) and PF127DA (II), respectively, and (B) their FT IR spectra.

Coating identity was evaluated by Fourier transform infrared spectroscopy (Figure 3.4- 5). There were many bands in the range of 700-1800 cm^{-1} assigned to the various alkyl groups present on the backbone of the PF127 polymer, proving successful phase transfer. There was also a remaining band at 2920 cm^{-1} assigned to the asymmetric stretch vibration of the methylene group of the OA, which led to the conclusion that OA remained on the surface of SPIO after phase transfer. After pG-SH conjugation, there were additional bands at 3390 cm^{-1} and 1720 cm^{-1}, which were assigned to the stretching of hydroxyl groups on the pG polymer and carbonyl group, respectively. After conjugation, the band at 2550 cm^{-1} assigned to the -S-H stretch was absent and the band at 805 cm^{-1}, which was in the range of C-S stretching, appeared and was only visible in the PF127DApG SPIOs. As a control, FT IR analysis of PF127DA coated SPIOs was also taken, where differences between the PF127DApG and PF127DA additional bands at 805 cm^{-1}, 1738 cm^{-1} and 1255 cm^{-1} on pG-SH samples could be observed (Figure 3.4- 6).

The hydrodynamic diameter determined by dynamic light scattering (DLS) was around 180 nm at 25°C, suggesting aggregation.[227] However, higher diameters of SPIOs coated with PF127 than expected were reported previously.[220, 228] Furthermore, the flat arrangement of particles in STEM images (Figure 3.4- 5)

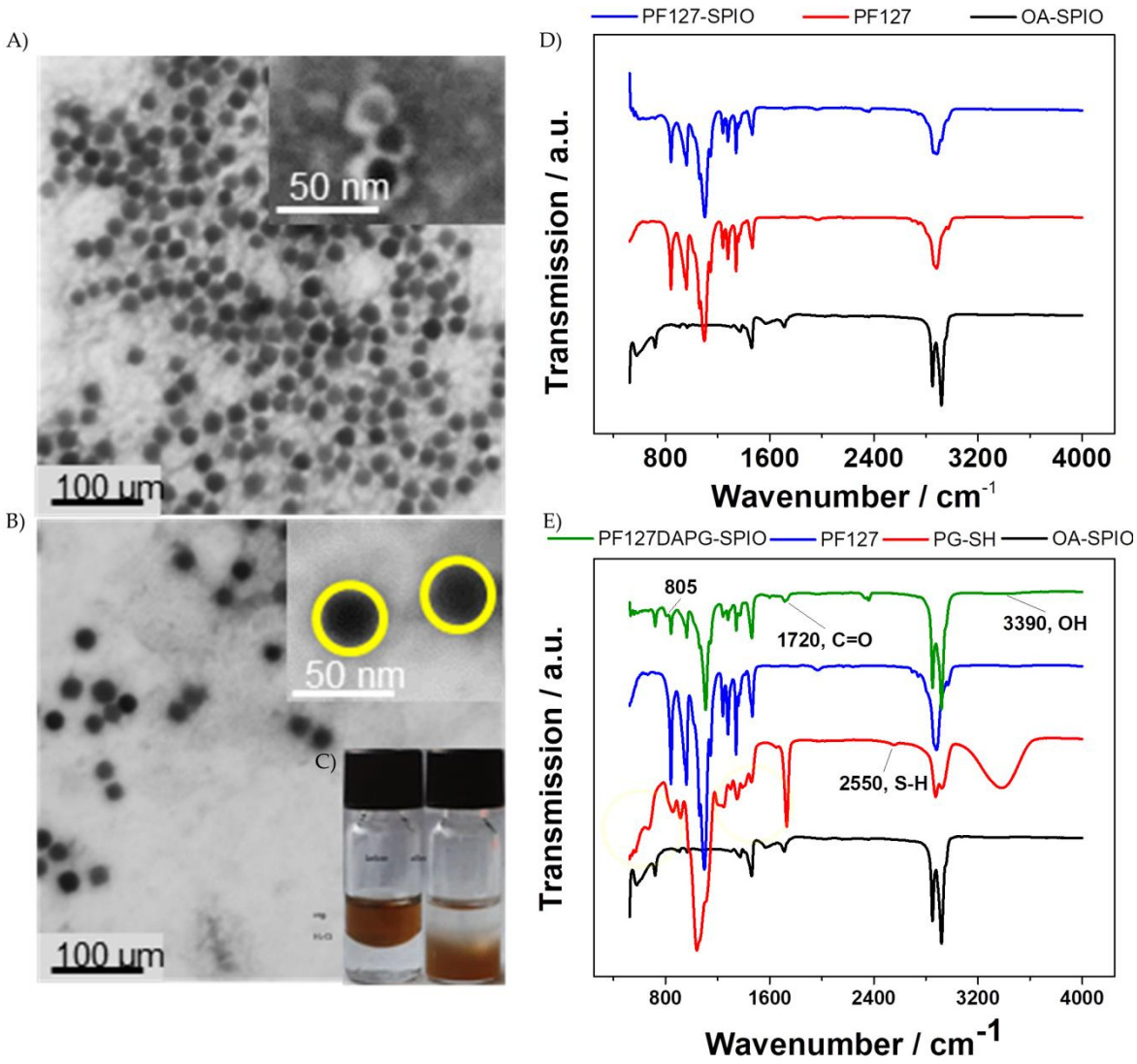

Figure 3.4- 5: (A), (B) STEM analysis of PF127 and PF127DApG SPIOs, respectively, (C) after phase transfer particles are completely dispersible in water, (D) and (E) FT IR proves successful coating of particles with copolymers.

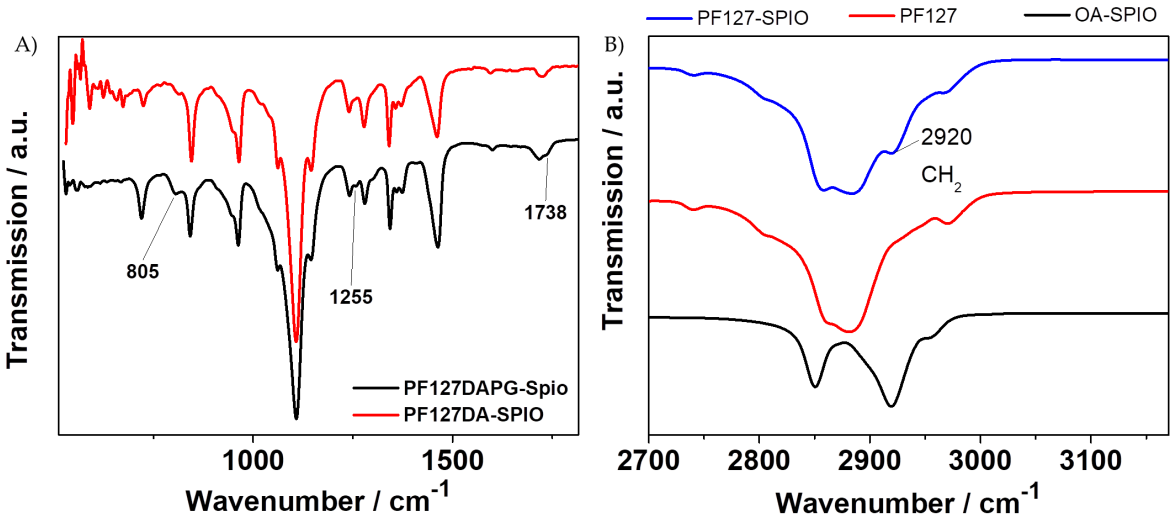

Figure 3.4- 6: FT IR analysis of PF127, PF127DA and PF127DApG coated SPIOs.

indicated that capillary forces during drying lead to apparent aggregation, but that those were not permanent in the solution. Therefore, it was assumed that if aggregation in solution occurred, it was rather transient than permanent.

To prove that coating of the PF127DApG SPIOs had not been covalently crosslinked and not absorbed on the magnetic core, both PF127 and PF127DApG particles were treated with urea. Urea is a small molecule which is used extensively as denaturation agent of proteins due to the ability to weaken hydrogen bonds and alter the hydrophobic interactions in aqueous solutions. Previous studies showed that urea increased critical micellar concentration and temperature of poloxamers, leading to phase separation of the poloxamer micellar solution due to the increased solubility of poloxamers in the presence of urea and de-micellization.[229-231] It had been proposed that urea either changes the structure of water (indirect way) or replaces water molecules in the hydration shell of the polymer without influencing water structure (direct way)[232] by disruption of the head group–counter ion interaction leading to the destabilization of micelles.[229] Indeed, urea destabilized PF127 SPIOs, which were impossible to resuspend due to the strong aggregation, while PF127DApG SPIOs remained in the suspension as shown by ultraviolet visible spectroscopy (UV-Vis, Figure 3.4- 7). This result suggested that coating of PF127DApG SPIOs was made of the crosslinked polymeric network, which was prone to disassociation. However, concentrations of urea (20 M) necessary for the destabilization of PF127 SPIOs were higher than reported by others,[229-232] which could be explained by higher stability of those particles because of the presence of a solid core that further stabilized the micelle.[233]

To analyze their stability, samples were incubated in solvents at different pH values and ionic strengths using monovalent and divalent salts (Figure 3.4- 8). Particles did not change their size with the change of pH value but rather ζ-potential. PF127 SPIOs were negatively charged at all measured pH values but became more negatively charged on higher pH. The similar trend was observed for PF127DApG SPIOs. Decrease of zeta potential at basic pH might be correlated

with the influence of OA on the surface of SPIOs, which was more deprotonated at basic pH values making particles more negatively charged. Further, crosslinking the PF127 made particles more positively charged, probably due to the protonation of the oxygen atom in the ester bond.

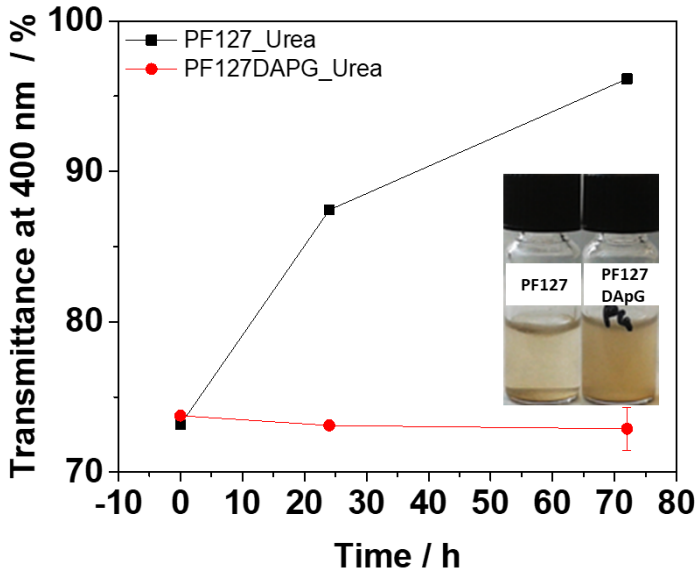

Figure 3.4- 7: Influence of urea on the stability of the SPIOs as determined by UV-Vis.

The addition of monovalent salt did not alter the stability of particles and they did not aggregate. In this case, a decrease in size could be explained by the dehydration of water layer from the surface of the particles, which became more evident in the case of PF127 SPIOs. On the other hand, divalent salt-induced aggregation of PF127DApG SPIOs at high salt concentrations (1 M). Divalent Ca^{2+} ions likely acted as bridges between negatively charged particles, inducing their aggregation. However, even at the highest concentrations of salt, PF127 SPIOs remained colloidally stable.

3.4.3 Thermo-responsive behavior of particles

Particles showed thermo-responsive behavior, which was monitored by DLS. PF127DApG SPIOs incubated from 4 °C to 41 °C decreased almost by two-fold and this change became most evident between 4 °C and 25 °C. On the other hand,

shrinkage of SPIO coated only with PF127 was much lower in the same temperature range (Figure 3.4- 9A). As a control, PF127DA coated SPIOs were also analyzed. The swelling of these nanoparticles resembled the swelling behavior of PF127 SPIOs (results not shown). Similar behavior was observed of unloaded nanogels (hydrogel nanoparticles) and micelles composed only of the respective polymers (Figure 3.4- 9B)

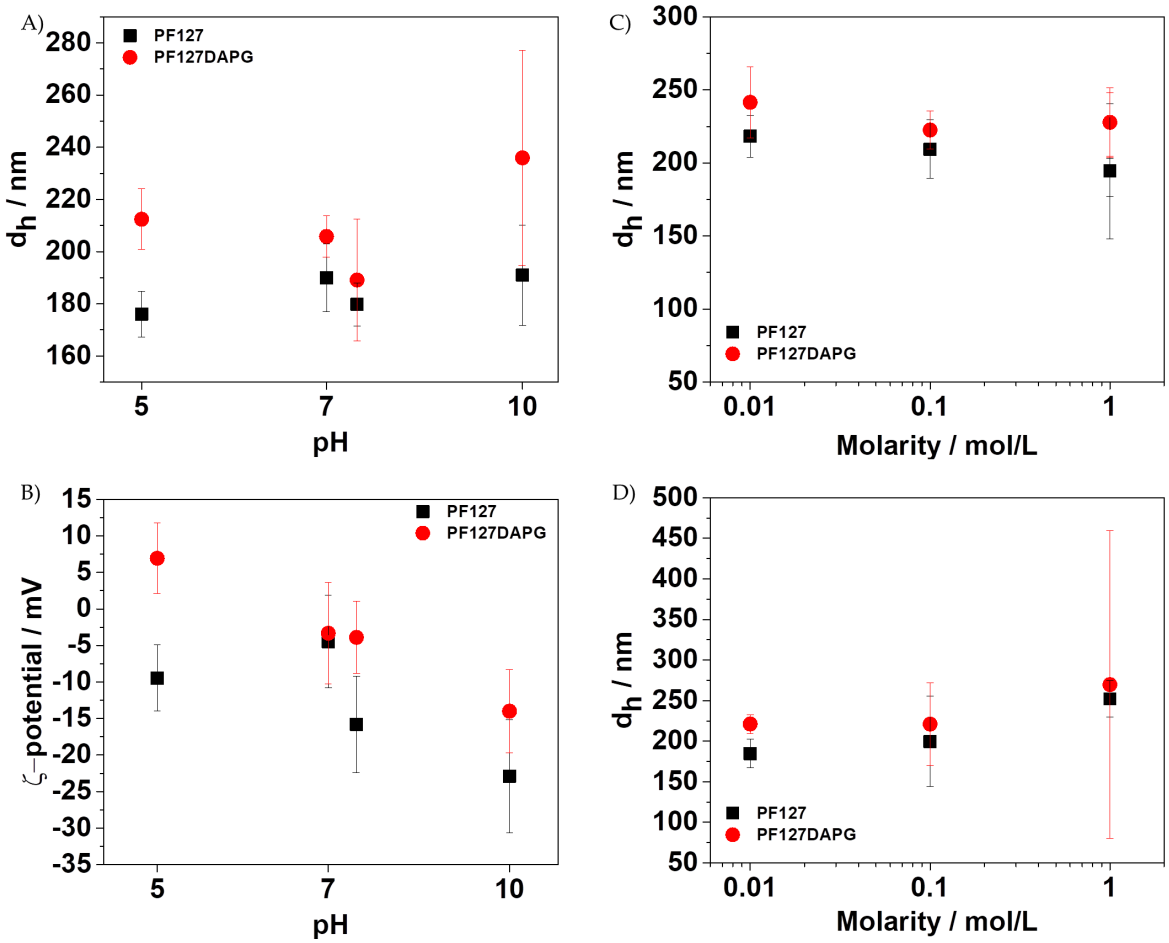

Figure 3.4- 8: Influence of pH on (A) size and (B) ζ-potential of SPIOs. (C) NaCl and (D) $CaCl_2$ salt on size of SPIOs.

A change of swelling ratio for micellar structures of PF127 crosslinked with polymers such as heparin or polyethyleneimine was observed before.[234-236] The higher thermo-responsiveness was explained by the hydrophobicity changes in the micellar structures and by electrostatic interactions between polymers. Reportedly, NP size changed up to 200 times in micellar constructs by varying

temperatures from 4 – 37 °C when polymers which contained both hydrophobic and hydrophilic regions were used.[234-236] As it is known that thiol modification renders pGs more amphiphilic,[17] aside from a better swelling through the hydrophilic PG, the amphiphilicity might in a similar manner imply that the PF127DApG coating could also exhibit sufficient hydrophobic interactions for a pronounced de-swelling above the lower critical solution temperature.

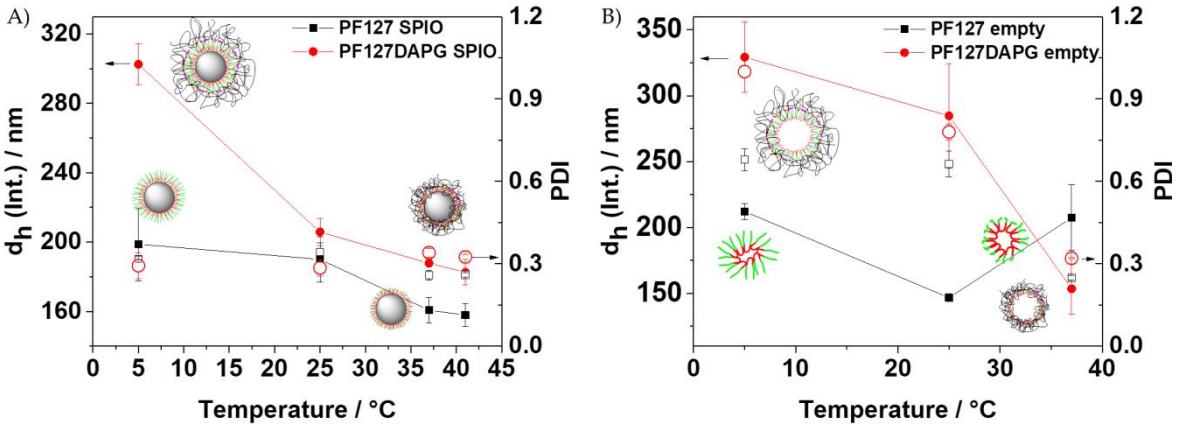

Figure 3.4- 9: Swelling behavior of (A) copolymer coated SPIOs. (B) Swelling behavior of empty PF127 micelles and PF127DApG nanogels. Full and empty symbols stand for hydrodynamic diameter d_h and polydispersity (PDI), respectively.

3.4.4 Magnetic properties of particles

MRI was firstly employed to evaluate magnetic properties of particles. The transverse relaxivity r2, as the ability of a contrast agent to alter T2, was determined at different temperatures. The transverse relaxivity r2 is the ability of a contrast agent to alter T2, which was calculated from transverse relaxation time measurements of samples with different SPIOs concentrations at 7 T. r2 was determined at different temperatures (Table 3.4- 1).

The transverse relaxivity r2 at 7 T of both types of SPIOs was significantly higher (330 mM-1 s-1 and 410 mM-1 s-1 for PF127 and PF127DApG SPIOs, respectively, measured at 25 °C) than relaxivity of commercially available products such as Ferumoxytol (Feraheme, 68 mM−1s−1, 7 T).[237] The higher transverse relaxivity of

the samples could be attributed to possible transient aggregation of particles in solution[238] as well as to the larger core size of the nanocrystals in comparison to ultra-small particles in commercial products. Apart from the core size, the coating could have a great impact on the relaxivity of SPIOs. Coating permeability and thickness influence water diffusion to the SPIO surface and therefore particle MRI performance.[239-241]

As PF127 SPIOs coating was comprised of poloxamer assemblies with the OA due to the hydrophobic-hydrophobic interactions, while PF127DApG layer on SPIOs was based on the crosslinked polymeric network, it probable that a hydrogel-like crosslinked polymeric network around SPIOs was more water permeable than the layer of PF127.[214, 242] Further, elevated temperatures decreased the relaxivity of both samples, and this change was greater for the PGPF127DApG SPIOs. At higher temperatures, polymers collapsed and were closer to the particle surface. In the case of the PF127DApG SPIOs, this contraction led to higher polymeric network density as compared to the PF127 SPIOs due to the presence of both pG and PF127. This suggested that with increased temperature, reduction of diffusive accessibility of water led to the decrease of relaxivity.[243]

Table 3.4- 1: r2 of samples measured at 7 T.

(Measurements and calculations were performed by Dr. T. Kampf)

T (°C)	r2 (mM^{-1} s^{-1})	
	PF127 SPIOs	**PF127DApG SPIOs**
25	334 ± 5	408 ± 10
37	310 ± 4	382 ± 14
55	290 ± 6	358 ± 8

Suitability of nanoparticles for MPI was analyzed firstly by MPS (Figure 3.4- 10A-C). The decay of spectra of higher harmonics decreased with rising temperatures (Figure 3.4- 10A-B), which might be attributed to the temperature-dependent change in viscosity of surrounding media.[244] However, decays of spectra of higher harmonics of PF127DApG and PF127 SPIOs markedly differed for PF127DApG

SPIOs (Figure 3.4- 10C) which performed better, although both systems contained the same magnetic cores.

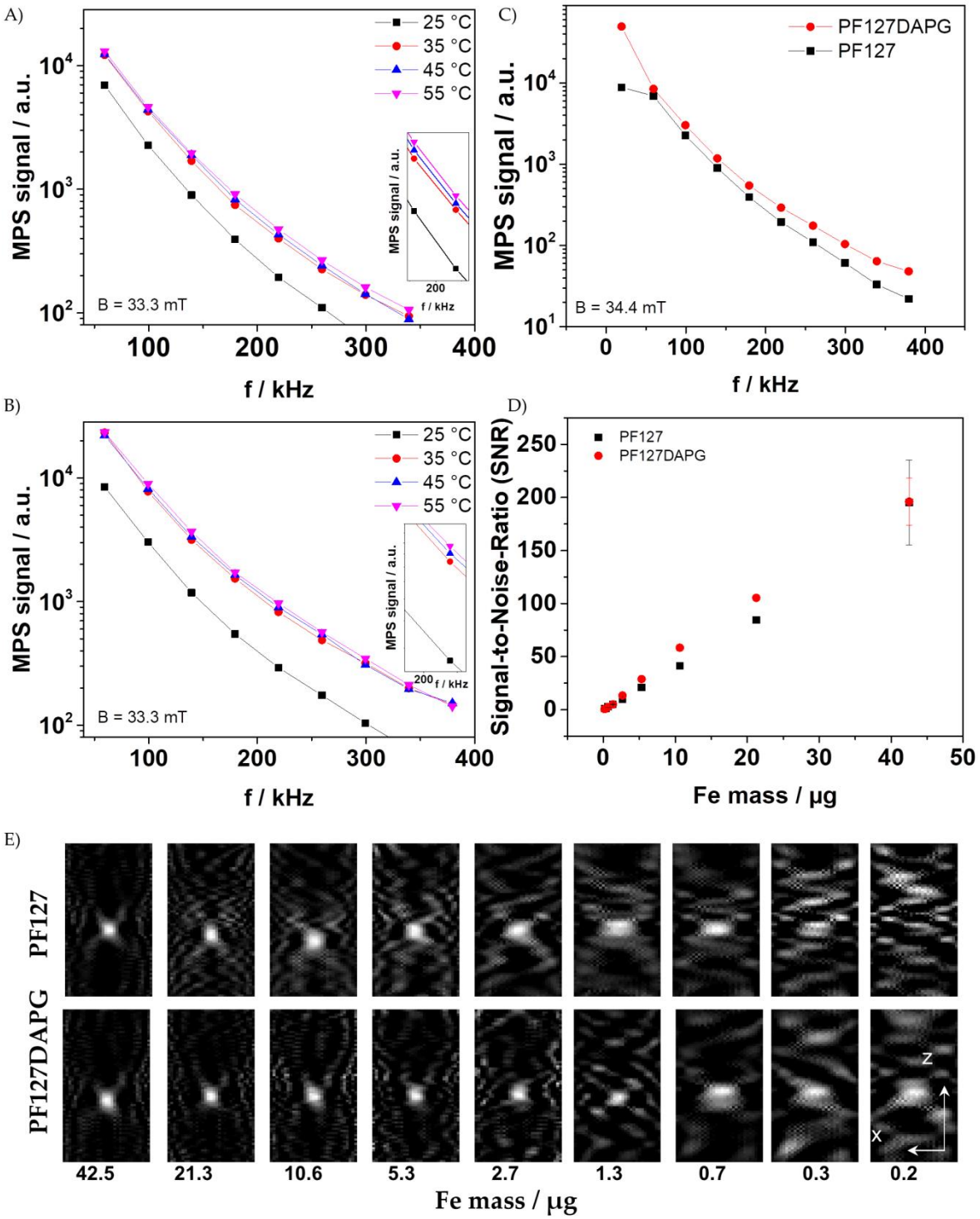

Figure 3.4- 10: (A) Influence of temperature on MPS performance of PF127 and (B) PF127DApG SPIOs. (C) The higher response of PF127DApG SPIOs in MPS measured at 25 °C. (D) Influence of coating on SNR in TWMPI and (E) TWMPI images of PF127 and PF127DApG SPIOs. (Measurements and analysis were performed by Dr. P. Vogel)

Similarly, PF127DApG SPIOs displayed a superior signal-to-noise (SNR) ratio in comparison to PF127 (Figure 3.4- 10D), when the same amount of SPIOs was used. Consequently, images with higher SNR resulting in a higher spatial resolution were obtained for PF127DApG SPIOs in MPI (Figure 3.4- 10E), where 5.3 μg of iron amount in PF127 SPIOs gave the same resolution as 1.3 μg of iron in PF127DApG SPIOs. This outcome could be attributed to the differences in the coating between two types of particles. Usually, the optimization of tracers for MPIs is based on the optimization of the core size, while coating is considered important only for the *in-vivo* studies.[245] This study, however, implicates that particle coating might have an essential influence on the MPI performance and should not be neglected during the optimization of the tracers.

3.4.5 *In-vitro* studies

Toxicity of nanoparticles towards L929 epithelial cells was evaluated via CellTiter Glo assay. Crosslinking of coating did not only improve r2 in MRI, the signal in MPS and resolution in MPI but also cytocompatibility (Figure 3.4- 11**)**. Coating of SPIOs by PF127 showed cytotoxicity probably due to its high amphiphilic nature, which can lead to the solubilization of the lipids from the cell membrane.[246] The presence of the biocompatible PG on the surface of SPIOs prevented PF127 dissociation and lowered the cytotoxicity of particles. PF127DApG SPIOs did not induce any toxicity on healthy human fibroblasts and malignant plasma cells. These results, therefore, suggest that PF127DApG SPIOs have high potential to be used in diagnostics.

Furthermore, PF127DApG SPIOs were incubated with *A. fumigatus* to access how these nanoparticles influence the biofilm formation. The results (Figure 3.4- 11) suggested that nanoparticles did not have antifungal properties as biofilm formation was not affected.

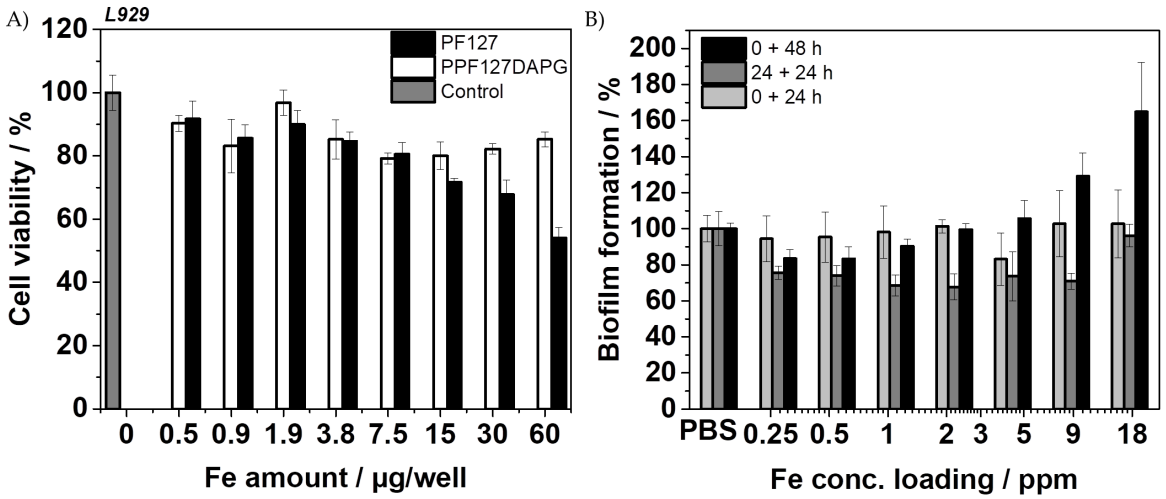

Figure 3.4- 11: Toxicity of particles towards L929 epithelial cells (A) and influence of PF127DApG particles on *A. fumigatus* biofilm formation (B).

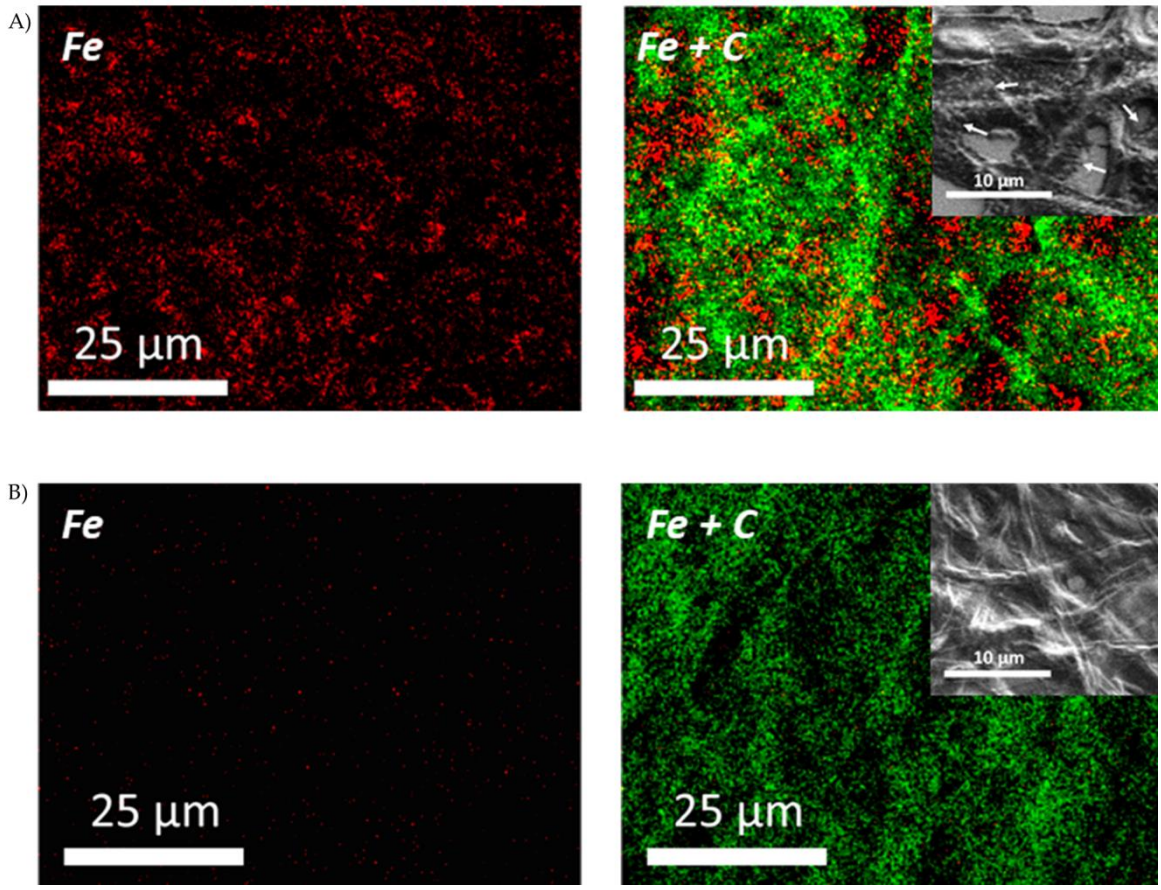

Figure 3.4- 12: SEM-EDX analysis of fungal biofilms treated with (A) PF127DApG and (B) PBS.

Fungi were also incubated with PF127DApG SPIOs and the distribution of iron in the biofilm was visualized by Scanning Electron Microscopy - Energy Dispersive

X-Ray Analysis (SEM-EDX, Figure 3.4- 12). Signal from iron only originated from samples treated with particles which were found attached predominantly to *A. fumigatus* hyphae or extracellular matrix.

After incubation with SPIOs, biofilm moved by the influence of the magnet, which further proved the accumulation of SPIOs within the biofilm (Figure 3.4- 13).

Finally, PF127DApG SPIOs uptake by fungi was analyzed by phenanthroline method, by measuring the iron content in the biofilms (Figure 3.4- 13).[247] Higher absorption of particles was observed after 24 h of incubation, suggesting that more particles attached to mature fungi than to germlings. However, when high amounts of SPIOs (18 ppm/well) were used, there was no difference between samples, indicating saturation.

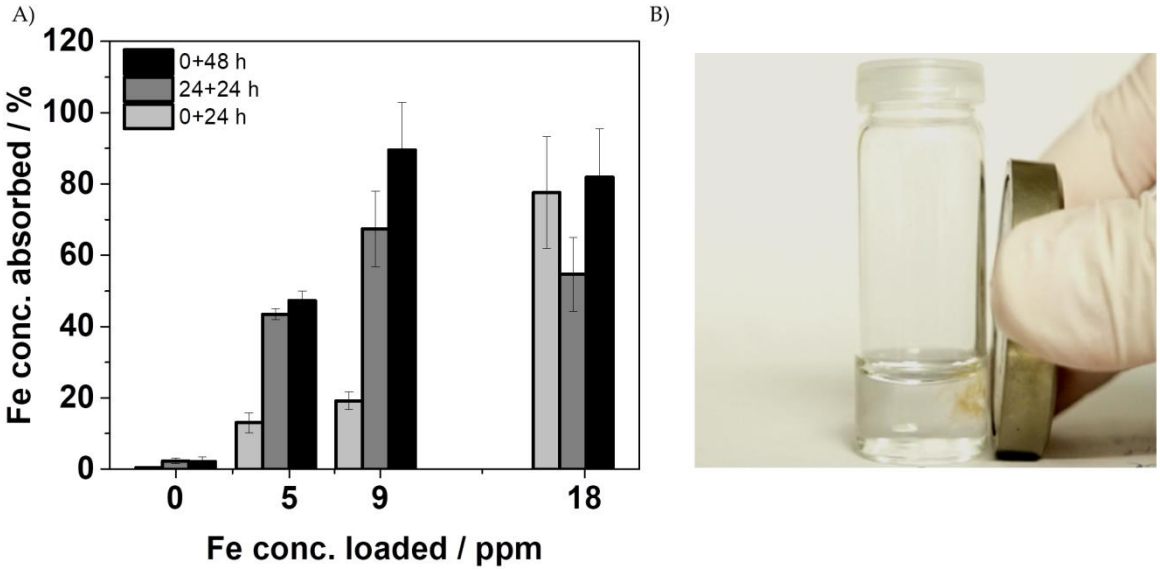

Figure 3.4- 13: (A) Accumulation of PF127DApG SPIOs in biofilm and (B) moving biofilm with a magnet.

3.4.6 Conclusions

In summary, this study demonstrates that crosslinking of the polymeric coating improved SPIO performance in MPI, MPS and MRI and highlights the importance of appropriate SPIOs coating for their application in imaging. The study shows that the type of coating besides the iron oxide core size should not be neglected in the optimization of the SPIOs. Lastly, as crosslinking of the polymeric network on

the surface of SPIOs with biocompatible PGs did not result in cytotoxicity, these tracers hold great promise for the application in diagnostics. However, as addressed previously, there is a need for targeted moiety on particles which would ensure the selectivity of particles towards fungal cells and biofilms for diagnostic purposes.

3.5 Binding affinity of dectin-1 decorated nanoparticles towards ß-glucans

3.5.1 Introduction

As stressed in previous sections, targeted delivery is a very important aspect for selective accumulation of nanoparticles on and in fungal biofilms as soon as the application is beyond *in-vitro* experiments.

There are only a few approaches reported up-to-date for targeting fungi *in-vivo*. The first is use of monoclonal antibody (mAb) JF5 as described by Gunzer and Wiehr et al.[248] The group labeled [^{64}Cu]DOTA with mAb JF5 and showed that this marker specifically recognized *Aspergillus fumigatus* hyphae, thus lung infection in a mice model. mAb JF5 bound to mannoprotein antigen secreted during hyphal growth of pathogenic fungi such as *A. fumigatus*.

Another approach that could be explored for targeted delivery is use of antifungal peptides.[249] When particular peptides, such as fluorescein-labeled cyclic peptides, are fluorescently labeled, they can trace the fungi in *in-vivo*.[250]

The last approach includes the use of proteins. In the very last months of this thesis, the work of Meagher et al. was published, which showed that dectin-1 could be used for targeted delivery of nanoparticles to fungi.[251] They showed that this approach increased the efficiency of amphotericin B (AmB) loaded liposomes against fungi. Dectin-1 is a protein naturally found on neutrophils, macrophages and dendritic cells. Its main function is to bind to β-glucans as soon as they emerge on the fungal cell wall during spore swelling. Because of these proteins, immune cells can recognize the fungi and fight against infection.[252-256] Dectin-1 contains a carbohydrate recognition domain (CRD), stalk region, a transmembrane domain (TM) and a cytoplasmic tail (cyto) while Fc fused dectin-1 (Fc dectin-1), used in this study consists of the CRD and stalk region of Dectin-1 coupled to the

Fc region of human IgG1 (Figure 3.5- 1).[257] Fc dectin-1 has two spots for ß-glucan recognition in comparison to Dectin-1 which contains only one spot and therefore is more sensitive towards glucan recognition.[257]

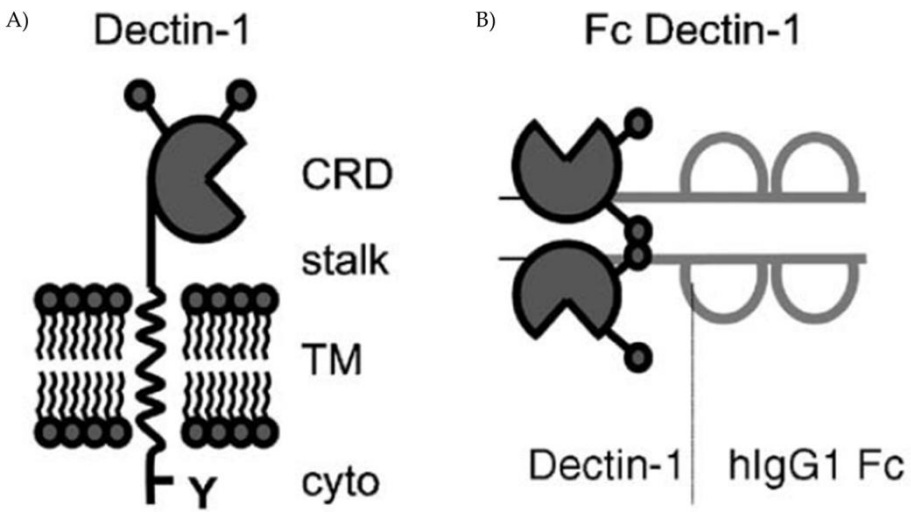

Figure 3.5- 1: Schematic representation of (A) Dectin-1 and (B) Fc dectin-1 used in this thesis.[257] Reprinted from Soluble Dectin-1 as a tool to detect β-glucans, Journal of Immunological Methods, Volume 314, Issues 1–2, L.M. Graham, S.V. Tsoni, J.A. Willment, D.L. Williams, P.R. Taylor, S. Gordon, K. Dennehy, G.D. Brown, Pages 164-169, Copyright (2020), with permission from Elsevier.

This section focuses on the optimization of coating of gold nanoparticles (GNP) with dectin-1 to explore binding affinity of nanoparticles towards β-glucans found on mature fungi. Affinity of Fc dectin-1 and Fc dectin-1 decorated GNPs towards soluble β-glucans was evaluated by surface plasmon resonance (SPR).

3.5.2 Coating of GNP with dectin-1

It is known that the gold surface could easily be coated with proteins by simple incubation. In this case, a large number of thiols in proteins are responsible for the absorption of proteins on gold.[258] Gold-sulfur (Au-S) interactions are so strong that the bond strength between them is almost as strong as the covalent bond.[259]

However, for the coating of GNPs with proteins containing lower amounts of thiols such as dectin-1, use of blocking proteins as bovine serum albumin was necessary to obtain stable colloid (results not shown). This step further

complicated the determination of protein concentration in the gold nanoparticle suspension, required for SPR studies. Moreover, this method acquired high amounts of proteins, and therefore was not preferred.

Therefore, dectin-1 was covalently bound to thioether poly(glycidol)s (pG) decorated GNPs via carboxyl-to-amine reaction.

3.5.2.1 Functionalization of GNPs with carboxyl groups (pG-GNPs)

Commercially available citrate coated GNP with a core size of 30 nm were firstly incubated with carboxyl-functionalized thioether pGs synthesized by Johanna Lutz (research group of Prof. Groll) as presented in Figure 3.5- 2.

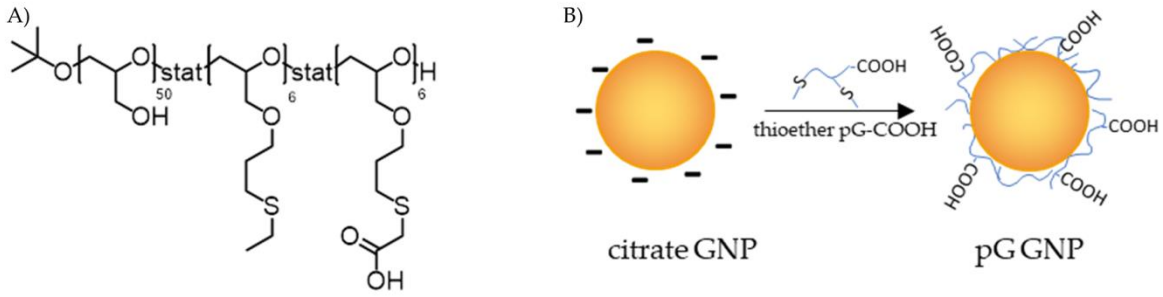

Figure 3.5- 2: (A) Carboxyl-functionalized thioether pGs and (B) coating strategy for carboxylation of citrate coated 30 nm GNPs.

As shown by Feineis et al.[260] coating of GNP with thioether polymers resulted in the preparation of very stable suspensions. A larger number of thioether per polymer chain led to the formation of polymer loops on the gold surface.[260]

Firstly, optimal amounts of polymer were determined by ultraviolet-visible (UV-Vis) spectroscopy. According to size increase (Figure 3.5- 3) and stability studies consisting of the use sodium chloride solution, it was estimated that polymer concentration of 0.04 mg/mL were enough to stabilize 2 mL of 30 nm GNPs.

Further, dynamic light scattering (DLS) was used for evaluation of the increase of the particle size by the addition of polymer (Table 3.5- 1). Results of analysis suggested that polymer concentrations below 40 µg/mL were not sufficient for complete coverage of GNPs since the increase of polydispersity index (PDI)

increased above 0.2.

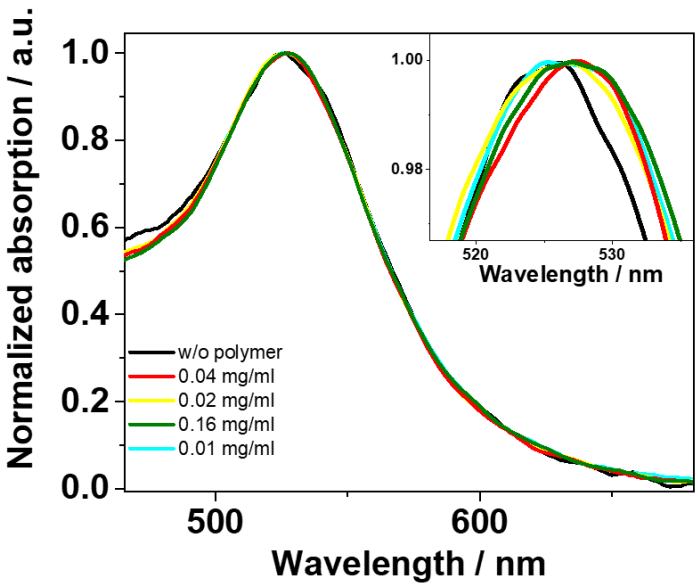

Figure 3.5- 3: Red shift of UV-Vis spectra of GNPs by coating with different amounts of polymers.

Table 3.5- 1: DLS analysis of GNPs with and without polymers.

Sample	d_h (nm)	Z-Ave (nm)	PDI
citrate coated GNP	38 ± 0	32	0.19
GNP + 0.078 mg/mL pG	45 ± 1	37	0.19
GNP + 0.039 mg/mL pG	44 ± 1	36	0.19
GNP + 0.020 mg/mL pG	44 ± 1	36	0.21
GNP + 0.004 mg/mL pG	48 ± 1	39	0.22

Finally, GNPs were incubated with sodium chloride solution and absorption spectra were analyzed by UV-Vis (Figure 3.5- 4). The salt assay is often used as a method for determination of optimal protein concentration for GNP coating,[261] but was used for the determination of the optimal concentration of polymers in this section. Addition of salt induced particle aggregation when polymer concentrations were low, recognized as the blue spectral shift. Also, samples which were not coated sufficiently by polymer turned blue after salt addition, which was visible by eyes as well (Figure 3.5- 4B). These results confirmed that optimal polymer concentration for the preparation of stable carboxyl-functionalized GNPs was above 0.02 mg/mL.

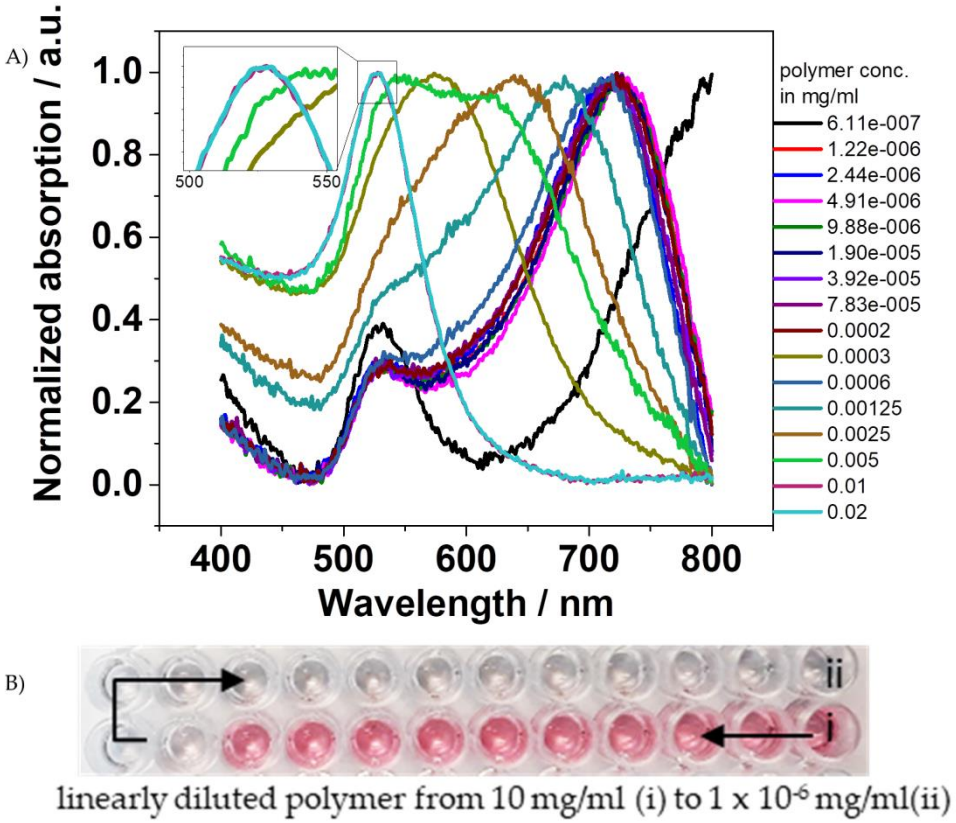

Figure 3.5- 4: Salt assay for determination of the optimal concentration of polymers for GNP coating. (A) UV-Vis spectra of samples and (B) change of color of the samples from red to blue where polymer concentration was not sufficient to coat the whole particle surface.

Therefore, based on these results, it was decided to coat GNPs with 40 µg/mL polymer.

3.5.2.2 Conjugation of Fc dectin-1 to GNP

After the successful coating of GNP with polymer, GNPs were conjugated to Fc dectin-1. Fc dectin-1 was used, since this protein has in comparison to natural dectin-1, two reactive spots towards β-glucans, which enabled higher binding affinity (results not shown). The latter was important because lower amounts of Fc dectin-1 could be used to evaluate the constant of dissociation (K_D) in SPR.

Fc dectin-1 was conjugated to carboxyl groups of the pG GNPs by carbodiimide chemistry (Figure 3.5- 5).[262] Carboxyl groups firstly reacted with 1-ethyl-3-(-3-dimethylaminopropyl) carbodiimide (EDC), and o-acylisourea active ester as an intermediate was formed. O-acylisourea further reacted with *N*-

hydroxysuccinimide (NHS) to form more stable intermediate, reactive towards amines. Without the NHS step, hydrolysis of o-acylisourea might occur, which would decrease the efficiency of the reaction. NHS-ester intermediate finally reacted with amines which were present naturally in Fc dectin-1.[262] Isourea by-product was also formed during the reaction,[262] and was eliminated by washing.

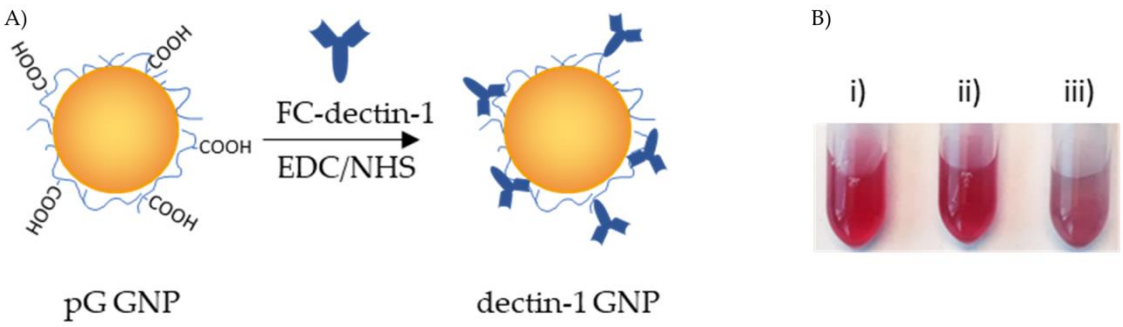

Figure 3.5- 5: (A) Immobilization of polymer-coated GNPs with Fc dectin-1. (B) Samples coated with (i) 50 μg, (ii) 25 μg and (iii) 12.5 μg Fc dectin-1.

Different amounts of Fc dectin-1 were used for coating of gold nanoparticles (Figure 3.5- 5B). Particles almost immediately turned blue after the addition of the lowest amounts of protein, which was further confirmed by DLS analysis by an increase of PDI value (Table 3.5- 2). Aggregation of particles with the lowest protein concentration could be explained by aggregation of two or more particles coupled to the same protein. On the other hand, 50 μg Fc dectin-1 was sufficient to coat the particles which were as polydisperse as particles before conjugation.

The size of GNPs increased to around 5 times after conjugation with Fc dectin-1, although no signs of GNP aggregation was observed by UV-Vis spectra (Figure 3.5- 6). Because of that, the hydrodynamic radius of free protein was measured and was around 150 nm, which was much higher than expected. This result suggested that only one protein was bound to the GNPs. Bounding studies done by the research group of Prof. Wajant encouraged this observation (results not shown), although further detailed studies are needed to confirm the hypothesis.

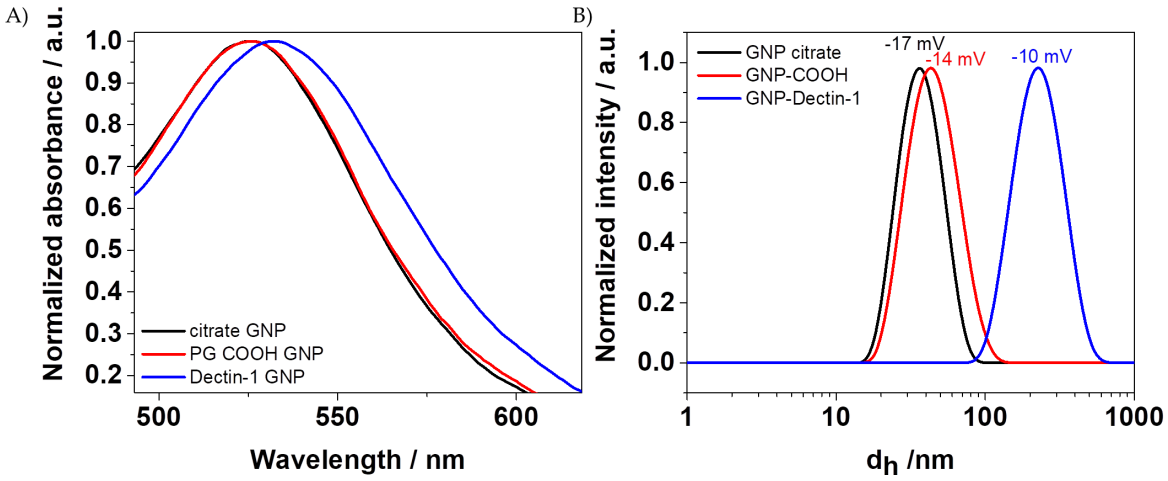

Figure 3.5- 6: (A) UV-Vis spectra and (B) DLS analysis of GNPs used in this study.

Table 3.5- 2: DLS analysis of GNPs with and without polymers.

Sample	d_h (nm)	Z-Ave (nm)	PDI
citrate coated GNP	38 ± 0	32	0.19
pG-GNP	46 ± 1	38	0.19
pG-GNP + 50 µg Fc dectin-1	180 + 5	156	0.13
pG-GNP + 25 µg Fc dectin-1	193 ± 43	164	0.21
pG-GNP + 12.5 µg Fc dectin-1	n.m.*	n.m.*	n.m.*
Fc dectin-1	153 ± 40	n.m.*	0.45

*n.m. – not measurable.

3.5.3 Binding affinity studies

The binding affinity of Fc dectin-1 towards diaminopropane derivative of β-glucan phosphate synthesized by the research group of Prof. Williams (Department of Surgery, Quillen College of Medicine, Center of Excellence in Inflammation, Infectious Disease and Immunity, East Tennessee State University, Johnson City, USA) was evaluated by surface plasmon resonance (SPR). SPR is commonly used method for real-time analysis of binding affinity and kinetics of protein-ligand interactions, where one of the molecules is immobilized on the thin gold layer (detector) and another one (analyte) is mobile. Small differences in the refractive index of gold surface which happen during binding of two molecules are detected and from the derived sensorgrams, K_D can easily be calculated.[263-265]

In this thesis, the binding affinity of Fc dectin-1 towards β-glucans was firstly

analyzed. Sugars were bound to the carboxymethylated dextran gold chips by EDC/NHS chemistry as described by Williams et al.[253] Several cycles were necessary to achieve binding of more than 1000 resonance units, probably due to the low amounts of amines present on the diaminopropane derivative of β-glucan phosphate. After polysaccharides were immobilized on the chip, a dilution series of known concentrations of Fc dectin-1 was injected into the system and sensorgrams were obtained (Figure 3.5- 7).

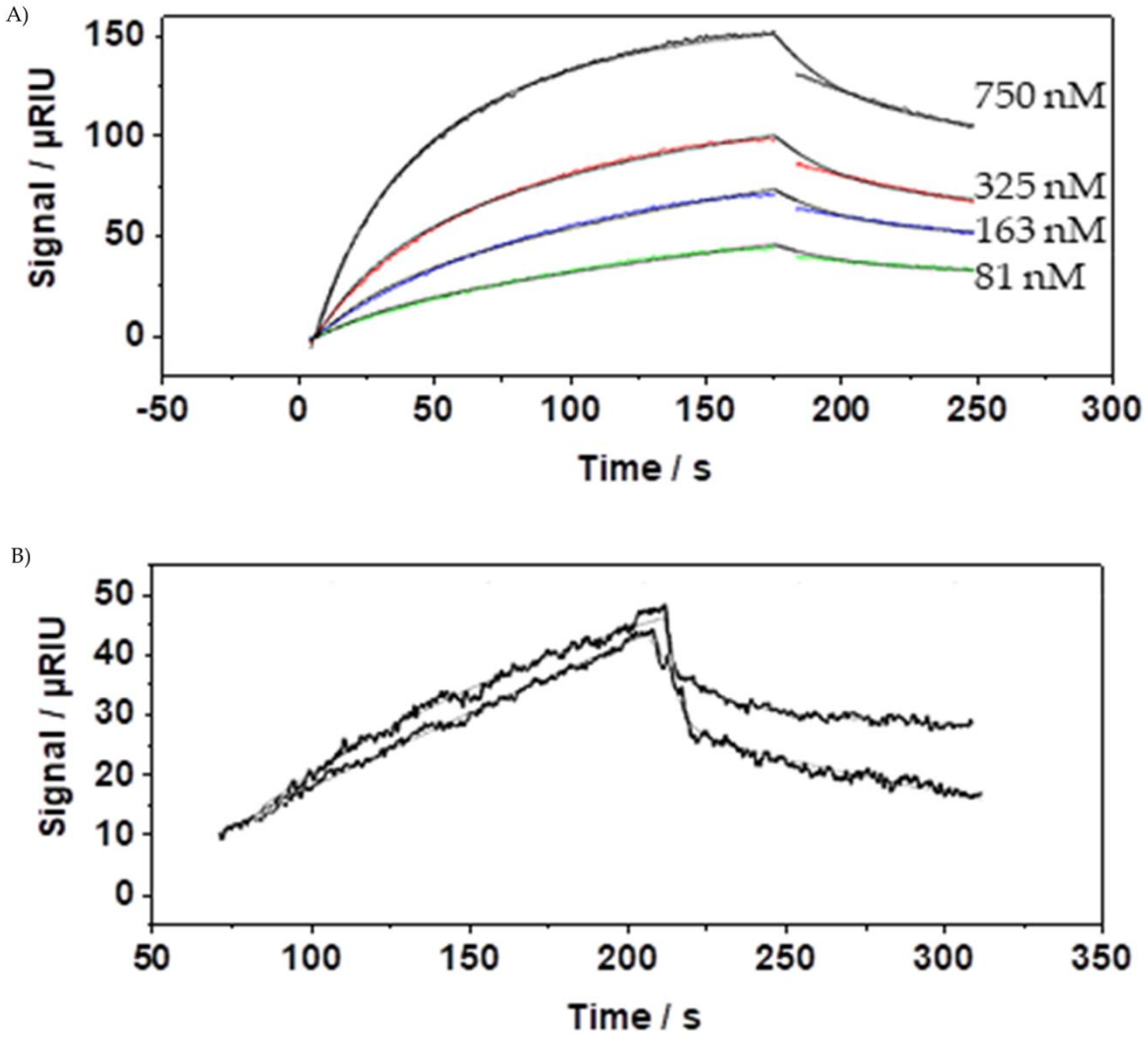

Figure 3.5- 7: SPR sensorgrams of the (A) Fc dectin-1-β-glucan phosphate interaction and (B) Fc dectin-1 GNP-β-glucan phosphate interaction. In (A) different concentrations of the Fc dectin-1-β-glucan phosphate were analyzed. In (B) only 66 nM of the Fc dectin-1-GNP β-glucan phosphate was analyzed.

K_D calculated in this study was 35 nM ± 20 nM, much higher than reported by

Williams et al. (2 pM) although they used dectin-1 with only 1 site for binding in their study.[253] Differences in the K_D value could be explained either by the device they used or by the possible aggregation of the protein which was reported in the **Section 3.6.2**.

Fc dectin-1 coated GNPs were also injected over the β-glucan immobilized sensor chip. However, due to the limited availability of the protein, only 66 nM of protein on the GNPs, as determined by micro BCA assay, that allowed calculation of K_D could be injected (Figure 3.5- 7B). Relative K_D value, in this case, was 11 nM ± 3 nM, almost 3 times lower than K_D of Fc dectin-1. This suggested possible multivalency of the Fc dectin-1 GNPs,[263] however, due to the limit of detection, further studies with the higher amount of GNPs used in SPR measurements would be necessary to confirm this.

3.5.4 Conclusions

This section focused on the coating of GNPs with Fc dectin-1 as a targeting molecule for *A. fumigatus*. Dectin-1 was conjugated covalently to GNPs decorated by pGs. Much higher values of K_D (lower affinity) of free ligand Fc dectin-1 towards soluble β-glucans as reported by other authors were reported. Furthermore, the results of binding affinity study between Fc dectin-1 coated GNPs and soluble β-glucans suggested a decrease of K_D, but more studies would be necessary to confirm the multivalency.

4 Summary and Outlook

This thesis aimed to evaluate the possibility to use nanoparticles as antifungal drug carriers as well as their potential application in screening and diagnostics of invasive aspergillosis. For this, the interaction of nanogels, superparamagnetic iron oxide nanoparticles (SPIOs) and gold nanoparticles (GNP) with fungal-specific polysaccharides, cells and biofilms was investigated.

Firstly, it was evaluated how the charge of nanogels influence their interaction with fungal cells. For this purpose, linear poly(glycidol)s (pG) and poly(2-methyl-2-oxazoline) (pMOx) polymers were synthesized by anionic and living cationic ring-opening polymerization, respectively. They were further functionalized with thiol groups for preparation of redox responsive nanogels by inverse miniemulsion. PG-based nanogels were quenched with low molecular weight acrylates to introduce different charged groups onto their surface, while nanogels prepared from partially hydrolyzed pMOx polymers served as an example of nanoparticles with a high density of positive charges due to the presence of amine groups. Results showed that negatively charged nanogels were internalized by the fungi to a much greater extent than positively charged ones. The latter particles were found mainly adsorbed on the cell wall of the fungi. Also, the study suggests that the interaction of particles with fungi starts after the formation of hyphae. *In-vitro* results showed that nanogels were up-taken by neutrophils, but this did not suppress the strong interaction of nanogels with *A. fumigatus* during co-incubation. On the other hand, only positively charged nanogels were internalized in Caco2 and epithelial cells. Since many antifungal drugs have amine groups in their structures, acrylates used for quenching in the inverse miniemulsion method can possibly react with them following the mechanism of Michael addition leading to change of drug chemistry. Because of that, alternative strategies for

preparation of nanogels without need for quenchers and surfactants were subsequently investigated.

Unlike mammalian cells, fungal cells contain an additional cell wall which is located on the outside of the plasma membrane. It has a complex structure based mostly on polysaccharides, from which some of them are hydrophobic. Therefore, it was investigated how the introduction of hydrophobic moieties along the hydrophilic backbone of the pG polymer of which the nanogel were synthesized, influences their interaction with fungi. Amphiphilicity of the particles was tuned by altering the number and length of thiol carrying alkyl side chains of pG. After reaching critical association concentration, polymeric aggregates were formed by self-assembly in water, followed by crosslinking of the thiol groups. Interaction of those vehicles with fungi-specific polysaccharide extracted from the cell wall was investigated. It was concluded that nanogels prepared from polymers with degree of functionalization of 10% had the strongest interaction, regardless the length of the alkyl chain. Moreover, uptake of nanogels was investigated by confocal laser scanning microscopy after encapsulation of a hydrophobic dye. It was concluded that nanogels with a degree of functionalization of around 10 % delivered the dye most successfully. Atomic force microscopy analysis of fungal cells showed that the morphology of the cell wall also changed upon the incubation with nanomaterials. Moreover, amphotericin B-loaded nanogels had a higher antifungal effect than the free drug. This profound effect was explained by the higher accumulation of drug-loaded particles on the fungal surface and their subsequent local drug release in comparison to free drug. Finally, drug-loaded nanogels showed improvements in lowering the cytotoxicity towards mammalian cells in comparison to free drug.

However, although nanogels were successful in the encapsulation and delivery of the antifungal drug, those particles exhibited a moderate to high size polydispersity. Therefore, an alternative strategy in their preparation with narrower size distribution was employed. For this purpose inverse nanoprecipitation of thiol functionalized pGs was shown to be successful. In

addition, it was possible to load freeze-dried nanogels with antifungal drug Itraconazole as well as hydrophobic and amphiphilic dyes by swelling dry nanogels with concentrated drug solution, the so-called "breathing-in" method. The results suggested that nanogels might serve as vehicles that deliver the cargo near the fungal cell wall, which was released and internalized by fungi while nanogels were not internalized. Drug-loaded particles exhibited better antifungal properties, such as two times lower minimal inhibitory concentration and longer effects in inhibition of biofilm formation than the free drug. Also, drug-loaded nanogels exhibited slightly lower toxicity towards red blood cells but had similar cytotoxicity profile towards liver and kidney cells, suggesting internalization by mammalian cells. This outcome addressed the significance of finding a targeting moiety for application of nanogels in *in-vivo* studies.

Further, the possibility to use nanoparticles to trace fungi via traveling wave magnetic particle imaging was investigated. Therefore, coating of SPIOs for magnetic particle imaging was optimized. It was demonstrated that crosslinking of the polymeric coating in hydrogel-like network with thiol functionalized pGs improved the particles' performance in traveling wave magnetic particle imaging and magnetic resonance imaging. Results highlighted the importance of appropriate SPIOs coating for their application as tracers. Moreover, these particles lowered cytotoxicity towards healthy fibroblasts and did not inhibit the biofilm formation by *A. fumigatus*.

Finally, it was investigated whether gold nanoparticles (GNPs) could be used as model particles for the assessment of targeting to *A. fumigatus*. For this purpose, Fc dectin-1 was chosen as a protein which conjugation to nanoparticles should lead to their selective accumulation in the place of the fungal infection. Fc dectin-1 was conjugated covalently to GNPs decorated with pGs, and binding affinity towards β-glucans was tested by surface plasmon resonance. Although results showed a decrease of binding affinity when protein was conjugated to particles, more measurements would be needed to confirm multivalency.

In summary, this thesis demonstrated evidence for the potential of pG nanogels

and pG coated nanoparticles for antifungal therapy and diagnostics of fungal infections caused by *A. fumigatus*. However, it is crucial to explore nanogel-fungi interactions in more detail using endocytosis markers. This could lighten up the endocytosis processes happening in the filamentous fungi. Also, more detailed live-imaging would enable monitoring the nanogel cleavage inside nanogels and cargo release into the cytoplasm. Furthermore, a more detailed analysis of changes in the cell wall structures uppon incubation with nanogels in by atomic force microscopy and by analysis of cell wall chemistry would be valuable. Finally, suitable nanoparticle modifications for efficient fungal targeting should be explored further. Although Fc dectin-1 showed promising results, more confirmatory studies, both *in-vitro* and *in-vivo* are necessary.

5 Zusammenfassung und Ausblick

Die vorliegende Arbeit befasst sich mit der Evaluation der Eignung von Nanopartikeln für das Screening, die Diagnose und als Wirkstofftransportsysteme für die Behandlung von invasiver Aspergillose. Hierzu wurde die Interaktion von Nanogelen, superparamagnetischen Eisenoxid Nanopartikeln (SPIO) und Gold Nanopartikeln (GNP) mit pilz-spezifischen Polysacchariden, dem Pilz *Aspergillus fumigatus* sowie Pilz-Biofilmen untersucht.

Zunächst wurde untersucht, wie die Ladung von Nanogelen die Wechselwirkung zwischen Nanogelen und Pilzzellen beeinflusst. Hierfür wurden Polymere auf der Basis von Poly(Glycidolen) (PG) und Poly(2-Methyl-2-Oxazolin)en (PMOx) jeweils durch anionische Polymerisation respektive lebende kationische ringöffnende Polymerisation synthetisiert. Die Polymere wurden danach mit Thiol-Gruppen funktionalisiert, um redox-sensitive Nanogele durch inverse Miniemulsionen herstellen zu können. PG-basierte Nanogele wurden mit niedermolekularen Acryl-funktionalen Molekülen gequenched, um so gezielt Ladungen einzuführen. Auf der anderen Seite dienten Nanogele, die aus teilweise hydrolysierten PMOx hergestellt wurden, als Beispiel für Nanogele mit hoher positiver Ladungsdichte. Interaktionsstudien der verschiedenen Nanogele mit Aspergillus fumigatus zeigten im Vergleich zu den positiv geladenen Partikeln eine viel höhere Aufnahme von negativ geladenen Nanogelen in den Pilz Die positiv geladenen Nanopartikel hingegen reicherten sich an der Zellmembran an. Diese Studie legte weiterhin nahe, dass eine Interaktion zwischen Partikeln und Pilzen wahrscheinlich erst nach der Ausbildung von Hyphae beginnt. Mittels Zellkultur-experimente wurden zudem nachgewiesen, dass die Nanogele auch von Neutrophilen aufgenommen wurden, was in Ko-Inkubationsexperimenten mit Pilzen die starke Wechselwirkung der Nanogele mit dem Pilz jedoch nicht negativ beeinflusste. Auf der anderen Seite wurden nur die positiv geladenen Nanogele

von Caco-2 - und Endothelzellen aufgenommen.

Da viele Antimykotika Aminogruppen in ihren Strukturen haben, ist die Verwendung von Acrylat-funktionalen Quenchern in der inversen Miniemulsion wegen der möglichen direkten Reaktion mit dem Wirkstoff möglicherweise problematisch. Deswegen wurden im weiteren Verlauf der Arbeit alternative Strategien für die Herstellung der Nanogele untersucht, bei welchen keine Quencher erforderlich sind.

Im Gegensatz zu Säugetierzellen enthalten Pilzzellen eine zusätzliche Zellwand, die sich außerhalb der Plasmamembran befindet. Sie hat einen komplexen, hauptsächlich Polysaccharid-basierten Aufbau, von denen einige hydrophob sind. Daher wurde untersucht, wie die Einführung hydrophober Einheiten entlang des PG-Polymerrückgrates, aus denen Nanogele synthetisiert wurden, die Wechselwirkung zwischen Nanogelen und Pilzen beeinflusst. Die Amphiphilie der resultierenden Partikel wurde durch Variation der Anzahl und Länge der Thiol-funktionalen Alkylseitenketten des PG eingestellt. Nanogele wurden durch Selbstassemblierung der amphiphilen PG bei Konzentrationen oberhalb der kritischen Aggregatbildungskonzentration in Wasser und nachfolgender oxidativer Kopplung der Thiolgruppen zu Disulfiden hergestellt. Untersuchungen der Wechselwirkung dieser Nanogele mit pilzspezifischen Polysachariden ergaben, dass die Polymere mit einem Funktionalisierungsgrad von 10% die größte Interaktion zeigten, und dies unabhängig von der Länge der Alkylseitenkette. Zusätzlich wurden Nanogele mit hydrophoben Fluoreszenzfarbstoffen beladen und hinsichtlich der Aufnahme durch Aspergillus fumigatus mittels Konfokalmikroskopie untersucht. Auch diese Studien zeigten, dass die Nanogele, die aus Polymeren mit dem Funktionalisierungsgrad von 10 % hergestellt wurden, von den Zellen am effizientesten aufgenommen wurden. Rasterkraftmikroskopische Untersuchungen zeigten zudem, dass sich die Zellwandmorphologie nach der Inkubation mit Nanogelen verändert. Zusätzlich konnte gezeigt werden, dass mit Amphotericin B beladende Nanogele eine bessere antimykotische Wirkung zeigten als das molekular gelöste Antimykotikum.

Dieser Effekt wurde durch die erhöhte Ansammlung von Wirkstoff-beladenden Partikeln an der Oberfläche des Pilzes und eine daraus resultierende höhere Aufnahmewahrscheinlichkeit im Vergleich zum freien Wirkstoff erklärt. Zudem wurde die Zytotoxizität gegen Säugerzellen durch den Einbau des Wirkstoffs in die Nanopartikel verbessert.

Um Nanogele mit einer engeren Partikelgrößenverteilung aus Thiol funktionalisierter PG herzustellen, wurde die inverse Nanofällung als alternatives Herstellverfahren untersucht. Mittels dieser Methode erhaltene gefriergetrocknete Nanogele konnten durch die sogenannte „breathing-in" Methode mit Antimykotikum oder auch Farbstoffen beladen werden. Hierbei werden die trockenen Nanogele mit einer konzentrierten Lösung der Substanz, mit denen die Partikel beladen werden sollen, gequollen. Auch hier legen Aufnahmestudien mit Aspergillus fumigatus nahe, dass die Nanogele den Wirkstoff an die Zellmembran transportieren wo er dann von den Zellen aufgenommen wird, während die Nanogele nicht aufgenommen werden. Darüber hinaus wurden anhand der wirkstoffbeladenden Partikel wieder bessere antimykotische Auswirkungen, beispielsweise eine zweimal geringere Minimale Hemm-Konzentration und längeren Hemm-Effekt der Biofilmformation, im Vergleich zu molekular gelöstem Wirkstoff gezeigt. Wirkstoff-beladende Nanogele zeigten eine bessere Verträglichkeit gegenüber roten Blutkörperchen, aber hatten ähnlicher zytotoxischen Effekt gegen Leber- und Nierenzellen wie der freie Wirkstoff, was durch die Aufnahme der Nanogele von Säugerzellen erklärt werden konnte. Dies betont die Wichtigkeit einer gezielten Wirkstoffabgabe der Nanogele für folgende in-vivo Studien.

Ferner wurden in dieser Arbeit die Möglichkeit der Anwendung von SPIOs für die Diagnostik mittels Traveling Wave Magnetic Particle Imaging erforscht. Untersuchungen zur Beschichtung der Partikel ergaben, dass vernetzte hydrogelartige Beschichtungen aus Thiolfunktionalisierte PGs die Nachweisbarkeit der Partikel mittels Traveling Wave Magnetpartikelbildgebung und Magnetresonanztomographie verbesserte. Diese Studie zeigte somit die

Wichtigkeit der SPIO-Beschichtung für diese Nachweismethode. Darüber hinaus verringerte diese Beschichtung die Zytotoxizität der Partikel gegenüber gesunden Fibroblasten und hemmten die Biofilmbildung von *A. fumigatus* nicht.

Schließlich wurde evaluiert, ob sich Gold Nanopartikel (GNP) als Modellpartikel für die Targetierung von *A. fumigatus* eignen. Zu diesem Zweck wurde das Fc Dectin-1 Protein an die Partikeloberfläche gebunden um damit eine selektive Anreicherung an der Pilz-Zellmembran zu erreichen. Dectin-1 wurde an der GNPs, die mit Carboxylfunktionalisierten PG dekoriert wurden, kovalent gebunden und die Bindungsaffinität für Betaglukane wurde mittels Oberflächenplasmonenresonanz-spektroskopie untersucht. Obwohl die Ergebnisse gezeigt haben, dass die Bindungsaffinität erhöht wurde, wenn das Protein an der GNP gebunden wurde, sind weiterführende Untersuchungen erforderlich, um eine Multivalenz zu bestätigen.

Zusammenfassend kann festgestellt werden, dass aus PG hergestellte Nanogele und mit PG beschichtete Nanopartikel ein großes Potenzial für die Anwendung in Therapie und als Diagnostika von Pilzerkrankungen haben, die von A. fumigatus verursacht werden. Weiterführende Untersuchungen sollten dafür die Interaktion zwischen Nanogelen und Pilzen detaillierter hinsichtlich Endozytosemarkern verfolgen. Zudem könnte ein detaillierteres Live-Imaging der Nanogelaufnahme die Spaltung der Nanogele innerhalb der Pilze und die Freisetzung des Wirkstoffes ermöglichen. Eine weitergehende Analyse der Zellwand-Morphologie und -Chemie nach der Inkubation mit Nanopartikeln könnte zudem den noch nicht genauer bekannten Einfluss der Nanopartikel auf die Zellwand aufklären. Schließlich sind weitere Untersuchungen zu Zielfindungsmolekülen für die Pilz-Zellwand als Grundlage für in-vivo Studien notwendig. Obwohl das Fc Dectin-1 Protein erfolgversprechende Ergebnisse gezeigt hat, sind mehr In-Vitro und In-Vivo Studien zur Optimierung erforderlich.

6 Experimental Part

6.1 Materials

2-methyl-2-oxazoline (98 %), methyl trifluoromethanesulfonate (MeOTf, 98 %), potassium tert-butoxy (KOtBu, 98 %), 4-dimethylaminopyridine (DMAP, 99 %), 3,3′-dithiopropionic acid (DTPA, 99 %), 4,4′-dithiodibutyric acid (DTBA, 95 %), polyethyleneglicol diacrylate (pEG-DA, Mw of 700 g/mol as given by the manufacturer), methanol (99.8 %), diethyl ether (98 %), dimethylformamide (DMF), dichlormethane (DCM) and anhydrous DMF (99.8 %), tetramethylsilane (TMS) as analytical standard for NMR spectroscopy, hexane (ChromasoLV®, 95 %), Cy5-maleimide, 2-hydroxylethyl acrylate (HEA, 96 %), 2-carboxyethyl acrylate (CEA), [2-(acryloyloxy)ethyl]trimethylammonium chloride solution (AEMA), span 80, tween 80 and alloxan monohydrate (98 %), p-toluenesulfonic acid (pTsOH, >98.5 %), ethyl vinyl ether (99 % with 0.1 % potassium hydroxide), calcium hydride (CaH_2, 99 %), dithiodibutyric acid (DTBA, 95 %), triethylamine (TEA, ≥99 %), calcofluor white aka fluorescence brightener (98 %), solubilized amphotericin B (Fungizone), oleic acid (99 %, OA), iron (III)-acetonate (99.9 %, $Fe(acac)_3$), iron (III) chloride hexahydrate (99 %), pluronics F127 (BioReagent, PF127), sodium oleate (98 %), trimethylamine N-oxide (95 %, TMAO), dithioerythritol (DTT, 97 %), and acryloyl chloride (97 %) were purchased from Sigma Aldrich, Germany, and were used as received. Hydrochloride acid (HCl, 37 %) and tetrahydrofuran (THF, 99.5 %) were purchased from Bernd Kraft and used as received. Hydrogen peroxide (H_2O_2, 30 %) Sodium hydrogen carbonate ($NaHCO_3$), magnesium sulfate ($MgSO_4$), dichloromethane, ether, ethanol, Irgacure 2595 (I2595) and sodium sulfate (Na_2SO_4) were purchased by Merck, Germany; tris(2-carboxyethyl) phosphine (TCEP, 98 %) from Carl Roth, Germany; calcium hydrate (92 %) from ABCR GmbH, Germany; chloroform (analytical reagent grade) micro BCA assay kit and phosphate-buffered saline (PBS) from Thermo

Fischer Scientific UK, and dicyclohexylcarbodiimide (DCC, 99 %) from Fluka Analytical, Germany, and were used as received; Cy5 maleimide was purchased from Lumiprobe GmbH, Germany, and ATTO 647N maleimide were purchased from ATTO-Tec GmbH, Germany. Dimethyl sulfoxide (DMSO), crystal violet (90 %), itraconazole (ITZ, 99 %), diethyl pyrocarbonate (95 %) and amphotericin B (AmB) synthesized by *Streptomyces* spp. were purchased from Alfa Aesar, Germany. Deuterated water (D_2O, 99.9 %), and dimethyl sulfoxide (DMSO-d6, 99.5 %) were purchased from Deutero GmbH (Kastellaun, Germany). All chemicals were used as received if not stated otherwise. Functional siRNA was delivered by the research group of Prof. Beilhack, and FITC-labeled siRNA was purchased from Biospring GmbH, Germany. Human recombinant dectin-1 with Fc tag was purchased from Sino Biological, USA. Poly(glycidol)s functionalized with carboxyl groups (pG-COOH) was synthesized by Johanna Lutz (AK Groll). 30 nm citrate coated gold nanoparticles (GNP) were purchased from Cytodyagnostics, Canada, from distributer Absource Diagnostics GmbH, Germany. CellTiter Glo assay was purchased from Promega, Germany and was used accordingly to instructions.

Membranes for dialysis were purchased from Spectrum Laboratories Inc. and were watered for 30 min prior use. For all experiments, Millipore water with the resistivity of less than 18.2 mΩ was used. Amberlite XAD16 resins were purchased from Alfa Aesar, Germany and were watered at least 30 min and washed extensively prior use to remove remaining salts.

6.2 Equipment and operating procedures

6.2.1 Chromatography

6.2.1.1 Gel Permeation Chromatography – Size-Exclusion Chromatography (GPC)

Depending on the solvent, GPC measurement was performed on one of the three systems, DMF GPC, water GPC, or chloroform GPC.

DMF GPC – analysis was performed on OMNISEC Systems (Malvern, Germany). The eluent DMF with the addition of 1 g/L LiBr had a flow rate of 1 mL/min. The

temperature of the injection was 20 °C, the working temperature was 45 °C and injection volume was 100 μL. The concentration range of polymers used for analysis varied from 0.25 mg/mL to 3 mg/mL.

This GPC system uses a right-angle light scattering (RALS) detector, a low angle light scattering (LALS) detector, a refractive index (RI) detector, a viscosity detector, a pre-column (Dguard, Organic Column 10 x 4.6 mm) and two separation columns: D2000 and D3000 (length: 300 mm, width: 7.8 mm, material: styrene divinyl-benzene, particle size: 6 μm). Molecular weights and polydispersity index (*Đ*) were calculated based on conventional calibration done using PMMA standards (Malvern, Germany).

Water GPC - water including 0.1 M $NaNO_3$ and 0.02 % NaN_3 was used as eluent in water GPC system (Viscotek GPCmax, Malvern, Herrenberg, Germany) with the flow rate of 0.7 mL/min with working temperature of 35 °C and injection volume of 100 μL. The system consisted of a multi-angle light scattering detector (Viscotek SEC-MALS 20), a refractive index (RI) detector (Viscotek VE3580), a viscosity detector (Viscotek 270) and Viscotek A-columns (length: 300 mm, width 8 mm, material: porous poly(hydroxy-methacrylate). Two different column sets were used for water SEC measurements, either A3000 (particle size: 6 μm) and A2000 (particle size: 8 μm) columns or two A6000 (particle size: 13 μm) columns. Molecular weights and *Đ* were calculated based on conventional calibration is done using pEG standards from Malvern using RI signal. Here, the polymer concentration was 1 mg/mL.

Chloroform GPC – analysis was performed on OMNISEC Systems from Malvern Instruments (Germany). The instrument operated at the flow rate of 0.7 mL/min with a working temperature of 35 °C and injection volume of 100 μL. The system consisted of a RI detector, and the sample was run on 2x Malvern LC4000L, 300 mm x 8 mm columns.

6.2.1.2 Prominence high-performance liquid chromatography (HPLC)

HPLC device (Shimadzu, Japan) was equipped with an autosampler, column compartment with oven and photodiode array detector. The chromatograph was equipped with Luna 5u C18(2)100A column with 5 μm particles size. 4.6 mm diameter and 150 mm in length. Data acquisition and analysis were done in LabSolutions software. The mobile phase comprised of 10 mM sodium acetate (pH 7.4) and acetonitrile (HPLC grade) in a volume ratio of 60:40, respectively. Samples with the injection volume of 10 μL ran with the flow rate of 1 mL/min for 15 min at the column temperature of 40 °C as described previously.[266] Photodiode array detector was set at a wavelength of 408 nm.

6.2.2 Spectroscopy

6.2.2.1 Proton nuclear magnetic resonance (^1H NMR)

^1H NMR spectra were recorded on a Bruker Biospin spectrometer (Germany) at 300 MHz. The solvent signals at δ of 4.76 ppm and 7.26 ppm were used as an internal reference for deuterated water (D_2O) and chloroform ($CDCl_3$), respectively. Chemical shifts were reported in parts per million (ppm).

6.2.2.2 Raman spectroscopy

Raman spectra were taken on Thermo Scientific DXR Raman Microscope Class I. The laser used was helium-neon (HeNe) low power, externally stabilized diode laser at 780 nm. The objective used was MPLAN 20x BF NA .40 with a working distance of 1.3 mm. The laser power was set to 18 mW (aperture 50 μm slit). The software used was Omnic 9.3.30.

6.2.2.3 Fourier transform infrared spectroscopy (FT IR)

FT IR analysis was done on Nicolet iS10. Dry sample was placed on the attenuated total reflection crystal (ATR) and spectra were taken from 525 cm^{-1} to 4000 cm^{-1}. Data were processed with Omnic Spectra software.

6.2.2.4 Fluorescence and ultraviolet-visible (UV-Vis) spectroscopy

Fluorescence spectra, fluorescence intensity and UV-Vis absorbance was estimated by a Spark 20M microplate reader (TECAN; Switzerland) using 96Nunc Thermo Fisher well plates, black or transparent for fluorescence and absorbance analysis, respectively.

UV-Vis measurements were also done on GENESYS 10S UV-Vis Spectrophotometer (Thermo Scientific™, Germany).

6.2.2.5 X-ray powder diffraction (XRD) spectroscopy

XRD patterns were recorded on XRD diffractometer D5005 (Siemens, Karlsruhe, Germany) with Cu Kα emission, using a step size of 0.02 ° and count time of 1.5 s/step° to 5 s/step°. Size of the nanocrystals was calculated following Scherrer equation[218]:

$$d = \frac{K\lambda}{\beta cos\theta} \quad (1)$$

where d is mean size of the crystalline domain, λ is X-ray wavelength (0.1541 nm), K is shape factor (0.89), β is full width at half-maximum in radians and θ is Bragg´s angle. The line width of the (311) plane refraction peak was used for the calculations.

6.2.2.6 Magnetic Particle Spectroscopy (MPS)

MPS experiments were performed by the research group of Dr. Volkes Behr by Dr. Patrick Vogel within a home-built benchtop MPS-device operating at a frequency of 19.95 kHz. The MPS-device consisted of a single excitation coil (transmit) and two receive coils assembled in a gradiometer setting.[267] The magnetic field strength could be adjusted in a range between 0 to 50 mT. The samples were prepared in 5 mm NMR glass tubes (Wilmad-LabGlass, Vineland, USA) with a defined volume of 50 µL to ensure comparable results. Each experiment was performed with a sequence length of 20 ms and a sampling rate of 100 MS/s and was averaged 10 times (duty cycle of 49 %). The data were acquired with a digital oscilloscope (HDO8038, Teledyne LeCroy, USA) and were corrected, processed and visualized

within a dedicated software package.[268]

6.2.2.7 Surface plasmon resonance (SPR)

SPR device used for binding affinity studies was Reichert 4SPR (AMETEK), Life Sciences, SPR Autolink with 4 channels. In these studies, 200 nm carboxylated dextran hydrogel coated SPR chips (Biacore, XanTec Bioanalytics GmbH, Germany) were used. Chips were activated with 200 nM EDC/NHS solutions mixed right before the experiment using the flow rate of 10 μL/mL (100 μL over 7 min). 3 mg/mL diaminopropane glucan phosphate from Prof. Williams was dissolved in 10 mM sodium acetate buffer, pH 4.5 and 100 μL was injected into device, using flow rate 10 μL/min for 8 min. Chip was washed with 500 μL running buffer (HEPES SPR buffer with 0.05 % of Tween 20) ad this procedure was repeated 4 times in total. The last time, carboxyl groups were quenched with 1M ethanolamine solution (pH 8.5). Running buffer was flowed for about 1 h. This procedure resulted in 1100 resonance units. For binding affinity studies linearly diluted Fc dectin-1 solutions or Fc dectin-1 GNPs suspensions in running buffer were loaded onto the chip and dissociated using glycine solution (pH 2) after each step.

6.2.3 Microscopy and imaging

6.2.3.1 Scanning (transmission) electron microscopy (S(T)EM) and energy-dispersive X-ray spectroscopy (EDX)

Electron microscopy images were taken by Zeiss Crossbeam 340, Oxford Instruments X-Max 50. Software used for data acquisition was SmartSEM.

6.2.3.1.1 STEM and SEM analysis of nanogels

For STEM of nanogels, samples were deposited on the carbon-coated copper grid, dried with filter paper and stained negatively with 2 % water solution of uranyl acetate. Excess of stain was removed by filter paper. For SEM of nanogels, 10 μL of nanogels in suspension were deposited on silica wafer and left to dry overnight on

air.

6.2.3.1.2 SEM of fungal specimens

Fungi (100 µL of $2 \cdot 10^5$ s/mL) were incubated for 24 h at 37 °C to the concentration of spore suspension with 100 µL of RPMI 1640 medium. After that, the medium was exchanged with 200 µL fresh medium in which nanogels were dispersed to a drug concentration of 1 x MIC. The pure drug was dissolved firstly in DMSO and then diluted to the desired concentration by RPMI medium. Nanogels without drug were dispersed to the concentration of 1 mg/mL, and for the control sample, the only medium was used. After an additional 2 h at 37 °C, fungal biofilms were washed twice with PBS and fixed with 4 % paraformaldehyde for 5 min. After that, samples were washed again twice with PBS and dried gradually with EtOH solution (20 %, 40 %, 50 %, 60 %, 70 %, 80 %, 90 % and 100 % of EtOH, v/v, 20 min each). Finally, samples were dried at the air for 2 days and were sputtered with Pt by Philipp Stahlhut (research group of Prof. Groll).

6.2.3.1.3 EDX

Elemental distribution of iron on the fungal biofilm was evaluated by Judith Friedlein on EDX INCA Energy 350 AzTec Advanced system on the SEM. An acceleration voltage of 2.0 kV was used with a silicon drift detector (Oxford Instruments, UK) and an aperture of 20 µm. Before analysis, biofilms were dehydrated using ethanol (40 %, 50 %, 60 %, 70 %, 80 %, 90 %, 100 % ethanol, 10 min each) and left to air dry.

6.2.3.2 Confocal laser scanning microscopy (CLSM)

CLSM was performed on Leica TCS SP8 STED. To monitor the nanogel uptake by the fungus wild type or GFP strain of *A. fumigatus* (400 µL, 1×10^6 s/mL) was incubated in RPMI 1640 medium at 37 °C, 5 % CO_2 with 100 µL dye-labeled or dye loaded nanogels (0.8×10^{11} p/mL as determined by nanoparticle tracking analysis). After incubation, samples were fixed in 1 % paraformaldehyde solution for 10 min

and washed with PBS. Before imaging, samples were transferred on the microscopic slide coated with a thin layer of poly-lysine. Samples were sealed with nail polish or Entellan® (Sigma Aldrich, Germany). The fungal wall was labeled by calcofluor white, which was dissolved in water to the concentration of 1 mg/mL with 100 μL of 100 mg/mL potassium hydroxide.

Fluorescence intensity was measured and quantified using ImageJ software (imagej.nih.gov) using minimally three different hyphae. Background intensity was subtracted from the areas of the same sizes to determine the mean relative fluorescence.[269]

6.2.3.3 Fluorescence microscopy

Fluorescence images were taken on Zeiss Axio Imager Z1m or Zeiss Axio Vert. A1.

6.2.3.4 Atomic Force Microscopy (AFM)

6.2.3.4.1 AFM measurements of nanogels

The analysis was done on Nanosurf FlexAFM with C3000 Controller (Nanosurf, Germany) using PPP-FMR cantilevers Pointprobe-Plus® Silicon-SPM-Sensor with force constant of 0.5-9.5 N/m from Nanosensors™. Software used for data processing was Nanosurf Easyscan 2 V3.5.

Samples of 40 μL in volume were spin-down on freshly cleaved mica at a rotation speed of 2500 rpm for 40 s, dried and analyzed using tapping mode.

6.2.3.4.2 AFM analysis of fungi

For AFM of fungal samples were left to dry out without introduction of ethanol and were analyzed without sputtering with Pt. AFM analysis of fungal hyphae was done by the research group of Dr. Ingmar Tessmer. Device Asylum Research MDF-3DTM AFM, using Olympus Microcantilevers OMCL-AC24OTSA-R3E cantilevers with spring constant of 2 N/m was used operating by the software version 060513 for the image manipulation.

6.2.4 MR-Relaxivity characterization

Nanocomposites were solved in water to prepare a dilution series starting from 250 μM Fe and filled in 5 mm NMR sample tubes (Wilmad-LabGlass, Vineland, USA). Samples were incubated at different temperatures (25 °C, 37 °C and 55 °C) in thermostat for at least 5 min prior measurements. Each tube was taken from the thermal bath separately and immediately measured inside the MR-scanner. Experiments were performed at a Bruker Biospec 70/30 (Bruker Biospin, Germany) at 300 MHz with a 72 mm quadrature birdcage coil for transmission and reception (Bruker Biospin, Germany) by Dr. Thomas Kampf. Transverse relaxation time T_2 was measured employing a multi spin-echo sequence with 200 spin echoes with an echo spacing of 5 ms. To prevent changes in temperatures, the measurement was kept as short as possible a 1d-projection of the with 64 sampling points at a bandwidth of 50 kHz were sampled (FOV of 39.7 mm). T_2 times were calculated in Matlab (MathWorks, Natick, MA, USA) using customized software. Data were fitted to a single exponential signal model considering the Rician distribution of noisy amplitude MRI data.[270] Subsequently transverse relaxation rates $R_2 = 1/T_2$ were calculated. Transverse relaxivity r_2 was then obtained by linear regression of the R_2–values versus the corresponding concentrations and plotted over the temperature for each nanocomposite.

6.2.5 Traveling wave magnetic particle imaging (TWMPI)

TWMPI experiments were performed within the TWMPI prototype by the research group of Dr. Volkes Behr by Dr. Patrick Vogel.[202] For imaging, the slice-scanning mode (SSM) sequence was used to visualize the central slice of the scanner.[203] The frequencies were set to f1=1050 Hz and f2=12150 Hz, the total acquisition time was 200 ms (20 ms sequence length and 10 times averaging) at a sampling rate of 100 MS/s. The gradient strength was set to 1.5 T/m, offering a high sensitivity and spatial resolution. After digitization (HDO8038, Teledyne LeCroy, USA), the data sets were corrected, processed and visualized.[268]

The samples were prepared in 0.5 mL Eppendorf caps (Eppendorf, Germany) and

positioned in the center of the TWMPI scanner. For sensitivity measurements, the signal-to-noise (SNR) value was determined from the magnitude of the Fourier transformed spectrum at frequency 47.55 kHz, which is the first left-handed sideband-harmonic of the fourth higher harmonic of f2: 4*f2-f1. For the reconstruction of the images, a standard Wiener filter with an appropriate point-spread-function (PSF) was applied to the re-gridded raw-images.[202]

6.2.6 Particle sizing

6.2.6.1 Dynamic light scattering (DLS)

Particle sizing was performed by dynamic light scattering (DLS) device NICOMPTM 380 ZLS from Particle Sizing Systems Nicomp (California, USA), measuring at angle 90 ° for the samples prepared in **Section 3.1**. All other samples were analyzed by Zetasizer Nano ZSP (Malvern, Germany) measuring backscattered light at 173 ° (n = 1.45, k = 0.001). ζ-potential of nanoparticles were evaluated by Zetasizer Nano ZSP (Malvern, Germany) by measuring samples at 13 °. If not otherwise noted, samples were measured at RT.

6.2.6.2 Nanoparticle tracking analysis (NTA)

NTA device Nanosight NS500 (Nanosight Ltd., UK) was used for determination of particle size vs. concentration in the medium. Samples were diluted 1000 to 10000 times to reach the optimal range and analyzed during flow. Minimal three measurements were analyzed. This method and device were used for determination of nanoparticle concentration as well.

6.2.7 Other

6.2.7.1 Storage of air- and water-sensitive substances

Air-sensitive chemicals and materials were stored in a glovebox LabMaster 130 (MBraun, Germany) under inert conditions with a controlled amount of humidity.

6.2.7.2 Single-Mode Reactor

Discover SPTM microwave (CEM GmbH, Germany) operated by the Synergy software was used for the synthesis of the poly(2-methyl-2oxazoline)s. The synthesis was performed in 10 mL or 35 mL vessels closed by silicone/PTFE caps. The reaction solution was stirred magnetically by 10 mm stirrer bar on medium speed during the synthesis.

6.2.7.3 Sonication

Samples were sonicated by Sonifier® W-250D (G. Heinmann, Ultraschall und Labortechnik, Ascwabisch Guend) using 10 % of amplitude, 0.4 s pulse and 0.6 s pause. The tip was always in the same position and height for all samples.

6.2.7.4 Freeze Drying

Lyophilization of the samples were done on two devices, either on Christ freeze drier type 101021 equipped with the Trivac D4B vacuum pump (Trivac Laybold Vakuum GmbH). The temperature inside the chamber was – 55 °C.

6.2.7.5 Karl Fisher titration

For estimation of water in acetone, C30S Coulometric KF Titrator was used.

6.2.7.6 Determination of iron concentration

The colorimetric 1.10-phenanthroline method was used for determination of iron content in iron oxide nanoparticle suspensions. For the first method, 10 μL of the sample was dissolved in 10 μL of 37 % HCl at 50 °C and under sonication. Further, 10 μL of dissolved iron oxide nanoparticles were diluted with 600 μL water, 50 μL 10 % hydroxylamine hydrochloride, 250 μL of 25 % sodium acetate and 100 μL of 0.25 % 1.10-phenanthroline monohydrate solution. Absorption was measured by UV Vis spectrometer at 510 nm. Measurements were done at least in duplicates, from samples dissolved separately. For the calibration curve, dilutions of iron reference standards (1000 ppm, Sigma Aldrich) was used.

6.2.7.7 Statistical analysis

Statistical analyses were performed using Statistica software v. 13.3 (StatSoft). Data was assessed through one-way ANOVA on Tukey's post-hoc test.

6.2.7.8 Micro BCA assay

15 μL of suspension was incubated with 10 μL of 100 mM potassium cyanide at 60 °C overnight to dissolve the particles. 135 μL of the HEPES buffer and 150 μL of the micro BCA assay solution were added to the samples. After 1 h at 37 °C, absorbance at 562 nm was measured by multiplate reader Spark20M. Standards were prepared from the known concentrations of Fc dectin-1 solutions: to 150 μL of standards, 10 μL of potassium cyanide solution and 150 μL of micro BCA assay solution were added followed by the incubation at 37 °C.

6.3 Methods

6.3.1 Synthesis of initiators, intermediates and polymers

6.3.1.1 Synthesis of poly(2-methyl-2-oxazoline) (pMOx)

6.3.1.1.1 Microwave-assisted synthesis of pMOx with 50 repeat units

Synthesis of poly(2-methyl-2-oxazolines) (pMOx) was done by cationic ring-opening polymerization under microwave conditions as reported by Hoogenboom et al.[126] Typically, in a flame dry flask, 0.369 g of MeOTf was dried under vacuum for 1 h. Under inert conditions, 16 mL of acetonitrile and 8.389 mL of distilled 2-methyl-2-oxazoline, resulting in monomer concentration in polymerization mixture of around 4 mol/l, were added and the solution was transferred to the microwave vial with the magnetic stirrer. Polymerization was performed in the microwave at 100 °C at 30 min, 60 min and 90 min or at 140 °C 10 min and 30 min at 5 bars in order to analyze the influence of temperature and reaction time on the synthesis. The reaction was quenched by the addition of piperidine (0.589 mL) or water (0.214 mL) under argon flow and the solution was stirred for overnight. On the next day, acetonitrile was evaporated, and the polymer was dissolved in methanol/chloroform solution (1:1, v/v) and precipitated in cold diethyl ether.

After precipitation, the sediment was separated by the centrifugation (4500 rpm, 5 min) and the washing procedure was repeated 2 times more. After that, the polymer was evaporated under reduced pressure. The yield of the reaction was 95 % ± 5 % for all experiments.

GPC analysis (3 g/mL) was made in DMF (Mn of 4640 g/mol, Đ of 1.4). ^{1}H-NMR (D_2O): δ (ppm) = 3.3-3.6 (m, NCH_2CH_2), 3.0-3.1 (d, CH_3), 2.8-2.9 (s, CH_3), 1.9-2.2 (m, NCOCH_3).

According to the ^{1}H-NMR, the number of repeat units of the polymer was 55.

6.3.1.1.2 Kinetic study of the polymer hydrolysis

Hydrolysis of the polymer was done in an oil bath as reported by Rosa et al.[118] For the synthesis, the polymer prepared by the synthesis at 100 °C and 60 min was chosen. Polymer stock solution (100 mL, polymer concentration of 0.0427 g/mL) in water was warmed to 120 °C in an oil bath. After temperature equilibration (45 min) to the polymer solution HCl was added to reach a concentration of 1 M (8.5 mL). Aliquots of 0.5 mL were withdrawn periodically (after 20 min, 40 min, 60 min, 80 min, 100 min and 145 min) and neutralized by 4 M NaOH (aq.) to a pH of 9. The obtained series were subsequently freeze-dried and lyophilized for evaluation of a conversion degree. The conversion was calculated by analysis of ^{1}H-NMR spectra (D_2O), by the formula:

Conversion (%)=(Integration of PEI backbone)/(Integration of pEI backbone + Integration of pMOx backbone) × 100 (2)

GPC analysis (3 g/mL) was made in DMF with or without the addition of a base, TEA (3 %, v/v).

^{1}H-NMR (D_2O): δ (ppm) = 3.3-3.6 (m, NCH_2CH_2), 3.0-3.1 (d, CH_3), 2.7-2.9 (s, NHCH_2CH_2), 1.9-2.2 (m, NCOCH_3).

6.3.1.1.3 Synthesis of a copolymer with predetermined pMOx-EI conversion degree

The procedure for the synthesis of the predetermined pMOx-EI conversion was done similarly as described in kinetic studies. Based on the results of kinetics studies, the time necessary to obtain a conversion degree of 30 % was selected (114 min). In one experimental set-up, the reaction mixture was cooled down and basified with 4 M NaOH (aq) to obtain a pH of 8.5. Subsequently, the polymer solution was dialyzed against water (MWCO of 1000 g/mol) for 3 days with regular water changes. The polymer solution was then freezing dried and lyophilized, resulting in a yield of the reaction of 30 ± 3 %. In another set-up, solvents were evaporated after hydrolysis under reduced pressure. The polymer was dissolved in chloroform and precipitated in cold diethyl ether and this procedure was repeated three times. Finally, the product was dried under reduced pressure, yielding the 90 % ± 2 % of the polymer.

6.3.1.1.4 Thiol functionalization of pMOx-EI

pMOx-EI was dissolved in dry DMF under argon to the concentration of 0.4 mg/mL. To the polymer solution, 1.1 molar equivalents of DCC and DMAP, in respect to the amount of polymer, were added. Then, the mixture was cooled in an ice bath and 1.1 equivalent of DTPA (598 mg/mL in dry and degassed DMF) was added under argon. The reaction mixture was warmed to the room temperature and stirred overnight. On the next day, the formed hydrogel was washed with DMF, THF and water. Then, 1.5 eq. of TCEP was added and the pH of the solution was adjusted to 6-7 by the addition of triethylamine (TEA). The reaction was completed after 4 h, after which DCC salt was removed by centrifugation and filtration. Thiol functionalized polymer was dialyzed for 1 day against with HCl acidified water at pH 3.5 (5 water changes) and 2 days against degassed water (3 water changes per day) using MWCO of 1000 g/mol. Finally, the polymer was freeze-dried. The yield of the reaction was 57 ± 3 %.

^{1}H-NMR (D_2O): δ (ppm) = 3.3-3.6 (m, NCH_2CH_2), 3.0-3.1 (d, CH_3), 2.7-2.9 (s,

NHC*H*$_2$C*H*$_2$), 2.4-2.6 (m, NCOC*H*$_2$C*H*$_2$SH), 1.9-2.2 (m, NCOC*H*$_3$).

6.3.1.2 Synthesis of poly(glycidol)s (pG)

6.3.1.2.1 Synthesis of ethoxy ethyl glycidyl ether (EEGE)

Glycidol (100 mL, 1 eq.) and ethyl vinyl ether (592 mL, 4.1 eq.) were mixed in 2 l three-neck flask in an ice bath until the solution became transparent. After pTsOH (2.85 g, 0.01 eq.) was added slowly, so the temperature did not rise above 20 °C, the solution was left to react for 6 h in an ice bath. The solution was then transferred to a separatory funnel and washed three times with saturated $NaHCO_3$ solution and dried with $MgSO_4$. Ethyl vinyl ether was evaporated under reduced pressure and dried with CaH_2 overnight. After that, the monomer solution was distilled under inert conditions and it was stored at the water and oxygen-free condition at 4 °C until use.

^1H NMR ($CDCl_3$): δ (ppm) = 4.7–4.6 (m, epoxy-$CH_2OCH(CH_3)OCH_2CH_3$), 3.8–3.3 (m, epoxy-$CH_2OCH(CH_3)OCH_2CH_3$), 3.1-3.0 (m, epoxy C*H*), 2.8–2.7 (m, epoxy C*H*) and 2.6–2.5 (m, ethoxy C*H*$_2$), 1.3–1.2 (m, epoxy-$CH_2OCH(CH_3)OCH_2CH_3$), 1.2–1.1 (m, epoxy-$CH_2OCH(CH_3)OCH_2CH_3$).

6.3.1.2.2 Synthesis of the poly(glycidol) acetate (pEEGE)

The synthesis of the polymer was done by the procedure described by Stichler et al.[135] In 100 mL dry flask 2 mmol (2 mL) of KOtBu was added drop-wise for 10 min in 120 mmol (17.5 mL) of EEGE under inert conditions. The mixture was then stirred for 12 h at 60 °C under argon. Subsequently, the reaction was left to cool to RT and 1 mL of MeOH added. Finally, solvents were evaporated by high vacuum (2.0×10^{-2} mbar).

6.3.1.2.3 Synthesis of the poly(glycidol)s (pGs)

Firstly, pEEGE was dissolved in THF to a concentration of 0.03 g/mL and 37 % HCl was added to a concentration of 1 mL/1 g of polymer. The reaction mixture was stirred for 30 min at RT after which the mixture stands for 5 min to separate

the sediment. Sediment was washed once more with THF and was dissolved in water to the concentration of 1 g polymer/20 mL water. Finally, polymers were dialyzed (3 days, 3 water changes per day, MWCO 3500 g/mol).

6.3.1.2.4 Thiol functionalization of pGs

Thiol functionalization of pG was done similarly to the functionalization of PMOx-co-EI described before. pG was dissolved in dry DMF under argon to the concentration of 1 g polymer/3 mL DMF. To the polymer solution, 1.1 molar eq. of DCC and DMAP, in respect to the amount of polymer, were added. Then, the mixture was cooled down in an ice bath and 1.0 eq. of DMPA (411 mg / 2.32 mL in dry and degassed DMF) was added under argon. The reaction mixture was warmed to the room temperature and stirred for 5 h. The formed hydrogel was washed with DMF, THF and water. Then, 1.7 eq. of TCEP was added and the pH of the solution was adjusted to 6-7 by the addition of triethylamine (TEA). The reaction was completed after 4 h, after which DCC salt was removed by centrifugation and filtration. Thiol functionalized polymer was dialyzed 3 days against degassed water (3 water changes per day) using MWCO of 3500 g/mol. Finally, the polymer was freeze-dried.

^1H NMR (D_2O): δ (ppm) = 1.15-1.30 (s, br, 9H, CH_3-1), 3.41-3.92 (m, C*H*2C*H*OC*H*2C*H*(C*H*2OH) CH_2 2, 7, 9, CH-3, 8), 4.36–4.44 (m, C*H*$_2$OCOCH$_2$CH$_2$SH), 2.48-2.66 (m, CH$_2$OCOC*H*$_2$C*H*$_2$SH).

Calculation of the functionalization degree (DF) is calculated by the follows:

3 protons from thiopropionate aresubtracted from x, the integral value equals five protons belonging to the glycidol repeat units:

DF (%) = 1/(1+ (x-3) /5) ×100

Linear pGs were modified to a predetermined DF following the same procedure. pGs were crosslinked with either DTPA or dithiobutyric acid (DTBA) to reach 5 %, 10 % or 20 % DF and subsequently reduced with TCEP to thiol groups. Thiol-functionalized polymers were dialyzed, lyophilized and stored at -20 °C under

argon atmosphere until use.

GPC data are presented in Table 3.2- 1.

6.3.1.3 Fluorescence labeling of polymers

Both polymers, pMOx-EI-SH and pG-SH were labeled in the same way. Typically, 596 mg of the polymer was dissolved in 60 mL of 0.1 M PBS with the addition of 900 mg TCEP hydrochloride. The pH of the solution was set to 6.5 by the addition of TEA and stirred for 20 min. After that, 2 mg of Cy5 dissolved in 200 μL DMF was added to the solution and stirred overnight at RT and in the dark. Finally, samples were dialyzed against deoxidated water (3 water changes per day, MWCO 1000 g/mol), freeze-dried and stored at -20 °C in the dark.

6.3.1.4 Synthesis of diacrylated poloxamer (PF127DA)

Synthesis of the diacrylated poloxamer was performed according to a previously reported procedure.[223] Dichlormethane (DCM), triethylamine (TEA) and diethyl ether were dried over with activated 3 Å molecular sieves for 24 h. 15 g of the vacuum-dried Pluronic F127 was dissolved in 120 mL DCM in a 250 mL flask. After addition of 0.67 mL of TEA, the solution was cooled to 0 °C in an ice bath, followed by dropwise addition of 0.60 mL solution of acryloyl chloride in 10 mL DCM. The yellowish reaction mixture was stirred for 12 h at 0 °C and another 24 h at room temperature under argon after which precipitate was visible in the solution. Finally, the solvent was partially evaporated, and TEA salts were removed by filtration. Product (PF127DA) was precipitated in a large excess of anhydrous ether dried over sieves, dissolved in anhydrous DCM, filtered again and washed with anhydrous ether. Finally, the product was dried in vacuum at 40 °C and stored at 4 °C.

GPC ($CHCl_3$, conventional calibration, Column Set 2 * LC4000L (Viskotec, Malvern, Germany)): Mw_{PF127} = 23256 g/mol, $Đ$ = 1.3; $Mw_{PF127DApG}$ = 23605, $Đ$ = 1.4.

6.3.1.5 Extraction of the β-(1-6)-glucan and solubilization

Extraction of the β-(1-6)-glucan was done following the protocol from Williams et al.[163] Briefly, lyophilized yeast (*Saccharomyces cerevisiae*, Sigma Aldrich, Germany) was extracted by sodium hydroxide, phosphoric and ethanol extraction, washed by water and lyophilized. After that, the product was dissolved in DMSO in the presence of urea and stirred in the presence of phosphoric acid until dissolution. Finally, solubilized β-(1-6)-glucan was purified by dialysis and freeze-dried.

6.3.2 Preparation of hydrogels

Synthesis of the hydrogels from the copolymer pMOx-EI, pMOx -SH and pG-SH were done in borate buffer at a pH of 8.4. Firstly, the polymer was dissolved in 0.05 M buffer in the concentration of 0.396 mg/μL. From this solution, 31.5 μL was taken and mixed with 15 μL of water solution of the crosslinker pEG-DA in the case of pMOx-EI and alloxan, H_2O_2 or pEG-DA in the case of pMOx-SH and pG-SH with different amounts (1×10^{-3} mmol, 2×10^{-3} mmol and 4×10^{-3} mmol). Buffers used for gelation of pMOx-EI and pG-SH were PBS for reaching a pH of 7.4 and borate buffer for pH of 8.5 and 9.5. Gelation time was determined by the vial inversion method. Subsequently, hydrogels were analyzed by Raman spectroscopy and FT IR.

6.3.3 Preparation of nanoparticles

6.3.3.1 Nanogel synthesis by miniemulsion

6.3.3.1.1 Synthesis of the cleavable pMOx-SH based nanogels

Nanogels were synthesized by inverse miniemulsion method, by keeping volume ration between aqueous and organic phase constant (1:10, respectively). Firstly, polymer pMOx-EI was dissolved in a selected buffer to a certain concentration. 31.5 μL of this solution was shortly vortexed with 315 μL organic phase composed from hexane and 30 mg/mL surfactant. The emulsion was sonicated in an ice bath and selected volume of the alloxan solution in water (32 mg/mL) was added. The

solution was sonicated again and magnetically stirred in an ice bath. After 20 min, quencher in a buffer (30 mg/mL) was added and the emulsion was stirred for an additional 20 min. The samples were then centrifuged at 5000 rpm for 1.5 min, the supernatant was discarded and replaced by pure hexane, after which centrifugation and washing steps were repeated. Nanogels were washed by THF in the same manner. Finally, samples were dialyzed against water using MWCO of 12000-14000 g/mol.

6.3.3.1.2 Synthesis of the cleavable pG-SH based nanogels

Nanogels were synthesized by inverse miniemulsion method already established by Groll et al.[17] Polymer (25 mg) was dissolved in 0.05 M borate buffer (62.5 μL) at pH 8.4. To this solution, 625 μL of organic phase consisted of hexane and surfactants Span 80 (14.06 mg) and Tween 80 (4.68 mg) with an HLB value of 7 was added. The emulsion was sonicated in an ice bath for 1 min after which 30 μL of alloxan solution (32 mg/mL) in water was added and the emulsion was sonicated for another 1 min. After 20 min of magnetic stirring in an ice bath, 30 μL of quencher in 500 μL buffer (30 mg/mL) was added and the emulsion was stirred for an additional 20 min. The samples were then centrifuged at 5000 rpm for 1.5 min, the supernatant was discarded and replaced by pure hexane, after which centrifugation and washing steps were repeated. Nanogels were washed by THF in the same manner. Finally, samples were dialyzed against water using MWCO of 12000-14000 g/mol with the addition of a small amount of ethanol (5 mL in 1.5 L water).

6.3.3.1.3 Synthesis of fluorescence-labeled nanogels

For the preparation of both cleavable fluorescence-labeled nanogels, one-third of the polymer was fluorophore-labeled and the rest of the synthesis parameters remained the same.

6.3.3.2 Nanogel synthesis by self-assembly

6.3.3.2.1 Determination of critical association/aggregation concentration (cac) of thiol-functionalized polymers

Cac of polymers was determined using two different approaches; by measuring the change in fluorescent intensity of 8-anilinonaphthalene-1-sulfonic acid (ANS) and by monitoring change of count rate by dynamic light scattering of linearly diluted samples. Tests were done with a minimum of two replicates.

ANS was dissolved in acetone (1 μM) and transferred to 96 non-transparent flat well plates and acetone was evaporated. Then, 200 μL of linearly diluted polymer solution in water was added to achieve a constant concentration of fluorescent dye ($6 \cdot 10^{-7}$ M), and fluorescence spectrum was taken after 24 h of incubation from 405 nm to 600 nm with exc. of 388 nm. For DLS measurements, samples were directly measured at 25 °C after dissolving in water.

6.3.3.2.2 Preparation of nanogels

Polymers were dissolved well above their cac (approx. 2 times their cac determined from the average value from both methods described previously). Briefly, 14 mg pG-PA5%, 7 mg of pG-PA10%, 1 mg of pG-PA20%, 7 mg of pG-BA5%, 3 mg of pG-BA10%, 1 mg of pG-BA20% were dissolved in 0.95 mL water and were added slowly to the DMSO while vortexing. After 3 h of incubation at RT, 15 μL of alloxan water solution (32 mg/mL) was added and after 30 min at RT, samples were dialyzed against water (MWCO 12000-14000 g/mol, 1.8 L water per change, 12 x water changes) and stored at 4 °C before use.

6.3.3.2.3 Stability of polymeric aggregates and nanogels in the presence of urea

Polymeric aggregates or nanogels prepared from polymers with DF of 10 % in the concentration of 7 mg/mL (pG-PA10%) and 3 mg/mL (pG-BA10%) in PBS were incubated with 400 μg/mL urea at RT. After pre-determined periods, samples were analyzed by DLS.

6.3.3.2.4 Loading with dye and drug

To evaluate the interaction of nanogels with fungus, nanogels were loaded with hydrophobic dye Oil red O (ORO). Loading of nanogels was done by polymer-to-drug approach since this method produced nanogels with higher loading compared to drug-to polymer approach (results not shown). Briefly, 14 mg pG-PA5%, 7 mg of pG-PA10%, 1 mg of pG-PA20%, 7 mg of pG-BA5%, 3 mg of pG-BA10%, 1 mg of pG-BA20% were dissolved in 0.95 mL water and were added slowly to the dye solution (2 mg/mL) in DMSO while vortexing. After 3 h of incubation at RT, 15 μL of alloxan water solution (32 mg/mL) was added and after 30 min at RT, samples were dialyzed against water (MWCO 12000-14000 g/mol, 1.8 L water per change, 12 x water changes). After dialysis, nanogels were diluted to 2 mL with water, and 50 μL was freeze-dried. Finally, dried samples were dissolved in 100 μL DMSO and fluorescence was measured on multiplate reader Spark 20M (exc: 590 nm; em: 550 nm).

Dye loading (DL) and encapsulation efficiency (EE) were estimated by the following formulas:

EE % = amount of encapsulated loading / amount of used loading x 100 % (3)

DL % = amount of encapsulated loading / amount of total mass of polymer and loading used for the preparation of nanogels x 100 % (4)

where the amount of encapsulated loading is equal to the concentration of loading multiplied by the volume of nanogel suspension.

Amphotericin B (AmB) was encapsulated in nanogels via hydrophobic interactions similarly as dye ORO with the exception that drug concentration in DMSO was 20 mg/mL before the addition of polymers. Since drug self-aggregate in nano-assembles of around 100 nm, it was necessary to incubate the nanogels with Amberlite XAD16 resins, used for extraction of this drug in the medium. This ensured that final nanogel suspension did not contain the free drug.[271] After dialysis, nanogels loaded with AmB were further treated with Amberlite XAD16 resins (300 mg per 0.8 mL) for at least 18 h at RT while shaking. This amount of resins was chosen based on the results of the study where a minimal amount of

resins necessary to extract the AmB solution in water was determined (results not shown). Indeed, after centrifugation of AmB loaded nanogels, no absorbance of AmB was observable by UV-Vis (data not shown). Resins were removed by syringe and samples were stored at 4 °C until further use. All reactions of drug loading experiments were done in the dark to prevent drug decomposition.

To determine the drug loading and encapsulation efficiency, nanogels were dispersed in 1 mL water. 200 µL of this suspension was added to 100 µL of 300 mM DTT solution in phosphate buffer. After 1 h of incubation at RT, 20 µL of this solution was mixed with 180 µL DMSO, and optical density was analyzed at 371 nm using Tecan microplate reader. Standards used for the calibration were used in the same way: 20 µL of standard AmB solution in DMSO was mixed with 20 µL phosphate buffer and 160 µL DMSO. The drug content in particles was also analyzed by HPLC.[266] DL, and EE of the drug in nanogels was calculated using the same calculations as described previously for dye loaded nanogels.

6.3.3.2.5 Interaction of nanogels with β-(1-6)-glucan phosphate

Nanogels with a concentration of 1 mg/mL as determined by freeze-drying were incubated with 0.03 mg/mL β-(1-6)-glucan phosphate in PBS. After predetermined time points, samples were analyzed by DLS. Size distribution was calculated using the CONTIN algorithm, which suits analysis of multimodal solutions with small residuals.[272]

6.3.3.3 Nanogel synthesis by nanoprecipitation for loading by ´breathing-in´

6.3.3.3.1 Preparation of nanogels

Nanogels were prepared by nanoprecipitation of polymer solution in acetone. In the standard procedure, 6 mg pG polymer with DF of 12 % if not stated otherwise was dissolved in 90 µL Millipore water and precipitated in 45 mL acetone with a water content of 18 % as determined by Karl Fischer titration. After 3 h, 30 µL of 32 mg/mL water solution of alloxan monohydrate was added and oxidation proceeded for 1 h after which 4 mL water was added. Samples were left to

evaporate acetone at RT overnight and washed three times by centrifugation (16100 x *g*, 15 min).

6.3.3.3.2 Loading of drug and dyes

For drug loading, nanogels were freeze-dried with the addition of glucose (10 % of polymer content) as a cryoprotectant. Then, 40 μL of drug solution in DMSO was added and samples were magnetically stirred for 3 h. In the very beginning, samples formed a soft gel, which with stirring transformed to liquid. Finally, samples were washed 3 times with water by centrifugation (16100 x *g*, 10 min).

Amount of encapsulated drug was estimated by measuring fluorescence spectra of samples on multiplate reader Spark 20M (exc. 260 nm, em. 375 nm) with the addition of DMSO. Standards were prepared by dissolution of the pure drug in DMSO and dilution with water to achieve the same DMSO to water v/v ratio as used for drug-loaded nanogels.

Encapsulation efficiency (EE) was estimated using the formula (3).

Drug loading (DL) was estimated using the formula (4).

Nanogels were loaded with hydrophobic dye Oil red O (ORO) and amphiphilic dye rhodamine 6g following the same procedure.

6.3.3.4 Preparation of tracers with magnetic properties

6.3.3.4.1 Synthesis of iron-oleate

Iron-oleate was synthesized as described previously in other studies.[215] Firstly, 5.4 g of iron (III) chloride hexahydrate was dissolved in 12.5 mL water and stirred for 30 min. Meanwhile, 18.4 g of sodium-oleate was dissolved in the mixture of hexane and ethanol (62.5 mL and 37.5 mL, respectively) which was followed by addition of 7.5 mL water and heating to 40 °C. Iron chloride solution was added, and the reaction mixture was heated to 60 °C under argon for 4 h. After this reaction, the solution was cooled to 50 °C and was transferred to the separatory funnel, lower phase was discarded, 18.8 mL of water was added, and the mixture was shaken for 10 s. The lower phase was discarded, and this procedure was

repeated 3 times in total. The solution was transferred to another flask with 6.25 g of anhydrous sodium sulfate. After 10 min, the sodium sulfate was filtered off, and the solvents from the iron oleate solutions were gradually evaporated with a vacuum.

6.3.3.4.2 Synthesis of 18 nm iron oxide nanoparticles

Aperture was composed of the 250 mL round flask with three necks (60 °), with Schlenk line, thermometer and air condenser. All glass joints were sealed with the few drops of 1-octadecene and heating was done using heating mantle. Particles were synthesized using the method described by Park et al.[215] Typically, 1-octadecene (3 g), oleic acid (1.254 g, 4.4 mmol) and iron-oleate (0.540 g, 0.6 mmol) were placed in the flask, and the reaction was treated by the high vacuum overnight (18 h). Then, the mixture was placed in the oil bath and heated to 80 °C by stirring at 450 rpm. The mixture was held at this temperature for 1 h. Then, argon/vacuum cycles were done few times, finishing with the argon and the apparatus was placed in the heating mantle. After 45 min, the inner temperature reached 318 °C. In this point, argon flow was stopped by closing the transfer line and after 30 min suspension turned black. The reaction was ended after 80 min by turning off the heating mantle. After the reaction mixture was cooled down, the flask was opened under argon flow and 100 mg of TMAO was added followed by purging of argon for 5 min. The reaction mixture was further heated until reflux and maintained at this temperature for 1.5 h. Finally, particles were washed several times with a mixture of hexane and acetone.

6.3.3.4.2 Phase transfer of iron oxide nanoparticles to water by PF127 (depicted as PF127 SPIOs)

In a typical procedure, poloxamer (200 mg) was dissolved in 8 mL chloroform and 200 μL SPIO suspension in hexane was added. The suspension was shortly stirred, and 2 mL water were added. Chloroform was slowly evaporated under reduced pressure (27 °C) and the particles were readily dispersible in water. After the

addition of 60 mL water, particles were centrifuged (4800 x *g*, 25 °C, 120 min) and washed 2 times with water.

6.3.3.4.3 Preparation of crosslinked polymer coating on iron oxide nanoparticles (depicted as PF127DA SPIOs) without pG-SH

200 mg of PF127DA was diluted in 8 mL chloroform and 200 μL SPIO stock solution in hexane was added. To this suspension, 2 mL of water were added, and the suspension was gently mixed, and vacuum treated to remove chloroform. After that, 0.5 % I2959 was added to reach 10 % of final solution (0.05 %). Samples were purged with argon for 15 min and incubated for 30 min at RT. Afterwards, samples were treated by UV light (365 nm) for 15 min under aluminum folium and washed (4800 x *g*, 25 °C, 120 min). Washing was repeated once more.

6.3.3.4.4 Preparation of crosslinked polymer coating on iron oxide nanoparticles with pG-SH

In a typical procedure, poloxamer PF127DA (200 mg) was dissolved in 8 mL chloroform and 200 μL SPIO suspension in hexane was added. The suspension was shortly stirred, and 2 mL water was added. Chloroform was slowly evaporated under reduced pressure (27 °C) and the particles were readily dispersible in water. For evaluation of influence of thiol to acrylate ratio on swelling of particles, samples were split into 3 glass containers (1000 μL each) and in each well various amounts of pG-SH were added to reach pG-SH to PF127DA molar ratios of 1:10, 1:20, 1:30 or 1:40 and pH was set to > 8 by addition of 2 M NaOH. Then DTT (1 eq. to pG-SH) was added, and the reaction proceeded for 30 min and after that 30 μL of HEA and samples were further incubated for 30 min. After the addition of 60 mL water, particles were centrifuged (4800 x *g*, 25 °C, 120 min) and washed 2 times with water. For further experiments, thiol to acrylate ratio of 1:20 was used.

6.3.3.4.5 Preparation of empty nanogels and micelles

Empty PF127 and PF127DA micelles and empty PF127DApG nanogels were prepared following the same procedure as described above, with the exception that pure hexane without SPIOs was added to the chloroform before the evaporation step. Here, washing steps were done by dialysis (MWCO of 100000 g/mol).

6.3.3.4.6 Stability studies

Several parameters were varied to examine their influence on swelling/deswelling and/or aggregation by dynamic light scattering:

- influence of temperature: at 4 °C, 25 °C, 37 °C and 46 °C in water;
- influence of pH value: pH 5, pH 7.4 and pH 10. pH value was adjusted by addition of NaOH/HCl. These measurements were done at 25 °C if not stated otherwise;
- influence of salt valence and concentration: 0.01 M, 0.1 M and 1 M salt solutions of NaCl and calcium chloride were evaluated at pH 7. These measurements were done at 25 °C if not stated otherwise.

Further, the stability of particles was evaluated in biological mediums, namely in PBS with and without 1 mg/mL urea. After incubation at 37 °C, the transmission was analyzed by UV-Vis (300 cm^{-1} – 700 cm^{-1}). Transmission at 400 cm^{-1} was taken for analysis of stability.

6.3.3.5 Preparation of Fc dectin-1 coated gold nanoparticles (GNPs)

6.3.3.5.1 Decoration of GNPs with carboxyl groups (pG GNPs)

Firstly, the optimal concentration of polymer to stabilize GNPs was determined. 2 mL of 30 nm citrate coated GNP were centrifuged for 30 min, 4500 x *g* at 4 °C. After that, 1800 µL of supernatant from each tube was discarded and sediments (400 µL) were combined in one tube with the addition of 400 µL water. 30 µL of the sample was transferred to a new container and 20 µL of polymer solution pG-COOH in water was added. After 18 h, 20 µL of the sample was transferred to 96

well plate and optical density was measured by multiplate reader Spark20M. Then, 20 μL of 20 % NaCl solution was added to the wells and optical density was recorded once again. The minimal concentration of polymer needed for the stabilization of particles was the one necessary to prevent the aggregation of nanoparticles visible as a blue shift of the maximum of absorption.

Coating of GNPs with optimal amounts of the polymer was as follows: 2 mL of 30 nm citrate coated GNP were centrifuged for 30 min, 4500 x *g* at 4 °C. After that, 1800 μL of supernatant from each tube was discarded and sediments (400 μL) were combined in one tube with the addition of 400 μL of water. To this suspension (800 μL) 533 μL of 0.04 mg/mL polymer solution in water was added. After 18 h at RT and in the dark, samples were washed by centrifugation 4500 x *g*, 30 min at 4 °C and supernatants were discarded. Samples were re-dispersed with water to 1 mL in total.

6.3.3.5.2 Conjugation of Fc dectin-1 to pG GNPs

50 μg of Fc dectin-1 was dissolved in 500 μL water and solvent was exchanged to 10 mM Na-acetate solution 8 (pH 5.2) using column. Protein concentration was set 50 μg/mL. 250 μL of the pG GNPs were transferred to a new tube. To this suspension, 18 μL of EDC ad 18 μL of NHS solution was added (EDC solution: 40 mg EDC in 0.45 μL water, NHS solution: 10 mg NHS dissolved in 0.45 μL water). GNPs were incubated with NHS/EDC solution for 10 min at RT. To this solution, 500 μL of the Fc dectin-1 solution was added and samples were incubated for 2 h at RT after which ethanoldiamine was added to concentration of 10 mM. Samples were washed by centrifugation and redispersed in running buffer for SPR (HEPES SPR buffer with 0.05 % of Tween 20).

6.3.4 Release studies

6.3.4.1 Release studies from nanogels prepared by self-assembly

For dye release studies, nanogels were incubated in PBS (pH 7.4) or in 0 mM, 10 mM, 50 mM, and 100 mM degassed DTT solution in PBS (pH 7.4) at 37 °C. After

determined time points samples were centrifuged, the supernatant was transferred to 96 well plates and concentration was estimated by multiplate reader Spark 20M, by measuring the absorbance at 560 cm^{-1}.

Because of the self-aggregation of the AmB, it was not possible to follow previously reported protocols of release studies using dialysis method. Therefore, drug release studies were done using Amberlite XAD16 resins for the extraction of free drug. Briefly, nanogels (200 μL) were diluted with degassed 1 x PBS, and 50 μL of DTT in PBS (to reach final 0 mM or 10 mM DTT total concentration) was added. pG-$BA_{10\%}$ and pG-$PA_{10\%}$ nanogels, AmB pure or Fungizone, were incubated over 50 mg Amberlite XAD16 resins at 37 °C with stirring (800 rpm) protected from light. At predetermined time points, (0 h, 4 h, 6 h, 18 h, 24 h, 48 h, and 72 h) 50 μL aliquots were taken and replaced with fresh DTT solution in PBS. Aliquots were further diluted with 250 μL PBS, and 75 μL of this solution was added to 1425 μL of 50 : 50 (v/v) MeOH : DMSO solution, filtered and analyzed using previously described HPLC method. The determined remaining drug in the suspension was subtracted from the starting drug amount in nanogels to obtain the amount of released drug, considering the dilution factor.

6.3.4.2 Release studies from nanogels prepared by nanoprecipitation for drug loading by "breathing-in" strategy

Empty nanogels were diluted in PBS to 3 mg/mL and placed in 96 well plates. DTT solution in PBS was added until final concentrations of 10 mM, 1 mM, 0.1 mM and 0 mM were reached. After selected time points, the absorbance at 600 nm was measured by a microplate reader Spark 20M.

Drug release from ITZ nanogels was analyzed similarly. Here, samples were placed in Eppendorf tubes and centrifuged (500 x g, 5 min) after selected time points. Amount of drug in the supernatant was determined by fluorescent measurements.

6.3.5 Cytocompatibility studies

6.3.5.1 Cytotoxicity of nanogels prepared by self-assembly towards Vero kidney cells and red blood cells (RBC) of AmB loaded nanogels

Blood samples (buffy coats) were delivered from Bavarian Red Cross (Blood donor service, German Red Cross, Wiesentheid) with the written informed consent of blood donor. Buffy coats belonged to the healthy donors and were centrifuged 4 times (1000 x *g*, 4 °C, 5 min) to eliminate blood plasma and proteins and washed with isotonic saline solution. Then, samples were subsequently diluted to 1:20 in isotonic saline (v/v). Further, AmB solution, Fungizone or nanogel suspension (20 µl) in AmB concentration of 100 µg/mL for AmB loaded nanogels as determined by UV-Vis and 1 mg/mL for empty nanogels were introduced to the erythrocytes (40 µl) in 96-well plate and incubated at 37 °C, 5 % CO_2 for 2 h or 24 h. As positive control was taken non-ionic detergent 0.1 % Triton X-100 solution (for 100 % of lysis) and blood with PBS was used as a negative control (for 0 % of lysis). The intensity of absorbance of the supernatant of the blood suspension was measured at 450 nm. Percent of RBC lysis was calculated as described by Evas et al.[273]

Cell toxicity tests were further done on kidney Vero kidney cells (generously delivered from Institute of Oncology, Würzburg) incubated at 37 °C, 5 % CO_2 in DMEM medium supplemented with 10 % fetal calf serum (FCS) and 1 % penicillin-streptomycin solution (P/S). Cells were seeded in 96 well plates (50000 cells/well), and after 24 h, the medium was changed with the medium containing AmB containing samples, empty nanogels (1 mg/mL) or 5 % DMSO. Since no high cytotoxicity was observed after 24 h excluding AmB pure sample, incubation proceeded for 48 h. Metabolically active cells were determined by the CellTiter-Glo® Luminescent Cell Viability Assay (Promega, Germany). After incubation of cells with the nanogels, the incubation medium was replaced with the CellTiter-Glo® reagent medium solution (50 %, v/v). The cells were incubated 10 min at RT with occasional shaking the plate, and the luminescence was recorded on Tecan Spectra Fluor Plus photometer (Tecan, Crailsheim, Germany).

Medium only with an addition of 50 % (v/v) CellTiter-Glo reagent® was used as blank. Samples were analyzed in four replicates.

6.3.5.2 Cytotoxicity of nanogels towards Vero kidney cells, liver cells and red blood cells (RBC) of ITZ loaded nanogels prepared by nanoprecipitation with drug loading by "breathing-in" strategy

Blood samples (buffy coats) were delivered from Bavarian Red Cross (Blood donor service, German Red Cross, Wiesentheid) with the written informed consent of blood donor. Buffy coats belonged to the healthy donors and were centrifuged 4 times (1000 x *g*, 4 °C, 5 min) to eliminate blood plasma and proteins and washed with isotonic saline solution. Then, samples were subsequently diluted to 1:20 in isotonic saline (v/v). 40 µL of RBC suspension was transferred to 96 well plates and 20 µL of ITZ nanogels or free drug was added. As positive control was taken non-ionic detergent 0.1 % Triton X-100 solution (for 100 % of lysis) and blood with PBS was used as a negative control (for 0 % of lysis). The absorbance of the supernatant of the blood suspension was measured at 576 nm. Percent of RBC lysis was calculated as described by Evas et al.[273]

6.3.5.3 Cytotoxicity studies of SPIOs nanoparticles

Toxicity of polymer-coated SPIO was assessed towards fibroblasts cells L929. Cells (2.5×10^4 per well, 500 µL medium DMEM 1 X GlutaMAX with the addition of 10 % FBS, 1 % P/S) were seeded in quadruplicates in 96 well plates. After 24 h, the medium was aspirated and replaced with fresh medium and containing iron oxide particles diluted in PBS. Cells were incubated with iron oxides for 48 h and viability was tested by CellTiter Glo assay.

6.3.6 Interaction of nanogels with mammalian cells

6.3.6.1 Interaction of endothelial cells with nanogels prepared by inverse miniemulsion

Human dermal microvascular endothelium (HMEC-1, ATCC) were cultivated in

MCDB 131 media (Thermo Fischer Scientific, Germany) with additional 10 ng/mL epidermal growth factor (EGF), 1 µg/mL hydrocortisone, 10 mM glutamine, fetal calf serum (FCS) (Thermo Fischer Scientific, Germany) to a final concentration of 10% and penicillin/streptavidin solution to a final concentration of 1 %. 5×10^5 cells/well in 2 mL of medium were seeded in 6 well-plate were with 22 mm sterilized coverslips. After 24 h, 100 µL of nanogels with the concentration of 1×10^{10} p/mL was added to the cells and incubated for further 24 h. After that, samples were fixed and stained with Hoechst 33258 (Life Technologies GmbH, Germany) and tetramethyl rhodamine B isocyanate labeled phalloidin (Life Technologies GmbH, Germany) following standard procedures. Samples were made in duplicates.

6.3.6.2 Interaction of Caco-2 cells with nanogels prepared by inverse miniemulsion

Caco-2 (HTB-37™, ATCC) were seeded in 6 well-plate with 22 mm sterilized coverslips to have 1×10^5 c/well with 2 mL Eagle's Minimum Essential Medium (EMEM) (ATCC) with additional 10 % fetal calf serum (FCS) (Thermo Fischer Scientific, Germany) and Pen/Strep to a final concentration of 1 %. After 24 h, 100 µL of nanogels with the concentration of 1×10^{10} p/mL was added to the cells and incubated for further 24 h. After that, samples were fixed and stained same as endothelial cells. Samples were made in duplicates.

6.3.7 Interaction of nanoparticles with fungal cells

6.3.7.1.1 Fungal organisms and inoculum preparation

Clinical isolate *Aspergillus fumigatus* wild type ATCC46645 strain or GFP positive AfS148 strain[150] were used throughout this thesis.[274] Fungi were grown on minimal medium agar at 37 °C for 3 to 4 days until sporulation and were harvested using 0.9 % (w/v) NaCl and 0.05 % (v/v) Tween 20 solution. Spores were filtered through a cell strainer, centrifuged (4000 x *g*) at 4 °C for 10 min and re-dispersed in 0.9 % NaCl 0.05 % Tween 20 solution and stored at 4 °C until use.

6.3.7.2 Uptake of nanoparticles

6.3.7.2.1 Interaction with nanogels prepared by inverse miniemulsion

GFP labeled *A. fumigatus* (400 µL, 1×10^6 s/mL) was incubated in RPMI 1640 medium (Fisher Scientific, Germany) with the addition of 10 % FBS at 37 °C, 5 % CO_2 with 100 µL of 0.8×10^{11} p/mL fluorescence dye-labeled nanogels as determined by NTA. After incubation, samples were fixed in 1 % paraformaldehyde solution for 10 min and washed with PBS. Before imaging, samples were transferred on the microscopic slide coated with a thin layer of poly-lysine. The fungal wall was labeled by Calcofluor White (Fluorescence Brightener, Sigma Aldrich, Germany), which was dissolved in water to the concentration of 1 mg/mL with 100 µL of 100 mg/mL potassium hydroxide. Samples were sealed with Entellan® (SigmaAldrich, Germany) and analyzed by confocal and fluorescence microscopy.

6.3.7.2.2 Interaction with ORO loaded nanogels prepared by self-assembly

To monitor the nanogel uptake by the fungus in its various stages, the samples were visualized by confocal laser scanning microscope. In these experiments, *A. fumigatus* (400 µL, 1×10^4 s/mL) was pre-incubated in RPMI 1640 medium at 37 °C for 24 h to form mycelium. After that, the medium was changed with medium containing fluorescently labeled nanogels, empty nanogels, or PBS. After incubation for 24 h, samples were fixed in 1 % paraformaldehyde solution for 5 min and washed with PBS. The fungal cell wall was labeled by calcofluor white, which was dissolved in water to the concentration of 1 mg/mL with the addition of 20 µL of 100 mg/mL potassium hydroxide. Before imaging, samples were transferred on the microscopic slide coated with a thin layer of poly-n-lysine. Coverslips were sealed with nail polish and samples were visualized using excitation at 365 nm and 488 nm for calcofluor white and ORO, respectively. Free dye was dissolved in DMSO and water to the same concentration as nanogels. For monitoring passive uptake of ORO loaded nanogels, incubation of fungus with nanogels proceeded at 4 °C.

6.3.7.2.3 Interaction with nanogels prepared by nanoprecipitation

To monitor the nanogel uptake by the fungus in its various stages, the samples were visualized by CLSM. In these experiments, *A. fumigatus* (400 µL, 1 x 10^4 s/mL) was pre-incubated in RPMI 1640 medium at 37 °C for 24 h to form mycelium. After that, the medium was changed with medium containing fluorescently labeled nanogels, empty nanogels, or PBS. After incubation for 24 h, samples were fixed in 1 % paraformaldehyde solution for 5 min and washed with PBS. The fungal cell wall was labeled by calcofluor white, which was dissolved in water to the concentration of 1 mg/mL with the addition of 20 µL of 100 mg/mL potassium hydroxide. Before imaging, samples were transferred on the microscopic slides coated with a thin layer of poly-n-lysine. Coverslips were sealed with nail polish and samples were visualized using excitation at 365 nm and 488 nm for calcofluor white and ORO/Rh6g, respectively. Free dye was dissolved in DMSO and water to the same concentration as nanogels. For monitoring passive uptake of ORO loaded nanogels, incubation of fungus with nanogels proceeded at 4 °C. For live-imaging, fungi were incubated in Petri dishes with a glass bottom in the chamber at 37 °C.

6.3.7.2.4 Interaction with SPIOs

Interaction of SPIOs with fungi was evaluation relatively by measuring the iron uptake by *A. fumigatus* by SEM/EDX. In this case, biofilm was grown on the sterilized silica wafer. Briefly, 100 µL of 1 x 10^6 s/mL were pre-grown in RPMI 1640 medium for 6 h in 24 well plates where silica wafer was previously placed with 0.4 mL medium. Then, 20 µL of 2 mM PF127DApG nanoparticles were added and samples were further incubated for 16 h at 37 °C, 5 % CO_2. As a control,the same volume of PBS was added. Samples were further prepared for EDX/SEM imaging, as explained in the characterization section. Interaction of SPIOs with fungal biofilm was also evaluated by determination of iron concentration in biofilms. *A. fumigatus* was seeded into flat-bottomed polystyrene 96 well plate. Biofilms were formed by adding 100 µL of 2 · 10^5 s/mL spore suspension in RPMI 1640 medium to 100 µL of SPIOs in the same medium for different times (0 + 24 h, 0 + 48 h,

24 + 24 h). Wells were then washed gently with PBS and fixed with 4 % paraformaldehyde and left to air dry. Biofilm was air-dried and incubated with 100 µL 65 % HNO_3 for 24 h. The analysis was done in quadruplicates. The concentration of iron in each sample was evaluated by the 1,10-phenanthroline method as described previously.

6.3.7.3 Antifungal effects of nanoparticles

6.3.7.3.1 Determination of minimal inhibitory concentration (MIC)

MIC determination was determined using the microdilution broth method.[275] The conidial inoculum was prepared in RPMI 1640 medium or minimal medium and quantified to achieve a final concentration of $2 \cdot 10^5$ s/mL. 100 µL of inoculum was transferred to 96 flat-bottom well plates and mixed with 100 µL linearly diluted drug-loaded, drug-free nanogels, free drug or PBS. Incubation proceeded at 37 °C, 5 % CO_2 for 48 h. Drugs were previously dissolved in DMSO to the concentration of 1 mg/mL and further diluted with the medium. MIC was defined as the lowest drug concentrations that caused complete inhibition of growth as observed visually under the microscope. Testing was performed in triplicates.

6.3.7.3.2 Biofilm formation and quantification

A. fumigatus was seeded into flat-bottomed polystyrene 96 well plate. Biofilms were formed by adding 100 µL of $2 \cdot 10^5$ s/mL spore suspension in RPMI 1640 medium to 100 µL of drug or drug-loaded nanogels in the same medium for different time points. Wells were then washed gently with PBS and fixed with 4 % paraformaldehyde and left to air dry.[9]

Biofilm biomass was quantified using a modified version of a protocol developed by of O'Toole et al. and Mowat et al.[9, 276] Briefly, after biofilm was air-dried, it was incubated with 100 µL of 0.5 % (w/v) crystal violet solution for 10 min and rinsed extensively with tapping water. Samples were left to air dry and were incubated with 100 µL 95 % ethanol for 5 min with gentle shaking until crystals were dissolved. Supernatants were transferred to the new 96 well plates and absorbance

was measured at 570 nm by Tecan multiplate reader. The test was done in triplicates.

6.3.7.3.3 Qualitative analysis of biofilm hydrophobicity by microsphere assay

100 μL of $2 \cdot 10^5$ s/mL spore suspension of *A. fumigatus* was mixed with 200 μL RPMI 1640 medium and incubated for 24 h at 37 °C. After that, the medium was exchanged to contain 1 mg/mL empty or of AmB loaded nanogels (2 x MIC) and incubated for further 24 h. After that, samples were washed with 0.2 M KNO_3 solution (pH 6.5) and treated with 1:1 v/v suspension of 0.5×10^9 particles/mL fluorescent orange sulphate-modified latex microspheres (0.5 μm, Sigma Aldrich, Germany) in the potassium nitrate solution as described previously[177] and incubated for 30 min at RT. After that, biofilms were washed and analyzed by fluorescent microscopy (exc. 450-490 nm, em. 500-550 nm, Blue ZEN Software 2.3 Lite).

6.3.8 Co-incubation of nanogels with fungi and mammalian cells

6.3.8.1 Co-incubation with nanogels prepared by inverse miniemulsion

The fungal suspension (*A. fumigatus* GFP positive AfS148 strain[150], 100 μL, $1 \cdot 10^6$ s/mL) were incubated 11 h at 37 °C in HEPES medium in 12 well chamber microscopic slides. Then, nanogels suspension (50 μL, 0.5×10^{11} p/mL) and mouse neutrophils (100 μL, $1 \cdot 10^5$ c/mL) were added and samples were incubated for further 3 h. Five types of samples were taken for analysis, fungus without neutrophils and nanogels, a fungus with nanogels and without cells, a fungus with nanogels and cells, cells with nanogels and without fungus and cells without fungus and nanogels. After that, samples were washed 2 times with PBS, fixed with 4 % paraformaldehyde and washed again twice with PBS. Cell core of the neutrophils was labeled with Hoechst 3886. Samples were washed and mounted with Fluoromount™ Aqueous Mounting Medium (Sigma Aldrich, Germany). Samples were visualized with confocal laser scanning microscopy.

Bibliography

1. Plenty of room; revisited. *Nature Nanotechnology* **2009,** *4*, 781.
2. Maynard, A. D. In *Nanotechnologies: Overview and Issues*, Nanotechnology – Toxicological Issues and Environmental Safety and Environmental Safety, Dordrecht, 2007//; Simeonova, P. P.; Opopol, N.; Luster, M. I., Eds. Springer Netherlands: Dordrecht, 2007; pp 1-14.
3. Wang, E. C.; Wang, A. Z., Nanoparticles and their applications in cell and molecular biology. *Integrative biology : quantitative biosciences from nano to macro* **2014,** *6* (1), 9-26.
4. Vance, M. E.; Kuiken, T.; Vejerano, E. P.; McGinnis, S. P.; Hochella, M. F., Jr.; Rejeski, D.; Hull, M. S., Nanotechnology in the real world: Redeveloping the nanomaterial consumer products inventory. *Beilstein Journal of Nanotechnology* **2015,** *6*, 1769-1780.
5. Matteucci, F.; Giannantonio, R.; Calabi, F.; Agostiano, A.; Gigli, G.; Rossi, M., Deployment and exploitation of nanotechnology nanomaterials and nanomedicine. *AIP Conference Proceedings* **2018,** *1990* (1), 020001.
6. Taylor, E.; Webster, T. J., Reducing infections through nanotechnology and nanoparticles. *International journal of nanomedicine* **2011,** *6*, 1463-1473.
7. Alastruey-Izquierdo, A.; Cadranel, J.; Flick, H.; Godet, C.; Hennequin, C.; Hoenigl, M.; Kosmidis, C.; Lange, C.; Munteanu, O.; Page, I.; Salzer, H. J. F., Treatment of Chronic Pulmonary Aspergillosis: Current Standards and Future Perspectives. *Respiration* **2018,** *96* (2), 159-170.
8. Thompson, G. R.; Patterson, T. F., Pulmonary Aspergillosis: Recent Advances. *Semin Respir Crit Care Med* **2011,** *32* (06), 673-681.
9. Mowat, E.; Butcher, J.; Lang, S.; Williams, C.; Ramage, G., Development of a simple model for studying the effects of antifungal agents on multicellular communities of Aspergillus fumigatus. *J. Med. Microbiol.* **2007,** *56* (9), 1205-1212.
10. Dinand, V.; Anjan, M.; Oberoi, J. K.; Khanna, S.; Yadav, S. P.; Wattal, C.; Sachdeva, A., Threshold of galactomannan antigenemia positivity for early diagnosis of invasive aspergillosis in neutropenic children. *J. Microbiol. Immunol. Infect.* **2016,** *49* (1), 66-73.
11. Moura, S.; Cerqueira, L.; Almeida, A., Invasive pulmonary aspergillosis: current diagnostic methodologies and a new molecular approach. *Eur. J. Clin. Microbiol. Infect. Dis.* **2018,** *37* (8), 1393-1403.
12. Cornely, O. A.; Koehler, P.; Arenz, D.; C. Mellinghoff, S., EQUAL Aspergillosis Score 2018: An ECMM score derived from current guidelines to measure QUALity of the clinical management of invasive pulmonary aspergillosis. *Mycoses* **2018,** *61* (11), 833-836.
13. Kaur, S.; Singh, S., Biofilm formation by Aspergillus fumigatus. *Med. Mycol.* **2013,** *52* (1), 2-9.
14. Cadena, J.; Thompson, G. R.; Patterson, T. F., Invasive Aspergillosis: Current Strategies for Diagnosis and Management. *Infectious Disease Clinics of North America* **2016,** *30* (1), 125-142.
15. Voltan, A. R.; Quindós, G.; Alarcón, K. P. M.; Fusco-Almeida, A. M.; Mendes-Giannini, M. J. S.; Chorilli, M., Fungal diseases: could nanostructured drug delivery systems be a novel paradigm for therapy? *International journal of nanomedicine* **2016,** *11*, 3715-3730.

16. Kabanov, A. V.; Vinogradov, S. V., Nanogels as Pharmaceutical Carriers: Finite Networks of Infinite Capabilities. *Angew. Chem. Int. Ed.* **2009,** *48* (30), 5418-5429.
17. Zilkowski, I.; Theodorou, I.; Albrecht, K.; Ducongé, F.; Groll, J., Subtle changes in network composition impact the biodistribution and tumor accumulation of nanogels. *Chem. Commun.* **2018,** *54* (83), 11777-11780.
18. Groll, J.; Singh, S.; Albrecht, K.; Moeller, M., Biocompatible and degradable nanogels via oxidation reactions of synthetic thiomers in inverse miniemulsion. *J. Polym. Sci., Part A: Polym. Chem.* **2009,** *47* (20), 5543-5549.
19. Kainthan, R. K.; Janzen, J.; Levin, E.; Devine, D. V.; Brooks, D. E., Biocompatibility Testing of Branched and Linear Polyglycidol. *Biomacromolecules* **2006,** *7* (3), 703-709.
20. Smriti, S., Biocompatible and Biodegradable Nanogels and Hydrogels for Protein/Peptide Delivery. **2013**.
21. Charvalos, E.; Tzatzarakis, M. N.; Van Bambeke, F.; Tulkens, P. M.; Tsatsakis, A. M.; Tzanakakis, G. N.; Mingeot-Leclercq, M. P., Water-soluble amphotericin B-polyvinylpyrrolidone complexes with maintained antifungal activity against Candida spp. and Aspergillus spp. and reduced haemolytic and cytotoxic effects. *J. Antimicrob. Chemother.* **2006,** *57* (2), 236-44.
22. Higa, L. H.; Schilrreff, P.; Perez, A. P.; Morilla, M. J.; Romero, E. L., The Intervention of Nanotechnology Against Epithelial Fungal Diseases. *Journal of Biomaterials and Tissue Engineering* **2013,** *3* (1), 70-88.
23. Paulo, C. S. O.; Vidal, M.; Ferreira, L. S., Antifungal Nanoparticles and Surfaces. *Biomacromolecules* **2010,** *11* (10), 2810-2817.
24. Yu, Y.; Albrecht, K.; Groll, J.; Beilhack, A., Innovative therapies for invasive fungal infections in preclinical and clinical development. *Expert Opinion on Investigational Drugs* **2020**, 1-11.
25. Latgé, J.-P., The pathobiology of Aspergillus fumigatus. *Trends Microbiol.* **2001,** *9* (8), 382-389.
26. von Lilienfeld-Toal, M.; Wagener, J.; Einsele, H.; Cornely, O. A.; Kurzai, O., Invasive Fungal Infection. *Dtsch Arztebl International* **2019,** *116* (16), 271-278.
27. Hohl, T. M.; Feldmesser, M., Aspergillus fumigatus: Principles of Pathogenesis and Host Defense. *Eukaryot. Cell* **2007,** *6* (11), 1953-1963.
28. Leroy, P.; Smismans, A.; Seute, T., Invasive Pulmonary and Central Nervous System Aspergillosis After Near-Drowning of a Child: Case Report and Review of the Literature. *Pediatrics* **2006,** *118* (2), e509-e513.
29. Gulati, M.; Bajad, S.; Singh, S.; Ferdous, A. J.; Singh, M., Development of liposomal amphotericin B formulation. *J. Microencaps.* **1998,** *15* (2), 137-151.
30. Rivero-Menendez, O.; Alastruey-Izquierdo, A.; Mellado, E.; Cuenca-Estrella, M., Triazole Resistance in Aspergillus spp.: A Worldwide Problem? *Journal of fungi (Basel, Switzerland)* **2016,** *2* (3), 21.
31. Walker, L. A.; Gow, N. A. R.; Munro, C. A., Fungal echinocandin resistance. *Fungal genetics and biology : FG & B* **2010,** *47* (2), 117-126.
32. Heinz, W. J.; Einsele, H., Caspofungin for treatment of invasive aspergillus infections. *Mycoses* **2008,** *51* (s1), 47-57.
33. Nivoix, Y.; Letscher-Bru, V.; Moghaddam, A.; Lioure, B.; Fohrer, C.; Bergerat, J.-P.; Bilger, K.; Natarajan-Amé, S.; Herbrecht, R.; Lutun, P.; Marcellin, L.; Launoy, A.; Freys, G.; Velten, M., Factors Associated with Overall and Attributable Mortality in Invasive Aspergillosis. *Clin. Infect. Dis.* **2008,** *47* (9), 1176-1184.
34. Basic & Clinical Pharmacology, 11th Edition. *Journal of Pharmacy Technology* **2010,** *26* (1), 45-45.

35. Soliman, G. M., Nanoparticles as safe and effective delivery systems of antifungal agents: Achievements and challenges. *Int. J. Pharm.* **2017,** *523* (1), 15-32.
36. Kim, K.-J.; Sung, W. S.; Suh, B. K.; Moon, S.-K.; Choi, J.-S.; Kim, J. G.; Lee, D. G., Antifungal activity and mode of action of silver nano-particles on Candida albicans. *BioMetals* **2009,** *22* (2), 235-242.
37. Hwang, I.-s.; Lee, J.; Hwang, J. H.; Kim, K.-J.; Lee, D. G., Silver nanoparticles induce apoptotic cell death in Candida albicans through the increase of hydroxyl radicals. *The FEBS Journal* **2012,** *279* (7), 1327-1338.
38. Ahmad, T.; Wani, I. A.; Lone, I. H.; Ganguly, A.; Manzoor, N.; Ahmad, A.; Ahmed, J.; Al-Shihri, A. S., Antifungal activity of gold nanoparticles prepared by solvothermal method. *Mater. Res. Bull.* **2013,** *48* (1), 12-20.
39. Boswell, G. W.; Buell, D.; Bekersky, I., AmBisome (Liposomal Amphotericin B): A Comparative Review. *The Journal of Clinical Pharmacology* **1998,** *38* (7), 583-592.
40. Hamill, R. J., Amphotericin B Formulations: A Comparative Review of Efficacy and Toxicity. *Drugs* **2013,** *73* (9), 919-934.
41. José Ramón Azanza, B. S., Joana Reis, Liposomal formulations of amphotericin B: differences according to the scientific evidence. *Rev Esp Quimioter* **2015,** *28* (6), 275-281.
42. Nikoomanesh, F.; Roudbarmohammadi, S.; Khoobi, M.; Haghighi, F.; Roudbary, M., Design and synthesis of mucoadhesive nanogel containing farnesol: investigation of the effect on HWP1, SAP6 and Rim101 genes expression of Candida albicans in vitro. *Artificial Cells, Nanomedicine, and Biotechnology* **2019,** *47* (1), 64-72.
43. Winnicka, K.; Sosnowska, K.; Wieczorek, P.; Sacha, P. T.; Tryniszewska, E., Poly(amidoamine) Dendrimers Increase Antifungal Activity of Clotrimazole. *Biol. Pharm. Bull.* **2011,** *34* (7), 1129-1133.
44. Svenson, S., The dendrimer paradox – high medical expectations but poor clinical translation. *Chem. Soc. Rev.* **2015,** *44* (12), 4131-4144.
45. Vicario-de-la-Torre, M.; Forcada, J., The Potential of Stimuli-Responsive Nanogels in Drug and Active Molecule Delivery for Targeted Therapy. *Gels* **2017,** *3* (2), 16.
46. Cao, Z.; Ziener, U., Synthesis of nanostructured materials in inverse miniemulsions and their applications. *Nanoscale* **2013,** *5* (21), 10093-10107.
47. Meng, F.; Zhong, Y.; Cheng, R.; Deng, C.; Zhong, Z., pH-sensitive polymeric nanoparticles for tumor-targeting doxorubicin delivery: concept and recent advances. *Nanomedicine* **2014,** *9* (3), 487-499.
48. Cheng, R.; Meng, F.; Deng, C.; Klok, H.-A.; Zhong, Z., Dual and multi-stimuli responsive polymeric nanoparticles for programmed site-specific drug delivery. *Biomaterials* **2013,** *34* (14), 3647-3657.
49. Miao, C.; Li, F.; Zuo, Y.; Wang, R.; Xiong, Y., Novel redox-responsive nanogels based on poly(ionic liquid)s for the triggered loading and release of cargos. *RSC Advances* **2016,** *6* (4), 3013-3019.
50. Kim, T. K.; Eberwine, J. H., Mammalian cell transfection: the present and the future. *Anal. Bioanal. Chem.* **2010,** *397* (8), 3173-3178.
51. Pócsi, I.; Prade, R. A.; Penninckx, M. J., Glutathione, Altruistic Metabolite in Fungi. In *Adv. Microb. Physiol.*, Academic Press: 2004; Vol. 49, pp 1-76.
52. Dai Hai, N.; Jong Hoon, C.; Yoon Ki, J.; Ki Dong, P., Disulfide-crosslinked heparin-pluronic nanogels as a redox-sensitive nanocarrier for intracellular protein delivery. *J. Bioact. Compatible Polym.* **2011,** *26* (3), 287-300.
53. Mura, S.; Nicolas, J.; Couvreur, P., Stimuli-responsive nanocarriers for drug delivery. *Nature Materials* **2013,** *12*, 991.

54. Li, D.; van Nostrum, C. F.; Mastrobattista, E.; Vermonden, T.; Hennink, W. E., Nanogels for intracellular delivery of biotherapeutics. *J. Controlled Release* **2017,** *259*, 16-28.
55. Singh, S.; Zilkowski, I.; Ewald, A.; Maurell-Lopez, T.; Albrecht, K.; Möller, M.; Groll, J., Mild Oxidation of Thiofunctional Polymers to Cytocompatible and Stimuli-Sensitive Hydrogels and Nanogels. *Macromol. Biosci.* **2013,** *13* (4), 470-482.
56. Zilkowski, I.; Ziouti, F.; Schulze, A.; Hauck, S.; Schmidt, S.; Mainz, L.; Sauer, M.; Albrecht, K.; Jundt, F.; Groll, J., Nanogels Enable Efficient miRNA Delivery and Target Gene Downregulation in Transfection-Resistant Multiple Myeloma Cells. *Biomacromolecules* **2019,** *20* (2), 916-926.
57. Ágoston, V.; Cemazar, M.; Kaján, L.; Pongor, S., Graph-representation of oxidative folding pathways. *BMC Bioinformatics* **2005,** *6* (1), 19.
58. Navath, R. S.; Wang, B.; Kannan, S.; Romero, R.; Kannan, R. M., Stimuli-responsive star poly(ethylene glycol) drug conjugates for improved intracellular delivery of the drug in neuroinflammation. *Journal of controlled release : official journal of the Controlled Release Society* **2010,** *142* (3), 447-456.
59. Adamo, G.; Grimaldi, N.; Campora, S.; Bulone, D.; Bondì, M. L.; Al-Sheikhly, M.; Sabatino, M. A.; Dispenza, C.; Ghersi, G., Multi-Functional Nanogels for Tumor Targeting and Redox-Sensitive Drug and siRNA Delivery. *Molecules* **2016,** *21* (11), 1594.
60. Dunn, S. S.; Tian, S.; Blake, S.; Wang, J.; Galloway, A. L.; Murphy, A.; Pohlhaus, P. D.; Rolland, J. P.; Napier, M. E.; DeSimone, J. M., Reductively Responsive siRNA-Conjugated Hydrogel Nanoparticles for Gene Silencing. *J. Am. Chem. Soc.* **2012,** *134* (17), 7423-7430.
61. Turner, J. J.; Jones, S.; Fabani, M. M.; Ivanova, G.; Arzumanov, A. A.; Gait, M. J., RNA targeting with peptide conjugates of oligonucleotides, siRNA and PNA. *Blood Cells, Molecules, and Diseases* **2007,** *38* (1), 1-7.
62. Mok, H.; Park, T. G., PEG-Assisted DNA Solubilization in Organic Solvents for Preparing Cytosol Specifically Degradable PEG/DNA Nanogels. *Bioconj. Chem.* **2006,** *17* (6), 1369-1372.
63. Novo, L.; van Gaal, E. V. B.; Mastrobattista, E.; van Nostrum, C. F.; Hennink, W. E., Decationized crosslinked polyplexes for redox-triggered gene delivery. *J. Controlled Release* **2013,** *169* (3), 246-256.
64. Averick, S. E.; Paredes, E.; Irastorza, A.; Shrivats, A. R.; Srinivasan, A.; Siegwart, D. J.; Magenau, A. J.; Cho, H. Y.; Hsu, E.; Averick, A. A.; Kim, J.; Liu, S.; Hollinger, J. O.; Das, S. R.; Matyjaszewski, K., Preparation of Cationic Nanogels for Nucleic Acid Delivery. *Biomacromolecules* **2012,** *13* (11), 3445-3449.
65. Shrivats, A. R.; McDermott, M. C.; Klimak, M.; Averick, S. E.; Pan, H.; Matyjaszewski, K.; Mishina, Y.; Hollinger, J. O., Nanogel-Mediated RNAi Against Runx2 and Osx Inhibits Osteogenic Differentiation in Constitutively Active BMPR1A Osteoblasts. *ACS Biomaterials Science & Engineering* **2015,** *1* (11), 1139-1150.
66. Kim, H.; Kim, B.; Lee, C.; Ryu, J. L.; Hong, S.-J.; Kim, J.; Ha, E.-J.; Paik, H.-j., Redox-responsive biodegradable nanogels for photodynamic therapy using Chlorin e6. *Journal of Materials Science* **2016,** *51* (18), 8442-8451.
67. Yang, H.; Wang, Q.; Huang, S.; Xiao, A.; Li, F.; Gan, L.; Yang, X., Smart pH/Redox Dual-Responsive Nanogels for On-Demand Intracellular Anticancer Drug Release. *ACS Appl. Mater. Interfaces* **2016,** *8* (12), 7729-7738.
68. Li, P.; Luo, Z.; Liu, P.; Gao, N.; Zhang, Y.; Pan, H.; Liu, L.; Wang, C.; Cai, L.; Ma, Y., Bioreducible alginate-poly(ethylenimine) nanogels as an antigen-delivery system

robustly enhance vaccine-elicited humoral and cellular immune responses. *J. Controlled Release* **2013,** *168* (3), 271-279.
69. Chen, L.; Xue, Y.; Xia, X.; Song, M.; Huang, J.; Zhang, H.; Yu, B.; Long, S.; Liu, Y.; Liu, L.; Huang, S.; Yu, F., A redox stimuli-responsive superparamagnetic nanogel with chemically anchored DOX for enhanced anticancer efficacy and low systemic adverse effects. *Journal of Materials Chemistry B* **2015,** *3* (46), 8949-8962.
70. Xue, Y.; Xia, X.; Yu, B.; Tao, L.; Wang, Q.; Huang, S.-W.; Yu, F., Selenylsulfide Bond-Launched Reduction-Responsive Superparamagnetic Nanogel Combined of Acid-Responsiveness for Achievement of Efficient Therapy with Low Side Effect. *ACS Appl. Mater. Interfaces* **2017,** *9* (36), 30253-30257.
71. Yang, H. Y.; Jang, M.-S.; Li, Y.; Lee, J. H.; Lee, D. S., Multifunctional and Redox-Responsive Self-Assembled Magnetic Nanovectors for Protein Delivery and Dual-Modal Imaging. *ACS Appl. Mater. Interfaces* **2017,** *9* (22), 19184-19192.
72. Hughes, J. P.; Rees, S.; Kalindjian, S. B.; Philpott, K. L., Principles of early drug discovery. *Br. J. Pharmacol.* **2011,** *162* (6), 1239-1249.
73. Tamargo, J.; Le Heuzey, J.-Y.; Mabo, P., Narrow therapeutic index drugs: a clinical pharmacological consideration to flecainide. *Eur. J. Clin. Pharmacol.* **2015,** *71* (5), 549-567.
74. Broe, M. E. D., Nephrotoxicity of drugs used in rheumatology: Analgesic nephropathy. *Oxford, UK: Oxford University Press* **2013**, 371-384.
75. Maziasz, T.; Kadambi, V. J.; Silverman, L.; Fedyk, E.; Alden, C. L., Predictive Toxicology Approaches for Small Molecule Oncology Drugs. *Toxicol. Pathol.* **2010,** *38* (1), 148-164.
76. Haley, P. J., Small Molecule Immunomodulatory Drugs: Challenges and Approaches for Balancing Efficacy with Toxicity. *Toxicol. Pathol.* **2011,** *40* (2), 261-266.
77. Meanwell, N. A., Improving Drug Design: An Update on Recent Applications of Efficiency Metrics, Strategies for Replacing Problematic Elements, and Compounds in Nontraditional Drug Space. *Chem. Res. Toxicol.* **2016,** *29* (4), 564-616.
78. Li, L.; Sun, J.; He, Z., Deep Penetration of Nanoparticulate Drug Delivery Systems into Tumors: Challenges and Solutions. *Curr. Med. Chem.* **2013,** *20* (23), 2881-2891.
79. Najeh Maissar, K.; Rubiana Mara, M., Colloidal Polymeric Nanoparticles and Brain Drug Delivery. *Curr. Drug Del.* **2009,** *6* (3), 261-273.
80. Zhou, Y.; Kopeček, J., Biological rationale for the design of polymeric anti-cancer nanomedicines. *J. Drug Targeting* **2013,** *21* (1), 1-26.
81. Haladjova, E.; Toncheva-Moncheva, N.; Apostolova, M. D.; Trzebicka, B.; Dworak, A.; Petrov, P.; Dimitrov, I.; Rangelov, S.; Tsvetanov, C. B., Polymeric Nanoparticle Engineering: From Temperature-Responsive Polymer Mesoglobules to Gene Delivery Systems. *Biomacromolecules* **2014,** *15* (12), 4377-4395.
82. Stubenrauch, K.; Voets, I.; Fritz-Popovski, G.; Trimmel, G., pH and ionic strength responsive polyelectrolyte block copolymer micelles prepared by ring opening metathesis polymerization. *J. Polym. Sci., Part A: Polym. Chem.* **2009,** *47* (4), 1178-1191.
83. Cho, H.; Bae, J.; Garripelli, V. K.; Anderson, J. M.; Jun, H.-W.; Jo, S., Redox-sensitive polymeric nanoparticles for drug delivery. *Chem. Commun.* **2012,** *48* (48), 6043-6045.
84. Hickey, J. W.; Santos, J. L.; Williford, J.-M.; Mao, H.-Q., Control of polymeric nanoparticle size to improve therapeutic delivery. *J. Controlled Release* **2015,** *219*, 536-547.
85. Elsabahy, M.; Wooley, K. L., Design of polymeric nanoparticles for biomedical delivery applications. *Chem. Soc. Rev.* **2012,** *41* (7), 2545-2561.
86. Williford, J.-M.; Santos, J. L.; Shyam, R.; Mao, H.-Q., Shape control in engineering of

polymeric nanoparticles for therapeutic delivery. *Biomaterials Science* **2015,** *3* (7), 894-907.
87. Fröhlich, E., The role of surface charge in cellular uptake and cytotoxicity of medical nanoparticles. *International journal of nanomedicine* **2012,** *7*, 5577-5591.
88. Sakai, T. I., Tsutomu; Higaki, Megumu ; Akiyama, Goichi ; Tsuneoka, Hiroshi, Therapeutic Effect of Stealth-Type Polymeric Nanoparticles with Encapsulated Betamethasone Phosphate on Experimental Autoimmune Uveoretinitis. *Investigative Ophthalmology & Visual Science* **2011,** *52*, 1516-1521.
89. Salmaso, S.; Caliceti, P., Stealth Properties to Improve Therapeutic Efficacy of Drug Nanocarriers. *Journal of Drug Delivery* **2013,** *2013*, 19.
90. Owens, D. E.; Peppas, N. A., Opsonization, biodistribution, and pharmacokinetics of polymeric nanoparticles. *Int. J. Pharm.* **2006,** *307* (1), 93-102.
91. Theis, T. S., U., Antifungal proteins: targets, mechanisms and prospective applications. *Cell. Mol. Life Sci.* **2004,** *61*, 437–455.
92. Valiante, V.; Macheleidt, J.; Föge, M.; Brakhage, A. A., The Aspergillus fumigatus cell wall integrity signaling pathway: drug target, compensatory pathways, and virulence. *Front. Microbiol.* **2015,** *6* (325).
93. Yang, N. J.; Hinner, M. J., Getting across the cell membrane: an overview for small molecules, peptides, and proteins. *Methods in molecular biology (Clifton, N.J.)* **2015,** *1266*, 29-53.
94. Taheri-Talesh, N.; Horio, T.; Araujo-Bazán, L.; Dou, X.; Espeso, E. A.; Peñalva, M. A.; Osmani, S. A.; Oakley, B. R., The Tip Growth Apparatus of Aspergillus nidulans. *Molecular Biology of the Cell* **2008,** *19* (4), 1439-1449.
95. Atkinson, H. A.; Daniels, A.; Read, N. D., Live-cell imaging of endocytosis during conidial germination in the rice blast fungus, Magnaporthe grisea. *Fungal Genet. Biol.* **2002,** *37* (3), 233-244.
96. Fischer-Parton, S.; Parton, R. M.; Hickey, P. C.; Dijksterhuis, J.; Atkinson, H. A.; Read, N. D., Confocal microscopy of FM4-64 as a tool for analysing endocytosis and vesicle trafficking in living fungal hyphae. *Journal of Microscopy* **2000,** *198* (3), 246-259.
97. Steinberg, G., Endocytosis and early endosome motility in filamentous fungi. *Curr. Opin. Microbiol.* **2014,** *20* (100), 10-18.
98. Nel, A. E.; Mädler, L.; Velegol, D.; Xia, T.; Hoek, E. M. V.; Somasundaran, P.; Klaessig, F.; Castranova, V.; Thompson, M., Understanding biophysicochemical interactions at the nano–bio interface. *Nature Materials* **2009,** *8* (7), 543-557.
99. Blanco, E.; Shen, H.; Ferrari, M., Principles of nanoparticle design for overcoming biological barriers to drug delivery. *Nat. Biotechnol.* **2015,** *33* (9), 941-951.
100. Nomura, T.; Tani, S.; Yamamoto, M.; Nakagawa, T.; Toyoda, S.; Fujisawa, E.; Yasui, A.; Konishi, Y., Cytotoxicity and colloidal behavior of polystyrene latex nanoparticles toward filamentous fungi in isotonic solutions. *Chemosphere* **2016,** *149*, 84-90.
101. Nomura, T.; Miyazaki, J.; Miyamoto, A.; Kuriyama, Y.; Tokumoto, H.; Konishi, Y., Exposure of the Yeast Saccharomyces cerevisiae to Functionalized Polystyrene Latex Nanoparticles: Influence of Surface Charge on Toxicity. *Environ. Sci. Technol.* **2013,** *47* (7), 3417-3423.
102. Lyden, A.; Lombardi, L.; Sire, W.; Li, P.; Simpson, J. C.; Butler, G.; Lee, G. U., Characterization of carboxylate nanoparticle adhesion with the fungal pathogen Candida albicans. *Nanoscale* **2017,** *9* (41), 15911-15922.
103. Stauber, R. H.; Siemer, S.; Becker, S.; Ding, G.-B.; Strieth, S.; Knauer, S. K., Small Meets Smaller: Effects of Nanomaterials on Microbial Biology, Pathology, and Ecology. *ACS Nano* **2018,** *12* (7), 6351-6359.

104. Rahme, K.; Chen, L.; Hobbs, R. G.; Morris, M. A.; O'Driscoll, C.; Holmes, J. D., PEGylated gold nanoparticles: polymer quantification as a function of PEG lengths and nanoparticle dimensions. *RSC Advances* **2013,** *3* (17), 6085-6094.
105. Wang, X.; Ishida, T.; Kiwada, H., Anti-PEG IgM elicited by injection of liposomes is involved in the enhanced blood clearance of a subsequent dose of PEGylated liposomes. *J. Controlled Release* **2007,** *119* (2), 236-244.
106. Verhoef, J. J. F.; Anchordoquy, T. J., Questioning the Use of PEGylation for Drug Delivery. *Drug delivery and translational research* **2013,** *3* (6), 499-503.
107. Chen, Z.; Lv, Z.; Sun, Y.; Chi, Z.; Qing, G., Recent advancements in polyethyleneimine-based materials and their biomedical, biotechnology, and biomaterial applications. *Journal of Materials Chemistry B* **2020,** *8* (15), 2951-2973.
108. Mees, M. A.; Hoogenboom, R., Full and partial hydrolysis of poly(2-oxazoline)s and the subsequent post-polymerization modification of the resulting polyethylenimine (co)polymers. *Polymer Chemistry* **2018,** *9* (40), 4968-4978.
109. Barz, M.; Luxenhofer, R.; Zentel, R.; Vicent, M. J., Overcoming the PEG-addiction: well-defined alternatives to PEG, from structure–property relationships to better defined therapeutics. *Polymer Chemistry* **2011,** *2* (9), 1900-1918.
110. Ulbricht, J.; Jordan, R.; Luxenhofer, R., On the biodegradability of polyethylene glycol, polypeptoids and poly(2-oxazoline)s. *Biomaterials* **2014,** *35* (17), 4848-4861.
111. Gaertner, F. C.; Luxenhofer, R.; Blechert, B.; Jordan, R.; Essler, M., Synthesis, biodistribution and excretion of radiolabeled poly(2-alkyl-2-oxazoline)s. *Journal of controlled release : official journal of the Controlled Release Society* **2007,** *119* (3), 291-300.
112. Luxenhofer, R.; Sahay, G.; Schulz, A.; Alakhova, D.; Bronich, T. K.; Jordan, R.; Kabanov, A. V., Structure-property relationship in cytotoxicity and cell uptake of poly(2-oxazoline) amphiphiles. *Journal of controlled release : official journal of the Controlled Release Society* **2011,** *153* (1), 73-82.
113. Kierstead, P. H.; Okochi, H.; Venditto, V. J.; Chuong, T. C.; Kivimae, S.; Fréchet, J. M. J.; Szoka, F. C., The Effect of Polymer Backbone Chemistry on the Induction of the Accelerated Blood Clearance in Polymer Modified Liposomes. *Journal of controlled release : official journal of the Controlled Release Society* **2015,** *213*, 1-9.
114. Zalipsky, S.; Hansen, C. B.; Oaks, J. M.; Allen, T. M., Evaluation of blood clearance rates and biodistribution of poly(2-oxazoline)-grafted liposomes. *J. Pharm. Sci.* **1996,** *85* (2), 133-137.
115. Konradi, R.; Pidhatika, B.; Mühlebach, A.; Textor, M., Poly-2-methyl-2-oxazoline: A Peptide-like Polymer for Protein-Repellent Surfaces. *Langmuir* **2008,** *24* (3), 613-616.
116. Hartlieb, M.; Bus, T.; Kübel, J.; Pretzel, D.; Hoeppener, S.; Leiske, M. N.; Kempe, K.; Dietzek, B.; Schubert, U. S., Tailoring Cellular Uptake and Fluorescence of Poly(2-oxazoline)-Based Nanogels. *Bioconj. Chem.* **2017,** *28* (4), 1229-1235.
117. Witzigmann, D.; Wu, D.; Schenk, S. H.; Balasubramanian, V.; Meier, W.; Huwyler, J., Biocompatible Polymer–Peptide Hybrid-Based DNA Nanoparticles for Gene Delivery. *ACS Appl. Mater. Interfaces* **2015,** *7* (19), 10446-10456.
118. de la Rosa, V. R., Poly(2-oxazoline)s as materials for biomedical applications. *J. Mater. Sci. Mater. Med.* **2014,** *25* (5), 1211-1225.
119. Lambermont-Thijs, H. M. L.; van der Woerdt, F. S.; Baumgaertel, A.; Bonami, L.; Du Prez, F. E.; Schubert, U. S.; Hoogenboom, R., Linear Poly(ethylene imine)s by Acidic Hydrolysis of Poly(2-oxazoline)s: Kinetic Screening, Thermal Properties, and Temperature-Induced Solubility Transitions. *Macromolecules* **2010,** *43* (2), 927-933.
120. Glassner, M.; Vergaelen, M.; Hoogenboom, R., Poly(2-oxazoline)s: A comprehensive overview of polymer structures and their physical properties. *Polym. Int.* **2018,** *67* (1),

32-45.
121. Weinhart, M.; Grunwald, I.; Wyszogrodzka, M.; Gaetjen, L.; Hartwig, A.; Haag, R., Linear Poly(methyl glycerol) and Linear Polyglycerol as Potent Protein and Cell Resistant Alternatives to Poly(ethylene glycol). *Chemistry – An Asian Journal* **2010,** *5* (9), 1992-2000.
122. Haag R, M. Q., Polyglycerols in Nanomedicine. *Pan Stanford Publishing Pte. Ltd.* **2016**, 107-200.
123. Thomas, A.; Müller, S. S.; Frey, H., Beyond Poly(ethylene glycol): Linear Polyglycerol as a Multifunctional Polyether for Biomedical and Pharmaceutical Applications. *Biomacromolecules* **2014,** *15* (6), 1935-1954.
124. Abu Lila, A. S.; Nawata, K.; Shimizu, T.; Ishida, T.; Kiwada, H., Use of polyglycerol (PG), instead of polyethylene glycol (PEG), prevents induction of the accelerated blood clearance phenomenon against long-circulating liposomes upon repeated administration. *Int. J. Pharm.* **2013,** *456* (1), 235-242.
125. Harris, J. M., *Poly(Ethylene Glycol) Chemistry: Biotechnical and Biomedical Applications*. Springer US: 2013.
126. Hoogenboom, R.; Fijten, M. W. M.; Thijs, H. M. L.; van Lankvelt, B. M.; Schubert, U. S., Microwave-assisted synthesis and properties of a series of poly(2-alkyl-2-oxazoline)s. *Designed Monomers and Polymers* **2005,** *8* (6), 659-671.
127. Verbraeken, B.; Monnery, B. D.; Lava, K.; Hoogenboom, R., The chemistry of poly(2-oxazoline)s. *Eur. Polym. J.* **2017,** *88*, 451-469.
128. Monnery, B. D.; Jerca, V. V.; Sedlacek, O.; Verbraeken, B.; Cavill, R.; Hoogenboom, R., Defined High Molar Mass Poly(2-Oxazoline)s. *Angew. Chem. Int. Ed.* **2018,** *57* (47), 15400-15404.
129. Wiesbrock, F.; Hoogenboom, R.; Schubert, U. S., Microwave-Assisted Polymer Synthesis: State-of-the-Art and Future Perspectives. *Macromol. Rapid Commun.* **2004,** *25* (20), 1739-1764.
130. Paulus, I., Untersuchung des Lösungs- und Aggregationsverhaltens polymeranalog Cystein-funktionalisierter Poly(2-alkyl-2-oxazoline), Master Thesis. **2017**.
131. Lambermont-Thijs, H. M. L.; Heuts, J. P. A.; Hoeppener, S.; Hoogenboom, R.; Schubert, U. S., Selective partial hydrolysis of amphiphilic copoly(2-oxazoline)s as basis for temperature and pH responsive micelles. *Polymer Chemistry* **2011,** *2* (2), 313-322.
132. Taton, D.; Le Borgne, A.; Sepulchre, M.; Spassky, N., Synthesis of chiral and racemic functional polymers from glycidol and thioglycidol. *Macromol. Chem. Phys.* **1994,** *195* (1), 139-148.
133. Keul, H.; Möller, M., Synthesis and degradation of biomedical materials based on linear and star shaped polyglycidols. *J. Polym. Sci., Part A: Polym. Chem.* **2009,** *47* (13), 3209-3231.
134. Fitton, A. O.; Hill, J.; Jane, D. E.; Millar, R., Synthesis of Simple Oxetanes Carrying Reactive 2-Substituents. *Synthesis* **1987,** *1987* (12), 1140-1142.
135. Stichler, S.; Jungst, T.; Schamel, M.; Zilkowski, I.; Kuhlmann, M.; Böck, T.; Blunk, T.; Teßmar, J.; Groll, J., Thiol-ene Clickable Poly(glycidol) Hydrogels for Biofabrication. *Ann. Biomed. Eng.* **2017,** *45* (1), 273-285.
136. Schaefer, S. Thiol-ene Cross-linked Poly(glycidol) / Hyaluronic Acid Based Hydrogels for 3D Bioprinting. University of Wuerzburg, Wuerzburg, Germany, 2018.
137. Guo, X.; Cheng, Y.; Zhao, X.; Luo, Y.; Chen, J.; Yuan, W.-E., Advances in redox-responsive drug delivery systems of tumor microenvironment. *Journal of Nanobiotechnology* **2018,** *16* (1), 74.

138. García Ruano, J. L.; Parra, A.; Alemán, J., Efficient synthesis of disulfides by air oxidation of thiols under sonication. *Green Chemistry* **2008,** *10* (6), 706-711.
139. Mather, B. D.; Viswanathan, K.; Miller, K. M.; Long, T. E., Michael addition reactions in macromolecular design for emerging technologies. *Prog. Polym. Sci.* **2006,** *31* (5), 487-531.
140. Resch, V.; Seidler, C.; Chen, B.-S.; Degeling, I.; Hanefeld, U., On the Michael Addition of Water to α,β-Unsaturated Ketones Using Amino Acids. *Eur. J. Org. Chem.* **2013,** *2013* (34), 7697-7704.
141. Landfester, K.; Willert, M.; Antonietti, M., Preparation of Polymer Particles in Nonaqueous Direct and Inverse Miniemulsions. *Macromolecules* **2000,** *33* (7), 2370-2376.
142. Nukolova, N. V.; Yang, Z.; Kim, J. O.; Kabanov, A. V.; Bronich, T. K., Polyelectrolyte Nanogels Decorated with Monoclonal Antibody for Targeted Drug Delivery. *Reactive & functional polymers* **2011,** *71* (3), 315-323.
143. Westmeier, D.; Solouk-Saran, D.; Vallet, C.; Siemer, S.; Docter, D.; Götz, H.; Männ, L.; Hasenberg, A.; Hahlbrock, A.; Erler, K.; Reinhardt, C.; Schilling, O.; Becker, S.; Gunzer, M.; Hasenberg, M.; Knauer, S. K.; Stauber, R. H., Nanoparticle decoration impacts airborne fungal pathobiology. *Proceedings of the National Academy of Sciences* **2018,** *115* (27), 7087-7092.
144. Ma, H.; Snook, L.; Tian, C.; Kaminskyj, S.; Dahms, T., *Fungal surface remodelling visualized by atomic force microscopy*. 2006; Vol. 110, p 879-886.
145. Ma, H.; Snook, L. A.; Kaminskyj, S. G. W.; Dahms, T. E. S., Surface ultrastructure and elasticity in growing tips and mature regions of Aspergillus hyphae describe wall maturation. *Microbiology* **2005,** *151* (11), 3679-3688.
146. Beauvais, A.; Fontaine, T.; Aimanianda, V.; Latgé, J.-P., Aspergillus Cell Wall and Biofilm. *Mycopathologia* **2014,** *178* (5), 371-377.
147. Tournu, H.; Carroll, J.; Latimer, B.; Dragoi, A.-M.; Dykes, S.; Cardelli, J.; Peters, T. L.; Eberle, K. E.; Palmer, G. E., Identification of small molecules that disrupt vacuolar function in the pathogen Candida albicans. *PLOS ONE* **2017,** *12* (2), e0171145.
148. Burgers, P. M. J.; Percival, K. J., Transformation of yeast spheroplasts without cell fusion. *Anal. Biochem.* **1987,** *163* (2), 391-397.
149. Gietz, R. D.; Schiestl, R. H.; Willems, A. R.; Woods, R. A., Studies on the transformation of intact yeast cells by the LiAc/SS-DNA/PEG procedure. *Yeast* **1995,** *11* (4), 355-360.
150. Lother, J.; Breitschopf, T.; Krappmann, S.; Morton, C. O.; Bouzani, M.; Kurzai, O.; Gunzer, M.; Hasenberg, M.; Einsele, H.; Loeffler, J., Human dendritic cell subsets display distinct interactions with the pathogenic mould Aspergillus fumigatus. *Int. J. Med. Microbiol.* **2014,** *304* (8), 1160-1168.
151. Hellebrekers, P.; Hietbrink, F.; Vrisekoop, N.; Leenen, L. P. H.; Koenderman, L., Neutrophil Functional Heterogeneity: Identification of Competitive Phagocytosis. *Frontiers in immunology* **2017,** *8*, 1498-1498.
152. Behzadi, S.; Serpooshan, V.; Tao, W.; Hamaly, M. A.; Alkawareek, M. Y.; Dreaden, E. C.; Brown, D.; Alkilany, A. M.; Farokhzad, O. C.; Mahmoudi, M., Cellular uptake of nanoparticles: journey inside the cell. *Chem. Soc. Rev.* **2017,** *46* (14), 4218-4244.
153. Štorha, A.; Mun, E. A.; Khutoryanskiy, V. V., Synthesis of thiolated and acrylated nanoparticles using thiol-ene click chemistry: towards novel mucoadhesive materials for drug delivery. *RSC Advances* **2013,** *3* (30), 12275-12279.
154. Diaferia, C.; Mercurio, F. A.; Giannini, C.; Sibillano, T.; Morelli, G.; Leone, M.; Accardo, A., Self-assembly of PEGylated tetra-phenylalanine derivatives: structural

insights from solution and solid state studies. *Sci. Rep.* **2016,** *6*, 26638.
155. Castelletto, V.; Ryumin, P.; Cramer, R.; Hamley, I. W.; Taylor, M.; Allsop, D.; Reza, M.; Ruokolainen, J.; Arnold, T.; Hermida-Merino, D.; Garcia, C. I.; Leal, M. C.; Castaño, E., Self-Assembly and Anti-Amyloid Cytotoxicity Activity of Amyloid beta Peptide Derivatives. *Sci. Rep.* **2017,** *7*, 43637.
156. Bennion, B. J.; Daggett, V., The molecular basis for the chemical denaturation of proteins by urea. *Proceedings of the National Academy of Sciences of the United States of America* **2003,** *100* (9), 5142-5147.
157. Desale, S. S.; Cohen, S. M.; Zhao, Y.; Kabanov, A. V.; Bronich, T. K., Biodegradable hybrid polymer micelles for combination drug therapy in ovarian cancer. *Journal of controlled release : official journal of the Controlled Release Society* **2013,** *171* (3), 339-348.
158. Kumari, S.; Sonu; Halder, S.; Aggrawal, R.; Sundar, G.; Saha, S. K., Effect of Urea on Solvation Dynamics and Rotational Relaxation of Coumarin 480 in Aqueous Micelles of Cationic Gemini Surfactants with Different Spacer Groups. *ACS Omega* **2018,** *3* (3), 3079-3095.
159. Ruiz, C. C., Micelle formation and microenvironmental properties of sodium dodecyl sulfate in aqueous urea solutions. *Colloids Surf. Physicochem. Eng. Aspects* **1999,** *147* (3), 349-357.
160. Trivedi, R.; Kompella, U. B., Nanomicellar formulations for sustained drug delivery: strategies and underlying principles. *Nanomedicine (London, England)* **2010,** *5* (3), 485-505.
161. Lee, H.-u.; Park, J. B.; Lee, H.; Chae, K.-S.; Han, D.-M.; Jahng, K.-Y., Predicting the chemical composition and structure of Aspergillus nidulans hyphal wall surface by atomic force microscopy. *J. Microbiol.* **2010,** *48* (2), 243-248.
162. Chavan, N. L.; Young, J. K.; Drezek, R. A.; Lewis, R.; Bikram, M., Interactions of Liposome Carriers with Infectious Fungal Hyphae Reveals the Role of β-Glucans. *Mol. Pharm.* **2012,** *9* (9), 2489-2496.
163. Williams, D. L.; McNamee, R. B.; Jones, E. L.; Pretus, H. A.; Ensley, H. E.; Browder, I. W.; Di Luzio, N. R., A method for the solubilization of a (1→3)-β-d-glucan isolated from Saccharomyces cerevisiae. *Carbohydr. Res.* **1991,** *219*, 203-213.
164. Molnár, E.; Kuntam, S.; Cingaram, P.; Peksel, B.; Suresh, B.; Fábián, G.; Fehér, L.; Bokros, A.; Medgyesi, Á.; Ayaydin, F.; Puskás, L., Combination of Small Molecule Microarray and Confocal Microscopy Techniques for Live Cell Staining Fluorescent Dye Discovery. *Molecules* **2013,** *18* (8), 9999.
165. Shin, H. Y.; Lee, J. Y.; Kim, E. J.; Kim, S. W., Rapid Quantification of Lipids in Acremonium chrysogenum Using Oil Red O. *Curr. Microbiol.* **2011,** *62* (3), 1023-1027.
166. Rispail, N.; De Matteis, L.; Santos, R.; Miguel, A. S.; Custardoy, L.; Testillano, P. S.; Risueño, M. C.; Pérez-de-Luque, A.; Maycock, C.; Fevereiro, P.; Oliva, A.; Fernández-Pacheco, R.; Ibarra, M. R.; de la Fuente, J. M.; Marquina, C.; Rubiales, D.; Prats, E., Quantum Dot and Superparamagnetic Nanoparticle Interaction with Pathogenic Fungi: Internalization and Toxicity Profile. *ACS Appl. Mater. Interfaces* **2014,** *6* (12), 9100-9110.
167. Hofmann, D.; Messerschmidt, C.; Bannwarth, M. B.; Landfester, K.; Mailänder, V., Drug delivery without nanoparticle uptake: delivery by a kiss-and-run mechanism on the cell membrane. *Chem. Commun.* **2014,** *50* (11), 1369-1371.
168. Moen, M. D.; Lyseng-Williamson, K. A.; Scott, L. J., Liposomal Amphotericin B. *Drugs* **2009,** *69* (3), 361-392.
169. Walker, L.; Sood, P.; Lenardon, M. D.; Milne, G.; Olson, J.; Jensen, G.; Wolf, J.; Casadevall, A.; Adler-Moore, J.; Gow, N. A. R., The Viscoelastic Properties of the

Fungal Cell Wall Allow Traffic of AmBisome as Intact Liposome Vesicles. *mBio* **2018,** *9* (1), e02383-17.
170. Wang, Y.; Ke, X.; Voo, Z. X.; Yap, S. S. L.; Yang, C.; Gao, S.; Liu, S.; Venkataraman, S.; Obuobi, S. A. O.; Khara, J. S.; Yang, Y. Y.; Ee, P. L. R., Biodegradable functional polycarbonate micelles for controlled release of amphotericin B. *Acta Biomater.* **2016,** *46*, 211-220.
171. Brajtburg, J.; Bolard, J., Carrier effects on biological activity of amphotericin B. *Clin. Microbiol. Rev.* **1996,** *9* (4), 512-531.
172. Adler-Moore, J. P.; Proffitt, R. T., Development, Characterization, Efficacy and Mode of Action of Ambisome, A Unilamellar Liposomal Formulation of Amphotericin B. *J. Liposome Res.* **1993,** *3* (3), 429-450.
173. Shimizu, K.; Osada, M.; Takemoto, K.; Yamamoto, Y.; Asai, T.; Oku, N., Temperature-dependent transfer of amphotericin B from liposomal membrane of AmBisome to fungal cell membrane. *J. Controlled Release* **2010,** *141* (2), 208-215.
174. Kang, C.-K.; Yamada, K.; Usuki, Y.; Ogita, A.; Fujita, K.-i.; Tanaka, T., Visualization analysis of the vacuole-targeting fungicidal activity of amphotericin B against the parent strain and an ergosterol-less mutant of Saccharomyces cerevisiae. *Microbiology* **2013,** *159* (5), 939-947.
175. Zheng, H.-Z.; Liu, H.-H.; Chen, S.-X.; Lu, Z.-X.; Zhang, Z.-L.; Pang, D.-W.; Xie, Z.-X.; Shen, P., Yeast Transformation Process Studied by Fluorescence Labeling Technique. *Bioconj. Chem.* **2005,** *16* (2), 250-254.
176. Boni, L. T.; Stewart, T. P.; Alderfer, J. L.; Hui, S. W., Lipid-polyethylene glycol interactions: II. Formation of defects in bilayers. *J. Membrane Biol.* **1981,** *62* (1), 71-77.
177. Brandão, I. d. S. L.; Oliveira-Moraes, H. M. d. S.; Souza Motta, C. M. d.; Oliveira, N. T. d.; Magalhães, O. M. C., Elastin increases biofilm and extracellular matrix production of Aspergillus fumigatus. *Braz. J. Microbiol.* **2018,** *49* (3), 675-682.
178. Peñalver, M. C.; Casanova, M.; Martínez, J. P.; Gil, M. L., Cell wall protein and glycoprotein constituents of Aspergillus fumigatus that bind to polystyrene may be responsible for the cell surface hydrophobicity of the mycelium. *Microbiology* **1996,** *142* (7), 1597-1604.
179. Ellepola, A. N. B. S., Lakshman P., Impact of Brief, Sequential Exposure to Fluconazole and Amphotericin B on the Cell Surface Hydrophobicity of oral Candida albicans Isolates Obtained from HIV Infected Patients *Microb. Ecol. Health Dis.* **2002,** *14* (3), 153-159.
180. Sawaya, B. P.; Briggs, J. P.; Schnermann, J., Amphotericin B nephrotoxicity: the adverse consequences of altered membrane properties. *J. Am. Soc. Nephrol.* **1995,** *6* (2), 154-164.
181. Zhang, X.; Achazi, K.; Steinhilber, D.; Kratz, F.; Dernedde, J.; Haag, R., A facile approach for dual-responsive prodrug nanogels based on dendritic polyglycerols with minimal leaching. *J. Controlled Release* **2014,** *174*, 209-216.
182. Sousa-Herves, A.; Wedepohl, S.; Calderón, M., One-pot synthesis of doxorubicin-loaded multiresponsive nanogels based on hyperbranched polyglycerol. *Chem. Commun.* **2015,** *51* (25), 5264-5267.
183. Vossen, L. I.; Wedepohl, S.; Calderón, M., A Facile, One-Pot, Surfactant-Free Nanoprecipitation Method for the Preparation of Nanogels from Polyglycerol-Drug Conjugates that Can Be Freely Assembled for Combination Therapy Applications. *Polymers* **2018,** *10* (4), 398.
184. Galindo-Rodriguez, S.; Allémann, E.; Fessi, H.; Doelker, E., Physicochemical Parameters Associated with Nanoparticle Formation in the Salting-Out,

Emulsification-Diffusion, and Nanoprecipitation Methods. *Pharm. Res.* **2004,** *21* (8), 1428-1439.
185. Miller, C. A., Spontaneous Emulsification Produced by Diffusion — A Review. *Colloids and Surfaces* **1988,** *29* (1), 89-102.
186. Martínez Rivas, C. J.; Tarhini, M.; Badri, W.; Miladi, K.; Greige-Gerges, H.; Nazari, Q. A.; Galindo Rodríguez, S. A.; Román, R. Á.; Fessi, H.; Elaissari, A., Nanoprecipitation process: From encapsulation to drug delivery. *Int. J. Pharm.* **2017,** *532* (1), 66-81.
187. Blackburn, W. H.; Dickerson, E. B.; Smith, M. H.; McDonald, J. F.; Lyon, L. A., Peptide-Functionalized Nanogels for Targeted siRNA Delivery. *Bioconj. Chem.* **2009,** *20* (5), 960-968.
188. Smith, M. H.; Lyon, L. A., Multifunctional Nanogels for siRNA Delivery. *Acc. Chem. Res.* **2012,** *45* (7), 985-993.
189. Chung, N.-O.; Lee, M. K.; Lee, J., Mechanism of freeze-drying drug nanosuspensions. *Int. J. Pharm.* **2012,** *437* (1), 42-50.
190. Arias, L. S.; Pessan, J. P.; Vieira, A. P. M.; Lima, T. M. T. d.; Delbem, A. C. B.; Monteiro, D. R., Iron Oxide Nanoparticles for Biomedical Applications: A Perspective on Synthesis, Drugs, Antimicrobial Activity, and Toxicity. *Antibiotics (Basel, Switzerland)* **2018,** *7* (2), 46.
191. Démuth, B.; Galata, D. L.; Szabó, E.; Nagy, B.; Farkas, A.; Balogh, A.; Hirsch, E.; Pataki, H.; Rapi, Z.; Bezúr, L.; Vigh, T.; Verreck, G.; Szalay, Z.; Demeter, Á.; Marosi, G.; Nagy, Z. K., Investigation of Deteriorated Dissolution of Amorphous Itraconazole: Description of Incompatibility with Magnesium Stearate and Possible Solutions. *Mol. Pharm.* **2017,** *14* (11), 3927-3934.
192. Lee, S.; Nam, K.; Kim, M. S.; Jun, S. W.; Park, J.-S.; Woo, J. S.; Hwang, S.-J., Preparation and characterization of solid dispersions of itraconazole by using aerosol solvent extraction system for improvement in drug solubility and bioavailability. *Arch. Pharmacal Res.* **2005,** *28* (7), 866-874.
193. Van Driessche, A.; Kocere, A.; Everaert, H.; Nuhn, L.; Van Herck, S.; Griffiths, G.; Fenaroli, F.; De Geest, B. G., pH-Sensitive Hydrazone-Linked Doxorubicin Nanogels via Polymeric-Activated Ester Scaffolds: Synthesis, Assembly, and In Vitro and In Vivo Evaluation in Tumor-Bearing Zebrafish. *Chem. Mater.* **2018,** *30* (23), 8587-8596.
194. Van de Ven, H.; Paulussen, C.; Feijens, P. B.; Matheeussen, A.; Rombaut, P.; Kayaert, P.; Van den Mooter, G.; Weyenberg, W.; Cos, P.; Maes, L.; Ludwig, A., PLGA nanoparticles and nanosuspensions with amphotericin B: Potent in vitro and in vivo alternatives to Fungizone and AmBisome. *J. Controlled Release* **2012,** *161* (3), 795-803.
195. Ishida, K.; de Castro, R. A.; Borba dos Santos, L. P.; Quintella, L. P.; Lopes-Bezerra, L. M.; Rozental, S., Amphotericin B, alone or followed by itraconazole therapy, is effective in the control of experimental disseminated sporotrichosis by Sporothrix brasiliensis. *Med. Mycol.* **2014,** *53* (1), 34-41.
196. Rhee, Y.-S.; Park, C.-W.; Nam, T.-Y.; Shin, Y.-S.; Chi, S.-C.; Park, E.-S., Formulation of parenteral microemulsion containing itraconazole. *Arch. Pharmacal Res.* **2007,** *30* (1), 114-123.
197. Serrano, D. R.; Hernández, L.; Fleire, L.; González-Alvarez, I.; Montoya, A.; Ballesteros, M. P.; Dea-Ayuela, M. A.; Miró, G.; Bolás-Fernández, F.; Torrado, J. J., Hemolytic and pharmacokinetic studies of liposomal and particulate amphotericin B formulations. *Int. J. Pharm.* **2013,** *447* (1), 38-46.
198. Ling, X.; Huang, Z.; Wang, J.; Xie, J.; Feng, M.; Chen, Y.; Abbas, F.; Tu, J.; Wu, J.; Sun, C., Development of an itraconazole encapsulated polymeric nanoparticle platform for effective antifungal therapy. *Journal of Materials Chemistry B* **2016,** *4* (10), 1787-1796.

199. Bobo, D.; Robinson, K. J.; Islam, J.; Thurecht, K. J.; Corrie, S. R., Nanoparticle-Based Medicines: A Review of FDA-Approved Materials and Clinical Trials to Date. *Pharm. Res.* **2016,** *33* (10), 2373-2387.
200. Schwab, K. E.; Gailloud, P.; Wyse, G.; Tamargo, R. J., LIMITATIONS OF MAGNETIC RESONANCE IMAGING AND MAGNETIC RESONANCE ANGIOGRAPHY IN THE DIAGNOSIS OF INTRACRANIAL ANEURYSMS. *Neurosurgery* **2008,** *63* (1), 29-35.
201. Graeser, M.; Thieben, F.; Szwargulski, P.; Werner, F.; Gdaniec, N.; Boberg, M.; Griese, F.; Möddel, M.; Ludewig, P.; van de Ven, D.; Weber, O. M.; Woywode, O.; Gleich, B.; Knopp, T., Human-sized magnetic particle imaging for brain applications. *Nature Communications* **2019,** *10* (1), 1936.
202. Vogel, P.; Rückert, M. A.; Klauer, P.; Kullmann, W. H.; Jakob, P. M.; Behr, V. C., Traveling Wave Magnetic Particle Imaging. *IEEE Trans. Med. Imaging* **2014,** *33* (2), 400-407.
203. Vogel, P.; Lother, S.; Rückert, M. A.; Kullmann, W. H.; Jakob, P. M.; Fidler, F.; Behr, V. C., MRI Meets MPI: A Bimodal MPI-MRI Tomograph. *IEEE Trans. Med. Imaging* **2014,** *33* (10), 1954-1959.
204. Vogel, P.; Rückert, M. A.; Klauer, P.; Kullmann, W. H.; Jakob, P. M.; Behr, V. C., First in vivo traveling wave magnetic particle imaging of a beating mouse heart. *Physics in Medicine & Biology* **2016,** *61* (18), 6620.
205. Vogel, P.; Rückert, M. A.; Kemp, S. J.; Khandhar, A. P.; Ferguson, R. M.; Herz, S.; Vilter, A.; Klauer, P.; Bley, T. A.; Krishnan, K. M.; Behr, V. C., Micro-Traveling Wave Magnetic Particle Imaging--Sub-Millimeter Resolution With Optimized Tracer LS-008. *IEEE Transactions on Magnetics* **2019**, 1-7.
206. Gleich, B.; Weizenecker, J., Tomographic imaging using the nonlinear response of magnetic particles. *Nature* **2005,** *435*, 1214.
207. Knopp, T.; Gdaniec, N.; Möddel, M., Magnetic particle imaging: from proof of principle to preclinical applications. *Physics in Medicine & Biology* **2017,** *62* (14), R124-R178.
208. Wu, K.; Su, D.; Saha, R.; Wong, D.; Wang, J.-P., Magnetic particle spectroscopy-based bioassays: methods, applications, advances, and future opportunities. *J. Phys. D: Appl. Phys.* **2019,** *52* (17), 173001.
209. Biederer, S.; Knopp, T.; Sattel, T. F.; Lüdtke-Buzug, K.; Gleich, B.; Weizenecker, J.; Borgert, J.; Buzug, T. M., Magnetization response spectroscopy of superparamagnetic nanoparticles for magnetic particle imaging. *J. Phys. D: Appl. Phys.* **2009,** *42* (20), 205007.
210. Löwa, N.; Knappe, P.; Wiekhorst, F.; Eberbeck, D.; Thünemann, A. F.; Trahms, L., Hydrodynamic and magnetic fractionation of superparamagnetic nanoparticles for magnetic particle imaging. *J. Magn. Magn. Mater.* **2015,** *380*, 266-270.
211. Starmans, L. W. E.; Burdinski, D.; Haex, N. P. M.; Moonen, R. P. M.; Strijkers, G. J.; Nicolay, K.; Grüll, H., Iron oxide nanoparticle-micelles (ION-micelles) for sensitive (molecular) magnetic particle imaging and magnetic resonance imaging. *PloS one* **2013,** *8* (2), e57335-e57335.
212. Li, X.; Wei, J.; Aifantis, K. E.; Fan, Y.; Feng, Q.; Cui, F.-Z.; Watari, F., Current investigations into magnetic nanoparticles for biomedical applications. *Journal of Biomedical Materials Research Part A* **2016,** *104* (5), 1285-1296.
213. Hufschmid, R.; Arami, H.; Ferguson, R. M.; Gonzales, M.; Teeman, E.; Brush, L. N.; Browning, N. D.; Krishnan, K. M., Synthesis of phase-pure and monodisperse iron oxide nanoparticles by thermal decomposition. *Nanoscale* **2015,** *7* (25), 11142-11154.

214. Paquet, C.; de Haan, H. W.; Leek, D. M.; Lin, H.-Y.; Xiang, B.; Tian, G.; Kell, A.; Simard, B., Clusters of Superparamagnetic Iron Oxide Nanoparticles Encapsulated in a Hydrogel: A Particle Architecture Generating a Synergistic Enhancement of the T2 Relaxation. *ACS Nano* **2011,** *5* (4), 3104-3112.
215. Park, J.; An, K.; Hwang, Y.; Park, J.-G.; Noh, H.-J.; Kim, J.-Y.; Park, J.-H.; Hwang, N.-M.; Hyeon, T., Ultra-large-scale syntheses of monodisperse nanocrystals. *Nature Materials* **2004,** *3*, 891.
216. Bronstein, L. M.; Huang, X.; Retrum, J.; Schmucker, A.; Pink, M.; Stein, B. D.; Dragnea, B., Influence of Iron Oleate Complex Structure on Iron Oxide Nanoparticle Formation. *Chem. Mater.* **2007,** *19* (15), 3624-3632.
217. Walker, J. M.; Zaleski, J. M., Magnetically Triggered Radical-Generating Fe3O4 Nanoparticles for Biopolymer Restructuring: Application to the Extracellular Matrix. *Chem. Mater.* **2015,** *27* (24), 8448-8456.
218. Scherrer, P., Bestimmung der Größe und der inneren Struktur von Kolloidteilchen mittels Röntgenstrahlen. *Nachrichten von der Gesellschaft der Wissenschaften zu Göttingen, Mathematisch-Physikalische Klasse* **1918,** *1918*, 98-100.
219. Gillich, T.; Acikgöz, C.; Isa, L.; Schlüter, A. D.; Spencer, N. D.; Textor, M., PEG-Stabilized Core–Shell Nanoparticles: Impact of Linear versus Dendritic Polymer Shell Architecture on Colloidal Properties and the Reversibility of Temperature-Induced Aggregation. *ACS Nano* **2013,** *7* (1), 316-329.
220. Jain, T. K.; Foy, S. P.; Erokwu, B.; Dimitrijevic, S.; Flask, C. A.; Labhasetwar, V., Magnetic resonance imaging of multifunctional pluronic stabilized iron-oxide nanoparticles in tumor-bearing mice. *Biomaterials* **2009,** *30* (35), 6748-56.
221. Dehvari, K.; Lin, K.-S.; Hammouda, B., Small-angle neutron scattering studies of microenvironmental and structural changes of Pluronic micelles upon encapsulation of paclitaxel. *Journal of the Taiwan Institute of Chemical Engineers* **2017,** *71*, 405-413.
222. Lai, J.-R.; Chang, Y.-W.; Yen, H.-C.; Yuan, N.-Y.; Liao, M.-Y.; Hsu, C.-Y.; Tsai, J.-L.; Lai, P.-S., Multifunctional doxorubicin/superparamagnetic iron oxide-encapsulated Pluronic F127 micelles used for chemotherapy/magnetic resonance imaging. *J. Appl. Phys.* **2010,** *107* (9), 09B318.
223. Zhu, W.; Wang, B.; Zhang, Y.; Ding, J., Preparation of a thermosensitive and biodegradable microgel via polymerization of macromonomers based on diacrylated Pluronic/oligoester copolymers. *Eur. Polym. J.* **2005,** *41* (9), 2161-2170.
224. Yuan-na Sun, G.-r. G., Gao-lai Du, Ya-jun Cheng, and Jun Fu Super Tough, Ultrastretchable, and Thermoresponsive Hydrogels with Functionalized Triblock Copolymer Micelles as Macro-Cross-Linkers *ACS Macro Letters* **2014,** *3* (5), 496-500
225. Cellesi, F. T., N.; Hubbell, J. A. , Materials for cell encapsulation via a new tandem approach combining reverse thermal gelation and covalent crosslinking. *Macromol. Chem. Phys.* **2002,** *203*, 1466–1472.
226. Bordoni, A. V.; Lombardo, M. V.; Wolosiuk, A., Photochemical radical thiol-ene click-based methodologies for silica and transition metal oxides materials chemical modification: a mini-review. *RSC Advances* **2016,** *6* (81), 77410-77426.
227. Theerasilp, M.; Sungkarat, W.; Nasongkla, N., Synthesis and characterization of SPIO-loaded PEG-b-PS micelles as contrast agent for long-term nanoparticle-based MRI phantom. *Bull. Mater. Sci.* **2018,** *41* (2), 42.
228. Gonzales, M.; Krishnan, K. M., Phase transfer of highly monodisperse iron oxide nanocrystals with Pluronic F127 for biomedical applications. *J. Magn. Magn. Mater.* **2007,** *311* (1), 59-62.
229. Pillai, S. A.; Lee, C.-F.; Ray, D.; Aswal, V. K.; Wang, M.-R.; Chen, L.-J.; Bahadur, P.,

Influence of urea on single and mixed micellar systems of Tetronics®. *J. Mol. Liq.* **2018,** *252*, 9-17.
230. Bharatiya, B.; Guo, C.; Ma, J. H.; Kubota, O.; Nakashima, K.; Bahadur, P., Urea-induced demicellization of Pluronic L64 in water. *Colloid. Polym. Sci.* **2009,** *287* (1), 63-71.
231. Ma, J.-h.; Guo, C.; Tang, Y.-l.; Chen, L.; Bahadur, P.; Liu, H.-z., Interaction of Urea with Pluronic Block Copolymers by 1H NMR Spectroscopy. *The Journal of Physical Chemistry B* **2007,** *111* (19), 5155-5161.
232. Roseman, M.; Jencks, W. P., Interactions of urea and other polar compounds in water. *J. Am. Chem. Soc.* **1975,** *97* (3), 631-640.
233. Dubertret, B.; Skourides, P.; Norris, D. J.; Noireaux, V.; Brivanlou, A. H.; Libchaber, A., In Vivo Imaging of Quantum Dots Encapsulated in Phospholipid Micelles. *Science* **2002,** *298* (5599), 1759-1762.
234. Zhang, W. G., K.; Wu, L.; Bahadur, R. K. C.; Moss, M. A.; Wang, Q.; Lu, X.; He, X., Synthesis and Characterization of Thermally Responsive Pluronic F127-Chitosan Nanocapsules for Controlled Release and Intracellular Delivery of Small Molecules. *ASC Nano* **2010,** *4* (11), 6757-6759.
235. Bae, K. H.; Lee, Y.; Park, T. G., Oil-Encapsulating PEO–PPO–PEO/PEG Shell Cross-Linked Nanocapsules for Target-Specific Delivery of Paclitaxel. *Biomacromolecules* **2007,** *8* (2), 650-656.
236. Choi, S. H.; Lee, S. H.; Park, T. G., Temperature-Sensitive Pluronic/Poly(ethylenimine) Nanocapsules for Thermally Triggered Disruption of Intracellular Endosomal Compartment. *Biomacromolecules* **2006,** *7* (6), 1864-1870.
237. Wei, H.; Bruns, O. T.; Kaul, M. G.; Hansen, E. C.; Barch, M.; Wiśniowska, A.; Chen, O.; Chen, Y.; Li, N.; Okada, S.; Cordero, J. M.; Heine, M.; Farrar, C. T.; Montana, D. M.; Adam, G.; Ittrich, H.; Jasanoff, A.; Nielsen, P.; Bawendi, M. G., Exceedingly small iron oxide nanoparticles as positive MRI contrast agents. *Proceedings of the National Academy of Sciences* **2017**, 201620145.
238. Li, L.; Jiang, W.; Luo, K.; Song, H.; Lan, F.; Wu, Y.; Gu, Z., Superparamagnetic iron oxide nanoparticles as MRI contrast agents for non-invasive stem cell labeling and tracking. *Theranostics* **2013,** *3* (8), 595-615.
239. Tong, S.; Hou, S.; Zheng, Z.; Zhou, J.; Bao, G., Coating Optimization of Superparamagnetic Iron Oxide Nanoparticles for High T2 Relaxivity. *Nano Lett.* **2010,** *10* (11), 4607-4613.
240. LaConte, L. E. W.; Nitin, N.; Zurkiya, O.; Caruntu, D.; O'Connor, C. J.; Hu, X.; Bao, G., Coating thickness of magnetic iron oxide nanoparticles affects R2 relaxivity. *J. Magn. Reson. Imaging* **2007,** *26* (6), 1634-1641.
241. Park, J. C.; Lee, G. T.; Kim, H.-K.; Sung, B.; Lee, Y.; Kim, M.; Chang, Y.; Seo, J. H., Surface Design of Eu-Doped Iron Oxide Nanoparticles for Tuning the Magnetic Relaxivity. *ACS Appl. Mater. Interfaces* **2018,** *10* (30), 25080-25089.
242. Lin, Y.; Wang, S.; Zhang, Y.; Gao, J.; Hong, L.; Wang, X.; Wu, W.; Jiang, X., Ultra-high relaxivity iron oxide nanoparticles confined in polymer nanospheres for tumor MR imaging. *Journal of Materials Chemistry B* **2015,** *3* (28), 5702-5710.
243. Izza Taib, N.; Agarwal, V.; Smith, N. M.; Woodward, R. C.; St. Pierre, T. G.; Iyer, K. S., Direct correlation of PNIPAM thermal transition and magnetic resonance relaxation of iron oxide nanoparticles. *Materials Chemistry Frontiers* **2017,** *1* (11), 2335-2340.
244. Draack, S.; Viereck, T.; Kuhlmann, C.; Schilling, M.; Ludwig, F., Temperature-dependent MPS measurements. *International Journal on Magnetic Particle Imaging* **2017,** *3* (1).

245. Du, Y.; Lai, P. T.; Leung, C. H.; Pong, P. W. T., Design of superparamagnetic nanoparticles for magnetic particle imaging (MPI). *International journal of molecular sciences* **2013,** *14* (9), 18682-18710.
246. Gonzales, M.; Mitsumori, L. M.; Kushleika, J. V.; Rosenfeld, M. E.; Krishnan, K. M., Cytotoxicity of iron oxide nanoparticles made from the thermal decomposition of organometallics and aqueous phase transfer with Pluronic F127. *Contrast media & molecular imaging* **2010,** *5* (5), 286-293.
247. Saywell, L. G.; Cunningham, B. B., Determination of Iron: Colorimetric o-Phenanthroline Method. *Industrial & Engineering Chemistry Analytical Edition* **1937,** *9* (2), 67-69.
248. Rolle, A.-M.; Hasenberg, M.; Thornton, C. R.; Solouk-Saran, D.; Männ, L.; Weski, J.; Maurer, A.; Fischer, E.; Spycher, P. R.; Schibli, R.; Boschetti, F.; Stegemann-Koniszewski, S.; Bruder, D.; Severin, G. W.; Autenrieth, S. E.; Krappmann, S.; Davies, G.; Pichler, B. J.; Gunzer, M.; Wiehr, S., ImmunoPET/MR imaging allows specific detection of Aspergillus fumigatus lung infection in vivo. *Proceedings of the National Academy of Sciences* **2016,** *113* (8), E1026-E1033.
249. Zhao, C.; Mendive-Tapia, L.; Vendrell, M., Fluorescent peptides for imaging of fungal cells. *Arch. Biochem. Biophys.* **2019,** *661*, 187-195.
250. Morisse, H.; Heyman, L.; Salaün, M.; Favennec, L.; Picquenot, J. M.; Bohn, P.; Thiberville, L., In vivo molecular microimaging of pulmonary aspergillosis. *Med. Mycol.* **2013,** *51* (4), 352-360.
251. Ambati, S.; Ferarro, A. R.; Kang, S. E.; Lin, J.; Lin, X.; Momany, M.; Lewis, Z. A.; Meagher, R. B., Dectin-1-Targeted Antifungal Liposomes Exhibit Enhanced Efficacy. *mSphere* **2019,** *4* (1), e00025-19.
252. Drummond, R. A.; Brown, G. D., The role of Dectin-1 in the host defence against fungal infections. *Curr. Opin. Microbiol.* **2011,** *14* (4), 392-399.
253. Adams, E. L.; Rice, P. J.; Graves, B.; Ensley, H. E.; Yu, H.; Brown, G. D.; Gordon, S.; Monteiro, M. A.; Papp-Szabo, E.; Lowman, D. W.; Power, T. D.; Wempe, M. F.; Williams, D. L., Differential High-Affinity Interaction of Dectin-1 with Natural or Synthetic Glucans Is Dependent upon Primary Structure and Is Influenced by Polymer Chain Length and Side-Chain Branching. *J. Pharmacol. Exp. Ther.* **2008,** *325* (1), 115-123.
254. Lin, J.; Wester, M. J.; Graus, M. S.; Lidke, K. A.; Neumann, A. K., Nanoscopic cell-wall architecture of an immunogenic ligand in Candida albicans during antifungal drug treatment. *Molecular Biology of the Cell* **2016,** *27* (6), 1002-1014.
255. Esteban, A.; Popp, M. W.; Vyas, V. K.; Strijbis, K.; Ploegh, H. L.; Fink, G. R., Fungal recognition is mediated by the association of dectin-1 and galectin-3 in macrophages. *Proceedings of the National Academy of Sciences* **2011,** *108* (34), 14270-14275.
256. Rieber, N.; Singh, A.; Öz, H.; Carevic, M.; Bouzani, M.; Amich, J.; Ost, M.; Ye, Z.; Ballbach, M.; Schäfer, I.; Mezger, M.; Klimosch, S. N.; Weber, A. N. R.; Handgretinger, R.; Krappmann, S.; Liese, J.; Engeholm, M.; Schüle, R.; Salih, H. R.; Marodi, L.; Speckmann, C.; Grimbacher, B.; Ruland, J.; Brown, G. D.; Beilhack, A.; Loeffler, J.; Hartl, D., Pathogenic fungi regulate immunity by inducing neutrophilic myeloid-derived suppressor cells. *Cell Host Microbe* **2015,** *17* (4), 507-514.
257. Graham, L. M.; Tsoni, S. V.; Willment, J. A.; Williams, D. L.; Taylor, P. R.; Gordon, S.; Dennehy, K.; Brown, G. D., Soluble Dectin-1 as a tool to detect β-glucans. *J. Immunol. Methods* **2006,** *314* (1), 164-169.
258. Kumar, S.; Aaron, J.; Sokolov, K., Directional conjugation of antibodies to nanoparticles for synthesis of multiplexed optical contrast agents with both delivery

and targeting moieties. *Nature Protocols* **2008,** *3*, 314.
259. Xue, Y.; Li, X.; Li, H.; Zhang, W., Quantifying thiol–gold interactions towards the efficient strength control. *Nature Communications* **2014,** *5*, 4348.
260. Feineis, S.; Lutz, J.; Heffele, L.; Endl, E.; Albrecht, K.; Groll, J., Thioether–Polyglycidol as Multivalent and Multifunctional Coating System for Gold Nanoparticles. *Adv. Mater.* **2018,** *30* (8), 1704972.
261. Wang, F.-a.; Lakshmipriya, T.; Gopinath, S. C. B., Red Spectral Shift in Sensitive Colorimetric Detection of Tuberculosis by ESAT-6 Antigen-Antibody Complex: a New Strategy with Gold Nanoparticle. *Nanoscale Research Letters* **2018,** *13* (1), 331.
262. Hermanson, G. T., Chapter 20 - Antibody Modification and Conjugation. In *Bioconjugate Techniques (Second Edition)*, Hermanson, G. T., Ed. Academic Press: New York, 2008; pp 783-823.
263. Tassa, C.; Duffner, J. L.; Lewis, T. A.; Weissleder, R.; Schreiber, S. L.; Koehler, A. N.; Shaw, S. Y., Binding affinity and kinetic analysis of targeted small molecule-modified nanoparticles. *Bioconj. Chem.* **2010,** *21* (1), 14-19.
264. Drescher, D. G.; Selvakumar, D.; Drescher, M. J., Chapter One - Analysis of Protein Interactions by Surface Plasmon Resonance. In *Advances in Protein Chemistry and Structural Biology*, Donev, R., Ed. Academic Press: 2018; Vol. 110, pp 1-30.
265. Drescher, D. G.; Ramakrishnan, N. A.; Drescher, M. J., Surface plasmon resonance (SPR) analysis of binding interactions of proteins in inner-ear sensory epithelia. *Methods in molecular biology (Clifton, N.J.)* **2009,** *493*, 323-343.
266. Hosotsubo, H.; Hosotsubo, K., Improved high-performance liquid chromatographic determination of Amphotericin B in human serum and plasma. *J. Pharm. Biomed. Anal.* **1989,** *7* (8), 975-979.
267. Tumanski, S., Induction coil sensors—a review. *Meas. Sci. Technol.* **2007,** *18* (3), R31-R46.
268. Vogel, P.; Herz, S.; Kampf, T.; Rückert, M. A.; Bley, T. A.; Behr, V. C., Low Latency Real-time Reconstruction for MPI Systems. *Int. J. Magn. Part. Imag.* **2017,** *3*.
269. Pinto-Almeida, A.; Mendes, T.; Armada, A.; Belo, S.; Carrilho, E.; Viveiros, M.; Afonso, A., The Role of Efflux Pumps in Schistosoma mansoni Praziquantel Resistant Phenotype. *PLoS ONE* **2015,** *10* (10), e0140147.
270. Gudbjartsson, H.; Patz, S., The Rician distribution of noisy MRI data. *Magn. Reson. Med.* **1995,** *34* (6), 910-914.
271. Venier-Julienne, M. C.; Benoît, J. P., Preparation, purification and morphology of polymeric nanoparticles as drug carriers. *Pharm. Acta Helv.* **1996,** *71* (2), 121-128.
272. Hassan, P. A.; Rana, S.; Verma, G., Making Sense of Brownian Motion: Colloid Characterization by Dynamic Light Scattering. *Langmuir* **2015,** *31* (1), 3-12.
273. Evans, B. C.; Nelson, C. E.; Yu, S. S.; Beavers, K. R.; Kim, A. J.; Li, H.; Nelson, H. M.; Giorgio, T. D.; Duvall, C. L., Ex vivo red blood cell hemolysis assay for the evaluation of pH-responsive endosomolytic agents for cytosolic delivery of biomacromolecular drugs. *JoVe-J. Vis. Exp.* **2013,** (73), e50166-e50166.
274. Hearn, V. M.; Mackenzie, D. W. R., Mycelial Antigens from Two Strains of Aspergillus fumigatus: An Analysis by Two-Dimensional Immunoelectrophoresis: Myzeliale Antigene aus zwei Stämmen von Asperillus fumigatus: Eke Analyse rnit der zweidimensionalen Immunelektrophorese. *Mycoses* **1980,** *23* (10), 549-562.
275. Pfaller, M. A., *Reference Method for Broth Dilution Antifungal Susceptibility Testing of Conidium-forming Filamentous Fungi: Proposed Standard*. NCCLS: 1998.
276. O'Toole, G. A.; Kolter, R., Initiation of biofilm formation in Pseudomonas fluorescens WCS365 proceeds via multiple, convergent signalling pathways: a genetic analysis.

Mol. Microbiol. **1998,** *28* (3), 449-461.